D5.3 Interaction between currents, wave, structure and subsoil

Christensen, Erik Damgaard; Sumer, B. Mutlu; Schouten, Jan-Joost; Kirca, Özgür; Petersen, Ole; Jensen, Bjarne; Carstensen, Stefan; Baykal, Cüneyt; Tralli, Aldo; Chen, Hao

Total number of authors:
19

Publication date:
2015

Document Version
Publisher's PDF, also known as Version of record

MERMAID

mermaidproject.eu

Seventh Framework Programme
Theme [OCEAN.2011-1]
"Innovative Multi-purpose off-shore platforms: planning, design and operation"
Grant Agreement no.: 288710
Start date of project*: 01 Jan 2012 - Duration: 48 month*

D5.3 Interaction between currents, wave, structure and subsoil

Deliverable: D5.3 Interaction between currents, wave, structure and subsoil	
Nature of the Deliverable:	Report/D5.3
Due date of the Deliverable:	July 2014
Actual Submission Date:	26th of February 2015
Dissemination Level:	Public
Produced by:	Erik Damgaard Christensen
Contributors:	Erik Damgaard Christensen, B. Mutlu Sumer, Jan-Joost Schouten, V.S. Özgür Kirca, Ole Petersen, Bjarne Jensen, Stefan Carstensen, Cüneyt Baykal, Aldo Tralli, Hao Chen, Pietro Danilo Tomaselli, Thor Ugelvig Petersen, Jørgen Fredsøe, Tim C. Raaijmakers, Andreas Kortenhaus, Jacob Hjelmager Jensen, Sina Saremi, Karsten Bolding, Hans Burchard
Work Package Leader Responsible:	Jan-Joost Schouten (Deltares) Erik Damgaard Christensen
Reviewed by:	B Mutlu Sumer/Erik Damgaard Christensen

Version	Date	Revised Pages	Description of Changes
1.0	14 May 2014		1st layout released, (J. Schouten)
1.1	26 Feb. 2015	All	Final report

Table of contents

1 Introduction 4
1.1 Background 4
1.2 MERMAID and Work Package 5 4
1.2.1 Deliverable D5.3 4
2 Dispersion processes related to Multi-use offshore platforms 7
2.1 Modelling of dispersion processes related to marine operations 7
2.1.1 Introduction 7
2.1.2 Spill during dredging operations 9
2.1.3 Sedimentation inside the barge 9
2.1.4 Overflow plumes 11
2.1.5 Air entrainment in overflow shafts 17
2.1.6 Dumping of sediment spoils 19
2.1.7 Conclusions 21
2.1.8 References 21
2.2 Dispersion in wave boundary layers 23
2.2.1 The process of longitudinal dispersion in an oscillatory boundary layer 24
2.2.2 Description of the numerical model 26
2.2.3 Results 30
2.2.4 Summary and Conclusion 39
2.2.5 References 40
3 Current with varying density interaction with vertical piles 43
3.1 Physical and numerical modelling 43
3.1.1 Physical models 46
3.1.2 Numerical models 51
3.2 Parameterisation of the effect of unresolved structures on stratified flow 66
3.2.3 Discussion 72
3.3 Modelling of mixing of saline layers, Ocean-models 73
3.4 References 79
3.5 Modelling of flow through a mussel farm 82
3.5.1 Introduction 82
3.5.2 Methodologies 83
3.5.3 Example applications 85
3.5.4 Borssele Offshore Wind Farm 91
3.5.5 Discussion and further work 94

3.5.6 References 95
4 Wave-structure interaction with structural components in a Multi-Use platform 97
4.1 Hydraulic model tests on OWC modules of platforms 97
4.1.1 Literature review of OWC devices 97
4.1.2 Set-up of model tests and test programme 100
4.2 Breaking wave interaction with secondary structures- physical and numerical analyses 103
4.2.1 Introduction 103
4.2.2 Breaking Waves 103
4.2.3 Air-entrainment in breaking waves 107
4.2.4 Wave loads on a vertical structure 110
4.2.5 Breaking waves-induced forces 112
4.2.6 A CFD approach to design the secondary structures of MUP's 113
4.2.7 References 119
4.3 Methods for current and wave interaction with fish cages: A review 123
4.3.1 Introduction 123
4.3.2 Main parameters in the analysis of fish cages 124
4.3.3 Hydrodynamic Flow Model 127
4.3.4 Hydrodynamic force model 128
4.3.5 Structural model 130
4.3.6 Hydroelastic analysis of net structure 132
4.3.7 Conclusion 133
4.3.8 References 133
5 Scour around typical Multi-use offshore platforms structures 136
5.1 Scour and backfilling around foundations 136
5.1.1 Highlights of numerical modelling of scour. A general review 137
5.1.2 Numerical modelling of scour and backfilling in the MERMAID project 139
5.1.3 List of publications produced during the project cycle on the topic 143
5.1.4 References 143
5.2 Edge Scour 146
5.2.1 References: 151
6 Discussion 152
6.1 References 153

1 Introduction

This chapter gives an introduction to deliverable D5.3 - Interaction between currents, waves, structure and subsoil – with respect to the MERMAID project. The deliverable focuses on the conditions in European waters such as the four sites that is addressed in the MERMAID project. The most important physical processes will be described and ways to technical address the challenges will be proposed.

1.1 Background

European oceans will be subject to massive development of marine infrastructure in the near future. Most important will be offshore wind farms, expansion of electricity connections, and further development and implementation of marine aquaculture. This will also lead to an increased need for marine infrastructure to support installation and the on-going operation of the facilities. However both economical costs and environmental impact have to be reduced in order to increase the feasibility of the use of ocean space.

Marine structures for offshore wind farms and aquaculture have to be installed at various sites and on much larger scale than earlier implementation of offshore structures in order to fulfil EU strategies (1) for reduction of fossil-based energy and (2) to become a major player in sustainable aquaculture. All these aspects are considered under the EU-funded project on the multi-use of offshore wind farms called “MERMAID”.

The FP7 Mermaid project deals with multi-use platforms to be located far offshore in European waters. In order to make the findings of the Mermaid project most practical, a special focus is on four specific sites. These sites are located in the Baltic Sea, North Sea, Atlantic Sea and the Mediterranean Sea.

1.2 MERMAID and Work Package 5

When studying the feasibility of an offshore multi-use platform design the interaction between the platform and the environment should be analysed in detail for reasons of technical and economic feasibility, environmental impact and assessing the potential of incorporating multiple functionalities including logistical aspects. Work package 5 of the MERMAID project focusses on the interaction between the multi-use offshore platforms (MUP), the meteorological and hydrodynamic conditions as well as the seabed. These environmental conditions vary significantly along the European seas.

The main objective of Work Package 5 (WP 5) is to support the design phase of Multi-Use offshore Platforms (MUP’s) with advanced and applicable tools based on extensive experience, available data and proposed dedicated research topics to be assessed under this WP 5.

1.2.1 Deliverable D5.3

For developing innovative designs of an offshore multi-use platform the interaction between the platform and the environment should be carefully analysed for reasons of design, environment impact and assessment of the potential for incorporating multiple functionality. Because of the fragmented nature of different functionalities and the incompatibility of the temporal and geographic scales the relevant processes account for, there is a need to develop new approaches.

Dredging during installation of offshore structures, spill and dispersion of fish food in aquaculture, deposition of dredged material and sedimentation of food and waste in aquaculture are all important aspects in the construction of Multi-use offshore platforms. In general the spreading of conservative matters on a medium to regional scale can often be analysed with today's mathematical models. However, the knowledge on the near field phenomena is not understood to the same degree. For instance the re-suspension of different substances, transport of fines into mussel farms, the near field settling of dredged materials are all areas which needs more attention. Further when it settles to the seabed the material will be under the influence of currents and waves. Especially the effect of waves needed more attention, and this topic has therefore been addressed in the project.

The offshore environment is typical more harsh than closer to the coastline. Further some of the structures in question for a MUOP have typical been used in more sheltered areas. This is in particular true for devices for aquaculture. Therefore the movement from sheltered coastal areas to exposed offshore environments calls for research and development making this transmission feasible. Many processes related to wave interactions with offshore structures are well understood. However the effect of breaking waves and in particular spilling breakers and their effect on structures is not known in detail. This can lead to very conservative and expensive design or even vulnerable designs. Therefore methodologies on wave, current structure interaction are an important aspect of the design of MUOP. Especially the interaction with extreme waves and spilling breakers that is common in offshore regions. A substantial part of the structural elements in for instance aquaculture structures are situated at the surface of the waves wherefore the interaction with the wave/breaking waves is of high importance. Methodologies dealing with these processes, such as physical model experiments and computational fluid dynamics (CFD), are addressed in this report.

A phenomenon often very important for structures at sea is the interaction between the structure and seabed, called scour. Scour is the erosion of the seabed at the foundations of offshore structures (e.g. mono-piles or gravity-based-structures) and cables, under the influence of waves and currents. For single mono-piles the scour development is generally well known. However for more complex structures and in particular multiple structures only little are known. Depending on the type of supporting structures for the wind turbines, e.g. are mono-piles or a four-legged jacket, and the local hydrodynamic conditions, the main objectives of the local scour assessment will be to (1) predict scour depths at the foundations as input for the structural design, (2) conceptual design and optimization of a scour protection layout for the foundations on the basis of analytical formulae, expert judgement and (3) provide a conceptual design for cable protection (e.g. to prevent freespan).

A third phenomenon concerning the interaction between the structure and seabed is liquefaction, which is a process, characterized by the loss of shearing resistance of initially solid soil skeleton. Liquefaction is preceded by progressive pore pressure generation and macroscopic weakening of the soil skeleton (degradation of its mechanical properties). This phenomenon may be caused either by cyclic loads, as those induced by water waves or earthquake excitements, or by monotonic loads (static liquefaction) when the initial state of soil is contractive.

This report describes studies focusing on the interaction between currents, waves, the subsoil and the multi-use offshore structure. The purpose of these studies was in general support the analyses of the technical feasibility of the MUOP. This report is a summary of all the detailed studies conducted under MERMAID on this interaction. Each study forms a "building block" for feasible design.

Together with the deliverable D5.2 this document forms the basis of guidelines for seabed support structure interaction (D5.4), guidelines on study approaches to support future feasibility studies of multi-use offshore platforms.

2 Dispersion processes related to Multi-use offshore platforms

2.1 Modelling of dispersion processes related to marine operations

Jacob Hjelmager Jensen, Sina Saremi, DTU-MEK

2.1.1 Introduction

Sustainable energy and resource exploitation in marine environment such as wind farms, wave energy extractors and aquaculture is moving towards massive infrastructural development, which results in a continuously increase in the usage of marine space, economic costs and their environmental impacts. Hence, offshore platforms combining multiple functions within the same infrastructure potentially offer significant economic and environmental benefits. The offshore construction activities including deployment of new structures, reconfiguration of existing platforms etc. are an inevitable part of the activities associated with the development. From an environmental perspective every marine operation, coastal construction or maintenance work contains a potential risk for causing impacts on the surrounding ecosystem, which may be considered positive or negative, good or bad.

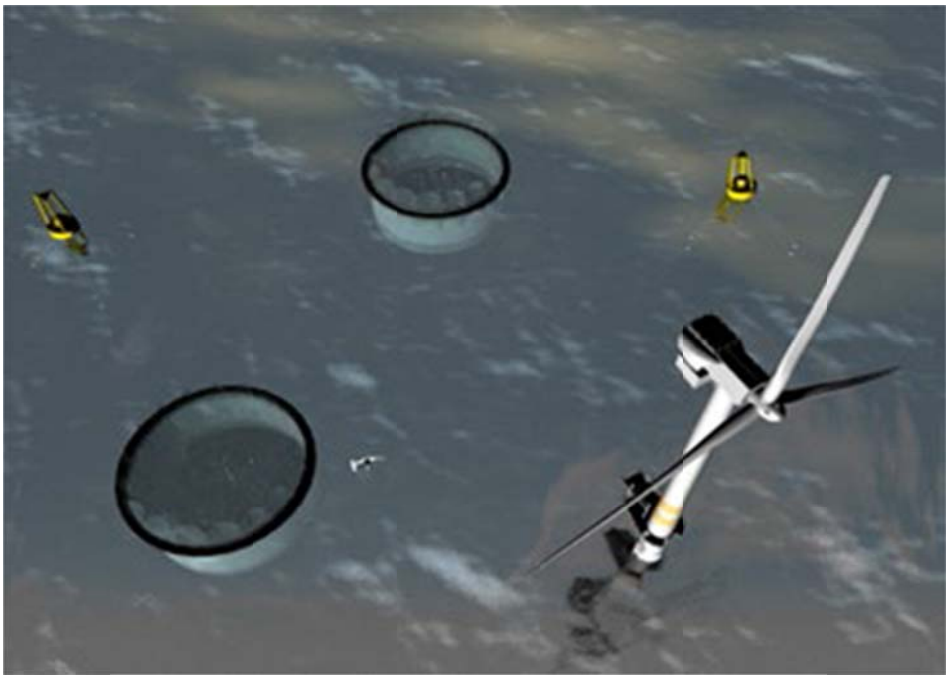

Figure 2.1 Conceptual design of multipurpose platforms

Dredging and excavation works are often considered as one of the major sources of environmental impacts. Such activities occur during coastal, estuarine and offshore projects. The sediment spill which overflows from the retaining barge or is released at the excavation grab often introduces high levels of sediment concentration in ambient waters. The coarser constituents of the spill material typically re-settle immediately and within the work area, but the finer fractions remain in suspension for longer periods. Depending on the local marine wildlife and the sensitivity of the

ecosystem to changes in environmental conditions such as that imposed by changes in turbidity, the spill during dredging and excavation operations is considered as a negative environmental impact.

Figure 2.2 Offshore dredging works

The amount of spill (in terms of volume rate and concentration) depends on the type of dredged material and the dredging/excavation equipment. The fine material may be advected by the ambient current and waves creating plumes of turbidity that can be dispersed into far-field waters. As a result, not only the environmental receptors in vicinity of the operation, but also receptors found further away from the project area may be exposed to these plumes. Advection, dispersion and fate of the sediment plume are function of the spill rate and its concentration, type of the sediment being spilled at the source, and the local conditions (waves, currents, water depth, etc.).

Disturbance of the benthic life and sediment re-suspension induced by the dredgers draghead is also considered as a potential risk to the environment. The impact from the draghead on the benthic life is more relevant in areas where the dredging takes place for the first time or if dredging recurs over considerably long return periods.

Other environmentally risky operations include the transportation and displacement of the dredged material. Unless the material is used for reclamation or for other construction purposes, a common approach is to relocate the dredged material on a barge to a designated disposal zone and dump it here. The disposal of the dredged material can either be through several valves at the bottom of the barge, or the use of quasi-instantaneous releases from split hoppers. The lower water content of the released material results in the formation of a density driven plume descending towards the seabed. The plume undergoes mixing and entrainment during its plunging, and this results in stripping and dispersion of its constituents as it descends. The coarse material in the load deposits in the vicinity of the dumping location, however the finer fractions remain longer in the water and it is these finer fractions that form the dispersive (passive) turbidity plume.

The environmental concerns with dumping of material are both on dispersion of fine material in form of turbidity plumes and the burial of benthic life at the dump site. The selection of suitable dump sites adhere to strict environmental appraisals, and therefore it's always desirable that the whole released material ends up in the designated area rather than being spread over a large area. Again, the behaviour of the disposal plumes is a function of both the characteristics of the released

material (concentration, type of material, etc.) and the local conditions (water depth, currents, waves, etc.).

In the following the main processes involved in sedimentation, overflow and disposal of dredged material during dredging and excavation activities will be described in more details and the influence of different driving parameters on the deposition and dispersion behavior of the sediments will be highlighted.

2.1.2 Spill during dredging operations

Dislodging the insitu material in dredging and excavation works is done by various types of dredging equipment with different capabilities. The most common types of dredging equipment are the TSHD (Trailing suction hopper dredger), cutter suction dredgers and the mechanical dredgers. Regardless of the dislodging technique, the dredged material (mixture of water and sediment) are often loaded into a hopper. The loading continues even after the hopper is filled up with the sediment-water mixture. The heavier fractions settle in the hopper and the finer fractions of the material are more likely to follow the excess water overflowing.

Figure 2.3 Trailing suction hopper dredger, Right: Mechanical Dredger

This loading operation continues until the desired amount of solid material has been achieved. The overflow discharging into the ambient waters result in formation of turbidity plumes close to the dredging site. The behavior of the overflow plume depends on the concentration and sediment characteristics. The characteristics of the overflowing sediment depend on the sedimentation and mixing processes occurring inside the hopper. The suction dredgers are equipped with suction pipes lowered down to the seabed with dragheads or cutters at their end. The disturbance of the benthic life and sediment re-suspension caused by the dredgers draghead or cutters may also result in adverse environmental impacts. Mechanical dredgers, either self-propelled or pontoon-mounted, use a backhoe or grab to dislodge the material and transfer them up into the barge. The spillage of sediment from the grab during its upward movement towards the water surface is another source of sediment release. The use of environmental friendly closed grabs prevents to some extent the spillage during the rising phase.

2.1.3 Sedimentation inside the barge

Being the source of the overflow discharge, it’s important to identify and describe the main mechanisms affecting the sedimentation and mixing inside the barge and their effect on the overflow mixture. Among the main mechanisms are the hindered settling pronounced in high

concentrations, mixing due to turbulence, overall flow patterns inside the barge and flocculation of cohesive sediments and breakup of lumps.

Figure 2.4 Multi-inlet barge

The dimensions of the barge, filling rate and arrangement of the inlet pipes also influence the sedimentation and overflow. In order to have an evenly distributed load in the barge, the inflow of dredged material is always tried to be as uniform as possible inducing highest possible mixing. Due to highly mixed environment and inflow of highly concentrated mixture from above into the barge, the concentration profiles in the barge are close to uniform. The average concentration inside the barge begins to rise as filling process starts, and reaches an equilibrium value which indicates the concentration at the overflow discharge. Owing to this, Jensen and Saremi (2014) developed a simple analytical model based on an integrated approach which estimates the variation in average sediment concentration inside the barge. The model results showed that the effect of the above mentioned mechanisms on final equilibrium concentration inside the barge (which is an indication of overflow concentrations) can be summarized in the non-dimensional loading factor $\beta = \frac{A \cdot w_s}{Q}$, where A is the total area of the barge, w_s is the sediments fall velocity and Q is the inflow rate into the barge. The loading factor is the ratio between the settling capacity inside the barge and the infilling rate. Small values of β is an indication of excess inflow of dredged material into the barge compare to its settling capacity, which then results in higher overflow concentrations. One of the main parameters affecting the accuracy of the estimation of overflow concentrations and sedimentation in a hopper is the sediments falling velocity. This was treated in Jensen and Saremi (2015). Aside from the overall effect of mixtures concentration on the hindered settling, the size variation in the mixture and the flocculation mechanisms also affect the settling rates considerably. The larger fractions with higher falling velocities create stronger return flows which results in further hindering of the finer fractions. Therefore, the size distribution of inflowing dredged material into the barge differs from the overflowing mixture. Therefore, when estimating the size distribution of overflow material, the transition of the mother material during sedimentation inside the barge should be taken into account. In Figure 2.5 the grain size concentration distribution of

inflowing material (initial concentration) and the overflowing material (final equilibrium concentration) has been shown (Jensen and Saremi, 2014).

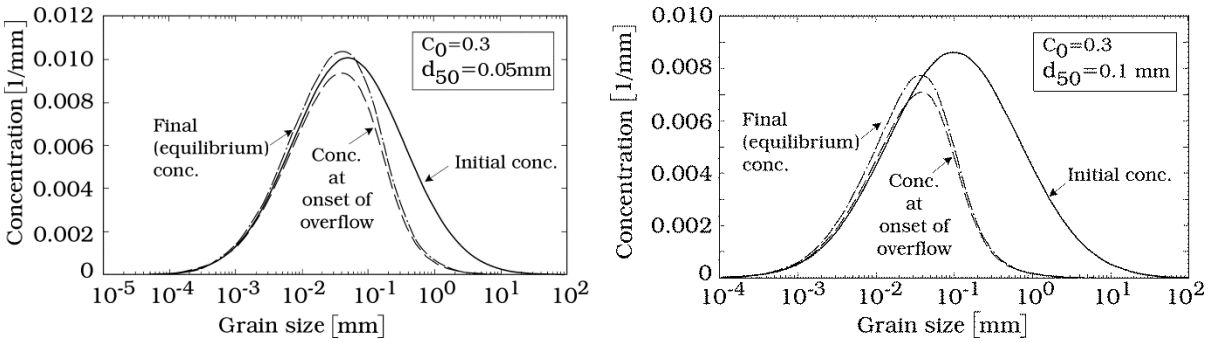

Figure 2.5 Multifraction dredged material concentration distribution. Note the difference in size distribution between initial inflow concentrations and the final overflow concentrations. Left: β=0.2, Right: β=3.0 (Jensen and Saremi, 2014)

Flocculation/breakup mechanisms also affect the sedimentation rates inside the barge, and therefore influence the overflow characteristics. However, due to the site-specific properties of the cohesive material, it is more difficult to parameterize and predict their behaviour in a general way. Considerable part of the flocs breaks up during the transmission from the seabed through the drag head pump and the pipes into the barge. Depending on the dimensions and the flow patterns inside the barge, they may undergo further break up, or in contrary begin to flocculate while settling inside the barge and result in higher settling rates. Accurate information about the in situ material characteristics is required in order to estimate the cohesive behaviour of the sediments.

2.1.4 **Overflow plumes**

The spill of dredged material into ambient waters during the dredging/excavation works, which contributes in formation of turbidity plumes, can be either from the barge overflow, or the material lost from the grab/backhoe while moving towards the surface. The two mentioned sources of sediment plumes, (although originating from the same in-situ material) have different sediment constituents. The size distribution of the barge overflow material contains more fine fractions, as the coarser fractions have already settled inside the barge (see previous section), whereas the grain distribution of the material spilled from the grabs follows the same distribution as of the mother material at the seabed. Therefore, the spill from the grabs is more likely to settle faster and show less dispersive behaviour compared to the material being overflowed from the barge. However, the movement of the grab over the whole water column may enhance the mixing of the spilled material. The overflow discharge from the barge enters the ambient water either from the surface (pouring from the sides of the barge) or from the bottom of the barge (through overflow shafts rigged inside the barge). The latter results in less dispersive overflow plumes, because it avoids the surface plunging and experiences smaller water depths. It's also the most common practice in trailer hopper dredgers.

Figure 2.6 Left: Overflow plume, Right: Spill from the grab

Regardless of type of the dredger and overflow configurations, the release of highly concentrated material into ambient waters shows certain behaviours and is affected by few main parameters. The presence of a continuous momentum source (falling though the overflow shaft, or plunging into water surface) characterizes the overflow discharge as a negatively buoyant jet entering the ambient environment with a downward velocity (W). If the ambient currents are negligible, the densimetric Froude number (F_d) is the measure to indicate if the overflow mixture is driven by the density gradients and settles with the least entrainment and dilution ($F_d < 1$), or is driven by the inertial forces and therefore due to the high levels of mixing and entrainment, the released material undergo excessive amounts of dilution and dispersion in the surrounding environment ($F_d > 1$). The desnsimetric Froude number is defined as the ratio between the inertial and buoyancy forces driving a buoyant jet:

$$F_d = \frac{W}{\sqrt{gd\frac{\rho_m - \rho_a}{\rho_a}}} \tag{2.1}$$

Where d is the initial diameter of the intruding jet into the ambient water (can be interpreted as the overflow shaft diameter), ρ_m is the density of the overflow mixture, ρ_a is the ambient density and g is the gravitational acceleration.

The second governing parameter influencing the behaviour of the overflow plumes is the presence of the local currents or similarly the trailing speed of the hoppers. The translation and shear dispersion due to the external currents interact with the entrainment mechanisms of the buoyant jet (the released overflow material) and enhances the dispersion and dilution rates inside the plume.

The effect of ambient currents (including vessel speeds) is presented by the non-dimensional velocity ratio ϵ, which is the ratio between the mean cross flow velocity ($\vec{U}$) and the buoyant jet velocity ($\overrightarrow{W}$):

$$\epsilon = \frac{\vec{U}}{\overrightarrow{W}} \tag{2.2}$$

The undesirable combination of a large velocity ratio and a fully inertial driven overflow ($F_d > 1$) results in fully mixed overflow material and quickly forms the turbidity plumes.

The water depth is another local parameter which influences the behaviour of the overflow plumes. In general, deeper the water becomes, both the entrainment mechanisms of the buoyant overflow jet itself, and the shear dispersion and translation due to the ambient currents have more time to dilute

and disperse the material before it reaches the bottom and rests over the bed. If the water is so deep that the plume reaches to a certain level of dilution where it loses its consistent “plume” properties (cannot be considered anymore as a negatively buoyant body), then the individual particles begin to fall out (rain out) with their own fall velocities and it can be considered as fully dispersed/mixed swarm of particles.

Marine dredging operations most often take place under calm sea conditions where extreme wave events don’t exist. Therefore the effect of waves on the plumes behaviour is limited to helical displacements beneath the crests and troughs and net effect of this motion on the overall descend and dispersion of the plume is negligible.

The detailed 3-dimensional computational fluid dynamic (CFD) tools are most accurate modelling tools in studying the near field behaviour of the buoyant jet/plumes in ambient environment. The high levels of sediment concentration in the overflow and disposal plumes indicates significant dynamic and occupancy interactions in between the two phases (water, sediment), which then requires a multiphase two-way coupled solution.

The application of the so-called “Boussinesq ” approximation which approximates the presence of the dispersing phase only to that of change in gravitational force on the flow, is insufficient. Including the flow displacement due to the sediment fall velocity and the forces due to the transient gradients in the density and momentum transfers due to the falling sediments are necessary for detailed calculations of the processes involved in the nearfield behaviour of the plumes. The CFD model developed, evaluated and used in Saremi (2014) to study the nearfield behaviour of the overflow plumes is based on the multiphase mixture method introduced by Ishii (2006). The model uses the Large Eddy Simulation (LES) approach to resolve the turbulent eddies and solves the equations of conservation of mass and momentum for the mixture as a whole. The model was used to evaluate the effect of governing parameters on overflow plumes nearfield behaviour. Below are graphical presentations of the model results of overflow plumes from the hoppers under stagnant and ambient currents.

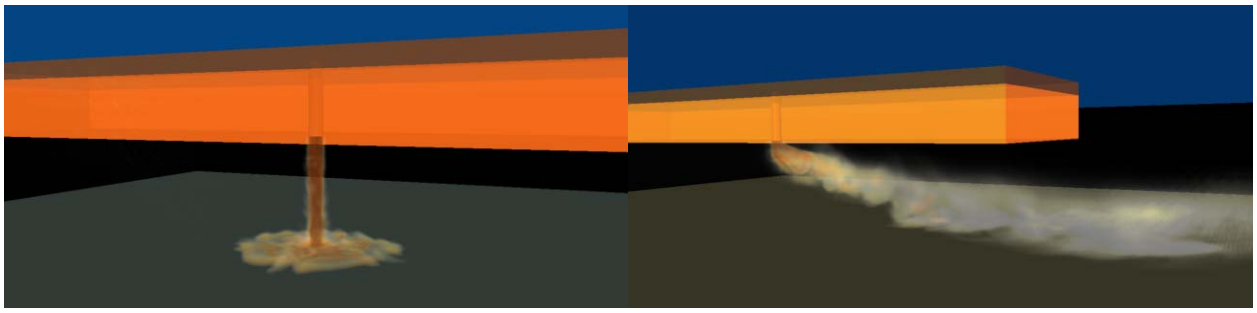

Figure 2.7 CFD simulations of the overflow plume. Left: Stagnant ambient, Right: Presence of ambient currents (Saremi, 2014)

The effects of three main parameters densimetric Froude number (F_d), velocity ratio (ϵ) and water depth (D) have been investigated and discussed thoroughly in Saremi (2014). Hereby the effect of the mentioned parameters will be presented and described briefly. In order to study the effect of the mentioned parameters on the settling and dispersive behavior of the overflow plumes, a down

scaled model ($\lambda = 100$) corresponding to a $18000\ m^3$ TSHD at $20\ m$ water depth with a single overflow pipe having diameter of 2.5 m has been modelled. Figure 8 presents the effect of velocity ratio (ϵ), by depicting the position of the centroid of the overflow plume under different velocity ratios, having the same densimetric Froude number ($F_d = 2.2$) and the same water depth ($D/d = 8$). The results show that at higher velocity ratios the plume is distracted earlier and the setting rate is decreased. In the extreme case of $\epsilon = 2$, the plume never settles and enters the mixed state immediately.

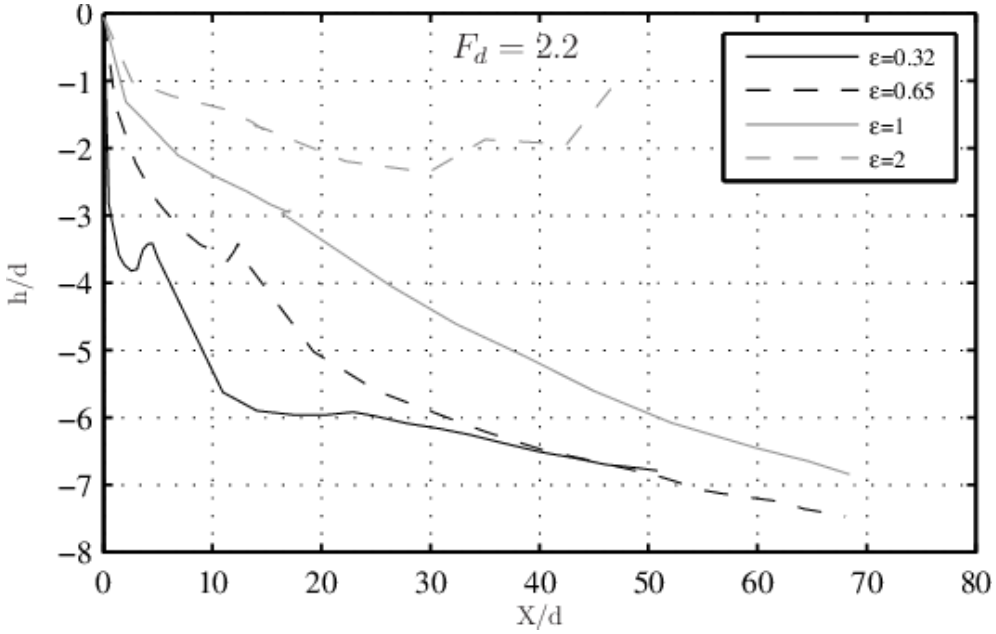

Figure 2.8 The path of plumes centroid with different velocity ratios under the same Fd (Saremi, 2014)

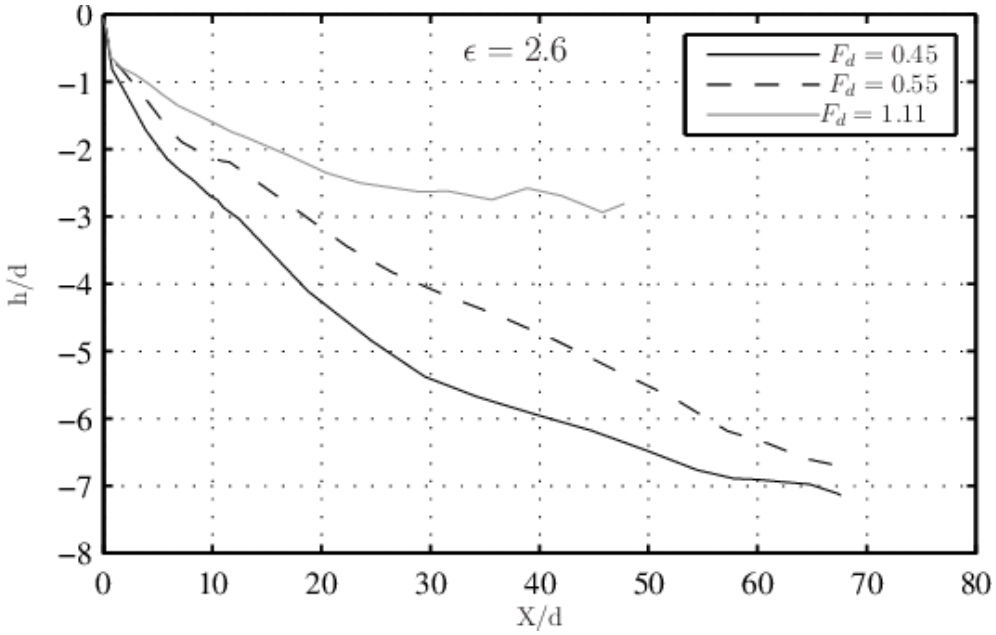

Figure 2.9 The path of plumes centroid with different F_d values under the same velocity ratio (Saremi, 2014)

The other characteristic parameter which describes the state and the behaviour of the overflow plume is the densimetric Froude number, which is function of the density of the overflowing mixture and the overflow rate entering the ambient environment. The latter is less variable, because it strongly depends on the dimensions of the overflow shaft, the barge draught and the rate which the barge is being filled. The density of the overflow mixture however is direct function of the overflow concentration which varies based on the type of the material being dredged. Figure 9 presents the effect of densimetric Froude number (F_d), by depicting the position of the centroid of the overflow plume under different Froude numbers, having the same velocity ratio ($\epsilon = 2.6$) and the same water depth ($D/d = 8$). In the presence of ambient currents, densimetric Froude numbers less than unity represent the dominance of buoyancy forces, which cause the plume to settle with least dilution and mixing. On the other hand, higher values of F_d means there exists considerable amount of mixing due to dominance of inertial forces in forces driving the plume. Combined with the excess shear and dispersion due to the ambient currents, it can be seen in Figure 2.9 that the case with $F_d > 1$ ends up in a fully mixed state and does not settle.

The other important parameter in determining the plumes behaviour is the water depth. It can be interpreted as the time available for the plume to undergo further entrainment and dilution due to both its own inertia and the ambient velocity field. This can be seen clearly in Figure 2.10, where the behavior of the plume under stagnant conditions in different water depths is depicted by means of shaded concentration contours. It can be seen that under similar conditions ($\epsilon = 0, F_d = 2.2$), deeper the water becomes, the plume becomes further mixed and dispersed.

(a) $D/d = 8$

(b) $D/d = 16$

(c) $D/d = 32$

(d) $D/d = 64$

Figure 2.10 CFD simulations of overflow discharge in stagnant water under different water depths. Fd=2.2 (Saremi, 2014)

In the presence of ambient currents ($\epsilon > 0$), the plume reacts to the change in water depth in a similar way as in the stagnant ambient conditions, as long as it is buoyancy driven. In higher velocity ratios the overflow plume begins to ignore the depth as it goes into the fully mixed stage

almost immediately. This can be seen in Figure 2.11, where in cases with $\epsilon < 1$ the plume follows the depth and in the case with $\epsilon > 1$ no matter what the water depth is, the plume follows the same path.

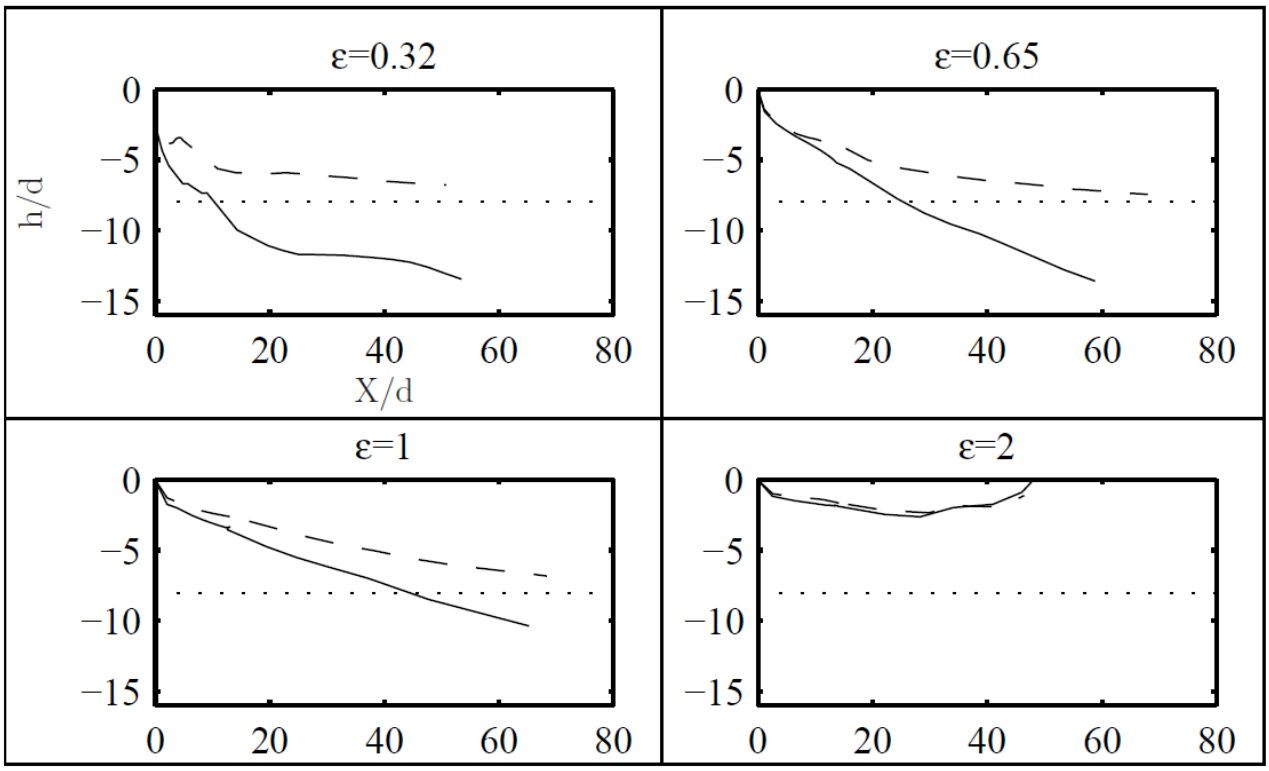

Figure 2.11 The path of plumes centroid at two water depths, D/d=8 (dashed line) and D/d=16 (solid line). The dotted line represents the position of the bed in the shallow case. Fd=2.2 (Saremi, 2014)

2.1.5 **Air entrainment in overflow shafts**

The operation of suction hopper dredgers is based on continuous loading of dredged material into the hopper, which is most often appended with the overflow of excess mixture of water and fine sediment. Earlier the overflow structures in the hoppers were simply of the weir-type, arranged on the sides of the hopper, where the mixture was released into marine waters. Since then, increased environmental awareness has prompted the design of more environment friendly systems that help reducing the temporal and spatial extend of the turbidity caused by the plumes. One of the first innovations was to relocate the release point further down below the water surface, by installing one or more dropshafts along the hopper. These shafts are usually circular and equipped with telescopic weir providing adjustable overflow rates during the dredging operation (Figure 2.12). The axial flow in dropshafts provokes air entrainment. The trapped air in the overflow mixture, once discharged from the bottom of the dredger, tends to segregate owing to its buoyancy and rises towards the open water surface. This induces an upward stream of bubbles counteracting with the settling solid particles in the mixture. The extra mixing and hindrance due to the rising bubbles rectifies the nearfield dispersion of the plume and drags it towards the surface, increasing the period of impact.

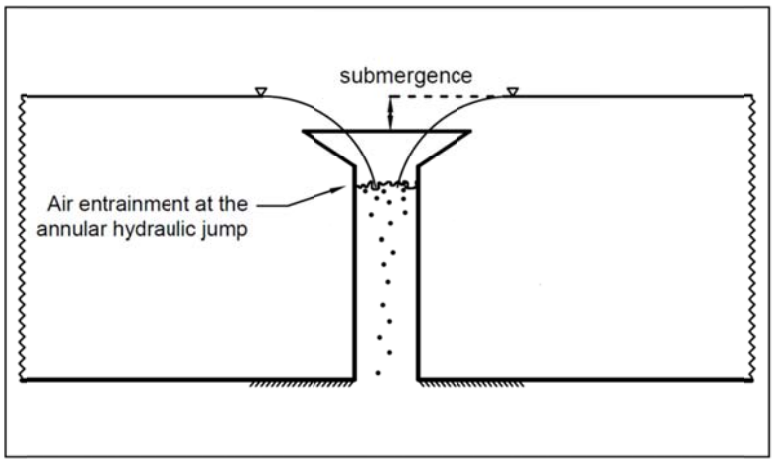

Figure 2.12 Schematic drawing of the overflow structure (Saremi, 2014)

The rate of air entrainment, as discussed in more details in Saremi (2014), decreases by either increasing the submergence of the overflow weir, decreasing the shaft diameter or reducing the Froude number inside the shaft. The physical constraints in the hoppers and the case specificity of different dredging projects limit the adjustability of the submergence level and the shaft diameter. Therefore a more feasible solution is to reduce the Froude number inside the shaft, which can be done by increasing the hydraulic resistance. This approach has been exercised in dredging industry by rigging a butterfly-type valve midway in the overflow shaft which creates a controllable hydraulic resistance inside the shaft by choking the flow. The valve is called the Green Valve or the Turbidity Valve owing to its role in reducing the air entrainment in the overflow mixture and consequently reducing the spatial and temporal extents of the turbidly plumes. In Saremi (2014), by the means of a multiphase CFD model, the performance of the valve has been investigated. In Figure 2.13 a graphical demonstration of the air-water interface from the CFD model results is presented, which shows the effect of the green valve in reducing the entraining air in the shaft. The model results show that the valve reduces the rate of air entrainment inside the shaft, but also results in reduced flow rate, which means it reduces the efficiency of the shafts in overflowing the dredged mixture from the hopper.

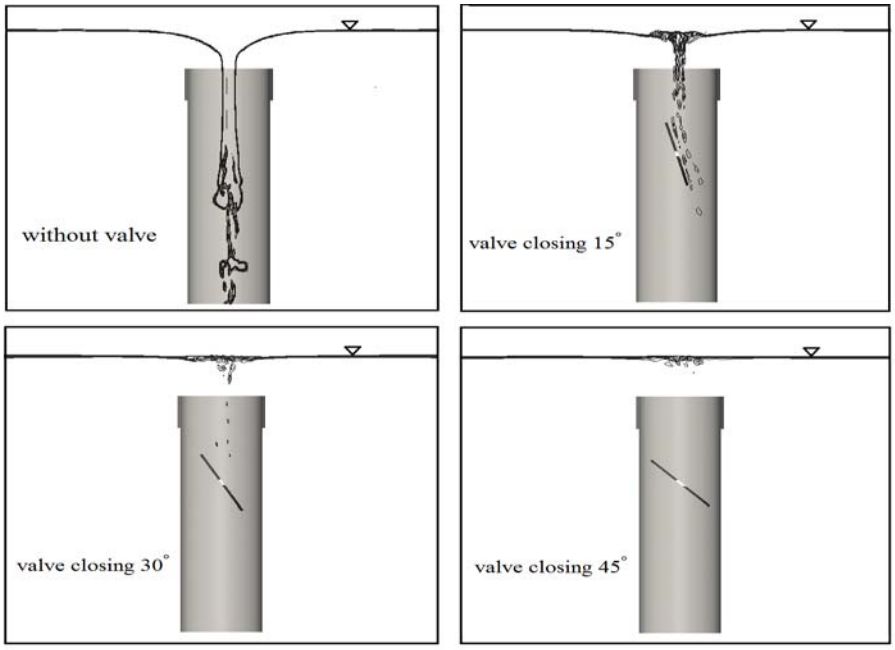

Figure 2.13 CFD simulation of the effect of the Green Valve on air entrainment. (Saremi, 2014)

2.1.6 **Dumping of sediment spoils**

The disposal of the dredged material can either be through number of valves at the bottom of the barge, or a quasi-instantaneous release of the whole material in splitting barges. It is always desired that the released material settle down to the bed at the relocation site as soon as possible with the least possible dispersion and mixing of material in the water column. However, depending on the material characteristics and the ambient conditions, the behaviour of the released material can vary as following.

Figure 2.14 Dredged material ready to dumped from a split hopper, Right: The sediment plume due to dispersion and mixing of fine material after dumping

The disposal material has a very high initial density which triggers a strong density driven descent. The induced velocity and density gradients inside and surrounding the released material are the basis of the entrainment mechanism which turns the released material into a spherical (ring) vortex

resembling an upside down mushroom. The plume keeps expanding due to the entrainment of the ambient water and consequently dilutes and loses its buoyant forcing. The convective descend of the plume continues until other mechanisms take over the buoyant forces in driving the plume. There are three different limiting processes which change the plumes behaviour from a density driven downfall. The first is the shear dispersion due to the ambient currents. In case of large ambient velocities, the dispersion from the ambient velocity field changes the entrainment mechanisms of the plume and enhances its mixing and dilution to a degree where the plume loses its buoyancy induced inertia and enters a fully mixed state over the water column. The second limiting mechanism is the exceedance of the individual particles fall velocity from that of the whole plume. This can happen in very late stages of plumes dilution and results in formation of a dispersed cloud of particles mixed in the ambient. The third is the limited water depth, which results in collapse of the density driven plume into the seabed, and formation of a horizontal density current over the bed spreading radially. Limiting the disposal plumes by the water depth may be favourable due to the least possible chance of mixing and dispersion of dredged material into the water column and the least possibility of formation of turbidity plumes travelling longer distances due to the ambient currents.

The dredged materials often consist of wide range of sediment types varying in size and weight, which affects the plumes behaviour in a more complicated way. As mentioned earlier in this report, the size/weight variation in sedimenting mixtures affects the individual grains fall velocity by enhancing the hindrance mechanism. Furthermore, large gradients in between the particles fall velocities can result in the stripping of finer fractions from the main buddy of the plume and formation of a light-weighted particle cloud being dispersed into the ambient. It can also result in the "rain out" of the coarser fractions from the bottom and therefore alleviating the buoyancy of the plume. The strong return flow due to faster settling fractions leaving the plume, besides its weakened buoyant forcing increases the mixing and dilution of the plume over the water column and turns it into a slow falling swarm or being dispersed by the ambient currents, ending up as turbidity plume.

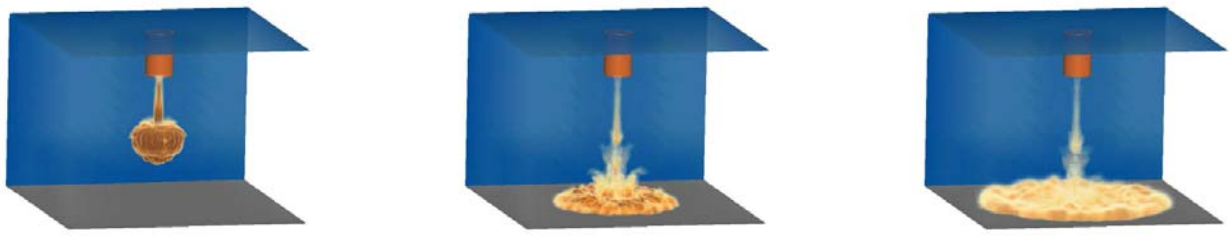

Figure 2.15 CFD simulations of sediment dumping into stagnant ambient (Saremi, 2014)

In order to model and study the detailed behaviour of the disposal plumes, it is necessary to use a multiphase two-way coupled method due to high levels of concentration and the impact both sediment and water has on each other. The same two-phase CFD model used to model the overflow plumes (as mentioned earlier), has been used to investigate the behaviour of the released material in stagnant water and to evaluate the models performance in capturing the various processes involved during the plumes life cycle (Saremi, 2014). In Figure 2.15 three snapshots of different stages (entrainment, collapse and density current over the bed) from the CFD model results simulating a material release experiment has been shown. The model is capable of resolving the dynamics of the

dumping process and can be used in further investigations of various mechanisms involved in plumes evolution.

2.1.7 Conclusions

Spillage and dispersion of dredged material into the ambient waters is one of the major environmental impacts during offshore/coastal construction and maintenance projects. Among the many adverse environmental impacts are increase in turbidity, burial of benthic life and introduction of contaminated material to the local ecosystem. The three main parameters determining the scales of the spillage and dispersion into the ambient are 1)The insitu sediment characteristics, 2) The type of dredging equipment and methods which determine the properties of the source of the spillage, 3) The ambient conditions including water depths, local currents and other external mechanisms.

If the constituents of the dredged material are mostly coarse grained (e.g. sand) with negligible amounts of fines, the spilled material settle soon and hardly contribute in formation of turbidity plumes. However, if there exists considerable amounts of fine sediment (fine sand and smaller) in the mother material, the chances are high for the spilled material to disperse, mix and form turbidity plumes which can remain in the water column for longer periods.

Using grabs or backhoes to dislodge the material increases the turbidity levels at the dredging site due to the spillage from the grab while removing the material towards the surface. Usage of closed grabs may have considerable effect in reducing this type of sediment spillage. The overflow spill from the barge is an inevitable process during dredging works. Using barges with overflow shafts rigged inside the barge (rather than overflowing from the sides of the barge to the water surface) and incorporating the Green valve (or similar techniques) to reduce the air entrainment into the overflow mixture will alleviate the mixing and hindered settling of the plumes. By trying to keep the β value inside the barge above unity, i.e. not exceeding the settling capacity of the barge, as explained earlier in this report and in further detail in Jensen and Saremi (2014), the volume of overflowing sediment will reduce considerably. The ambient condition is the other important influencing factor. Strong local currents or high trailing speeds of the hoppers result in enhanced mixing and dispersion of the spilled sediment. At the dumping sites, deeper the water becomes, there will be higher chance for the plume to undergo excess dilution and mixing in the water column before reaching the bed.

The above mentioned measures however may reduce the efficiency and may prolong the dredging works which are not desirable. In order to satisfy the environmental concerns and the progress and efficiency of the dredging works, an optimum balance should always be sought.

2.1.8 References

Bray, R. (2008). Environmental aspects of dredging. CRC Press

Ishii, M. (2006). Thermo-Fluid Dynamics of Two-Phase Flow. Springer US, Boston, MA.

Jensen, J. and Saremi, S. (2014). ”Overflow Concentration and Sedimentation in Hoppers” J. Waterway, Port, Coastal, Ocean Eng., 140(6), 04014023.

Jensen, J. and Saremi, S. (2015). ”Effects of Mixing on Hopper Sedimentation in Clearing Mixtures” J. Waterway, Port, Coastal, Ocean Eng [Accepted].

Saremi, S. (2014). Density driven currents and deposition of fine materials (Doctoral dissertation). Technical University of Denmark, Lyngby, Denmark.

2.2 Dispersion in wave boundary layers

V.S. Özgür Kirca (ITU), B. Mutlu Sumer (DTU)

Construction operations in the marine environment may require vast amount of dredging by means of different methods. During the handling and disposal process of the excavated (dredged) sediment, various amounts of this material will be spread into the marine environment. Eventually the dredged material is either used as fill material for other parts of the construction or is disposed to a stockpile area in the sea. Since the marine environment, especially near-bed region, is highly dynamic in terms of current and/or wave action, the disposed sediments will go through a series of transport and mixing processes (i.e. advection, diffusion, dispersion). It is of great importance to understand the mechanics of these processes for planning and management of marine dredging operations.

Dispersion in bottom boundary layers is the most dominant of all these mixing processes qualitatively and quantitatively. In this process, the joint action of shear (mean velocity gradient) and wall-normal turbulence fluctuations in the boundary layer near bed disperses the sediment particles away from each other. The dispersion coefficient is the measure for rate of dispersion of particles (see Sumer, 2013 chp. 4 for a detailed account of the subject).

Longitudinal dispersion in steady boundary layers have drawn quite a lot of attention from the start of the second half of 20th century (Taylor, 1953, 1954; Aris, 1956; Elder, 1959; Fischer, 1966, 1967; Sayre, 1968; Chatwin, 1973; Sumer, 1973, 1974, 1977; Pedersen, 1977; Fischer et al., 1979; Chatwin and Sullivan, 1982; Allen, 1982; Smith, 1983; Demuren and Rodi, 1986). The findings of these studies were often applied to channels, atmospheric boundary layers, rivers, tidal inlets and estuaries.

The wave boundary layers, on the other hand, are formed over the seabed under waves. They are characterised with a very small vertical extent (in the order of magnitude of 20-30 cm at most), with a very strong shear and turbulence, two important “ingredients” for dispersion. Unlike the steady boundary layer case, there are not many studies in the literature dealing with dispersion process in unsteady boundary layers, particularly oscillatory or wave boundary layers. Aris (1960) was the first to deal with the dispersion of a solute in periodically altering flows, albeit for the laminar case. Chatwin (1975) investigated the longitudinal dispersion of passive neutrally buoyant dispersant in oscillatory pipe flow in their analytical study. Smith (1982) and Yasuda (1982, 1984) studied dispersion process in oscillatory two dimensional boundary layers which resembles tidal flow boundary layer rather than wave boundary layer. Yasuda (1989) extended their previous research to dispersion of suspended (heavy) particles. Mei and Chain (1994) conducted a theoretical study in which they demonstrated the dispersion of small suspended particles in wave boundary layers, including the convection due to the steady streaming. These works all used time-invariant eddy viscosity when describing the turbulent flow. Ng (2004) studied the dispersion process in oscillatory boundary layers using a time-dependent turbulent diffusivity and found out that the time-dependency of eddy viscosity could not be neglected since it generated a difference of up to 30% in terms of dispersion coefficients. Recently, Mazumder and Paul (2012) carried out a numerical study in which they modelled the dispersion of suspended sediments in oscillatory boundary layer including the settlement, temporary storage and re-entrainment processes.

The present research aims at getting an understanding of the process of dispersion of the surface sediment in a stockpile area where excavated sediment is stockpiled temporarily (or permanently). The process is studied numerically, using a random-walk model (e.g., Sumer, 1973), with the input data for the mean and turbulence characteristics of the flow picked up from a two-equation k-ω RANS model (Fuhrman et al., 2013) and plugged in the random-walk model. The dispersion model is first run for the steady flow case and the results are compared with the ones in the literature. Then the model is run for different oscillatory flow cases with different sediment characteristics. One of the end-products of the present study is a simple, accurate and fast numerical model which may be used to assess the dispersion characteristics (e.g. dispersion coefficient) of dredged sediments in different wave/current conditions which is a function of the wave parameters as well as the sediment characteristics. This section can be attributed as the summary and draft of a scientific journal paper which will be published later on the topic of dispersion in wave boundary layers.

2.2.1 The process of longitudinal dispersion in an oscillatory boundary layer

In Figure 2.16, an oscillatory boundary layer is shown, where Figure 2.16a is the time variation of the free stream velocity ($U_0(\omega t) = U_{0m}\sin(\omega t)$) and Figure 2.16b is the time variation of the Reynolds averaged velocity profile, $\overline{u}(\omega t, y)$. A lump of dispersant (composed of many particles) is released in the form of a point source at x = 0 and t = 0 (i.e. ωt = A). These particles are subject to two effects as in the steady boundary layer case: (1) The turbulent motion in the y-direction; v', and (2) the streamwise motion in the x-direction; $\overline{u}(\omega t, y)$. The process, however, is more complex than the steady flow case since the Reynolds average streamwise velocity is not only a function of the wall-normal distance, but also a function of the phase, ωt. As can be seen in Figure 2.16c, particle 1 and 2 experience a series of different velocity magnitudes from instant A to instant E. The velocities of these two particles can even have opposite signs as shown in instant E, leading to progress in opposite directions. This implies that the particles are prone to disperse farther and farther apart in the streamwise direction. Thus, the end result will be the progressive dispersion of the dispersant in the streamwise direction, the *longitudinal dispersion*.

Let X be the longitudinal position of the particles at time t. Then the mean velocity of the particles would be

$$U_s = \frac{d\overline{X}}{dt} \tag{2.3}$$

which is expected to be equal to zero, since there is no net mass transfer in an oscillatory flow. As the particles get more and more dispersed, the variance of particle positions gets larger and larger. Just as in the steady flow case, the magnitude of dispersion is quantified by the dispersion coefficient, D_1, which is one half of the rate of change of variance of particle positions:

$$D_1 = \frac{1}{2}\frac{d\overline{X^2}}{dt} \tag{2.4}$$

Physical considerations as well as empirical data reveals that in steady boundary layers dispersion coefficient attains to a limit value in the far field (i.e. as $t \rightarrow \infty$). This is expected to be valid also in the oscillatory boundary layer case.

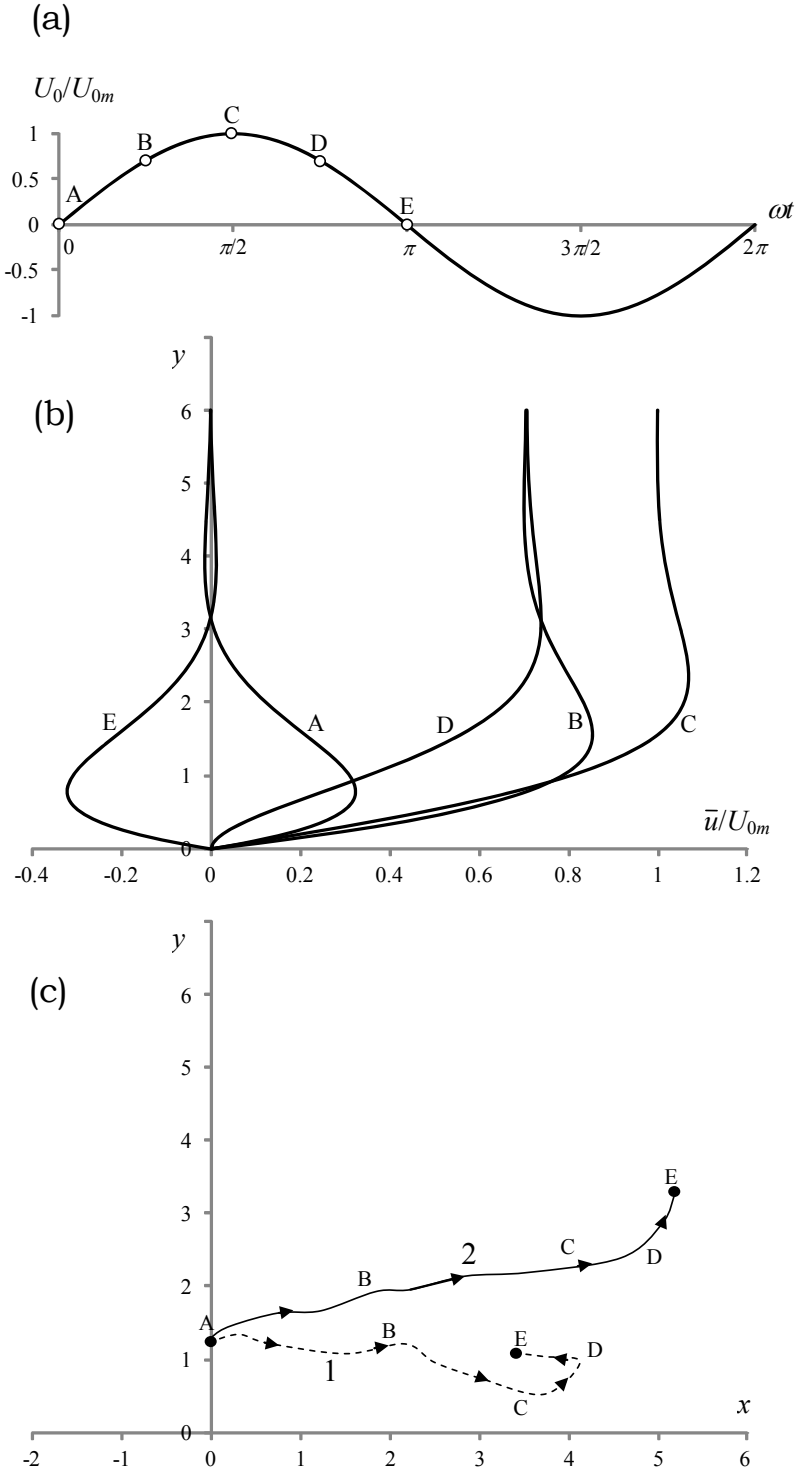

Figure 2.16: Longitudinal dispersion in an oscillatory turbulent boundary layer.

2.2.2 Description of the numerical model

As stated above, the numerical model has two components: (1) the flow model that will yield the phase-dependent velocity and turbulent kinetic energy profiles, and (2) the random-walk model that will allow the simulation of the dispersion process based on the tracking of a single-particle for multiple times with the input from the flow model. These components are explained below.

Hydrodynamic and turbulence model: MatRANS

Two-equation turbulence closure models for Reynolds Averaged Navier-Stokes (RANS) equation have been widely used in fluid mechanics and coastal engineering for solving various problems related to turbulent boundary layers. These models either use the k-ω or k-ε turbulence closure. In these models it is possible to solve the Reynolds averaged velocities (i.e. mean velocities) along with turbulent shear stresses and turbulence kinetic energy on a time-averaged or phase resolved basis.

In the present study the k-ω model developed by Furhman et al. (2013), MatRANS, has been used for the mean flow and turbulence input necessary for the longitudinal dispersion simulations. The model solves simplified versions of the horizontal component of the incompressible Reynolds-averaged Navier-Stokes (RANS) equations, combined with the two-equation k-ω turbulence closure model of Wilcox (2006). The considered RANS equation reads:

$$\frac{\partial \overline{u}}{\partial t} = -\frac{1}{\rho}\frac{\partial \overline{p}}{\partial x} + \nu \frac{\partial^2 \overline{u}}{\partial y^2} + \frac{\partial}{\partial y}\left(\nu_T \frac{\partial \overline{u}}{\partial y}\right) \tag{2.5}$$

where u, v and w are the streamwise, wall-normal and lateral velocity components, respectively. p is pressure, ρ is specific mass of fluid, ν and ν_T are laminar and turbulent viscosity terms (kinematic viscosity), respectively. Overbar denotes the Reynolds averaging. The turbulence model consists of two respective transport equations for the turbulent kinetic energy (per unit mass) $k = \frac{1}{2}\left(\overline{u'^2} + \overline{v'^2} + \overline{w'^2}\right)$, where the prime denotes fluctuating component, as well as the specific dissipation rate ω (Furhman, 2012):

$$\frac{\partial k}{\partial t} = \nu_T\left(\frac{\partial \overline{u}}{\partial y}\frac{\partial \overline{u}}{\partial y}\right) - \beta^* k\omega + \frac{\partial}{\partial y}\left[\left(\nu + \sigma^* \frac{k}{\omega}\right)\frac{\partial k}{\partial y}\right] \tag{2.6}$$

$$\frac{\partial \omega}{\partial t} = \alpha\frac{\omega}{t}\nu_T\left(\frac{\partial \overline{u}}{\partial y}\frac{\partial \overline{u}}{\partial y}\right) - \beta\omega^2 + \frac{\sigma_d}{\omega}\frac{\partial k}{\partial y}\frac{\partial \omega}{\partial y} + \frac{\partial}{\partial y}\left[\left(\nu + \sigma\frac{k}{\omega}\right)\frac{\partial \omega}{\partial y}\right] \tag{2.7}$$

Here, the turbulent (eddy) viscosity is defined as:

$$\nu_T = \frac{k}{\tilde{\omega}}, \qquad \tilde{\omega} = \max\left\{\omega, C_{\lim}\frac{\left|\partial \overline{u}/\partial y\right|}{\sqrt{\beta^*}}\right\} \tag{2.8}$$

Since the flow model does not give the turbulent fluctuations separately but only the turbulent kinetic energy ($k = \frac{1}{2}\left(\overline{u'^2} + \overline{v'^2} + \overline{w'^2}\right)$), wall-normal turbulence fluctuating velocity, $\overline{v'^2}$, is estimated by the following approximation suggested by Nezu and Nakagawa (1993):

$$\overline{v'^2} \approx 0.17 \cdot 2k \tag{2.9}$$

In the model, a no-slip condition is imposed at the bottom boundary, where the velocity is zero. For the turbulent kinetic energy, a zero-gradient is used at the bottom boundary (i.e. $\partial k/\partial y = 0$). On the upper boundary, a frictionless lid is considered, whereby the shear stress and vertical derivatives of all variables are set to zero. Also note that, considering the oscillatory flow conditions, all the convective terms are excluded from the equations (although the model itself has a provision for steady streaming). For all the details of the MatRANS model, including the model coefficients and additional options such as inclusion of convective terms and turbulence suppression, Fuhrman (2012) and Fuhrman et al. (2013) can be consulted.

Random-walk dispersion model

Random-walk model is a particle based model where a number of particles are released from a point source (or a line or plane source) one after another and tracked from time zero to a time *t*. The ensemble average as well as variance of particle positions are used to deduce the dispersion characteristics. The particles left into a turbulent flow domain are expected to move with respect to the Langrangian parameters dictated by the flow. Since turbulence is one of the major actors of the process, the turbulent fluctuations of particle velocities are simulated by a random element in the model. The model was first used for the purpose of simulating dispersion processes by Sullivan (1971) for neutrally-buoyant particles and by Sumer (1973) for heavy particles in two-dimensional steady boundary layers. Once the process is formulated in Eulerian sense, it is possible to calculate and track the path of each released particle as they migrate through the statistical field variables (Sumer, 1973).

A suspended heavy particle released into a turbulent flow would presumably have a downward settling velocity, w_s, which would act in combination with the vertical turbulent fluctuations. The heavy particle may be settled upon approaching the bed; and may or may not be re-suspended subsequently. The settlement and subsequent re-suspension makes the problem further complex. In many previous studies, it was assumed that the particles were always kept in suspension, or in other words the amount of settling particles were readily compensated by equal amount of particles re-suspended into the flow domain. This assumption has been legitimately employed by many researchers dealing with longitudinal dispersion (Sayre, 1968; Sullivan, 1971; Sumer, 1973, 1974; Mei and Chain, 1994). In the present study, although termination of suspension is allowed, the particles are always kept in the flow domain and moved with the near-bed velocity (i.e. as bed load). In other words, they are not let to come to a rest position.

In the present model, the flow domain is defined in between two parallel plates (i.e. a 2D tunnel) as shown in Figure 2.17 (both for steady and oscillatory flow cases). The hydrodynamic model is run for the half-space first and then the flow domain for dispersion model is defined by *mirroring* the hydrodynamic model output. Two cases are considered: (1) Steady flow case where the flow is driven by a constant pressure gradient and (2) Oscillatory flow case where the free stream velocity is varying in a sinusoidal manner. In the present model, the wall is taken as smooth wall over which a viscous sub-layer forms. When particles get very close to the wall, they may get stuck in this

viscous sub-layer since the turbulence fluctuations are very small herein. To prevent this, the particles are not let closer to the wall than a certain distance, δ_b. This distance is taken to be 30 in terms of *wall units*. In other words:

$$\delta_b = 30 y^+ = \frac{30}{\mathrm{Re}_f} y \tag{2.10}$$

where Re_f is the friction Reynolds number defined as $\mathrm{Re}_f = hU_f/\nu$, U_f is the friction velocity in steady flow case or the amplitude of the friction velocity, U_{fm}, in oscillatory flow case. Note that a similar action was taken both by Sullivan (1972) and Sumer (1973), who applied random-walk method for longitudinal dispersion in steady flow. So, the domain of y for the particle positions becomes:

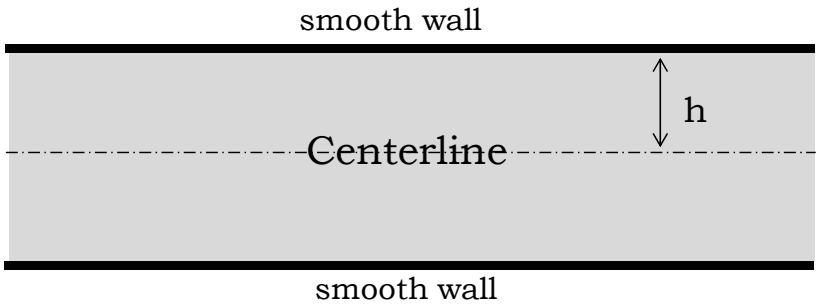

Figure 2.17: The flow domain in the model.

$$\delta_b < y < \left(2h - \delta_b\right) \tag{2.11}$$

where h is the half thickness of the tunnel. Note that for the open channel flow case h corresponds to the water depth and the multiplier 2 disappears. The particles are initially released from $x = 0$ in the form of a line source at the instant $t = 0$. If N particles are released, the initial y position of the nth particle, y_{n0}, can be calculated by

$$y_{n0} = \delta_b + \frac{2\left(h - \delta_b\right)}{N+1} n \tag{2.12}$$

Once a particle is released, it will move in small discrete steps (i.e. jumps). Each step will take a time Δt and the particle will change its streamwise and vertical (wall-normal) positions from x and y to $x+\Delta x$ and $y+\Delta y$, respectively. The timestep Δt is actually a function of the distance from the wall and for oscillatory flow also a function of the phase (i.e. time):

$$\Delta t = \frac{l}{\sqrt{\overline{v'^2}}} \tag{2.13}$$

Here $\sqrt{\overline{v'^2}}$ is the standard deviation of the wall-normal velocity component. The statistical character of the wall-normal velocity fluctuations are represented by normal distribution whose mean is zero ($\overline{v} = 0$) and variance is a function of the wall-normal distance and for oscillatory flow also a function of the phase (i.e. time), $\overline{v'^2}(\omega t, y)$. This statistical parameter is extracted from the flow model output via eq.(2.8). Note that the turbulence fluctuations of the velocity in streamwise direction are neglected, since it is known that the contribution of diffusion in the overall mixing process is negligible compared to dispersion (by a factor of $O(10^{-2})$). l, on the other hand, is a length scale of turbulence defined as (Sumer, 1973):

$$l(y)=\int_0^h \frac{\overline{u'(\lambda)u'(y)}}{\sqrt{\overline{u'^2(\lambda)}}\sqrt{\overline{u'^2(y)}}}\,d\lambda \tag{2.14}$$

Here, l should not be confused with the Prandtl mixing length. Although eq.(2.14) is initially defined for steady turbulent flow, it is expected to be valid also for the oscillatory flow provided that the flow is fully turbulent (i.e. $Re_w = {U_{0m}}^2/\omega\nu > 10^6$). One would expect that l scales with y close to the wall and then attain to a constant value. Based on the experimental findings of previous researchers, Sullivan (1972) and Sumer (1973) adopted the below approach to formulate l:

$$l(y) \cong \min\{y,\ 0.21h\} \tag{2.15}$$

In the present study, eq. (2.15) is modified in order to facilitate a smoother transition at $y = 0.21h$:

$$l(y) \cong \begin{cases} 0.21\left\{\tanh\left[\left(\dfrac{y}{0.21}\right)^3\right]\right\}^{1/3} & ,0 < y \le h \\ 0.21\left\{\tanh\left[\left(\dfrac{2h-y}{0.21}\right)^3\right]\right\}^{1/3} & ,h < y \le 2h \end{cases} \tag{2.16}$$

The Δy distance that the particle *intends* to jump in the vertical at each timestep can be formulated as such:

$$\Delta y = b\cdot(v' - w_s)\cdot\Delta t \tag{2.17}$$

The vertical fluctuation velocity v' is randomly calculated by

$$v' = a\cdot\sqrt{\overline{v'^2}}\,(\omega t, y) \tag{2.18}$$

Here the coefficient a is a random variable whose probability density function (p.d.f.) satisfies normal distribution with a mean of 0 and standard deviation of 1 (i.e. standard normal variable). Thus, v' can either be positive or negative, which will also affect the direction of particle's vertical jump. The coefficient b can be shown to be at the order of 1.254 by ensemble averaging the absolute value of eq. (2.16) and equating it to l. Comparison of the model results for the steady flow case with the values in the literature revealed that the results exhibit a better fit when b is increased by 13%, namely for $b = 1.42$. This is the only tuning that is applied to the present dispersion model.

As stated above, when a particle intends to jump outside the domain of y, it is *bounced back* from the borders (i.e. boundaries) of the y domain and kept inside the flow region. For neutrally buoyant particles, the particle intending to get out of the y domain is bounced back from the bottom or top boundaries to a point in the domain which has the same distance from the boundary with the initially intended location of travel, albeit in the opposite direction. For a heavy particle intending to jump beyond the upper boundary, the bouncing process will be the same with that of a neutrally-buoyant particle. However, for the bottom boundary the process will be different since the settling velocity should be treated as a *passive actor* as far as the bouncing is concerned. In other words, it is expected that a heavy particle released in still water would sit on the bed at rest and would not bounce back significantly no matter what its settling velocity is. Thus, for reconciliation with this basic physical principle, in the present model the contribution of the settling velocity to the particle's downward jump is always in the trend of keeping the particle as close as possible to the bottom boundary. As a result, the particle may end up on the bottom boundary. Although this is the

termination of suspension, it is not a complete settlement since the particle will keep moving with the near bed velocity (i.e. with $\overline{u}(\delta_b)$). The particle will be moved in contact with bed until the randomly assigned vertical fluctuating velocity exceeds the settling velocity (i.e. $v' > |w_s|$). This condition can be satisfied instantly or it may take for some timesteps for the particle to be re-suspended into the flow, depending on the intensity of bed-generated turbulence and settling velocity.

Accordingly, the new vertical location of the particle, y_2, can be calculated by:

$$y_2 = \begin{cases} y + \Delta y & , \quad \delta_b < y + \Delta y < (2h - \delta_b) \\ 2(2h - \delta_b) - (y + \Delta y) & , \quad y + \Delta y \geq (2h - \delta_b) \\ \max\left\{\delta_b \, , \left[2\delta_b - (y + \Delta y) - 2b \cdot w_s \cdot \Delta t\right]\right\} & , \quad y + \Delta y \leq \delta_b \end{cases} \tag{2.19}$$

As the particle jumps up and down in the flow domain, it will be advected by the flow in the streamwise direction. The Eulerian streamwise velocity of the flow, $\overline{u}(\omega t, y)$, varies as a function of wall-normal distance and also the phase (i.e. time) in the case of oscillatory flow. A particle released in such a flow field will experience a *time dependent* Langrangian velocity, U_p, as it is drifted on its path. The distance travelled by a particle from time t to time $t+\Delta t$ is:

$$\Delta x = \int_t^{t+\Delta t} U_p \, dt \tag{2.20}$$

For the steady boundary layer case, eq. (2.20) can easily be expressed in terms of Eulerian velocity:

$$\Delta x = \underbrace{\frac{1}{(y_2 - y)} \int_y^{y_2} \overline{u}(y) \, dy}_{\text{average Langrangian velocity of the particle}} \cdot \Delta t \tag{2.21}$$

It is not such straightforward to solve eq. (2.20) for oscillatory boundary layer case since the flow is temporally varying (i.e. unsteady). Hence, in the present model a numerical calculation of average particle velocity for each timestep is conducted, as defined below:

$$\Delta x = \int_t^{t+\Delta t} U_p \, dt \approx \underbrace{\frac{1}{M} \sum_{m=0}^{M} \overline{u}\left(\omega(t + {}^{m}\!/_{M}\,\Delta t), y + {}^{m}\!/_{M}\,(y_2 - y)\right)}_{\text{average Langrangian velocity of the particle}} \cdot \Delta t \tag{2.22}$$

Here, M is an integer which designates the resolution of numerical integration. It holds the following condition:

$$\frac{1}{M} \leq \min\left\{\frac{T}{1000 \cdot \Delta t}, \frac{h}{1000 \cdot (y_2 - y)}\right\} \tag{2.23}$$

Note that if the particle is bouncing from any of the flow boundaries, then eq. (2.22) should be evaluated separately from particle initial position to the boundary and from boundary to particle final position.

2.2.3 **Results**

Since the flow model that is used in the present study has been validated against many cases (Fuhrman et al., 2010; Fuhrman, 2012; Fuhrman et al., 2013), no details will be given on this account to save space. The results of the dispersion model is presented below for steady boundary layer and the oscillatory boundary layer cases separately.

Steady boundary layer case

Many studies concerning dispersion in a 2D steady boundary layer showed that the dispersion coefficient can be non-dimensionalised by the friction velocity (U_f) and the boundary layer thickness (i.e. water depth for open channel flow, h). This is basically because dispersion in steady boundary layer can be formulated through the *velocity-defect law*. Using the Aris concentration moment transformation approach, Sumer (1974) evaluated the dispersion coefficient of heavy suspended particles in a 2D turbulent open channel in the non-dimensional form as:

$$\frac{D_1}{U_f h} = function(\beta) \tag{2.24}$$

where β is the non-dimensional settling velocity in the form of $\beta = w_s / \kappa U_f$ and κ is the Von Kármán constant. Likewise, h and U_f are used for non-dimensionalising the distance, velocity and time such as:

$$X = \frac{x}{h},\ Y = \frac{y}{h},\ T = \frac{t U_f}{h},\ U = \frac{u}{U_f} \tag{2.25}$$

Sumer (1974) also stated that the non-dimensional dispersion coefficient for neutrally buoyant particles simplified to the value that had been first evaluated by Elder (1959):

$$\left(\frac{D_1}{U_f h} \right)_{\beta=0} = 5.5 \sim 6.0 \tag{2.26}$$

Note that the result of eq. (2.26) shows the range depending on the value of κ=0.40~0.42. Sumer's (1974) results indicated that the dispersion coefficient increases with the settling velocity. Sumer (1974) also noted that the method they used has validity for $\beta < 1$.

As shown in Figure 2.17, the flow domain is defined in between two parallel plates. The thickness of the tunnel (distance between the parallel plates) was taken to be $2h$ = 29 cm[1], which corresponds to a boundary layer thickness of h = 14.5 cm. The friction velocity in the flow was U_f = 8 cm/s whereas the mean cross-sectional velocity was $V \approx 2$ m/s. The preliminary runs performed for different number of particles (not shown here for reasons of space) showed that for number of particles greater than approximately 5000 the statistical variables become independent of number of particles. Thus, the present simulations were carried out with N=20000 particles. The simulations were conducted for a non-dimensional time of T=40, which corresponds to t=22 s with the present flow parameters. The vertical and horizontal particle positions were recorded at different times during the simulations, with more frequent intervals at early stages. Numerical simulations were repeated for different settling velocities (i.e. heavy particles).

Fig. 2.18 shows the mean particle positions for different times of the simulation. As can be seen, the mean particle velocity (i.e. velocity of the particle cloud) is almost identical with the mean cross-sectional velocity. In other words, Eulerian velocity and Langrangian velocity are equal, as one will expect in a steady ($\partial / \partial t = 0$) and uniform ($\partial / \partial x = 0$) flow environment.

[1] Note that this is the dimension of the oscillatory flow tunnel in DTU Hydraulics Laboratory, where Jensen et al. (1989) conducted their tests.

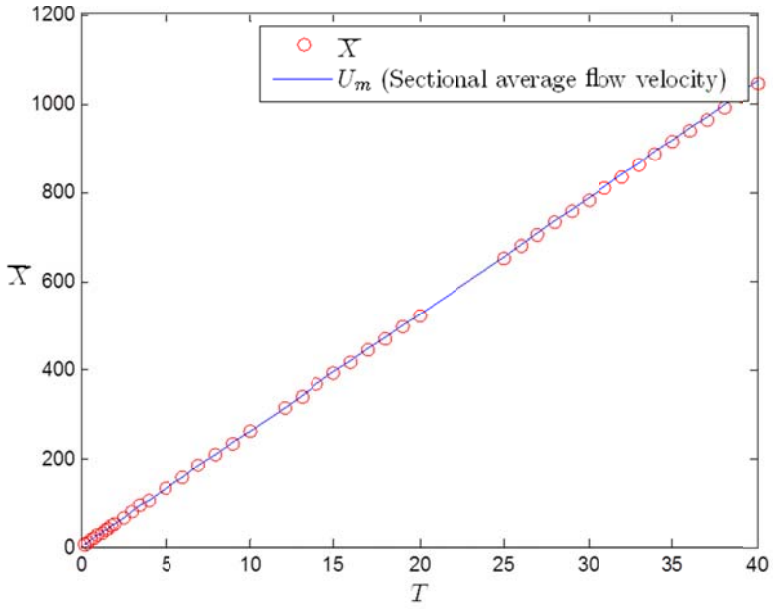

Fig. 2.18: Non-dimensional mean particle X positions versus non-dimensional time, β=0.

Fig. 2.19 shows the variance of particle X positions with time. Initially the variance increases very swiftly, but after approximately T=5 its rate of change becomes constant. This is in conjunction with the well-known nature of mixing processes in steady flow; fast in early times of the release of the dispersant and attaining to a certain limit rate at large times (i.e. in the far field).

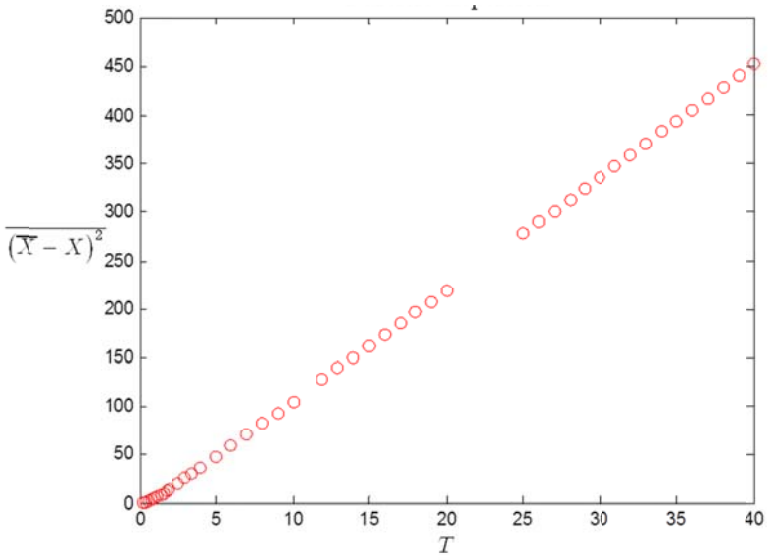

Fig. 2.19: Change of variance of particles with time, W=0 (β=0).

When the same simulation is conducted for a heavy particle with β=0.3 the picture changes. *Fig. 2.20* shows the particle mean X positions with time. The velocity is decreased since the particles' mean position is closer to the bed due to the settling velocity of the particles. Indeed, *Fig. 2.20* shows that the particles attain a constant velocity after T=7, which is slower than the sectional average flow velocity.

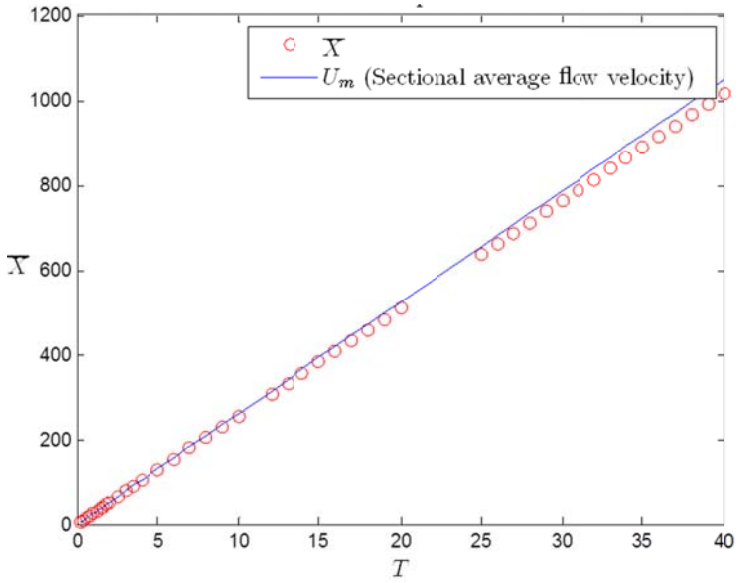

Fig. 2.20: Non-dimensional mean particle X positions versus non-dimensional time, β=0.3.

The concentration of particles, $c(x,y,t)$, can be defined as the number of particles per unit area. The non-dimensional particle concentration, C, can then be defined as

$$C(X,Y,T) = c\frac{h^2}{N} \tag{2.27}$$

Sumer (1974) stated that the zeroth moment of concentration with respect to longitudinal axis gives a concentration moment C_0, a function of Y and T only. Based on Aris (1956), its analytical solution for large times of the dispersion process is:

$$C_0(Y,T) = \frac{\sin \pi\beta}{\pi\beta}\left(\frac{1-Y}{Y}\right)^{\beta} \quad , \qquad T > 7.5 \tag{2.28}$$

Note that for the present case (i.e. flow between two parallel plates), Y is replaced with $2Y$. In *Fig. 2.21* the zeroth concentration moment at T=40 is given for a heavy particle with β=0.3 along with the analytical profile. A good agreement can be seen. Although not clear, the slight deviation in the upper half can be attributed to the presence of the top wall.

Fig. 2.22 facilitates a direct comparison between the dispersions of neutrally buoyant particles and heavy particles. In this figure the time variation of dispersion coefficients for neutrally buoyant and heavy (β=0.3) particles are given. It can be seen that the dispersion coefficient increases fast at the early stages and attains to a limit value as expected. The dispersion values in the literature for neutrally buoyant particles (Elder, 1959) and for β=0.3 (Sumer, 1974) are also shown in the figure and can be seen that the model is in accordance with these.

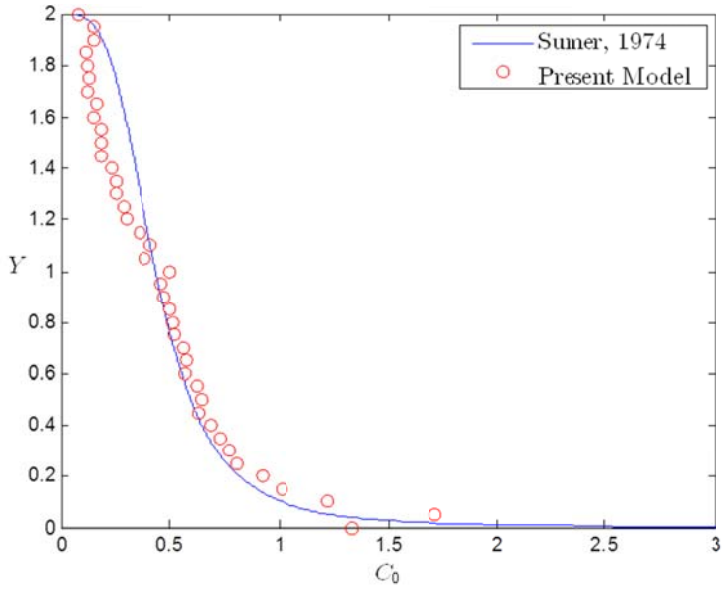

Fig. 2.21: Model results of zeroth moment of concentration for large times results compared with analytical solution, β=0.3.

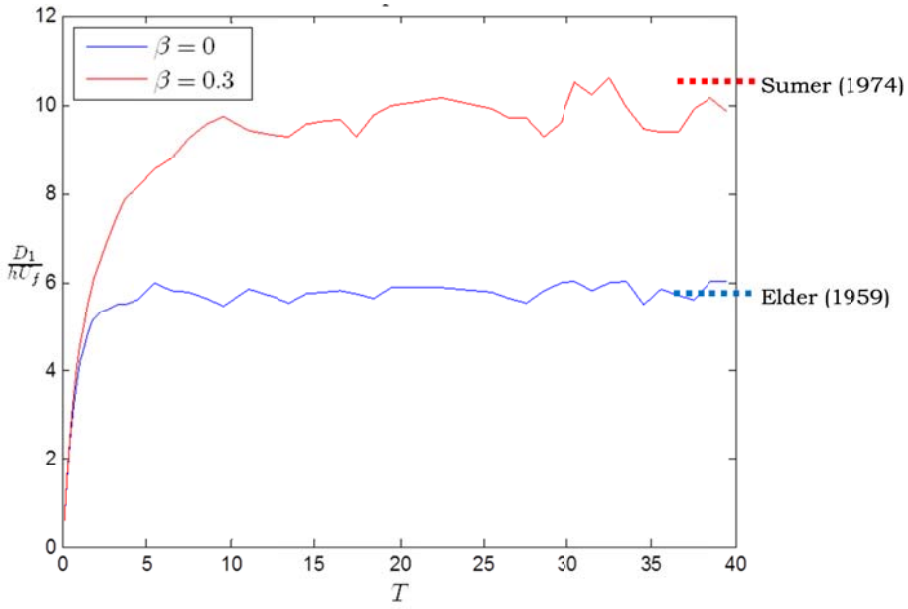

Fig. 2.22: Time variation of non-dimensional dispersion coefficients for β=0 and β=0.3.

The numerical simulation has been repeated for particles with different settling velocities. The results of these simulations are presented in *Fig. 2.23* in terms of the ratio of dispersion coefficient of neutrally buoyant particles to that of heavy particles. Along with the model results, the analytical solution of Sumer (1974) and numerical solution of Sayre (1968) are also given. The model results agree generally well with the analytical solution. The reason why the heavy particles bear a higher dispersion coefficient compared to neutrally buoyant particles is that heavy particles spend a longer time closer to bed where the velocity gradient and turbulent fluctuations are higher. Therefore, they experience a stronger dispersion process.

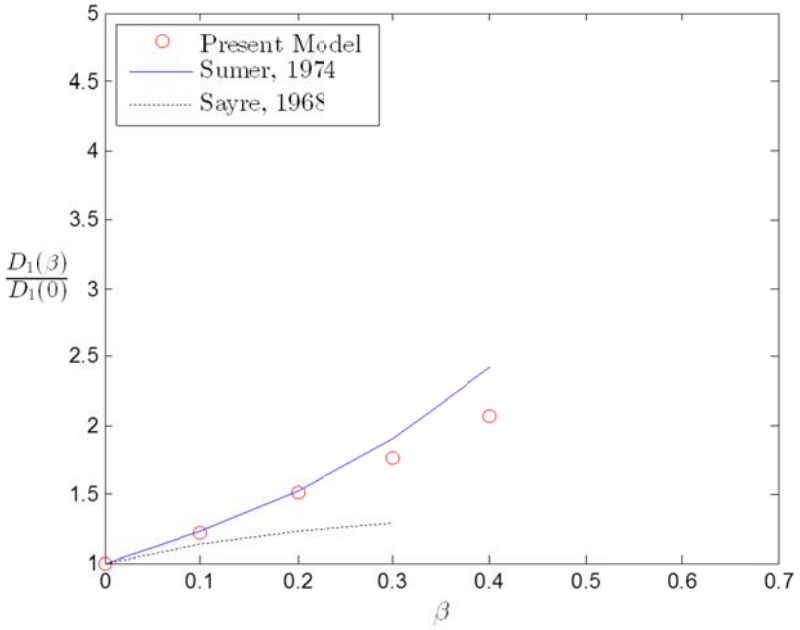

Fig. 2.23: Ratio of dispersion coefficient for heavy particles to that of neutrally buoyant particles versus the non-dimensional settling velocity (β).

Oscillatory boundary layer case

Using the same rationale as in eq.(2.24), the dispersion coefficient in the case of turbulent oscillatory boundary layer can be non-dimensionalised. But this time, the non-dimensional dispersion coefficient will not only be a function of the settling velocity, but also be a function of the ratio between the wave Reynolds number (Re_w) to the boundary Reynolds number (Re):

$$\alpha = \frac{Re_w}{Re} = \frac{U_{m0}a/\nu}{U_{m0}h/\nu} = \frac{a}{h} \tag{2.29}$$

As can be seen from the above equation, α is a measure of the longitudinal amplitude of the oscillatory motion to the thickness of flow domain (i.e. the maximum possible extent of boundary layer). Thus, the non-dimensional dispersion coefficient in the case of oscillatory flow becomes:

$$\frac{D_1}{U_{fm}h} = function(\alpha, \beta) \tag{2.30}$$

The thickness of the flow domain (i.e. an oscillatory tunnel) is the same with steady flow case, $2h$ = 29 cm, which corresponds to a maximum boundary layer extent of h = 14.5 cm. For the first run, the amplitude of the friction velocity in the flow was U_{fm} = 8 cm/s whereas the free stream velocity was $U_{0m} \approx 2$ m/s, all compatible values with the case of steady flow (note that this is the flow case described as test 10 in Jensen et al., 1989). Simulations have been conducted with N=20000 particles, just as in the steady boundary layer case.

The results for neutrally buoyant particles are given in Fig. 2.24 and Fig. 2.25. As can be seen from Fig. 2.24, the particle cloud moves back and forth obeying the flow. The non-dimensional amplitude of the oscillations is 21.4, which is equal to α. The variance of particle X positions with time is shown in Fig. 2.25. Different from steady flow case, the variance of particles does not

increase with a constant rate, but they exhibit some undulations. It is striking to see that the time intervals which corresponds to the highest rate of change of variance (highest dispersion coefficients) are around the flow reversals. The overall non-dimensional dispersion coefficient is around 0.50, a factor 12 smaller than that of the oscillatory flow.

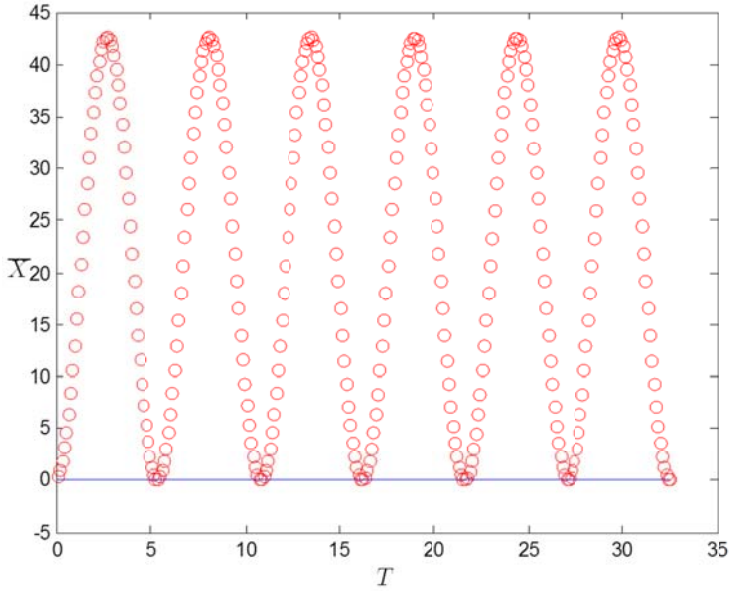

Fig. 2.24: Non-dimensional mean particle X positions versus non-dimensional time in oscillatory flow case β=0, α=21.4 ($Re_w = U_{0m}{}^2/\omega\nu = 6.2\times10^6$).

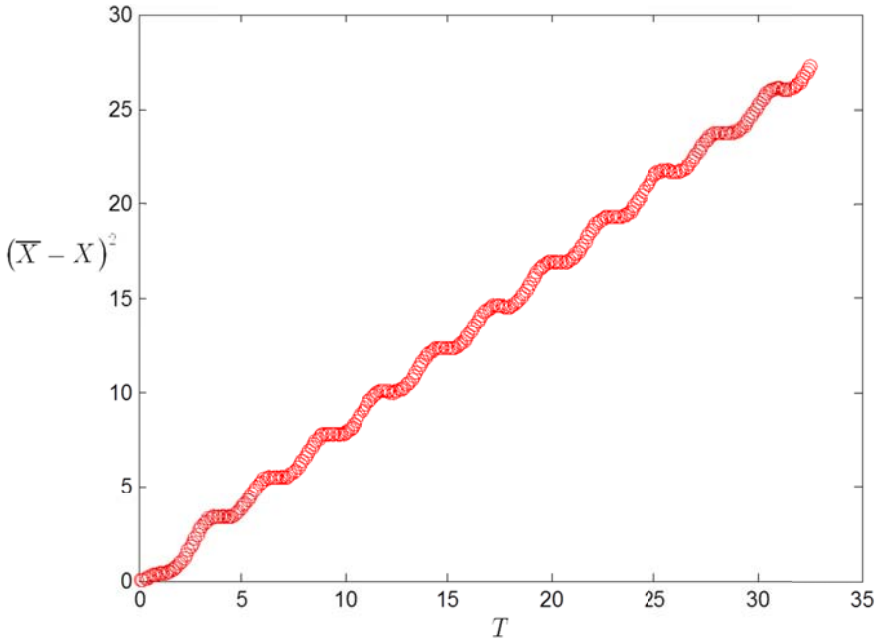

Fig. 2.25: Change of variance of particles with time for oscillatory flow case, β=0, α=21.4 ($Re_w = U_{0m}{}^2/\omega\nu = 6.2\times10^6$).

When the same simulation is repeated with a heavy particle of β=0.3, the picture is a bit different. Fig. 2.26 and Fig. 2.27 present the profile of zeroth concentration moment for large times and the time variation of particle positions' variance, respectively. When Fig. 2.26 is compared with Fig. 2.21, it is seen that the mean particle Y position in the oscillatory flow case is even lower than the case of steady flow. Also the concentration profile in Fig. 2.26 shows that turbulence cannot counterbalance the settling tendency of particles as dominantly as in the steady boundary layer case.

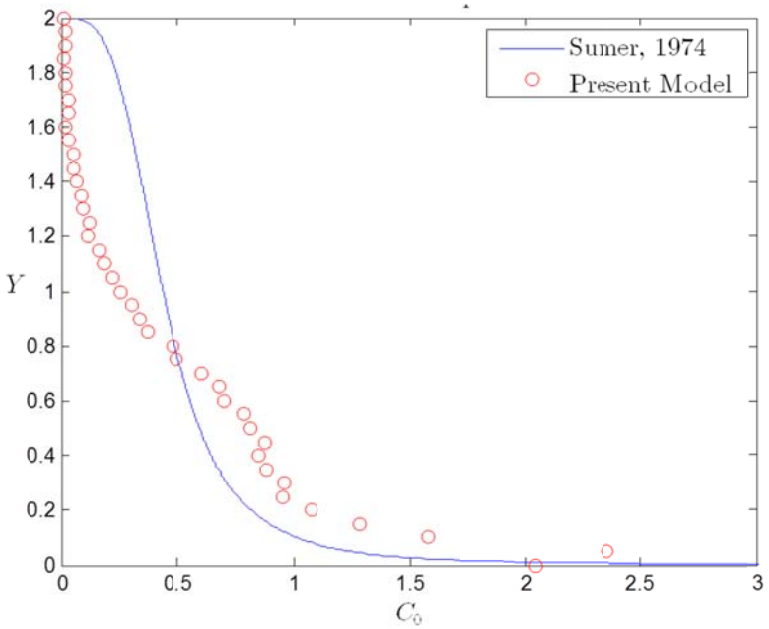

Fig. 2.26: The zeroth concentration moment of heavy particles for oscillatory flow, β=0.3, α=21.4 ($Re_w = U_{0m}^2/\omega\nu = 6.2\times10^6$).

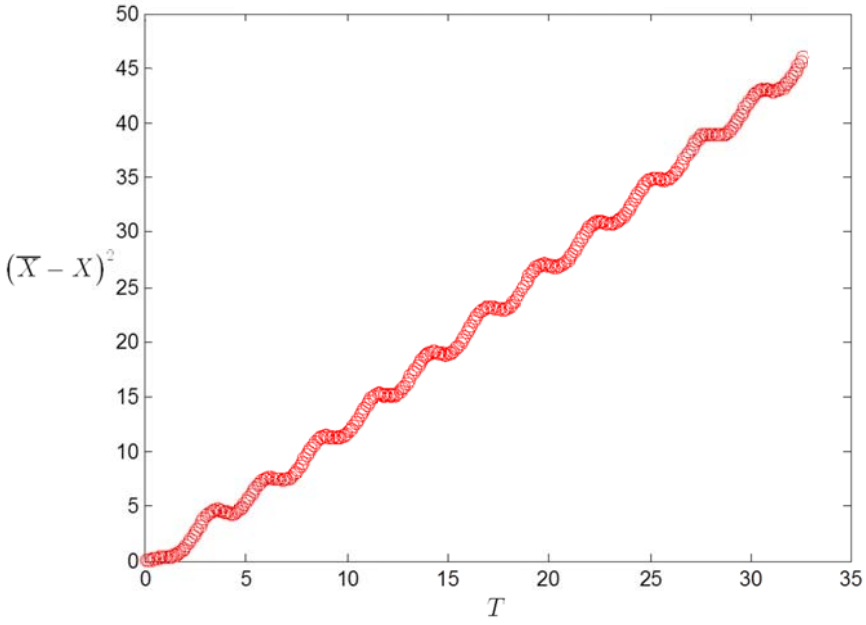

Fig. 2.27: The change of variance of particle X positions with time for oscillatory flow, β=0.3, α=21.4 ($Re_w = U_{0m}^2/\omega\nu = 6.2\times10^6$).

As one might expect similar to the steady flow case, the dispersion coefficient is increased with the introduction of settling velocity. The picture is qualitatively similar to the case of neutrally buoyant particles, yet the dispersion coefficient is increased significantly. From *Fig. 2.27*, the period-averaged (overall) dispersion coefficient for heavy particles with β=0.3 is around 0.85.

The above exercise has been repeated for three other cases of oscillatory flow: α= 10.7 ($Re_w = 1.5\times10^6$), α= 32 ($Re_w = 1.4\times10^7$) and α= 96 ($Re_w = 6.3\times10^7$). The variation of non-dimensional dispersion coefficient with non-dimensional settling velocity for all these flow conditions is given in *Fig. 2.28*. In this figure, the results for steady boundary layer case (i.e. $\alpha = \infty$) is also included for comparison. It is striking to see that the behaviour of dispersion coefficient with increasing settling velocity is very similar to that of steady flow (although the dispersion coefficient is significantly smaller compared to the steady flow case).

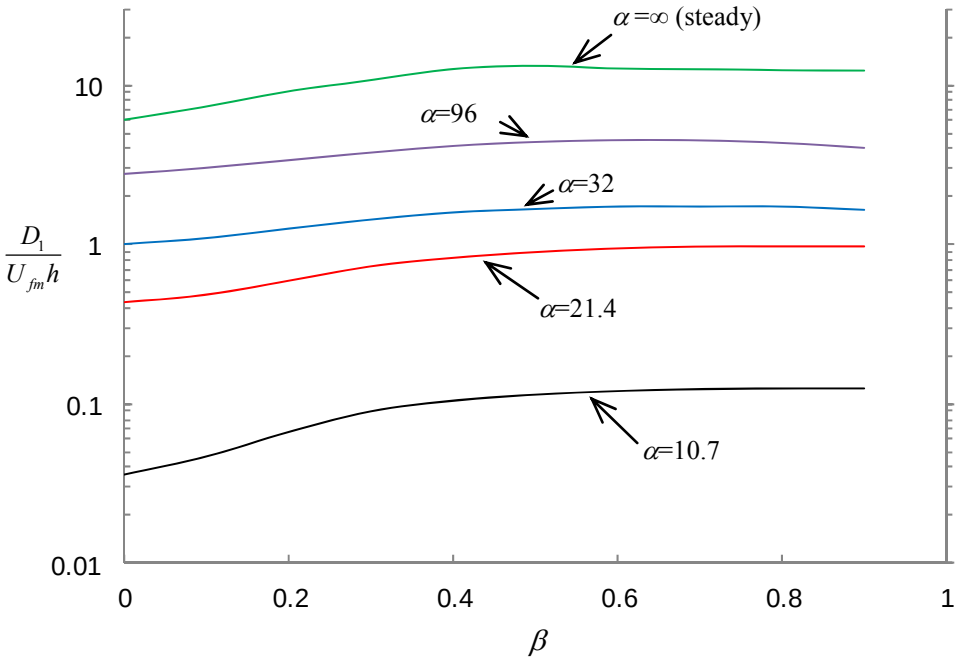

Fig. 2.28: Variation of non-dimensional dispersion coefficient (D_1/U_{fm} h) with non-dimensional settling velocity (β).

For neutrally buoyant particles, variation of non-dimensional dispersion coefficient with α is given in *Fig. 2.29*. In this figure, the value for steady flow (i.e. α=∞) is also shown. Like expected, the dispersion behaviour tends to approach asymptotically to that of steady flow as the amplitude of the motion increases.

Unfortunately, for oscillatory flow case, a direct comparison of the results of the present study with the values in the literature is not possible.

2.2.4 **Summary and Conclusion**

In the present study, the dispersion process of suspended sediments in wave boundary layers is studied. The subject of concern is an important and practical problem to be addressed, regarding the marine operations of offshore structures such as multi-use platforms, energy cables, pipelines, offshore wind farms, etc. These kinds of structures require vast amount of dredging and disposal of fine sediments which remain suspended for most of the time.

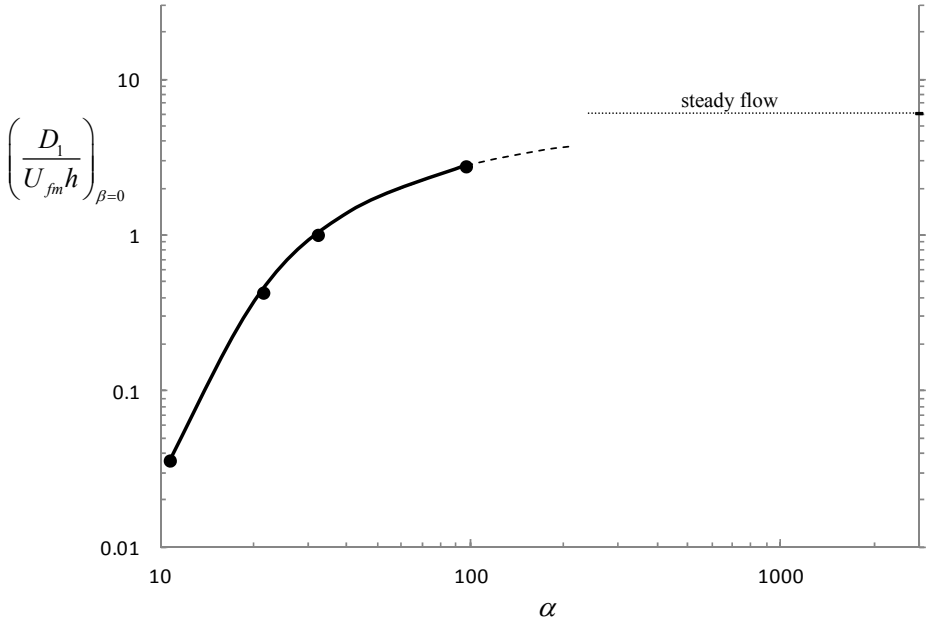

Fig. 2.29: Variation of non-dimensional dispersion coefficient (D_l/U_{fm} h) for neutrally buoyant particles with non-dimensional amplitude (α).

The problem is modelled by means of a Langrangian numerical model that unites a k-ω RANS model and a random-walk numerical scheme. Once the model was set up, validation and tuning of the model has been conducted for the steady flow case. Model results for different oscillatory flow conditions were presented and these results were discussed.

The conclusions drawn from the present study can be summarized as follows:

- The results for steady flow case shows that the model is in conjunction with the given values in the literature and well-represents the physics of the process for suspended particles unless the settling velocity is significantly high.
- In the case of oscillatory flow, the variance of particle positions does not increase monotonously as in steady flow case, but it exhibits some undulations. These undulations reflects the time variation of dispersion coefficient. The highest dispersion coefficients (steepest slope of the variance of particles with time) generally correspond to the flow reversal phases.
- In the oscillatory flow case dispersion is significantly less than that of the steady flow. The primary reason for this decrease comes out to be the lower shear and turbulence experienced by the particles.
- The dispersion coefficient increases with the settling velocity for oscillatory flow in a similar manner with the steady flow case. The apparent reason for increase of dispersion

coefficient is, again, that heavy particles moving closer to bed experience a higher shear (i.e. velocity gradient) and turbulence throughout their paths, which presumably disperses them farther and farther.

- When the wave Reynolds number increases, or in other words the amplitude of the motion increases, dispersion coefficient increases significantly. The reason is the increased extent of the oscillatory boundary layer towards the main body of the flow, such that more portion from the free stream region is being included in the boundary layer. The dispersion coefficient of particles in oscillatory boundary layers are expected to get closer asymptotically to the values of the steady flow case as the amplitude of the motion increases. This has also been demonstrated in the study.
- For oscillatory flow case, a direct comparison of the results of the present study with the values in the literature is not possible. Nevertheless, the results of Mazumder and Paul (2012) indicate to the same order of magnitude with the present findings, while the results of Ng (2004) are approximately a factor two larger.

2.2.5 References

Allen, C. M. (1982). Numerical simulation of contaminant dispersion in estuary flows. Proceedings of the Royal Society of London. A. Mathematical and Physical Sciences, 381(1780), 179-194.

Aris, R. (1960). On the dispersion of a solute in pulsating flow through a tube. Proceedings of the Royal Society of London. Series A. Mathematical and Physical Sciences, 259(1298), 370-376.

Chatwin, P. C. (1973). A calculation illustrating effects of the viscous sub-layer on longitudinal dispersion. The Quarterly Journal of Mechanics and Applied Mathematics, 26(4), 427-439.

Chatwin, P. C. (1975). On the longitudinal dispersion of passive contaminant in oscillatory flows in tubes. Journal of Fluid Mechanics, 71, pp 513-527.

Chatwin, P. C., & Sullivan, P. J. (1982). The effect of aspect ratio on longitudinal diffusivity in rectangular channels. Journal of Fluid Mechanics, 120, 347-358.

Demuren, A. O., & Rodi, W. (1986). Calculation of flow and pollutant dispersion in meandering channels. Journal of Fluid Mechanics, 172, 63-92.

Elder, J. W. (1959). The dispersion of marked fluid in turbulent shear flow. Journal of fluid mechanics, 5(04), 544-560.

Fischer, H.B. (1966). Longitudinal Dispersion in Laboratory and Natural Streams. Tech. Report KH-R-12, California Institute of Technology, Pasadena, California.

Fischer, H.B. (1967). The mechanics of dispersion in natural streams. J. Hydraul. Div., Proc. ASCE, vol. 93, p. 187.

Fischer, H.B., List, E.J., Koh, R.C.Y., Imberger, J. and Brooks, N.H. (1979). Mixing in Inland and Coastal Waters. Academic Press, Inc.

Fuhrman, D. R. (2012). MatRANS: A Matlab-based RANS + k-ω model for turbulent boundary layer and sediment transport simulations. Model Description (obtainable from the author).

Fuhrman, D. R., Dixen, M., & Jacobsen, N. G. (2010). Physically-consistent wall boundary conditions for the k-ω turbulence model. Journal of Hydraulic Research, 48(6), 793-800.

Fuhrman, D. R., Schløer, S. & Sterner, J. (2013). RANS-based simulation of turbulent wave boundary layer and sheet-flow sediment transport processes. Coastal Eng. 73, 151-166.

Jensen, B. L., Sumer, B. M., & Fredsøe, J. (1989). Turbulent oscillatory boundary layers at high Reynolds numbers. Journal of Fluid Mechanics, 206, 265-297.

Mazumder, B. S., & Paul, S. (2012). Dispersion of settling particles in oscillatory turbulent flow subject to deposition and re-entrainment. European Journal of Mechanics-B/Fluids, 31, 80-90.

Mei, C. C., & Chian, C. (1994). Dispersion of small suspended particles in a wave boundary layer. Journal of physical oceanography, 24(12), 2479-2495.

Nezu, I., Nakagawa, H. (1993). Turbulence in open channel flow. Taylor & Francis, London

Ng, C. O. (2004). A time-varying diffusivity model for shear dispersion in oscillatory channel flow. Fluid dynamics research, 34(6), 335-355.

Sayre, W.W. (1968). Dispersion of mass in open-channel flow. Hydraulic Papers, No. 3, Colorado State University, Fort Collins.

Smith, R. (1982). Contaminant dispersion in oscillatory flows. Journal of Fluid Mechanics, 114, 379-398.

Smith, R. (1983). Longitudinal dispersion coefficients for varying channels. Journal of Fluid Mechanics, 130, 299-314.

Sullivan, P. J. (1972). Longitudinal dispersion within a two dimensional shear flow. Journal of Fluid Mech., 49, 551-576.

Sumer, B. M. (1973). Simulation of dispersion of suspended particles. Journal of the Hydraulics Division, 99(10), 1705-1726.

Sumer, B. M. (1974). Mean velocity and longitudinal dispersion of heavy particles in turbulent open-channel flow. Journal of Fluid Mechanics, 65(01), 11-28.

Sumer, B. M. (1977). Settlement of solid particles in open channel flow. Journal of the Hydraulics Division, 103(11), 1323-1337.

Sumer, B. M. (2013). Lecture notes on turbulence. Downloadable from: http://www.external.mek.dtu.dk/personal/bms/turb_book_update_30_6_04.pdf

Taylor, G.I. (1953). Dispersion of soluble matter in solvent flowing slowly through a tube. Proc. Roy. Soc. London, A, vol. CCXIX, p.186.

Taylor, G. I. (1954). Diffusion and mass transport in tubes. Proceedings of the Physical Society. Section B, 67(12), 857.

Wilcox, D. C. (2006). Turbulence Modeling in CFD, 3rd edn. La Canada, California: DCW Industries, Inc.

Yasuda, H. (1982). Longitudinal dispersion due to the boundary layer in an oscillatory current: theoretical analysis in the case of an instantaneous line source. Journal of the Oceanographical Society of Japan, 38(6), 385-394.

Yasuda, H. (1984). Longitudinal dispersion of matter due to the shear effect of steady and oscillatory currents. Journal of Fluid Mechanics, 148, pp 383-403.

Yasuda, H. (1989). Longitudinal dispersion of suspended particles in oscillatory currents. Journal of Marine Research, 47(1), 153-168.

3 Current with varying density interaction with vertical piles

3.1 Physical and numerical modelling

Background

One concern when installing structures offshore in exposed waters is to develop reliable and robust designs that can retain the structural integrity and withstand the environmental loads from waves, winds or currents. Though complex this is in principle well known and engineering guidelines and design codes are well established (see e.g. Horner, 1965; Sumer and Fredsoe, 2006). The other side of the coin, the impact of such structures on the surroundings, is described to a lesser extent. This will be in focus in the following sections.

All swimmers have noticed eddies behind ones legs when standing at the beach in the wave driven currents or when looking downstream a bridge pier in a current. These current patterns are the result of the interaction between the structure and the passing flow. The flow exerts a load on the structure and by reaction the structure impose a drag on the flow, which responds e.g. by generating lee eddies or vortex streets.

In a marine environment these interactions may be separated into what could be termed near-field effects, which are the violent eddies observed immediately behind the structure, but also increased levels of turbulence, waves, possibly internal waves and mixing. These near-field processes will normally rapidly fade away, such that farther away the remaining footprints may be an observed increased resistance to the flow or permanent changes in the vertical stratification.

When a current passes a mono pile, several processes can influence the mixing. To a large extent the mixing will be related to the turbulence generated by the drag resistance from the bridge pier. This means that energy will be extracted from the mean flow and in the first step be transformed into internal waves and turbulent kinetic energy. The drag force from a monopole in a steady currents can be described by:

$$F_D = \rho C_D A\, U^2 \tag{3.1}$$

where F is the resultant drag force, ρ is the fluid density, C_D is the drag coefficient describing the specific shape and surface properties of the structure, A is the projected area of the structure and U is the current speed. The transformation typically happens in several steps. First large and very pronounced eddy structures entangling the structure are formed. These eddy structures are the lee or wake flow behind the pier, the horseshoe vortex that is initiated in front of the structure due to for instance a shear layer in the flow, and turbulence generated in the boundary layer around the structure.

In Figure 3.1 typical flow structures around a pier are illustrated.

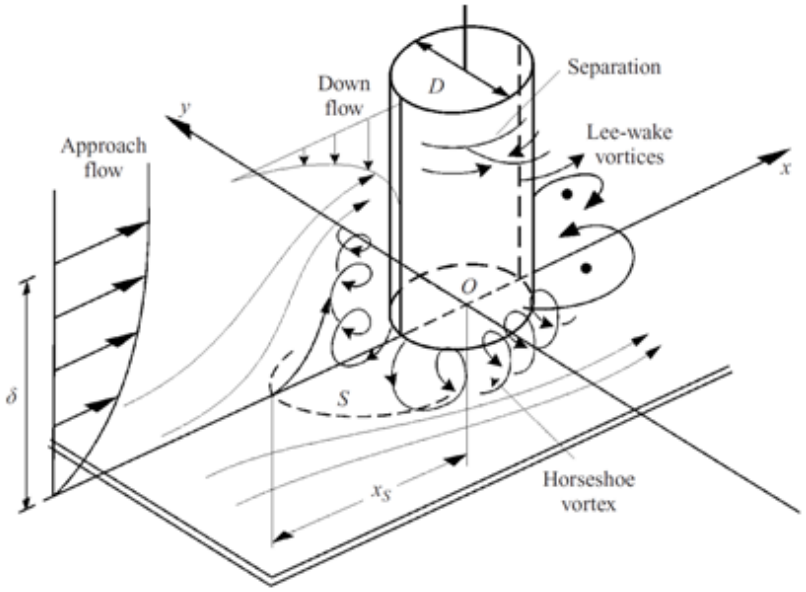

Figure 3.1 Sketch of large turbulent flow structures generated by the presence of a vertical py-lon in a channel flow (Sumer and Fredsoe, 2006)

The lee wake is generated by the separation of the flow around the structure. At sufficiently large Reynolds numbers the separation will lead to vortex shedding where an alternating process will produce a vortex on each side of the pier. For a vertical cylinder the vortices will have a vertical axis. If the pier or cylinder is sufficiently long or the depth/diameter ratio sufficiently large, the 2D coherent flow structure will break up in a 3D turbulent flow structure. This normally happens within, say, 5-10 diameters downstream. The distance varies with the Reynolds number, the shape of the pier, the roughness of the pier, and the level of shear and turbulence in the ambient current. If the wake is relatively shallow, it will have a more two-dimensional structure and will retain its structure for a longer distance (Jones *et al.,* 2007*)*. This means that if the structure is sufficiently wide the wake will be 2D horizontally and the mixing is expected to be quite different from the one found for a full 3D break-up of the wake.

The horseshoe vortex is generated by the shear in the flow, i.e. the increase of flow speed away from the seabed. The horseshoe vortex is generated in front of the pier and translated and stretched by the flow around the pier. The axis of the vortex is horizontal, and therefore the flow will to a large extent rotate in a vertical plane. This has a potentially large impact on the mixing, as it tends to turn the water column "upside-down". However, if the horseshoe vortex is generated at the seabed, it might not reach the interface between saline and fresh water if this is near the surface. If the flow is strongly stratified, the horseshoe vortex may be generated at the sheared density interface. This may increase the effect of the horseshoe vortex significantly.

The turbulence generated in the boundary layer around the structure will typically be fully three-dimensional and at a much smaller scale than the wakes and the horseshoe vortices. It may still have an effect on the mixing, as it is three-dimensional and will be present in the interface of two fluid layers. Especially if the surface of the pier is rough due to for instance marine growth. If the pier is not cylindrical but includes for instance abrupt changes along the pier the picture may be more

complicated as large-scale eddies or secondary currents may be introduced. Typical features of importance may be voluminous scour protection, sudden change of the structure geometry for instance from an ellipse cross section to a rectangular shape and any extrusions like ladders, boat landings, icebreaking cones or fouling.

The production of turbulence by the structure, P_S can be described by the work of the drag force, i.e.

$$P_S = U\, F_D \tag{3.2}$$

The turbulence will partly start to decay through the turbulent cascade process and partly contribute to the vertical mixing of across density interfaces. Using an energy concept, the vertical mixing across a density interface may be seen as a conversion of kinetic (turbulent) energy to potential energy (ΔE_P), changing the vertical centre of mass of the water column as it lifts denser water upwards working against gravity. This mixing or conversion process is assumed to take place with a certain efficiency, often expressed by a so-called Richardson number, $\Delta E_P = R_f P_S$, describing the fraction of the production of turbulence that actually is gained as potential energy instead of being dissipated into heat. However, the mixing efficiency may not always be a constant as it may depend on the details of the turbulence generation process as outlined above. In natural flows the fraction is typically a few per cent. When structures are present less is known about the mixing processes and especially the quantification of it. Stigebrandt (1992) studied flow across bridge pilings in the waters between Danish islands Funen and Zeeland and estimated a 0.6% effect on the discharge, but did not quantify effects on the mixing. Attempts have been made by Miller and Valle-Levinson (1996) to quantify the effects of bridge piers across Chesapeake Bay based on field measurements. They concluded that the piling induced mixing was much lower than the naturally occurring processes.

As is understood from the discussion above the source of the turbulence and mixing is focussed around the structure, while in natural water bodies, the effect may occur at large distances. An example may be additional mixing and resistance from bridge piers in the entrance to an estuary that has a strong local effect on the flow, while the impacts may occur far away, e.g. by changes in the exchange discharges or changes in the mixing by dissipating internal waves. Therefore any study of impacts and effects will have to cover a large range of spatial and temporal scales and may therefore need to combine several methodologies. Below is described studies comprising physical laboratory experiments, detailed numerical modelling and numerical models a basin and ocean scales that each addresses different aspects of the problem.

In the context of the MERMAID project, the effects on the environment from a massive build-out with Multi Use Platforms, is a concern. Therefore this has been a central part of the evaluation of MUP concepts in MERMAID. First is described a series of physical experiments, addressing in detail the forces and flows induced by a monopole structure in a stratified flow as well as a quantitative description of the mixing. These basic results are used as verification of a very detailed CFD model of the same processes. The CFD model can extend the parameter range studied in the physical experiments, as well as giving insight into detail of the flow structure around the structure that are not easily accessible in the laboratory. The detailed results are condensed into a so-called parameterization, expressing the forces and mixing in terms of some basic variables. This is then used in basin-scale and regional oceanographic models to quantify the long term impacts from MUP's on the surrounding environment.

3.1.1 Physical models

Stefan Carstensen[1], Erik Damgaard Christensen[1], Ole Petersen[2], and Bjarne Jensen[2]
1) DTU-MEK
2) DHI

Turbulence generated by vertical piles in a current with constant density undergoes a cascade process that transforms the non-isotropic turbulence into isotropic turbulence that eventually dissipates into heat. In a current with varying density, however, turbulence will to some degree have mixed the interface between the layers of different density. The part of the turbulence which mixes the layers is gained as potential energy instead of being dissipated into heat, and it can be said that a vertical redistribution of the density profile has taken place as a result of the mixing.

Insight on the magnitude of the vertical redistribution of the density profile by vertical piles in current with varying density can be deducted from a recent experimental study carried out by DHI. Here mixing behind vertical structures in a two-layered stratified current was investigated. In the following a condensation of the findings as it pertains to the present situation is given.

The experiments were conducted in the 3 m wide, and 1 m deep current flume at DTU-MEK, see Figure 3.2. The facility has a carriage which facilitates to tow model structures with a maximum velocity of 2 m/s, enabling the flume to be used as a towing tank. Two bulkheads were constructed at either end of the measuring section. The bulkheads separated the water in the measuring section from the water in the rest of the flume. A stratified water column was established between the two bulkheads and various vertical structures were mounted under the carriage and dragged through the stratified water column. In this way a current without shear was simulated. The advantage of this experimental technique is that that the contribution from the natural mixing of the current shear is absent in the measurements. This simplifies the interpretation of the results.

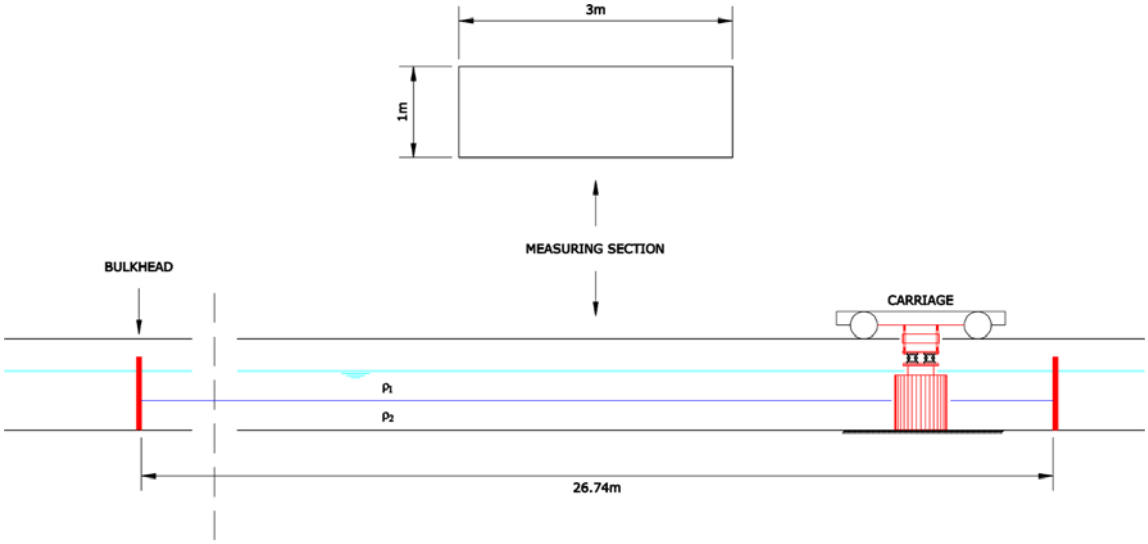

Figure 3.2 Test set-up for case where current was simulated by moving the carriage

The following quantities were measured in the experiments: (1) carriage position and velocity, (2) the total force on the vertical structure in the in-line and cross-flow direction, and (3) vertical density profile at two locations. Here the carriage velocity was derived from the time series of the

carriage position. The density profile was likewise derived from simultaneous measurement of salinity/conductivity and temperature profiles using algorithms for computation of fundamental properties of seawater. The salinity and temperature profiles themselves were established by traversing point measuring devices through the water column while simultaneously recording the position of the devices with a distance sensor, in this case a simple potentiometer.

A typical experiment consisted of a number of tows with the carriage. Density profiles were measured in between the carriage tows when the water column had come to rest. The carriage velocity and total in-line force was used to work out the input of (turbulent) kinetic energy to the flow. Provided that the skin friction (heat generation) is much smaller than the form drag, then the kinetic energy may to a first approximation be taken as the work performed by the simulated current:

$$E_{kin} \approx W = \sum_{t_0}^{t} -F_x U \Delta t \tag{3.3}$$

where, F_x is the total in-line force, U is the carriage velocity and t is time. The potential energy, E_{pot}, of the water column was derived from the measured density profiles:

$$E_{pot} = A \int_0^h \rho g z dz \tag{3.4}$$

where A is the surface area of the flume between the bulk heads, ρ is the density, g is the gravity (taken as 9.815m/s2), z is the vertical coordinate, and h is the water depth. The integration was performed using the trapezoidal method.

The development of the density profile during a typical experiment is presented in Figure 3.3. Six salinity profiles were measured before, in between, and after the twenty tows performed in the experiment. A constant number of tows were performed between two successive measurements of the density profile; and the input of kinetic energy from one run to the other was practically constant given identical carriage velocity and length travelled by the carriage. The figure shows that the density increased in the upper part of the water column, decreased in the lower part and there was a lowering of the interface along with a slight decrease in the slope of the salinity profile at the interface.

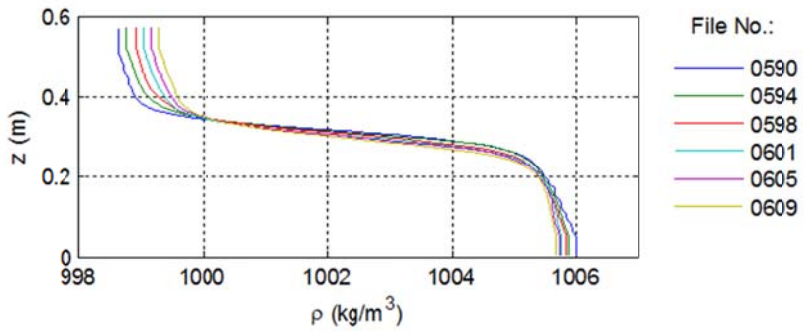

Figure 3.3 Salinity and density profiles before, during, and after a typical experiment. The density (or salinity) increased in the top of the water column, decreased in the bottom of the water column and the interface was lowered

The potential energy calculated for each of the measured density profiles in the experiment (Figure 3.3) is plotted against the input of kinetic energy as gray circles in Figure 3.4. There was some scatter in the data points although a clear trend of linear increase in potential energy with the input of kinetic energy was noticeable. The scatter primarily originated from differences in the depth-averaged density, ρ_A. For the given experiment, the depth-averaged density had a mean value of 1002.6 kg/m^3 with a standard deviation of 0.010 kg/m^3. Mass balance requires that the depth-averaged density be the same during an experiment provided of course that water or salt is not lost or gained. No trend has been observed in the depth-averaged density; hence the differences was considered due to measuring accuracy. The effect of the difference in depth-averaged density on the calculated potential energy was removed by recalculating the potential energy, $(E_{pot})_{corrected}$, using the mean depth-averaged density, $\overline{\rho_A}$.

$$\left(E_{\text{pot}}\right)_{\text{corrected}} = E_{\text{pot}} \cdot \frac{\overline{\rho_A}}{\rho_A} \tag{3.5}$$

The corrected potential energy has also been plotted in Figure 3.4Figure 3.3, the filled circles. As seen from the figure, the corrected potential energy removes most of the scatter at the data points and the trend of linear increase in the potential energy with the input of kinetic energy is enhanced.

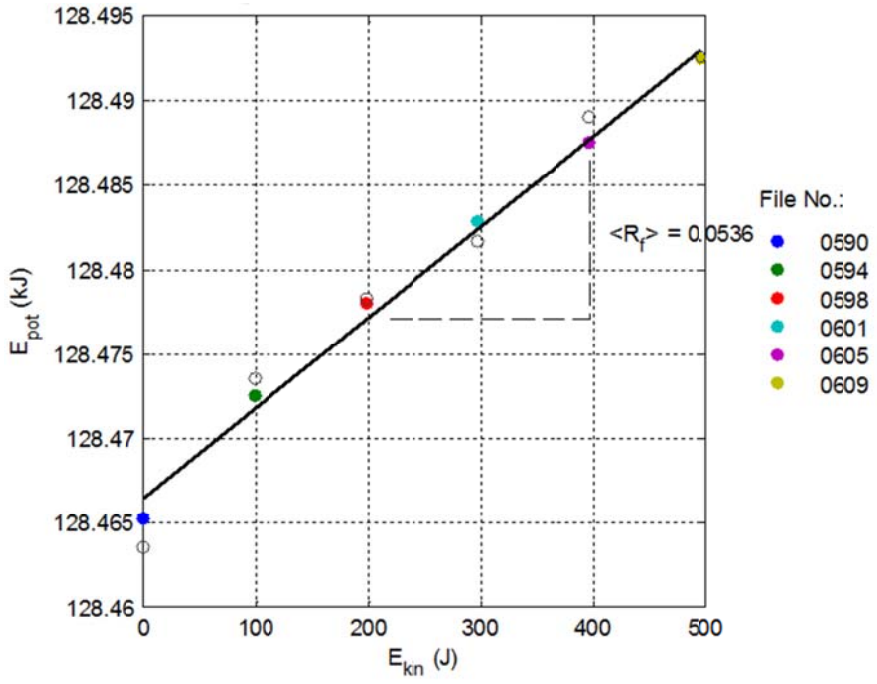

Figure 3.4 Increase in potential energy versus input of kinetic energy for the typical experiment, see Figure 3.3. Gray circles are the potential energy before correction for differences in depth-average density.

Figure 3.3 and Figure 3.4 clearly shows that a part of the turbulence redistributes the vertical density profile and is gained as potential energy instead of being dissipated into heat. The efficiency of the mixing process is defined

$$R_f^T = \frac{\text{Energy gained}}{\text{Energy produced}} \quad \left(= 1 - \frac{\text{Energy dissipated}}{\text{Energy produced}}\right) \tag{3.6}$$

This is essentially the bulk flux Richardson number. As the depth-averaged flux Richardson number (the mixing efficiency) is the ratio of increase in potential energy to the input of kinetic energy, it may be found as the slope of the straight line fitted to the data points in Figure 3.4.

For the given experiment (Figure 3.3 and Figure 3.4), a depth-averaged flux Richardson number of 5.4% was found. In this experiment the primary model tested was towed through the water column at a velocity of 0.21 m/s and the current angle of attack was 0 degrees. Table 3.1 list the test conditions for the primary and secondary experiments performed in the study. Experiments with low current speed were contained a larger number of tows to ensure that measuring accuracy of the change in potential energy did not affect the results.

Table 3.1 Test conditions. The stratified water column had a difference in salinity of 10. The interface was in both the primary and secondary experiments located at mid-depth.

Model	Simulated current speed	Water depth	Current angle of attack	Number of experiments	Number of tows per experiment
	(m/s)	(m)	(degrees)	(-)	(-)
(1) Primary	0.05 – 0.29	0.571	0 – 15	9	32 – 10
(2) Secondary	0.07 – 0.21	0.500	0	3	24

The primary model is depicted in Figure 3.5 and sketched in Figure 3.2 The primary model was an elliptic pile with a plinth on top. The major and minor axis of the elliptic cross-section was 0.571 m and 0.235 m, respectively. The height of the elliptic pile was 0.531 m. The plinth had a rectangular cross section with a length of 0.285 m and a width of 0.132 m. The secondary model only considered the elliptic cross-section by lowering the water depth in the experiment to 500mm.

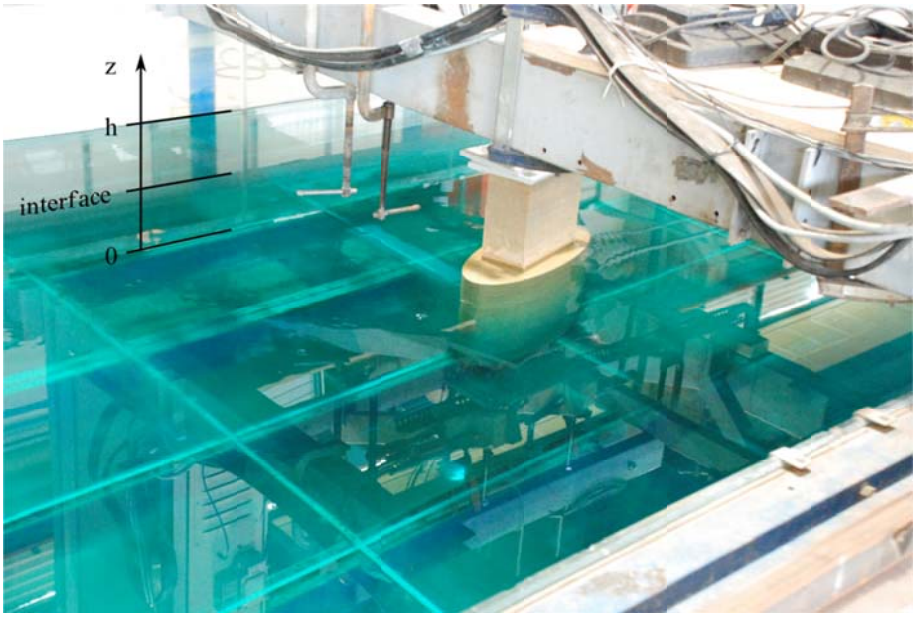

Figure 3.5 The primary model is towed through a two-layered stratified water column with an non-zero angle of attack. At the far glass side wall the stratified water column has been highlighted. The bottom layer with a salinity of 10 has been dyed blue. The top layer is fresh water with salinity of approximately 0.

In Figure 3.6, the measured mixing efficiency has been plotted as a function of the current velocity. The figure shows that the mixing efficiency for the primary model was generally in the order of 5% to 6%. However, at a current velocity in the order of 0.1m/s, a sharp increase in the mixing efficiency was observed.

The trend for the secondary model is comparable to that of primary model. However, generally the mixing efficiency is larger for the secondary model. This is attributed to the input of turbulent kinetic energy at the transition between the elliptic cross-section and the plinth for the primary model. This turbulent kinetic energy is located far from the interface of the stratified water column and thus contributes to a lesser degree to the mixing. This turbulent kinetic energy thus primarily shows up in the denominator of bulk flux Richardson number which results in a lower mixing efficiency relative to the situation without this part of the turbulent kinetic energy input, i.e. the secondary model. Supplementary tests with increased density stratifications to check whether the peak in the mixing efficiency was related to the wave celerity of the internal gravity wave. However, no coincidence between wave celerity of the internal gravity wave and the peak in the mixing efficiency was found in with these supplementary tests. No conclusive explanation has been found for the peak in the mixing efficiency, but the supplementary test did suggest that the peak in the mixing efficiency is not related to the wave celerity of the internal gravity wave.

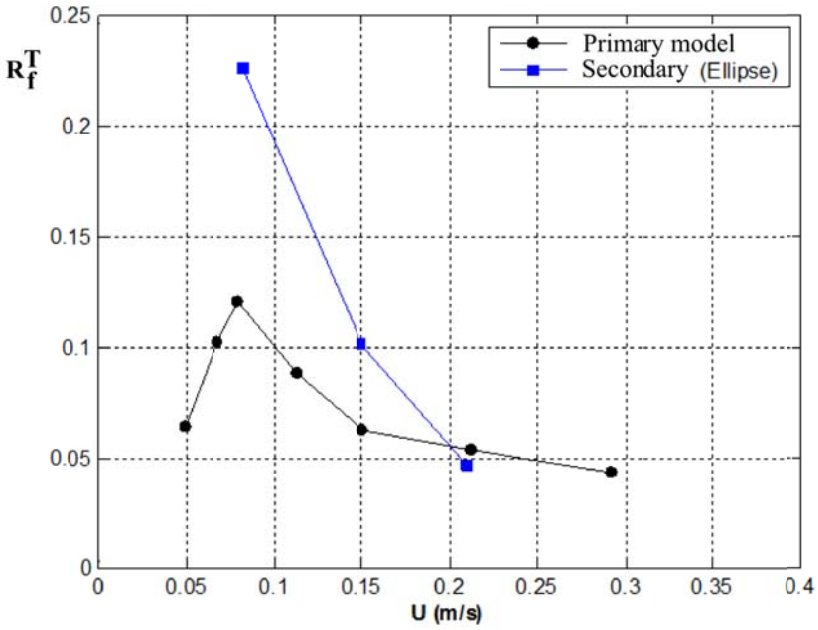

Figure 3.6 Mixing efficiency as a function of current velocity for the primary and secondary model at a current angle of attack equal 0.

Various current angles of attack were tested for the primary model. The results are given in Figure 3.7. The figure shows that there was a tendency of a slight increase in the mixing efficiency with increasing current angle of attack. However, the number of data points was not sufficient for a finite conclusion to be drawn. It should, however, be kept in mind that the in-line force, and thus the input of turbulent kinetic energy, increased significantly with the angle of attack. Hence, the actual mixing, for comparable current velocities, will increase with the angle of attack.

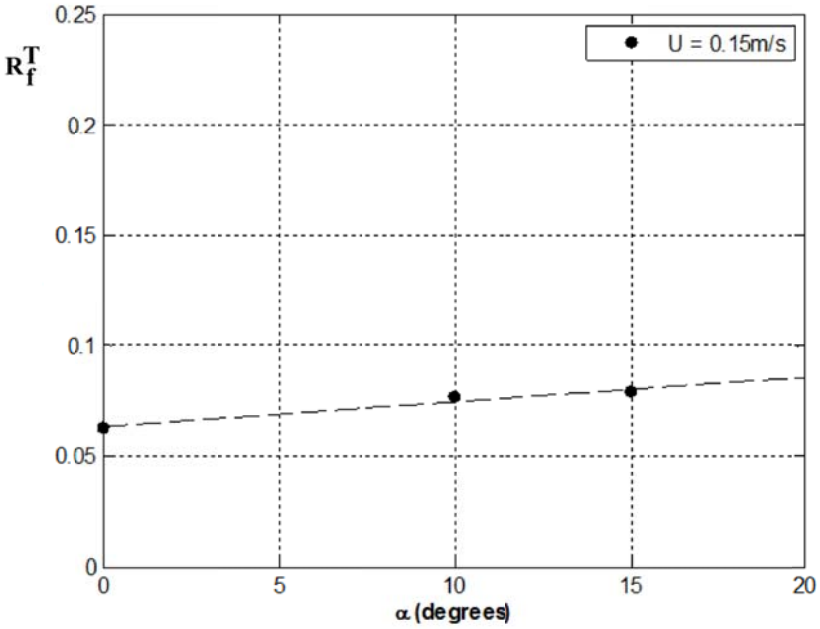

Figure 3.7 Mixing efficiency as a function of current angle of attack, α, for the primary model.

3.1.2 **Numerical models**

Bjarne Jensen[2], Erik Damgaard Christensen[1], Ole Petersen[2], and Stefan Carstensen[1]

1) DTU-MEK
2) DHI

In addition to the physical investigations a numerical study was performed. The main objective was to establish and validate a numerical model based on the physical model test results. Following this work the model was applied to investigate new bridge pier designs which were not included in the physical model experiments. This was not a part of the work described in this report.

The numerical model was based on the open source CFD libraries OpenFoam® where the Navier-Stokes equations were solved based on a finite volume discretization on a collocated grid arrangement. A mixture model was applied where two phase fractions simulated water with two different densities and the mixing due to the flow around the bridge piers. The equations were closed by a Large Eddy Simulation (LES) turbulence model where the k-equation model was applied as an extension of the standard Smagorinsky LES model.

Three different bridge pier models were included as shown in Figure 3.8. Shape No. 1 and 2 corresponds to those included in the physical model experiments. Shape No. 3 is a rectangular shape and was included as a reference with known drag coefficient. Table 3.2 presents the simulations conducted for this work. The simulations were divided into two phases. The first phase was focused on drag and lift forces in a steady current and uniform density (run nos. 1-18). The second phase investigated the mixing efficiency in a steady current with density stratification (run nos. 19-29).

Shape No 1 Shape No 2 Shape No 3

Figure 3.8 Bridge pier shapes included for validating the numerical model.

Table 3.2 *Run list for numerical simulations*

Ru	Shape No	Stratificatio n	Curren	Curren
1	1,	Homogeneou	0.5m/s	0 deg
2	1,	Homogeneou	0.8m/s	0 deg
3	1,	Homogeneou	1.0m/s	0 deg
4	1,	Homogeneou	1.5m/s	0 deg
5	1,	Homogeneou	2.0m/s	0 deg
6	1,	Homogeneou	2.8m/s	0 deg
7	1,	Homogeneou	3.5m/s	0 deg
8	1,	Homogeneou	4.2m/s	0 deg
9	2,	Homogeneou	0.5m/s	0 deg
10	3,	Homogeneou	0.5m/s	0 deg
11	1,	Homogeneou	0.5m/s	15 deg
12	1,	Homogeneou	0.8m/s	15 deg
13	1,	Homogeneou	1.0m/s	15 deg
14	1,	Homogeneou	1.5m/s	15 deg
15	1,	Homogeneou	2.0m/s	15 deg
16	1,	Homogeneou	2.8m/s	15 deg
17	1,	Homogeneou	3.5m/s	15 deg
18	1,	Homogeneou	4.2m/s	15 deg
19	1,	Stratified	0.3m/s	0 deg
20	1,	Stratified	0.4m/s	0 deg
21	1,	Stratified	0.5m/s	0 deg
22	1,	Stratified	0.7m/s	0 deg
23	1,	Stratified	1.0m/s	0 deg
24	1,	Stratified	1.3m/s	0 deg
25	1,	Stratified	2.0m/s	0 deg
26	2,	Stratified	0.7m/s	0 deg
27	2,	Stratified	1.0m/s	0 deg
28	2,	Stratified	1.3m/s	0 deg
29	2,	Stratified	2.0m/s	0 deg

The model domain covered an upstream distance at 40m and a downstream distance at 100m or 500m depending on the objective of the individual simulation. Simulations with uniform density for calculation of drag coefficients were performed with the short domain at 100m, while the simulations with density stratification and mixing were performed with the 500m domain in order to resolve the downstream mixing processes. A distance at 60m was included on both sides of the pier. It is important to notice that the numerical simulations were all performed at prototype (full) scale. Figure 3.9 presents the two model domains (including bridge pier No 1) with a downstream distance at 100m and 500m, respectively.

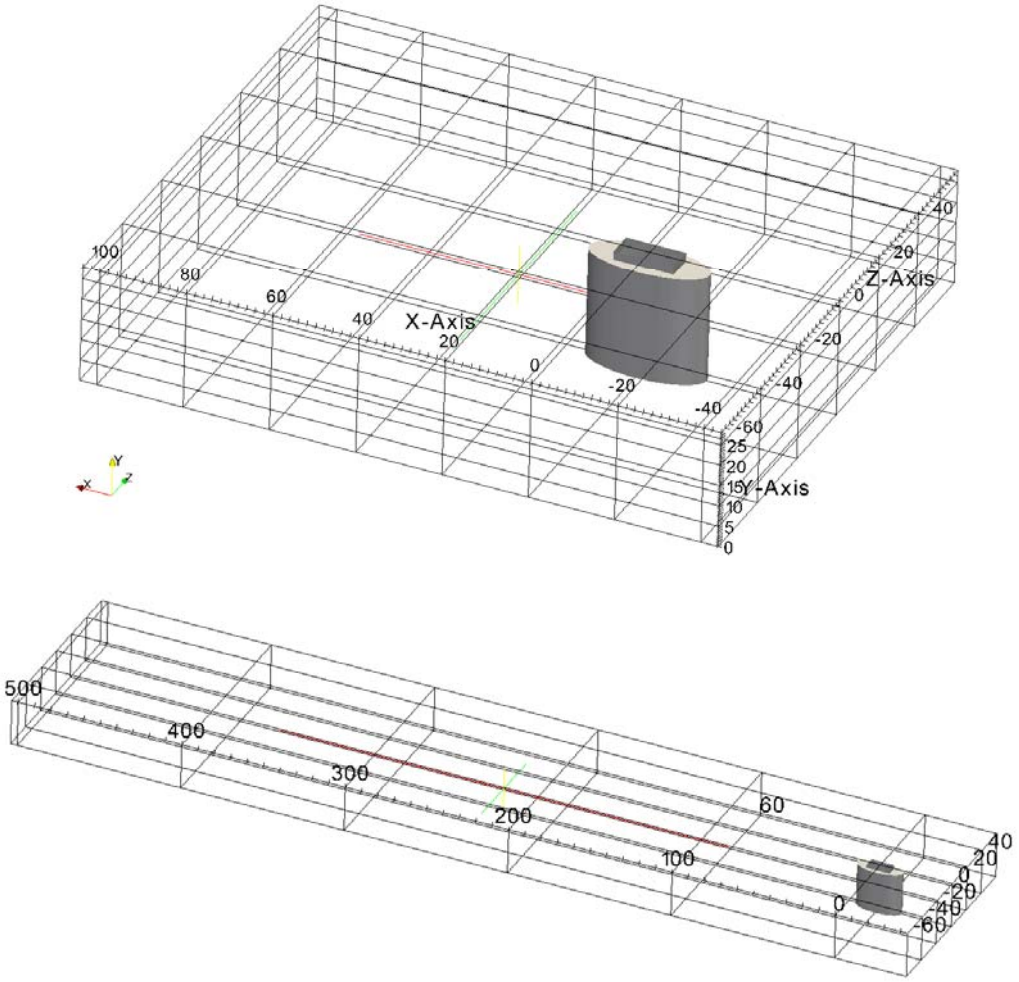

Figure 3.9 Overview of the short model domain with a downstream distance at 100m (top) and the long model domain with a downstream distance of 500m (bottom).

The computational grid was set up to give a sufficient resolution to resolve the characteristic flow features involved in the mixing process, while at the same time the total number of grid cells was kept at a level where the simulations could be finalized within a reasonable time.
Some of the considerations on which the computational mesh was based were:

The velocity gradient in the boundary layer around the structure can be resolved when the nearest horizontal grid extension is in the order of 1-2 roughness heights. For a structure with mussels, this gives a roughness of 5-15cm and a resolution of 0.05m.

The vertical and horizontal extension of the horseshoe vortex is in the same order of magnitude as the displacement depth. The displacement depth will be approximately 10% of the depth of the upper layer (≈ 15m). This means that the horseshoe vortex can be resolved with cells of 10-30cm.

The horizontal size of the wake is approximately half the width of the structure (≈ 5m). The wakes can be resolved with 0.5m large grid cells.

The plinth is 2-5m high. Here the resolution is $\Delta z = \Delta x \approx 0.25\text{-}0.5$m.

Internal waves will not be the limiting factor for the grid resolution.

An example of the computational mesh is given in Figure 3.10 and Figure 3.11 in terms of bridge pier No 1. The mesh was set up with the minimum cell size at the pier surface at 0.1m. The depth was resolved with 0.2m cells for the drag simulations and down to 0.1m cells for the mixing simulations. The horizontal resolution extending away from the pier started at 0.1m at the pier surface and was stretched up to 0.5m at a distance of twice the pier length. A further stretching was applied from here on resulting in a maximum horizontal cell size at 1m. The total number of grid cells for the large 500m domain was approximately 12.5 million cells.

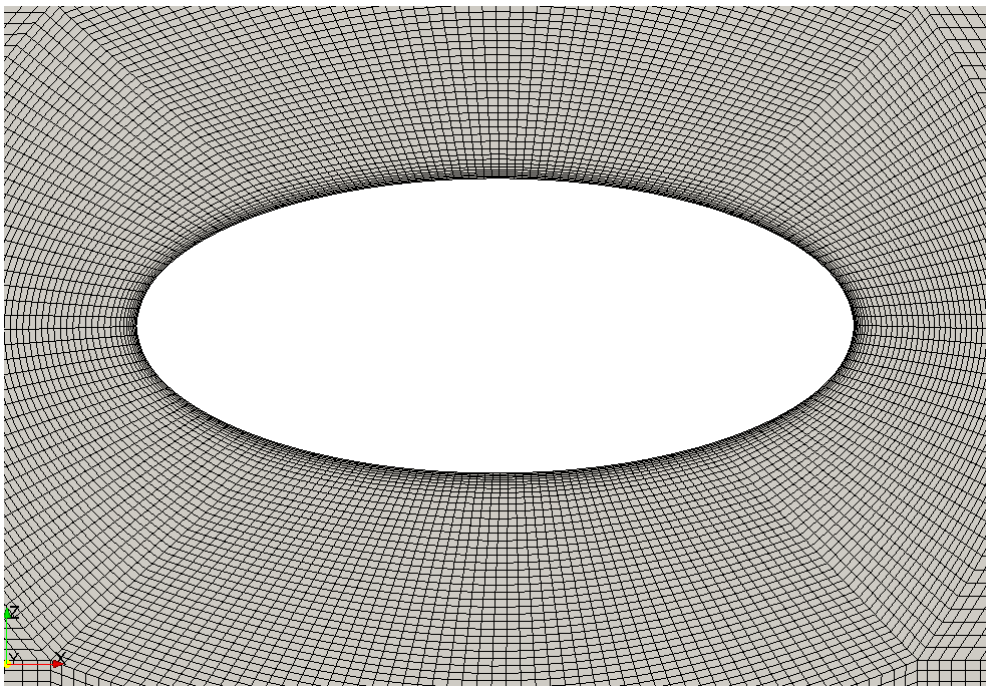

Figure 3.10 Zoom of the computational grid around bridge pier No 1

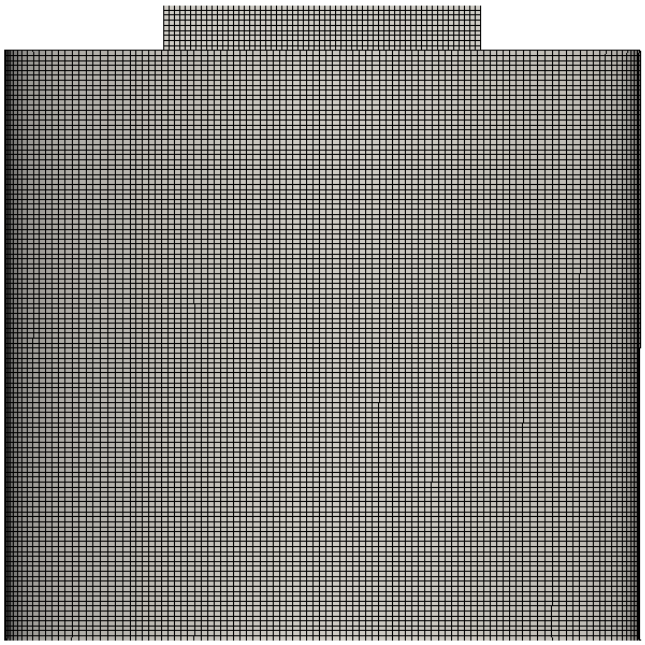

Figure 3.11 Computational grid at bridge pier No 1. Total pier height: 28m.

Figure 3.12 presents the results for bridge pier shape No 1 given as drag coefficients compared to the physical model experiments scaled to prototype scale. In general, good agreement was seen between the numerical simulations and the physical model experiments. For the lowest velocities, the physical model experiments provided a decrease in the drag coefficient, which was believed to be due to measurement uncertainties as the forces were becoming small compared to the resolution on the force gauges. It was believed that the correct physical behavior was represented by the numerical simulations, where the drag coefficients showed a more constant variation over the entire velocity range tested.

The current direction was seen to affect the drag in terms of a larger drag coefficient when the angle was changed to be different from 0 degree. Again a good agreement was found compared to the physical model tests, where the same variation in drag was seen going from 0 to 15 degrees.

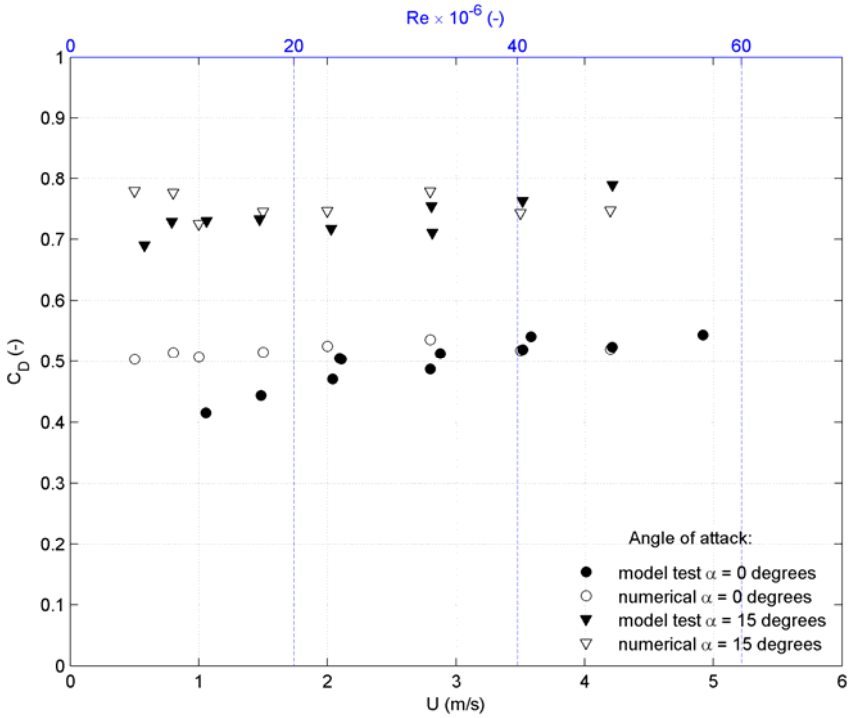

Figure 3.12 Drag coefficients for bridge pier shape No 1 in uniform current and uniform density. Run Nos 1-8 (0 degree current) and run Nos 11-18 (15 degrees current). The same frontal projected area is used for both 0 and 15 degrees current angle. Results from the physical model experiments are shown for comparison. For these scaling has been made to prototype scale.

The flow around pier No 1 is visualized for a current angle at 0 and 15 degrees in Figure 3.13 and Figure 3.14. Streamlines have been initialized downstream the bridge pier and tracked both backward and forward. With the 0 degree current, the flow was relatively symmetrical where two large horizontal eddies formed downstream the pier. For the 15 degrees current, a large eddy was generated in the upper half of the water column near the surface which was dragged up on the leeside of the pier. This created a highly unsymmetrical flow pattern.

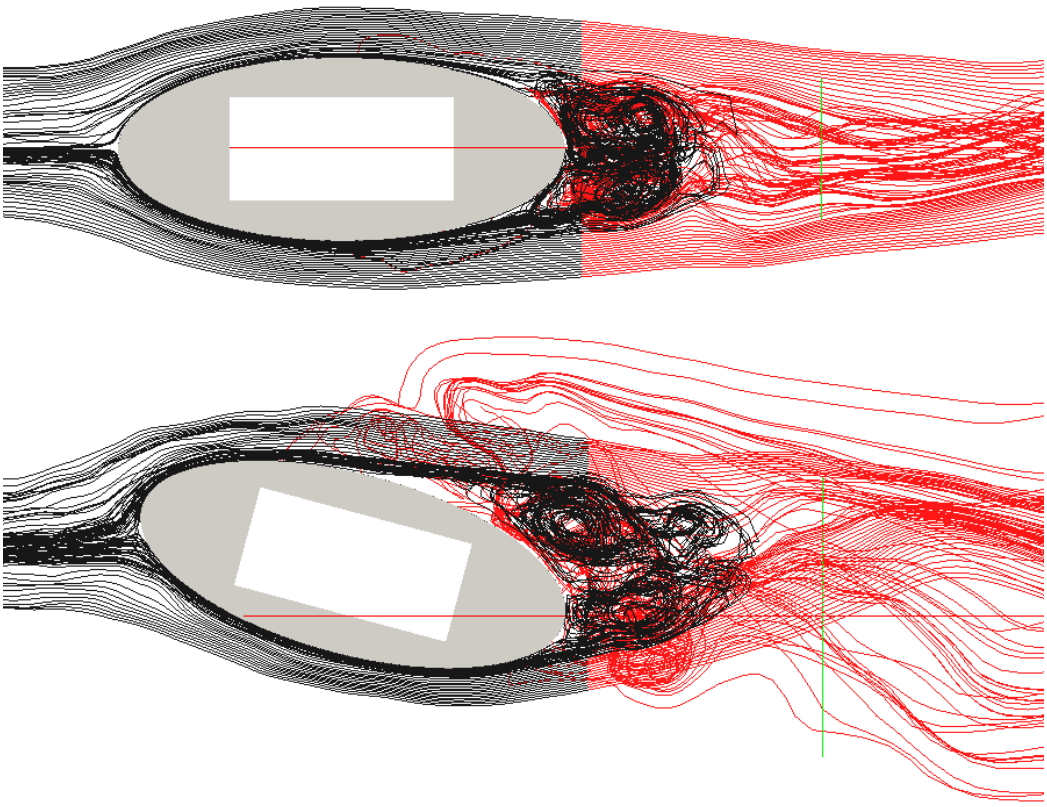

Figure 3.13 Flow around pier No 1 visualised by streamlines initialised downstream the pier at a depth of 14m. Black lines are tracking backwards, red lines are tracking forward. Current angle at 0 degree (run No 1) is shown in the top view and 15 degrees (run No 11) in the bottom view.

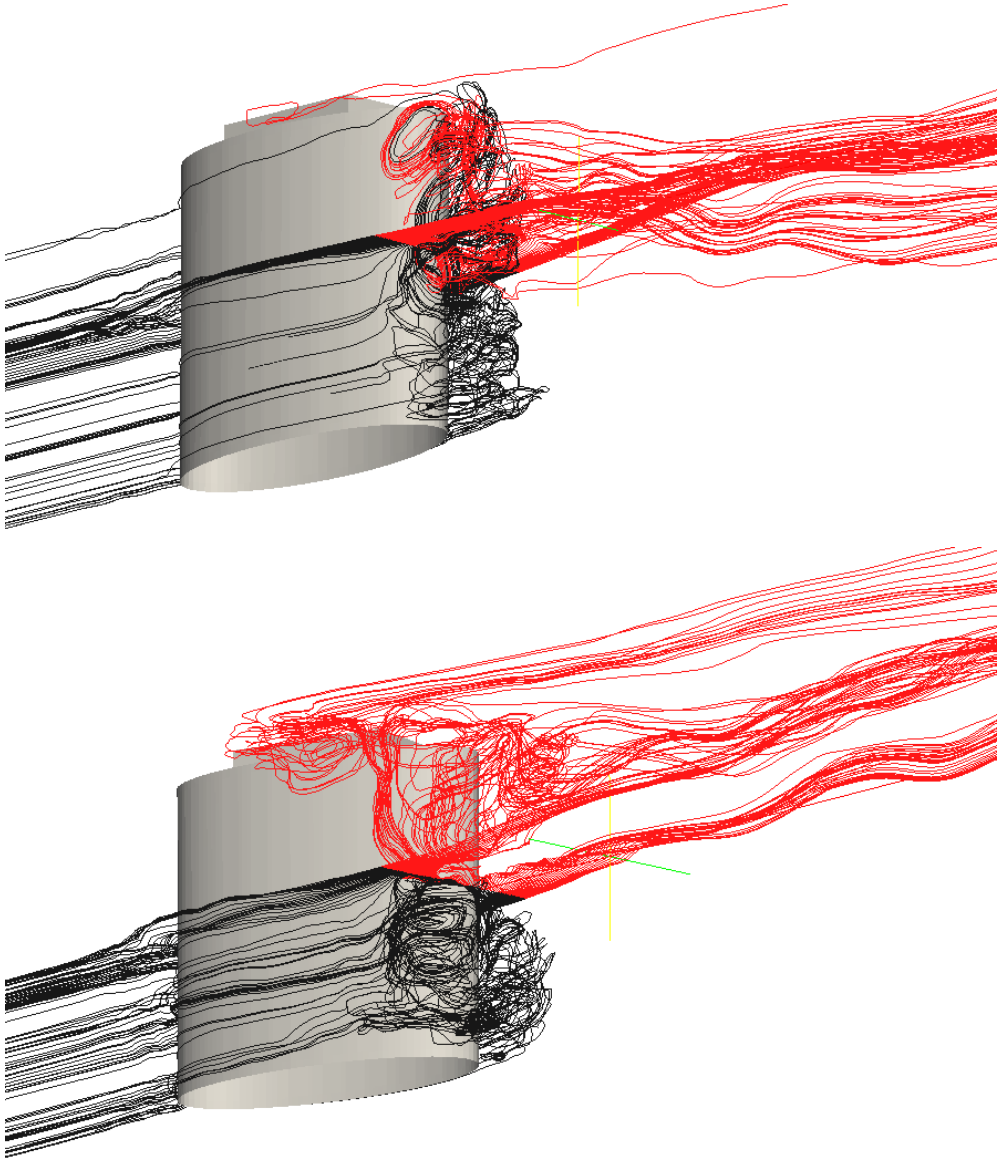

Figure 3.14 Flow around pier No 1 visualised by streamlines initialised downstream the pier at a depth of 14m. Black lines are tracking upstream, red lines are tracking downstream. Current angle at 0 degree (run No 1) is shown in the top view and 15 degrees (run No 11) in the bottom view. Total pier height: 28m.

The effect of different pier shapes was investigated by including simulations of three different shapes as presented in Figure 3.8. For a current velocity at 0.5 m/s, the drag coefficients were found as shown in Table 3.3. A geometrical representation of the three shapes and streamline visualizations are given in Figure 3.15. Here it is noted that the drag force increased for pier no. 1 compared to pier no. 2. The difference between the two pier shapes was the plinth on top of the elliptical shape which introduced a higher total drag force.

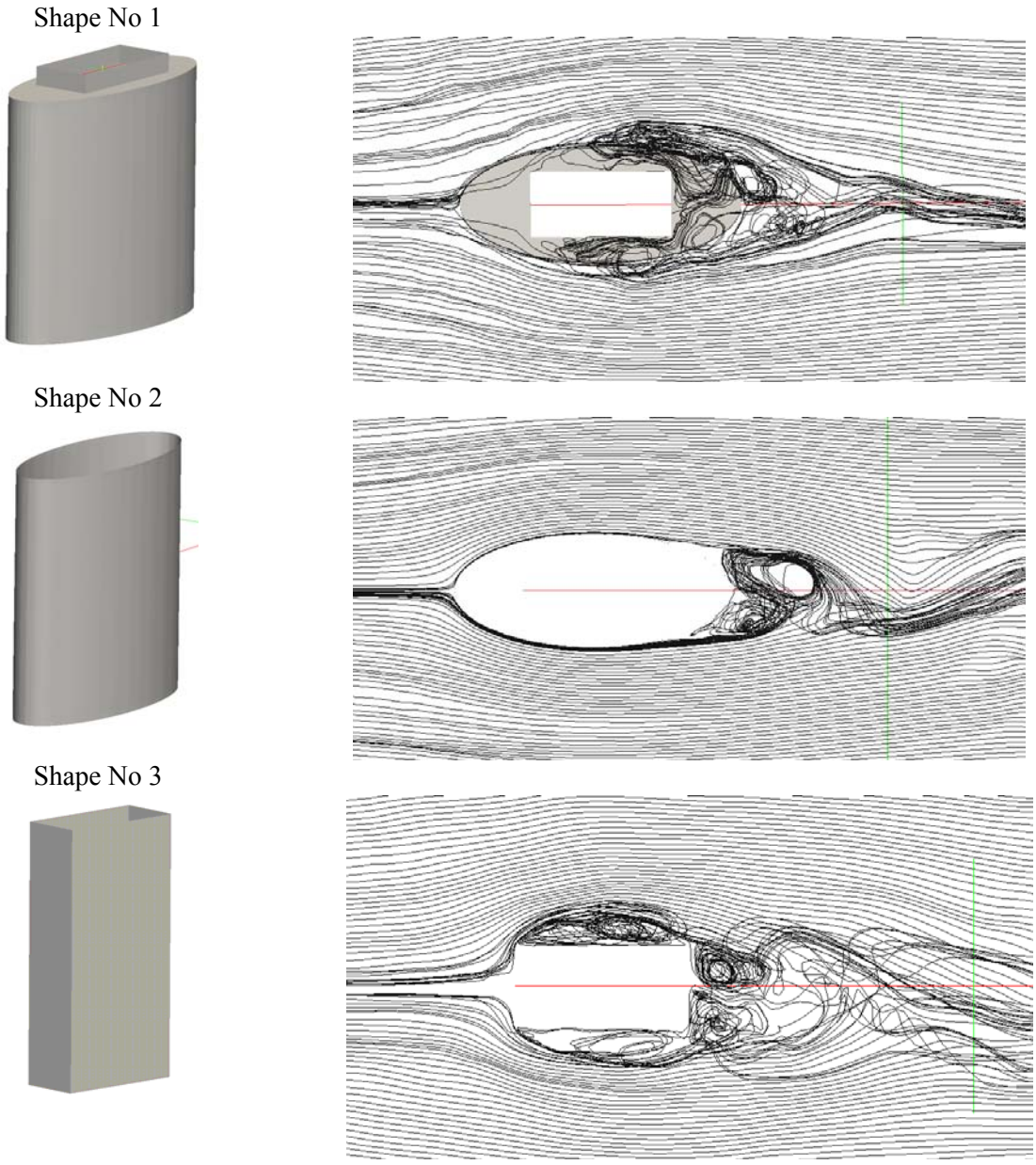

Figure 3.15 Geometrical shapes and streamline visualization for shape Nos 1-3 (run Nos 1, 9, and 10). Streamlines initialized upstream the structure. Total pier height: 28m.

Table 3.3 Drag coefficients for pier shape Nos 1-3 at current velocity 0.5m/s.

Pier shape No	**Drag**
1, elliptical shape with plinth on top	0.51
2, elliptical shape	0.44
3, rectangular box	1.40

Figure 3.16 presents the results for bridge pier shape No 1 given as lift coefficients and the lift coefficients from the physical model experiments scaled to prototype scale. The simulations and comparisons were performed for a 15 degree current angle.

For the highest velocities, a good comparison was seen between the physical model tests and the numerical simulations; however, when the current velocity decreased, a large deviation was found. While the physical model tests presented an increase in the lift coefficient for decreasing velocities, the tendency was towards a constant lift coefficient in the numerical simulations.

The increase in the physical model tests at low velocities was due to the smaller scale in the laboratory tests which induced laminar effects, changing the position of the separation point and thereby the lift coefficient. At these low velocities the numerical model was assumed to give a better representation of the prototype lift forces.

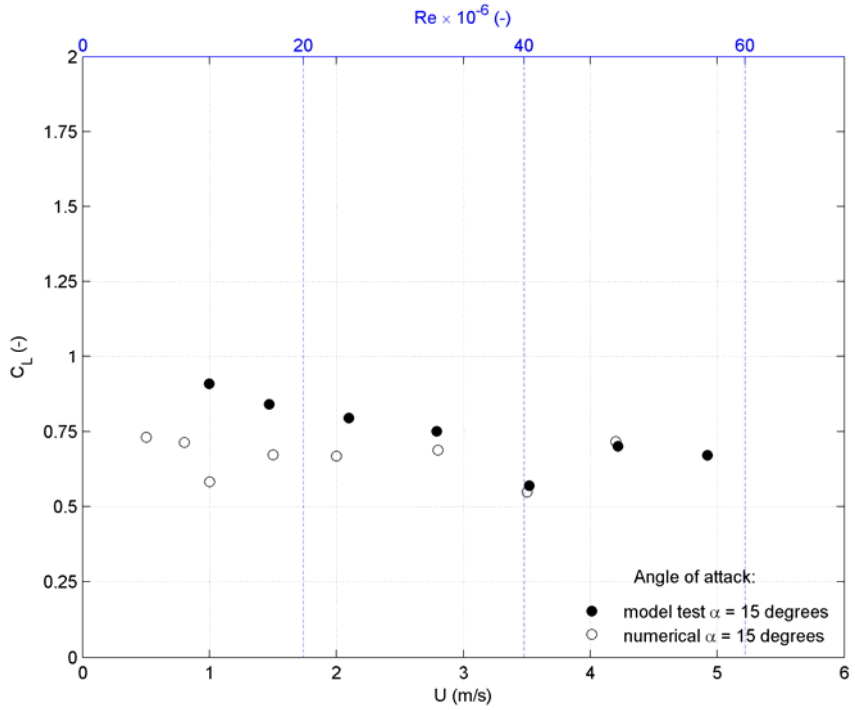

Figure 3.16 Lift coefficients for bridge pier shape No 1 in uniform current and uniform density at a current angle of 15 degrees. Run Nos 11-18. Results from the physical model experiments are shown for comparison. For these scaling has been made to prototype scale.

The effect on the mixing efficiency of different pier shapes and current angles was investigated in a stratified uniform current. The investigations include run Nos 19-29 in the run matrix given in Table 2.1. These simulations covered the same conditions as included in the physical model experiments. A part of the turbulent kinetic energy was converted into potential energy by vertical mixing, while the rest was dissipated into heat. The mixing efficiency can be defined as the increase in potential energy relative to the production of kinetic energy. This is identical to the depth-integrated flux Richardson number:

$$< R_f >= \frac{\Delta E_{pot}}{E_{kin}} \tag{3.7}$$

where the potential energy, E_{pot}, over a specific horizontal reference area may be derived from the density profile as:

$$E_{pot} = A \int_0^h \rho g z dz \tag{3.8}$$

where A is the horizontal reference area upstream and downstream the pier, see Figure 3.17 Figure 2.19, and the input of kinetic energy per run as:

$$E_{kin} \approx W = \overline{F_D}\,\overline{U}\Delta t \tag{3.9}$$

where F_D is the drag force, U is the current velocity and t is time.

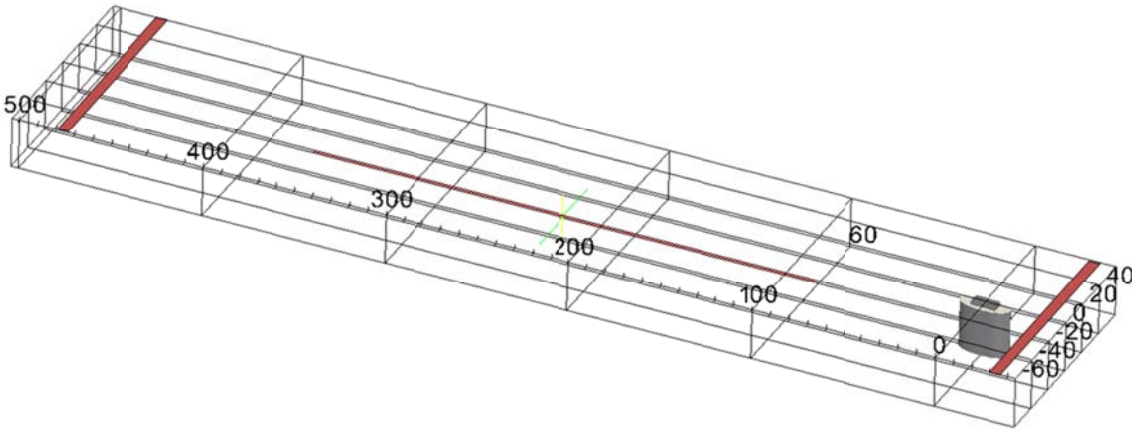

Figure 3.17 Reference area, A, marked with red upstream and downstream the bridge pier.

Data was extracted upstream and downstream the bridge pier both as slices over the width for time and spatial averaging and as time series in discrete points. Figure 3.18 shows the time series of the density at a point just above the stratification at a downstream distance of 20m and 400m. This indicated whether a steady state solution was reached in terms of mixing.

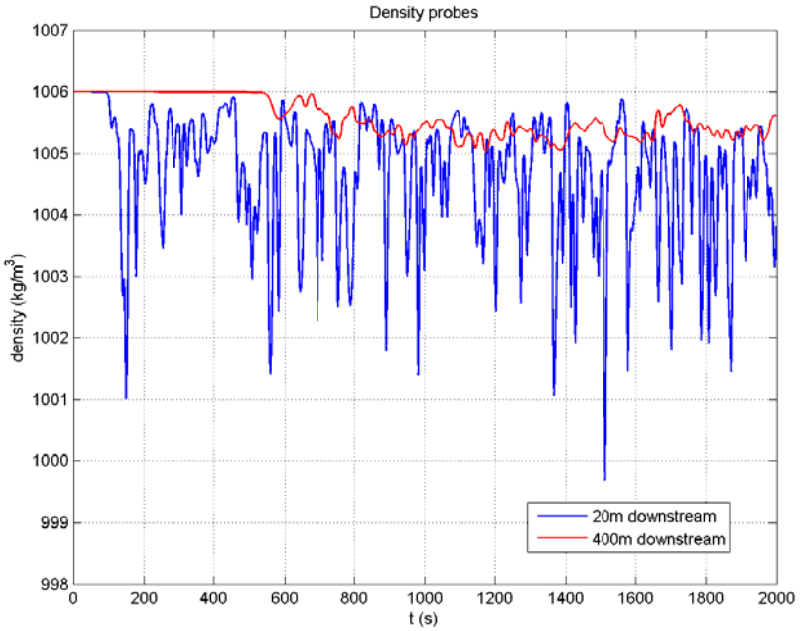

Figure 3.18 Density time series at 20m and 400m downstream the bridge pier. U= 0.7m/s (run No 22). Vertical position immediately above the stratification.

When the mixing had reached steady state, based on extracted time series of density, data were extracted both upstream and downstream the bridge pier for calculation of the mixing efficiency. Figure 3.19 shows an example of the density profiles upstream and 400m downstream respectively

used for calculating the differences in potential energy. Figure 3.20 shows the force time series for the bridge pier used for calculating the work performed in terms of kinetic energy.

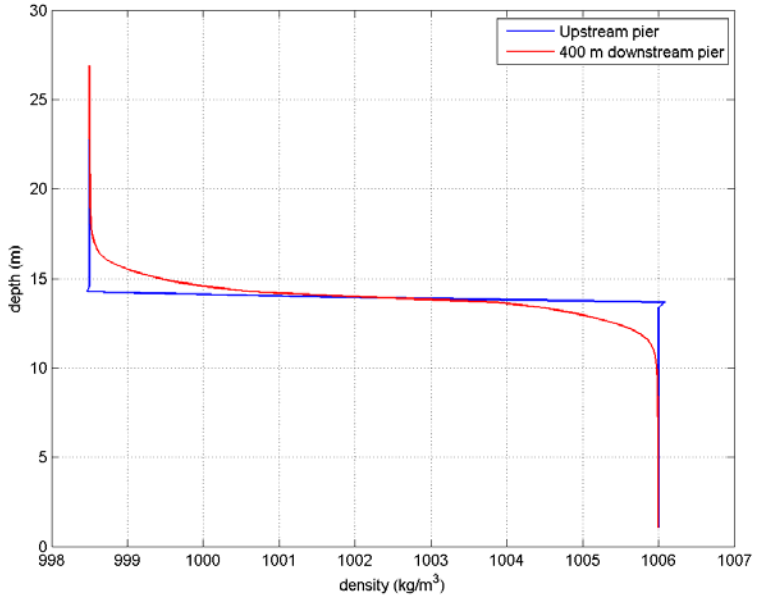

Figure 3.19 Vertical density profiles upstream and 400m downstream the bridge pier at time = 2000s. U=0.7m/s (run No 22). Average across the width of the domain.

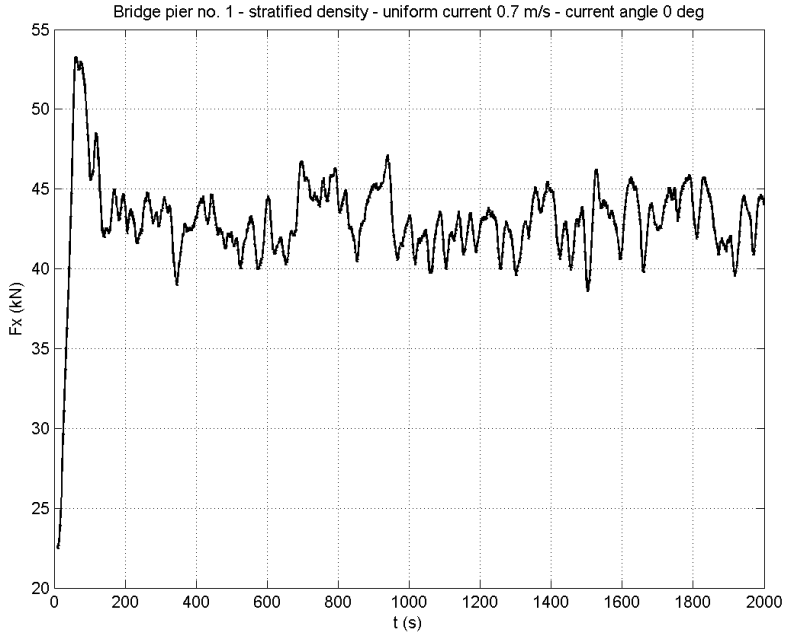

Figure 3.20 Force time series for bridge pier No 1 with stratified density distribution and uniform current with a current angle at 0 degree (run No 22).

Figure 3.21 and Figure 3.22 present the mixing efficiency given as the flux Richardson number as function of the current velocity for bridge pier Nos 1 and 2 with a current angle at 0 degree. The numerical results are shown together with the results from the physical model experiments. In general, the results from the numerical simulations followed the results from the physical model experiments; however, some differences were seen at the lowest current velocities. At high current

velocities, the mixing efficiency was going towards a constant value at around 5% for bridge pier No 1 and 6% for bridge pier No 2, meaning that the mixing in general was comparable for the two pier layouts. For a decreasing current velocity, bridge pier No 2 was seen to give a higher mixing efficiency compared to bridge pier No 1. This was explained by the increased drag force for pier no. 1 resulting from the plinth on top of the elliptical pier. Despite the increased drag force the effect on the mixing from the plinth was relatively small due to its position near the free water surface and therefore not in proximity of the density stratification. At the same time the increased drag force appears in the denominator of the depth-integrated flux Richardson number which gives a relatively smaller mixing efficiency for pier no. 1 with the plinth.

Figure 3.23 presents an example of the mixing around bridge pier No 1 with a current angle at 0 degree. The interface between the bottom and top layer is shown as an iso-surface, while the densities over the depth are shown on a vertical slice.

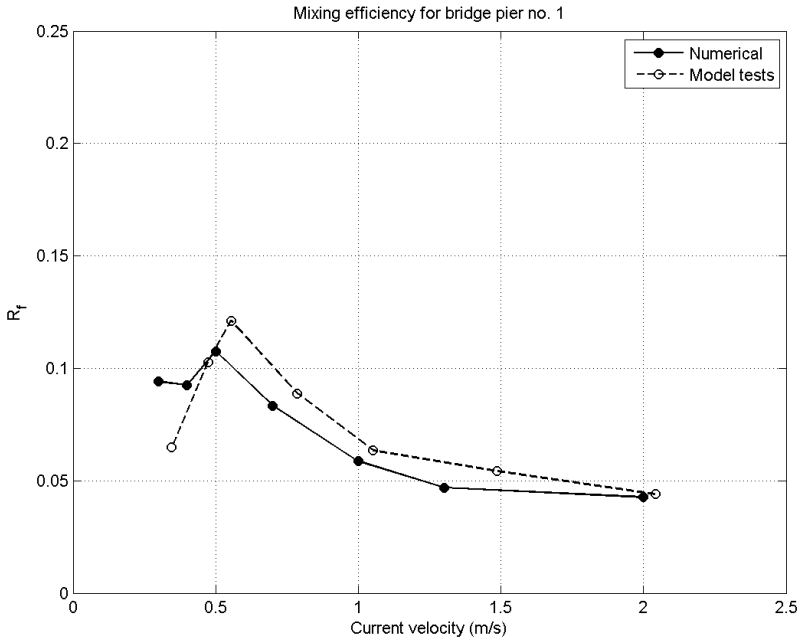

Figure 3.21 Mixing efficiency for bridge pier No 1 as function of the current velocity with a salinity difference at 10 psu and a current angle of attack at 0 degree (run Nos 19-25). Results from the physical model experiments are shown for comparison. For these scaling has been made to prototype scale.

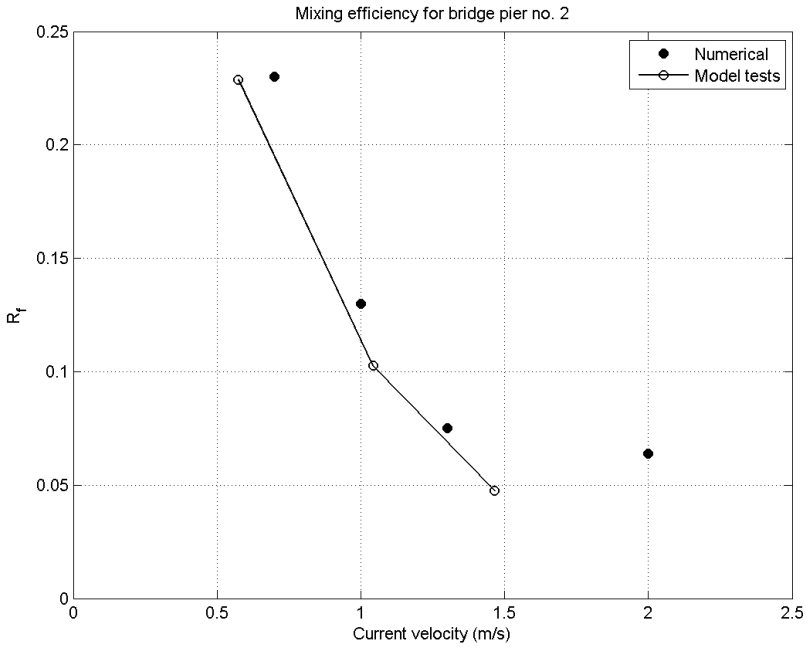

Figure 3.22 Mixing efficiency for bridge pier No 2 as function of the current velocity with a salinity difference at 10 psu and a current angle of attack at 0 degree (run Nos 26-29). Results from the physical model experiments are shown for comparison. For these scaling has been made to prototype scale.

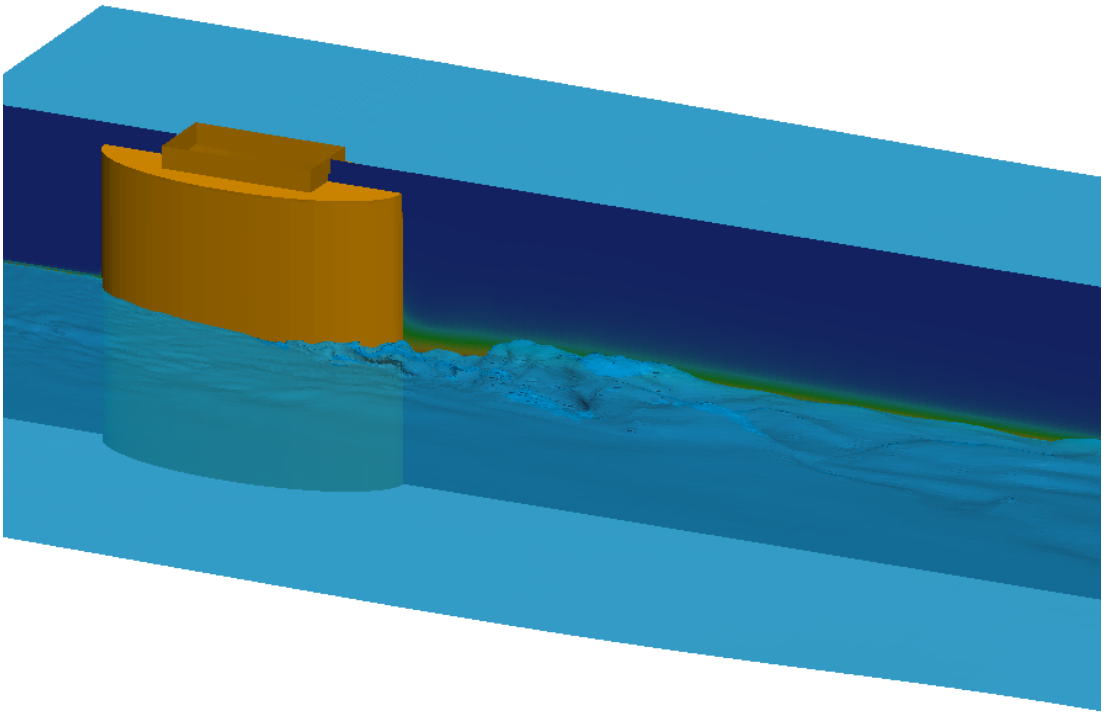

Figure 3.23 Surface at an intermediate density (ρ=1002.25kg/m3) for bridge pier shape No 1 at a current velocity at 0.7m/s and an angle at 0 degree (run No 22). Total pier height: 28m.

3.2 Parameterisation of the effect of unresolved structures on stratified flow

Ole Petersen[2], Bjarne Jensen[2], Stefan Carstensen[1] and Erik Damgaard Christensen[1],
1) DTU-MEK
2) DHI

Parameterisation of structure-induced mixing in stratified and sheared flow is incorporated in the three-dimensional hydrostatic equations of motion for geophysical coastal sea and ocean dynamics. Such structures may be foundations of wind turbines, bridge piers, ventilation or protection islands or similar structures.

For geophysical coastal sea and ocean dynamics, usually the three-dimensional hydrostatic equations of motion with the Boussinesq approximation and the eddy viscosity assumption are used (see e.g. Haidvogel and Beckman (1999) or Kantha and Clayson (2000)).

The approach used here to consider structure induced drag and mixing is well known from meteorology, where resistance by e.g. canopies needs to be described (Häggkvist and Svensson, 1990) or in heat transfer where the effect of discrete roughness elements on the heat transfer is considered (Taylor *et al.*, 1984).. Within boundary layer meteorology, the combined effects of vertical heat transfer (i.e. buoyancy flux) and momentum flux has been carefully studied, for example by introducing the Monin-Obukhov similarity length scale (Turner, 1973). However, only little work on the effects of singular structures on the vertical mixing in stratified flows exists.

The principle of the parameterization is that the details of the processes in the vicinity of the structure is neglected and replaced with an empirical relation that relates the upstream conditions to the downstream effects, focusing only on the permanent changes. Thus the e.g. the horseshoe vortices and the eddy streets downstream are not resolved only the integral drag and the permanent changes in vertical structure are described.

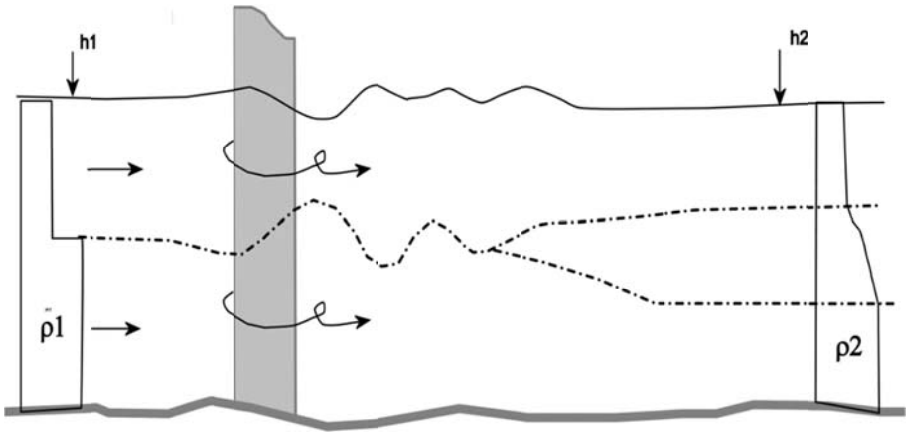

Figure 3.24. Resistance and mixing across a single vertical structure in a stratified flow. In the parameterization the downstream effects described by h_1 and ρ_1 are related to the upstream conditions (ρ_1 and h_1) , neglecting the details of the processes in the vicinity of the structure.

Below is outlined a methodology developed here to enable a description f the mixing and resistance effects from single structures in large scale oceanographic models.
The classical u and v -momentum equations in three-dimensional hydrostatic ocean models, extended with a drag resistance for structures in the water column, can typically be given as:

$$\partial_t u + u\,\partial_x u + v\partial_y u + w\partial_z u = -g\,\partial_x \eta + \int_0^\eta \partial_x b dz + \partial_x(A_h \partial_x u) + \partial_y\left(A_h \partial_y u\right) + \partial_z(A_z + A_{z0} + \nu)\partial_z u - fv + f_x \quad (3.10)$$

$$\partial_t v + u\,\partial_x v + v\partial_y v + w\partial_z v = -g\,\partial_y \eta + \int_0^\eta \partial_y b dz + \partial_x(A_h \partial_x v) + \partial_y\left(A_h \partial_y v\right) + \partial_z(A_z + A_{z0} + \nu)\partial_z v + fu + f_y \quad (3.11)$$

The vertical velocity is calculated by means of the incompressibility condition:

$$\partial_x u + \partial_y v + \partial_z w = 0 \quad (3.12)$$

Here u, v, and w are the ensemble averaged velocity components with respect to the x,y and z direction, respectively. The vertical coordinate, z ranges from the bottom – $H(x,y)$ to the surface $\zeta(x,y)$ with t denoting time. A_z is the vertical eddy viscosity, $\nu = \mu/\rho$ the kinematic viscosity, A_{z0} a parameterisation factor describing increased turbulence by the structure, f is the Coriolis parameter, and g is the gravitational acceleration. f_x, f_y are drag resistance terms with the dimension of acceleration. The horizontal mixing is parameterised by terms containing the horizontal eddy viscosity, A_b. The buoyancy, b is defi**n**ed as:

$$b = -g\,\frac{\rho - \rho_0}{\rho_0} \quad (3.13)$$

with the potential density, ρ , and a reference density, ρ_o. The second terms on the right-hand sides of equations (3.1) and (3.2) are the internal (due to density gradients) and the first term the external (due to surface slopes) pressure gradients. In the former, the deviation of surface density from reference density is neglected (see Burchard and Petersen (1997)). The derivation of equations (3.1) and (3.2) has been shown in numerous publications; see e.g. Haidvogel and Beckmann (1999) or (Burchard, 2002).

The transport – diffusion equation for salinity and temperature (not shown) reads:

$$\partial_t S + u\,\partial_x S + v\partial_y S + w\partial_z S = \partial_x(K_h \partial_x S) + \partial_y\left(K_h \partial_y S\right) + \partial_z(K_z \partial_z v) \quad (3.14)$$

here $K_z = \frac{A_z}{\sigma_T}$ is the turbulent vertical diffusivity, σ_T is the turbulent Schmidt number, and K_h is the horizontal diffusivity. The density is related to the salinity and temperature using an equation of state $\rho = \rho(S,T)$. The equation for the potential temperature is of a similar form as the salinity equation.

The turbulence is described using the *k-ε* model with dynamic equations for the turbulent kinetic energy, k, and its dissipation rate, ϵ , reading:

$$\partial_t k + u\,\partial_x k + v\partial_y k + w\partial_z k = \partial_x(K_h \partial_x k) + \partial_y\left(K_h \partial_y k\right) + \partial_z(K_z \partial_z k) + P_{SHEAR} + P_B - \epsilon \quad (3.15)$$

$$\partial_t \epsilon + u\,\partial_x \epsilon + v\partial_y \epsilon + w\partial_z \epsilon = \partial_x(K_h \partial_x \epsilon) + \partial_y\left(K_h \partial_y \epsilon\right) + \partial_z(K_z \partial_z \epsilon) + \frac{\epsilon}{k}(C_{1\epsilon}\,P_{SHEAR} + C_{3\epsilon} P_B - C_{2\epsilon}\epsilon) \quad (3.16)$$

with the turbulent Schmidt numbers, σ_k and σ_ϵ and the empirical parameters $c_{1e} - c_{3e}$ which have been calibrated for a wide range of flow situations undisturbed by obstacles.

The shear production is $P_{SHEAR} = \nu_T((\partial_z u)^2 + (\partial_z v)^2)$ and the buoyancy term representing the upward flux of buoyancy is $P_B = -K_z N^2$, where the buoyancy frequency is

$$N^2 = -g\partial_z \rho/\rho(\partial_z u)^2 \quad (3.17)$$

The closure of the momentum equations is then made using the eddy viscosity defined by

$$\nu_T = c_\mu \frac{k^2}{\epsilon} \quad (3.18)$$

where c_μ can be an empirical constant in the case of a standard $k-\epsilon$ model or a function of shear and stratification for more advanced models. In the former case the turbulent Prandtl number is a function of the gradient Richardson number.

For a simplified analysis, assuming turbulence source terms being in a local equilibrium, the balance can be written as

$$P_{SHEAR} - K_z N^2 - \epsilon = 0 \tag{3.19}$$

Using the flux Richardson number R_f this can be written as

$$1 - R_f - \frac{\epsilon}{P_{SHEAR}} = 0 \tag{3.20}$$

where, $R_f = -K_z N^2 / P_{SHEAR}$ describes the mixing efficiency.

3.2.1 **Drag**

The drag and lift force per unit height on a section of a vertical structure exposed to a steady current can be written as

$$F_D(z) = \frac{1}{2}\rho C_D d U^2 = \frac{1}{2}\rho S_D U^2 \tag{3.21}$$

$$F_L(z) = \frac{1}{2}\rho C_L d U^2 = \frac{1}{2}\rho S_D U^2 \tag{3.22}$$

Where C_D is the non-dimensional drag coefficient, C_L the lift coefficient, d a characteristic width of the structure and U the magnitude of the incoming velocity. For convenience a force-coefficient is introduced as $S_D = C_D \cdot d$ and $S_L = C_L \cdot d$. Only horizontal components of the force are assumed to be significant. The direction of the drag and the lift forces are stream-wise and normal directions, respectively, as shown in Figure 3.25. The alignment of the structure itself, θ, is directed along a possible bridge trace.

The dimensionless drag and lift coefficients may be a complicated function of vertical position as well as of various hydrographical parameters such as current speed, current direction or stratification and shear.

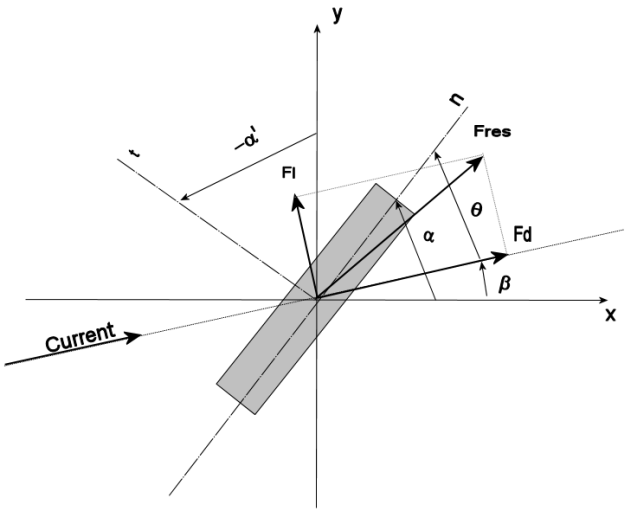

Figure 3.25 Alignment of structure given by α in a xy-coordinate system or $-\alpha'$ relative to true North with counter-clockwise directions. The direction n is normal to the bridge trace and t along the trace. The resultant force vector is F_{RES}. The component aligned with the current direction is the drag F_D and normal to this the lift F_L. The current direction is β and the incident angle of the current θ

To convert the drag and lift forces into an acceleration aligned with x and y axes in eq. (3.10) and (3.11) they need to be divided by the density and an area parameter, a, and rotated as:

$$f_x = \frac{1}{a\rho}(F_D \cos\beta + F_L \sin\beta) \tag{3.23}$$

$$f_y = \frac{1}{a\rho}(-F_D \sin\beta + F_L \cos\beta) \tag{3.24}$$

Formally, a can be seen as a Dirac-delta function. In a numerical model context, a represents the area of the element or grid-cell.

3.2.2 **Mixing**

The effect of the drag will be to initiate an energy cascade, creating turbulence and mixing downstream the structure. Schematically this can be described as the mean kinetic energy in the incoming flow being converted to turbulence, the rate being the production by the drag force, as depicted below. Part of the turbulence initially goes through large coherent eddies, e.g. the downstream vortex street, before decaying into turbulence. The turbulence in turn is partly dissipated into heat, partly used to mix a stably stratified water column, thereby increasing the potential energy of the water column.

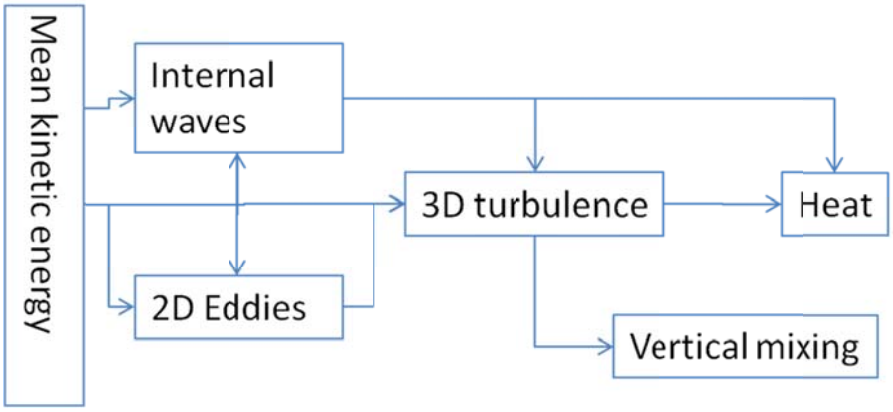

Figure 3.26 Energy conversions in a stratified turbulent flow

Because the spatial resolution of the numerical model is relatively coarse (say 500 m) most of these processes will take place within one element, as seen on the numerical model scale; there is a local equilibrium between the production of turbulence by the drag and the mixing and heat dissipation. Consequently outside the element where the structure resides, the effects will be i) a sink of mean kinetic energy and, ii) a change in thermal and potential (by the vertical mixing) energy. In the models used here, no balance is made for thermal energy, thus only the vertical mixing is accounted for.

In the literature there exist a few suggestions for describing turbulence associated with structures, e.g. using discrete element turbulence models. However, models for the associated mixing seem relatively scarce.
A method following the methods introduced by Svensson and Häggkvist (1990) has been suggested by Rennau *et al.* (2010), extending the standard $k\epsilon-$model to include the structure-induced turbulence production as

$$P_{STRUC} = f_x u + f_y v \tag{3.25}$$

such that the total production of turbulent kinetic energy is given as $P = P_{SHEAR} + P_{STRUC}$.
This will give the correct production of turbulence and the correct energy balance. However, an empirical correction is necessary in the ϵ equation, adjusting the turbulence length scale. This will introduce some inconsistency as the turbulence from the structure will be generated at a much smaller scale than the surrounding turbulence, while the $k\epsilon$ model can only describe one integral length scale. However, results by Rennau *et al.* (2010) in the Baltic Sea demonstrate that the model can be calibrated to provide realistic estimates of the turbulence dynamics.

An alternative and more direct method is suggested here, which uses the definition of a structure-induced flux Richardson number. Indirectly this assumes that the turbulence is in equilibrium at the structure. Assuming that the effects of the structure on the turbulence and mixing can be treated as a small incremental effect, a structure flex Richardson number R_f' is defined as

$$K_z' = R_f' P_{ST} / N^2 \tag{3.26}$$

where K_z' represents the additional vertical diffusivity due to the structure induced turbulence. This gives a direct relation between the structure induced vertical mixing coefficient and the additional turbulence produced by the structure, which for a given stratification and structure-induced mixing efficiency, described by N^2 and R_f', gives the increase in vertical diffusivity for a given input of

turbulent energy P_{ST} . For numerical reasons N^2 is assumed to be limited so $N^2 < N_{crit}^2$, where $N_{crit}^2 = 10^{-6}$. This assumption avoids unrealistically large diffusivities in areas where there is no or very weak stratification. In such areas the permanent effect of the structure induced mixing will be insignificant anyway. The critical value corresponds roughly to a vertical salinity gradient at 10^{-4} PSU/m. Using Reynolds analogy in an inverse manner this can finally be related to the eddy viscosity as

$$\nu_T' = \sigma_T K_z' \tag{3.27}$$

The use of Reynolds analogy can be discussed as there are situations where the assumption of a linear gradient-flux relationship is not valid, as discussed by e.g. Large (2000) in his derivation of the KPP mixing scheme. However, the approach is in line with the general concept of the modelling used here.

The resulting mixing can then be included in the equation for transport of salt as

$$\begin{aligned} &\partial_t S + u\partial_x S + v\partial_y S + w\partial_z S \\ &\qquad = \partial_x(K_h \partial_x S) + \partial_y\big(K_h \partial_y S\big) + \partial_z\big((K_z + K_z')\partial_z S\big) \end{aligned} \tag{3.28}$$

The equation for the potential temperature can be modified accordingly.

In the present study, the bulk mixing efficiency has been measured in the laboratory, where the structures have been towed through a still, stratified water body. The bulk mixing efficiency is here defined as

$$\int_{-H}^{\eta} K_z' N^2 dz = \overline{R_f'} \int_{-H}^{\eta} P_{ST} dz \tag{3.29}$$

In the laboratory experiments the structure-induced bulk mixing efficiency was estimated by applying the relation to measured profiles of density and of P_{STRUC} as:

$$\partial_t \int_{-H}^{\eta} gz dz = \rho_0 \overline{R_f'} \int_{-H}^{\eta} P_{ST} dz \tag{3.30}$$

from which $\overline{R_f'}$ can be determined. Assuming the structure-induced vertical diffusion coefficient is vertically constant, this can then be estimated from (3.26) . The extra eddy viscosity can then be calculated accordingly from (3.27).

Further, the assumption in (3.30) that the structure induced diffusivity is vertically constant may appear restrictive, as there are relatively large variations in the structure shapes and also in the velocity. However, for many structures the drag forces are relatively constant, because the largest part of the structures normally is close to the seabed, while the current speeds are lower here also. Thus for bottom mounted structures this simpler assumption may be to be justifiable.

The laboratory experiments indicated a dependency of the $\overline{R_f'}$ on the current speed or, presumably, on an internal Froude number. Therefore it is suggested to normalize the velocity dependency using a densimetric Froude number defined by:

$$F_D = \frac{U}{c} \tag{3.31}$$

where U is the vertically averaged flow speed and c is celerity of the internal wave. The celerity can be estimated as $c = 0.5\,HN$ with N being the buoyancy frequency. Formally, the factor will vary between 0.3 - 0.5 depending on the stratification.

3.2.3 **Discussion**

The parameterizations are implemented in the ocean models MIKE 3 FM and GETM and may readily be implemented in other standard ocean models. The parameterization discussed above is related to a single vertical monopole. For other structure types, e.g. fish cages or caisson structures, the factors in the parameterization may vary and can in principle be determined by a series of experiments or model calculations as above.

3.3 Modelling of mixing of saline layers, Ocean-models

Karsten Bolding and Hans Burchard , BB

For a study of the effects of off-shore wind farms on the exchange of saline waters between the North Sea and the Baltic Sea, Rennau et al. (2012) carried out an extensive modeling study for the Western Baltic Sea. The model domain for that study is shown in fig. 1.

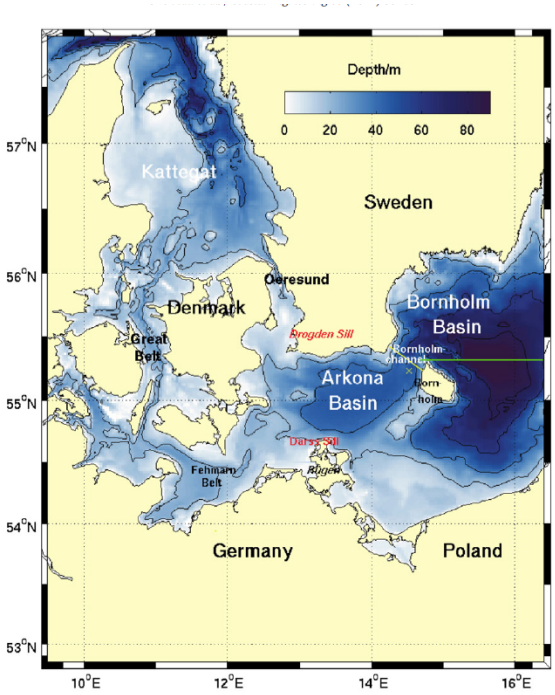

Figure 3.27: Model domain in the Western Baltic Sea for the study by Rennau et al. (2012). This figure is taken from Rennau et al. (2012).

Saline inflows into the Baltic Sea which occur at various spatial and temporal scales have the effect of ventilating different layers of waters in the Western and Central Baltic Sea by supplying often suboxic or anoxic waters with oxygenated inflow waters. Medium-intensity inflows occur mainly through the Oeresund (see Figure 3.27) and several of them are typically observed each year. Their pathway leads southwards from Drogden Sill, and then turns eastwards to flow into the Arkona Sea through the channel north of Kriegers Flak. These inflows have been described in detail by Burchard et al. (2005) and Sellschopp et al. (2006). Such inflows would typically ventilate the thermocline and halocline areas of the Western and Central Baltic Sea. Larger inflows occur less often and propagate mainly through the Great Belt and Fehmarn Belt and over the Darss Sill. Those may be baroclinic (stratified) when stable high air pressure systems govern the meteorological forcing with little wind. Then a dense bottom current may develop and enter the Baltic Sea through Darss Sill with high salinity, and generally high temperature and low oxygen concentrations (since the baroclinic inflows typically happen during summer months). Baroclinic inflows have been described in detail by Feistel et al. (2004). Much more important are the so-called (barotropic) Major Baltic Inflows (MBIs) which occur about once per decade and which are characterised by mixed waters of high salinity entering mainly across Darss Sill. Such inflows are known to ventilate most parts of the Central Baltic Sea such that the Baltic Sea is almost void of hydrogen sulfate for a

few months. The conditions under which MBIs occur have been described in detail by Matthäus and Frank (1992). An extensive review on Baltic Sea inflows and their environmental consequences has been compiled by Reissmann et al. (2009).

A major characteristic of all these inflows is the complex pattern of entrainment of upper, less saline waters into the inflowing waters which propagate as dense bottom currents. This dilution of the inflows leads to decreased density and therefore to a reduced potential of the inflows to reach deeper layers and ventilate them. With this, entrainment of ambient waters into saline inflows into the Baltic Sea is a major environmental process which needs to be reproduced by numerical models. It would furthermore be critical to increase this natural process by human interventions such as the construction of offshore wind farms and bridges.

When using numerical models to simulate mixing and entrainment in coastal seas, it is not sufficient to have a good turbulence closure model in place (see section 2.4), but also artificial mixing introduced by the discretisation of the dynamic equations needs to be minimised. Burchard and Rennau (2008) developed a method to quantify numerical mixing and applied it to a model simulation of the Western Baltic Sea (Rennau and Burchard, 2009). They could show that up to 50% of the mixing analysed by the numerical model was due to numerical mixing.

During the last decade, installations of offshore wind farms have in coastal waters have massively increased. This also happens in the region of the Western Baltic Sea where Germany, Denmark and Sweden are constructing tens of wind farms with up to 100 wind turbines each. Since many of these installations are constructed directly in the pathways of inflowing saline waters, it has been discussed whether additional mixing and entrainment due to these installations could have effects on the oxygenation of the Baltic Sea. In a pilot study, Rennau et al. (2012) simulated hydrodynamics in the Western Baltic Sea during the year 2004 with and without the effect of mixing due to offshore wind farms. Burchard and Rennau (2012) used a slightly different way of parameterising mixing due to structures than the way presented in section 2.4. Their approach was adopted from Svensson and Häggkvist (1990) who developed their parameterization for air flow through forest canopies. In that method, the equations for the turbulent kinetic energy and the dissipation rate are extended by production terms due to structure friction. This procedure introduces a new empirical parameter to the dissipation rate equation which is calibrated using a one-dimensional water column model to reproduce structure-induced vertical buoyancy flux calculated by a non-hydrostatic RANS model including a cylindrical structure (see Figure 3.28 and Rennau et al., 2012). This parameterization was then implemented into the General Estuarine Transport Model (GETM, www.getm.eu, Burchard and Bolding, 2002).

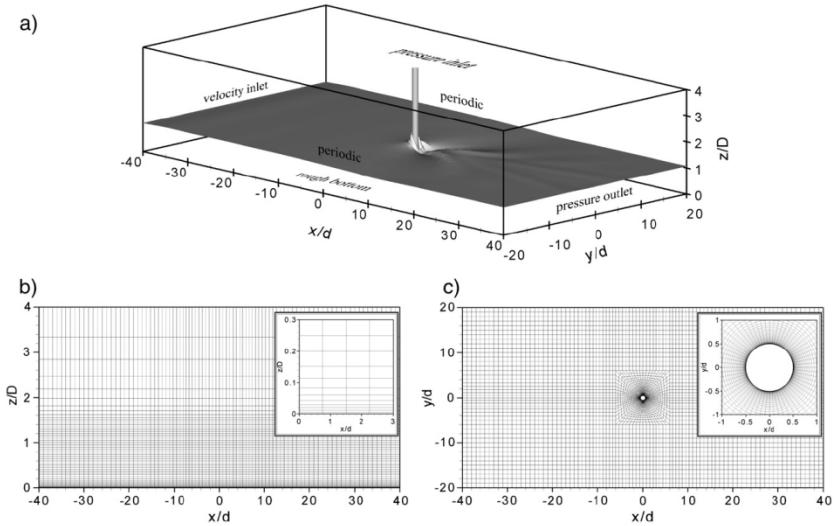

Figure 3.28: Non-dimensional computational domain for three-dimensional high resolution RANS simulations by Rennau et al. (2012). (a) Definition sketch of complete computational domain with the cylinder in the centre, boundary conditions assigned by the text and interface position indicated by the shaded plane. (b) Side view and (c) top view of the numerical grid. Small panels showing the refined resolution at the bottom and cylinder, respectively. This figure is taken from Rennau et al. (2012).

Figure 3.29 shows the location and extent of offshore wind farms as they have been implemented in the model simulations by Rennau et al. (2012). For the realistic simulations, all existing and projected wind farms have been taken into account. In addition, to get an estimate of a maximum worst case scenario, an unrealistically extensive wind farm distribution has been investigated, indicated by the large boxes in Figure 3.29. For all cases, cylindrical wind turbine foundations with a diameter of 10m has been assumed, which is higher than the constructions carried out. Two different structure-induced mixing efficiencies have been investigated; a strong mixing case and weak mixing case.

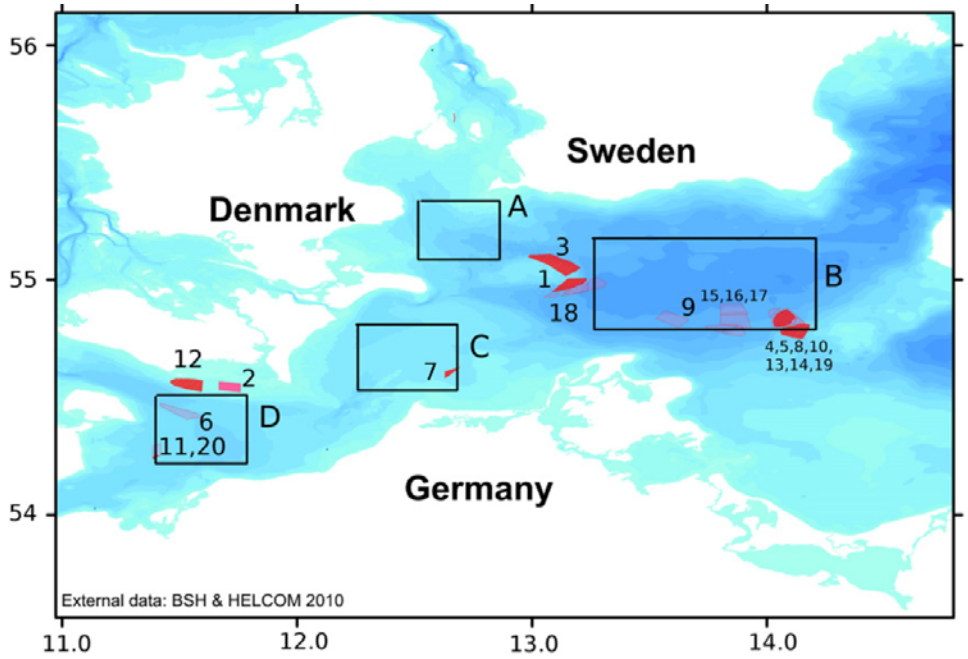

Figure 3.29: Distribution of offshore wind farms (OWFs) in the Western Baltic Sea (external data from Bundesamt für Seeschifffahrt und Hydrographie, see Marnet website at www.bsh.de, situation in April 2009) as used for the realistic simulations by Rennau et al. (2012). The black rectangles indicated by A, B, C and D are the OWF's for the unrealistically extensive distribution. This figure is taken from Rennau et al. (2012).

The investigation of single medium-intensity inflow events shows that there may be certain events with higher densities that are strongly diluted by the offshore wind farms (density differences of up to 3 psu for the unrealistic scenario with weak mixing in Mar 2004). Although the strong mixing during this inflow event can be regarded as a single extreme event, we analyse it to see how a strong mixing signal affects the ventilation in the Bornholm Sea. In average, as shown by Figure 3.30c, the change in transport of highly saline water is negligibly small. It can be assumed that a complete dilution of the highest density classes has a negligible effect since the total transport into the Bornholm Sea connected to these classes is small.

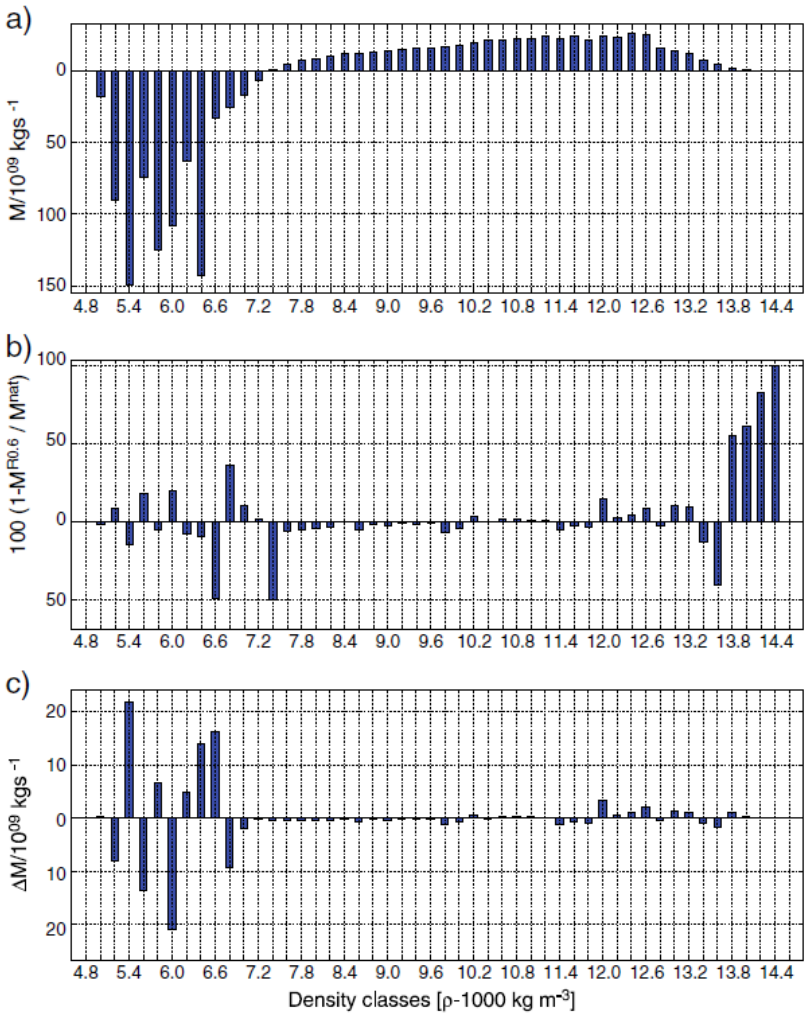

Figure 3.30: Western Baltic Sea simulation: monthly mean (averaged over Nov 2003, Mar 2004, Jun 2004 and Jul 2004 during which relative strong inflow activity was detected) water mass transport M across a transect at Bornholm Channel (see fig. 1 for the location), shown as contributions from density classes. a) water mass transport M for reference scenario (REF); b) difference in% between reference (REF) and the realistic case with strong mixing; c) difference in water mass transport ΔM between reference (REF) and the realistic case with strong mixing. This figure is taken from Rennau et al. (2012).

To investigate how mean salinities are affected for the four OWF scenarios, the bottom salinity of the reference case (REF) is compared to the four off-shore wind farm scenarios by taking the 12 month mean bottom salinity of the natural case and subtracting the mean bottom salinity of each of the four cases (see Figure 3.31). The bottom salinity decreases found for the cases with realistic off-shore wind farm distribution are in the order of up to 0.2 psu. Interestingly, in the Arkona Sea the saline bottom waters seem to be less diluted by off-shore wind farms when strong mixing is assumed. This may be explained by the fact that dense bottom currents are decelerated by off-shore wind farms such that entrainment of less saline ambient waters may be locally reduced. However, for the realistic scenario with strong mixing, bottom salinities are reduced more significantly than for the weak mixing realistic scenario, which is consistent with a net increase in mixing and which is more relevant for the ventilation of intermediate layers in the Bornholm Sea. A different picture is found for the two cases with unrealistically extensive off-shore wind farm distributions, where

the mean bottom salinity is decreased by up to 0.3 psu for weak mixing and by up to 0.6 psu for strong mixing.

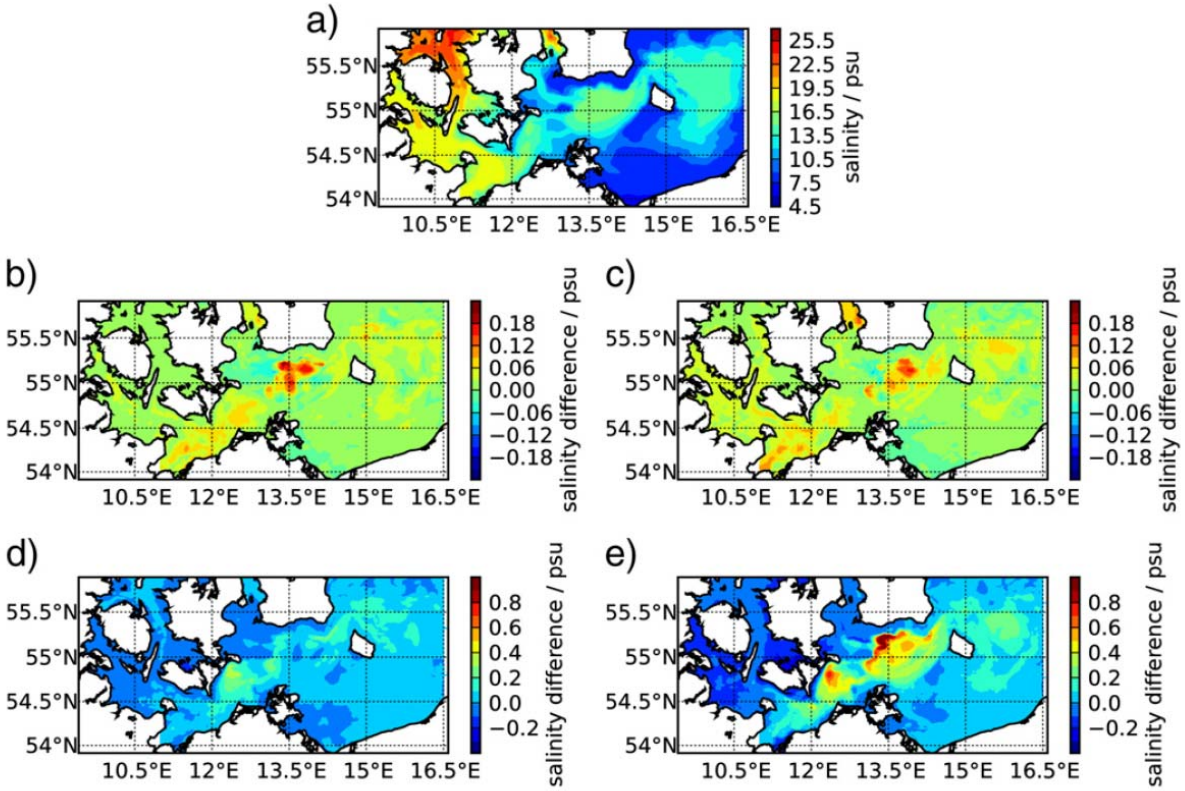

Figure 3.31: Western Baltic Sea simulation by Rennau et al. (2012); annual mean (year 2004) of bottom salinity and bottom salinity difference due to offshore wind farms: a) reference scenario REF; b) scenario REF — realistic with weak mixing; c) scenario REF — realistic with strong mixing; d) scenario REF — unrealistic with weak mixing; e) scenario REF — unrealistic with strong mixing. This figure is taken from Rennau et al. (2012).

It requires a careful analysis by Rennau et al. (2012) to see any significant changes in saline inflows due to the offshore wind farms. Since almost all inflows into the Baltic Sea proper have to pass the Bornholm Channel just east of the Western Baltic Sea region with potential wind farm impact, a study of the near-bottom salt and mass inflow in that region has been made. One result is that the impact of wind farm mixing leads to spatially and temporally varying changes in bottom salinity, with decreases for realistic wind farm distributions by 0.0059±0.491 psu for weak mixing and by 0.0222±0.469 psu for strong mixing. Clearly, these changes are small compared to the natural variability and also small compared to the variability of the impact itself. In contrast to this negligible reduction scenarios with over-exaggerated wind farm distribution led to reduction in bottom salinity in the Bornholm Channel by 0.1728±0.595 psu for weak mixing and 0.4222±0.560 psu for strong mixing.

The statistical analysis by Rennau et al. (2012) of the net salt transport into the Bornholm Sea quantified in terms of density classes reveals that the salt transport in the four highest density classes of 0.2 kg m^{-3} width each are partially or completely vanishing in the scenario with realistic wind farm distribution and strong mixing. However, the relative contribution of these high salinity

classes to the net salt inflow is small, since only during short single events thee high densities are obtained.

In the framework of the Rennau et al. (2012) study the impact of realistic wind farm distributions on the Baltic Sea ecosystem, according to the present planning state, has been estimated to be small. Even if a structure-induced mixing efficiency of twice the best guess is assumed, bottom salinities in the Arkona Sea are decreased only locally by about 0.2 psu. In the most extreme month during the entire simulation period, ventilation of the Bornholm Sea occurred about 2 m higher in the water column. This is in accordance with the finding that only the highest density classes vanish due to wind farm mixing. Those contribute however only little to the total ventilation. It should however be noted that a coverage of large parts of the Western Baltic Sea with offshore wind farms could lead to more significant impacts, such as substantial bottom salinity decreases in the Arkona Sea and the Bornholm Channel.

3.4 References

Brennan, D. (2001): The Numerical Simulation of Two-Phase Flows in Settling Tanks, PhD Thesis, Imperial College of Science, Technology and Medicine.

Burchard, H., and O. Petersen, (1997) Hybridisation between σ and z coordinates for improving the internal pressure gradient calculation in marine models with steep bottom slopes, Int. J. Numer. Meth. Fluids, 25, 1003–1023, 1

Burchard, H., and K. Bolding, GETM – a general estuarine transport model. Scientific documentation, Tech. Rep. EUR 20253 EN, European Commission, 2002.

Burchard, H., Lass, H., Mohrholz, V., Umlauf, L., Sellschopp, J., Fiekas, V., Bolding, K., Arneborg, L., 2005. Dynamics of medium-intensity dense water plumes in the Arkona Sea, Western Baltic Sea. Ocean Dynamics 55, 391–402.

Burchard, H. and H. Rennau (2008). Comparative quantification of physically and numerically induced mixing in ocean models. Ocean modelling 20: 293-311

Christensen, Erik D. (2006): Large eddy simulation of spilling and plunging breakers, Coastal Engineering 53, pp 463-485.

Engelund, F.A. and Christensen, Leif (1969): Lagdelte og inhomogene væd-skers hydraulik, Polyteknisk Forlag, København.

Feistel, R., Nausch, G., Matthäus, W., Hagen, E., 2003. Temporal and spatial evolution of the Baltic deep water renewal in spring 2003. Oceanologia 45, 623–642.

Haidvogel, D. B., and A. Beckmann, Numerical Ocean Circulation Modelling, vol. 2 of Series on Environmental Science and Management , Imperial College Press, London, 1999

Jones, G.R., Nash, J.D., Doneker, R.L., and Jirka, G.H., 2007, "Buoyant Surface Discharges into Water Bodies. I: Flow Classification and Prediction Methodology", J. Hydraulic Engineering, Vol. 133, Nr. 9, 1010-20

Jürgensen, Carsten (1989): Entrainment introduced by Piers, Dams, and Ships in a Stratified Channel Flow, Series Paper 48, Institute of Hydrodynamics and Hydraulic Engineering, Technical University of Denmark.

Kantha, L. H., and C. A. Clayson, Numerical models of oceans and oceanic processes, vol. 66 of International Geophysics Series, Academic Press, 2000.

Kim, W.-W., Menon, S. (1999): An unsteady incompressible Navier–Stokes solver for large eddy simulation of turbulent flows. Int. J. Numer. Methods Fluids 31, pp 983–1017.

Lass, H.U., V. Mohrholz, M. Knoll, and H. Prandke (2008): On the impact of a pile on a moving stratified flow, J. Mar. Sys., 74, 505–527.

Matthäus, W., Frank, H., 1992. Characteristics of major Baltic inflows — a statistical analysis. Continental Shelf Research 12, 1375–1400.

Menon, S., Yeung, P.-K., Kim, W.-W. (1996): Effect of subgrid models on the computed interscale energy transfer in isotropic turbulence. Comput. Fluids 25 (2), pp 165– 180.

Miller, J L; and Valle-Levinson, A (1996): The effect of bridge piles on stratification in lower Chesapeake Bay. Estuaries 19(3), 526-539.

Møller, J.S., N.-E. O. Hansen, and F. Jakobsen (1997): Mixing in stratified flow caused by obstacles, Coastal Engineering 4, pp 97–111.

Pedersen, Flemming Bo (1980): A Monograph on Turbulent Entrainment and Friction in Two-layer Stratified Flow, Series Paper 25, Institute of Hydro-dynamics and Hydraulic Engineering, Technical University of Denmark.

Ottesen Hansen, N-E; and Møller, J S (1990): Zero blocking solution for the Great Belt Link. In: Physical Oceanography of Sea Straits (Ed. L. Pratt). NATO ASI Series C, 318, 153-169.

Reissmann, J.H., Burchard, H., Feistel, R., Hagen, E., Lass, H.U., Mohrholz, V., Nausch, G.,Umlauf, L., Wieczorek, G., 2009. Vertical mixing in the Baltic Sea and consequences for eutrophication — a review. Progress in Oceanography 82, 47–80.

Rennau, H. and H. Burchard (2009). Quantitative analysis of numerically induced mixing in a coastal model application. Ocean dyn. 59: 671-687

Rennau, H., Schimmels, S., & Burchard, H. (2012). On the effect of structure-induced resistance and mixing on inflows into the Baltic Sea: A numerical model study. Coastal Engineering, 60, 53–68. doi:10.1016/j.coastaleng.2011.08.002

Rocca, M. La, et al. (2008): Experimental and numerical simulation of three-dimensional gravity currents on smooth and rough bottom, Physics of Fluids 20, 106603.

Sagaut, Pierre (2006): Large Eddy Simulation for Incompressible Flows, Springer, ISBN 1434-8322.

Sellschopp, J., Arneborg, L., Knoll, M., Fiekas, V., Gerdes, F., Burchard, H., Lass, H.U., Mohrholz, V., Umlauf, L., 2006. Direct observations of a medium-intensity inflow into the Baltic Sea. Continental Shelf Research 26, 2393–2414

Stigebrandt, Anders (1992): Bridge-Induced Flow Reduction in Sea Straits with Reference to Effects of a Planned Bridge across Öresund, Ambio Vol. 21, No. 2 (Apr., 1992), pp. 130-134

Svensson, U., and K. Häggkvist, A two-equation turbulence model for canopy flows, Journal of Wind Engineering and Industrial Aerodynamics, 35, 201–211, 1990.

Taylor, P. A., Lee, R. J. (1984) Simple guidelines for estimating wind speed variations due to small scale topographic features. Climatological Bulletin, 18, 2, p 3-21

Turner, J. (1973). Buoyancy Effects in fluids. Cambridge University Press.

Versteeg, H.K.; Malalasekera, W. Pearson (1995): An introduction to Compu-tational Fluid Dynamics. The Finite Volume Method. Education Limited, ISBN 0-582-21884-5.

Villiers, E. De (2006): The Potential of Large Eddy Simulation for the Modelling of Wall Boundary Flows, PhD Thesis, Imperial College of Science, Department of Mechanical Engineering.

Yoshizawa, A. (1986): Statistical theory for compressible turbulent shear flows with application to sub-grid modelling. Phys. Fluids, A Fluid Dyn. 29 (7), pp 2152–2164.

Özgökmen, T.M. et al. (2007): Large eddy simulation of stratified mixing in two-dimensional dam-break problem in a rectangular enclosed domain, Ocean Modelling 16, pp 106-140.

Özgökmen, T.M. et al. (2008): Large eddy simulation of stratified mixing in a three-dimensional lock-exchange system, Ocean Modelling, doi 10.1016/ j.ocemod.2008.09.006.

Sumer, B., M., Fredsoe, J. (2006). Hydrodynamics Around Cyclindrical Structures. World Scientific, pp. 546.

Zdravkovich M. M. (2003): Flow around circular cylinders Volume 2: Applica-tions, Oxford University Press, USA, ISBN 9780198565611.

3.5 Modelling of flow through a mussel farm

Jan-Joost Schouten, Aldo Tralli, Deltares

3.5.1 Introduction

Among the main challenges in coastal and offshore engineering is the complexity of the phenomena affecting the development. This complexity includes the multiple physical and chemical phenomena interacting in the coastal environment and their multiple spatial and temporal scales at which those phenomena occur.

Aquaculture is one of those examples of complex phenomenon. Extractive aquaculture is the cultivation of aquatic organisms that draw their resources directly from the ecosystem in which they are located. The most common are shellfish and macro algae that draw either phytoplankton or inorganic nutrients from the surrounding water. This is in contrast to "fed" aquaculture, such as finfish cultures, that are fed using food pellets originating from sources outside the system.

Extractive aquaculture therefore depends on local resources (nutrients or primary production) and on resources that are transported into the system by currents from adjacent basins and run-off from land. The natural system therefore sets limits on the maximum yield of these forms of aquaculture. If the food intake rate of the aquatic farms exceeds the local productivity, the system can become depleted, which will also negatively influence the yield of the farms.

This is captured by the concept of carrying capacity of a system. This concept has been used in many different ways. In the current context we concentrate on:

1. The stocking density of cultivated species at which harvests are maximized (i.e. the production carrying capacity)
2. The stocking of farm density above which unacceptable ecological impacts occur (i.e. the ecological carrying capacity)

Carrying capacity (production or ecological) depends for a large part on food availability. Depletion of resources can occur at the scale of a whole ecosystem. There are examples of semi-enclosed bays that have been overstocked by mussel farms, where the nutrient dynamics and the phytoplankton communities changed due to overgrazing (Cranford et al. 2007). As mussels cannot efficiently filter particles smaller than about 3μm, small picoplankton starts to dominate the plankton community. Subsequently this abundance of picoplankton facilitated an invasion of tunicates that can feed on very small particles (McKindsey et al. 2007). Such radical ecosystem shifts are detrimental to the industry and to the environment. In recent decades, several model and tools have been developed to assess carrying capacity of ecosystems for aquaculture, most specifically for shellfish (McKindsey et al. 2006; Grant et al. 2007; Ferreira et al. 2008; Byron et al. 2011). The more sophisticated ones comprise mussel growth models, coupled to primary production models, based on water quality and ecosystem circulation models (Guyondet et al. 2010).

Depletion can also occur at much smaller scales. Within aquaculture farms, there are distinct differences in algal concentration with respect to e.g. mussel ropes (Petersen et al. 2008) and for bed-cultures there are strong horizontal and vertical gradients (Dolmer 2000; Petersen et al. 2013). Depletion is strongly linked to local hydrodynamics. Horizontal advection and vertical mixing determine the food availability for shellfish. Stocking densities within farms have a major influence on growth rates (Cubillo et al. 2012).

This present study forms a part of a larger study program conducted at Deltares with the objective to analyse the effect of small scale processes on the large scale ecosystem processes with respect to carrying capacity. This is conducted by means of numerical modelling. The study approach here is to couple small scale resolving hydrodynamic modelling with ecosystem-scale water quality modelling. This is further described in the sections below.

3.5.2 **Methodologies**

Models operating at ecosystem-scale tend to have a spatial resolution that is far too large to resolve the small-scale boundary layer processes that occur near shellfish or algae. The scales of mussel or seaweed farms are much smaller – not exceeding a single grid cell of an ecosystem model. Within a mussel farm, the spacing of rafts is in the order of magnitude of several metres, while the mussel ropes within the rafts are spaced at yet smaller intervals. The ropes themselves will differ in thickness, but are typically in the order of 10-20 centimetres in diameter. So processes at these scales are simply not resolved in ecosystem models.

To economise on computing power and calculation times, the underlying ecosystem-scale hydrodynamic models tend to resolve turbulence only in the vertical direction. They take into account the turbulence generation at the seabed, at the water surface and (in case of stratified systems) at thermo- or pycnoclines, but ignore turbulence generation in the horizontal directions. In order to simulate the water movement within a mussel farm (or a seaweed farm) and to assess possible small-scale depletion, turbulence generated around the ropes, nets, pillars and other structures is very relevant. In order to describe the flow through structures such as mussel farms or seaweed farms the full 3D matrix needs to be resolved. This requires a different type of model.
Computational fluid dynamics modelling can resolve the full turbulence matrix and can also be performed with very small time-steps. It is however much more computationally expensive than models that operate at spatial scales of a whole ecosystem.

Multiscale coupling

Over the past few years, Deltares has been developing software tools to nest a detailed CFD model into a large-scale model. The aim is to optimize the computational resources and the accuracy of the prediction, by using the appropriate tool for each physical scale.
It is in fact known that, while large scale hydrodynamics have a well-defined mean velocity and pressure profile in the vertical axis and a time scale in the order of 12 hours (a tidal cycle), the flow behaviour in the neighbourhood of a small hydraulic structure is fully three-dimensional, and the time scales of interest are typically those of the turbulent motion (in the order of 1 s).
From the procedural point of view, it has been elected to develop said coupling procedure between Deltares' Delft3D-flow (D3D) and the commercial CFD code StarCCM+ (developed and distributed by CD-ADAPCO). The coupling is achieved in two steps:

- Importing the D3D bathymetry into StarCCM+
  Bathymetry data are usually available as a cloud of points, whose coordinates are given as an [x,y,z] triplets, defined in a given frame of reference: within StarCCM+, the cloud of point is turned into a surface mesh by means of a triangulator. Said surface mesh is then treated as a generic wall boundary.

- Establishing a procedure to exchange data (velocity, pressure, water level…) from one computational grid to the other. The main issue affecting the data exchange is the fact that the D3D data are computed on a 2-Dimensional grid, while CFD is performed on a 3D grid.

The small scale processes as well as the large scale ecosystem processes are very different for inshore as is for offshore waters. For aquaculture purposes offshore becomes more and more relevant. Therefore, two cases will be considered, i.e. an inshore (Slaak) and offshore (Borssele) application.

Multi-domain coupling

Further to coupling fine-scale CFD modelling to large scale hydrodynamics, Deltares is also developing techniques to simulate a fully integrated ecosystem model. The ecosystem model includes hydrodynamics, coupled to water quality, primary production and ultimately to grazer growth.

The CFD model is designed to

- capture the appropriate hydrodynamics, using the flow field of the D3D model as boundary conditions
- take into account all relevant effects of mussels on their environment, such as
  - local eddies
  - 3D turbulence effects
  - Wave motion
  - Deformation and motion of the nets
  - Effect of the surroundings, such as support structures, adjacent artefacts…
- Feed information on grid and hydrodynamic parameters, algal concentrations and other substances back into the D3D model and/or an ecosystem model.

The CFD model is coupled to the generic ecosystem model, called D-WAQ, Generic Ecological model (GEM). This model calculates dissolved nutrients, oxygen, salinity, various species of phytoplankton and detritus. Extensive descriptions of this model are available (Blauw et al. 2009; Troost et al. 2010).It uses processes including:

- primary production, algal respiration and mortality
- light extinction through the water column
- decay of organic material
- nitrification and denitrification
- re-aeration
- sedimentation and resuspension
- burial of organic material

The GEM is extended with a dynamic energy budget model for the various grazers (Troost et al. 2010). This is intended as a stepping stone towards a fully integrated modelling tool that can be used to optimise aquaculture at different spatial scales.
Currently, the effort is focussed toward:

1. A full coupling between the CFD model output and Delwaq, so that the Delwaq library can be used to calculate all relevant biogeochemical processes including mussel growth, respiration and

uptake of food and other particles. An alternative approach would be to import the Delwaq library into StarCCM+

2. Extend the coupling between the CFD model and Delwaq into a full two-way coupling that is able to take into account the effect of changing mussel volumes and filtration activities on the fine-scale hydrodynamics.

This document discusses the a) setup and b) first results of the application of the CFD model for aquaculture mussel farming. In the sections below the first findings of the inshore and subsequently an offshore application is described.

3.5.3 Example applications

Slaak in the Oosterschelde

The Oosterschelde is a system that is characterised by large populations of cultivated and wild shellfish (mussels, cockles, Japanese oysters, American razor clams). The total biomass of shellfish is so large that it can potentially turn over the total volume of the system within a few days (4-5 days), while the residence time of water in the system averages about 2 months. Hence the shellfish have strong control over all the processes in the water column that determine primary production (light availability, nutrient cycling). The system appears to be close to (or even exceeding) its production carrying capacity for shellfish.

Location

Slaak is a branch in the northern section of the Oosterschelde that is currently predominantly used for mussel cultivation and mussel seed capture.

Figure 3.32: The Oosterschelde with Slaak indicated in the red oval.

The branch is located close to the locks linking the saline Oosterschelde to the fresh water Krammer-Volkerak.

The reason for the selection of this specific area as a test case for the coupling is the fact that excessive carrying capacity has been observed and measured, thus providing good benchmark data. The likely reasons for the measured nutrients depletion are the high density of farming nets, together with the blind alley shape of the Slaak: the only water circulation is given by the flooding/drying of the tidal basin.

Figure 3.33: Closer image of the Slaak channel in the Northern branch of the Oosterschelde

3.1.2 Aquaculture structures

The main channel of Slaak has large amounts of mussel cultures, as visible on the satellite image in Figure 3.34.

Figure 3.34: Mussel cultures in Slaak, Google Earth picture slightly contrast enhanced.

The bulk of these aquaculture structures are suspended net cultures. There are also a few seed mussel collectors in the channel. In previous years several measurements with respect to flow and chlorophyll have been collected, making this a suitable site for testing this new model approach.

Coupled model systems

The Generic Ecosystem Model

The ecosystem model for the Oosterschelde is based on a hydrodynamic model for this system, set up in Delft 3D-Flow (Figure 3.35). The domain extends beyond the storm surge barrier as the North Sea and the Oosterschelde mutually influence each other. In the current model water movements are modeled on a 3D grid with 10 vertical sigma layers. Meteorological forcing is based on the hourly measurements by the KNMI measurement station at Wilhelminadorp.

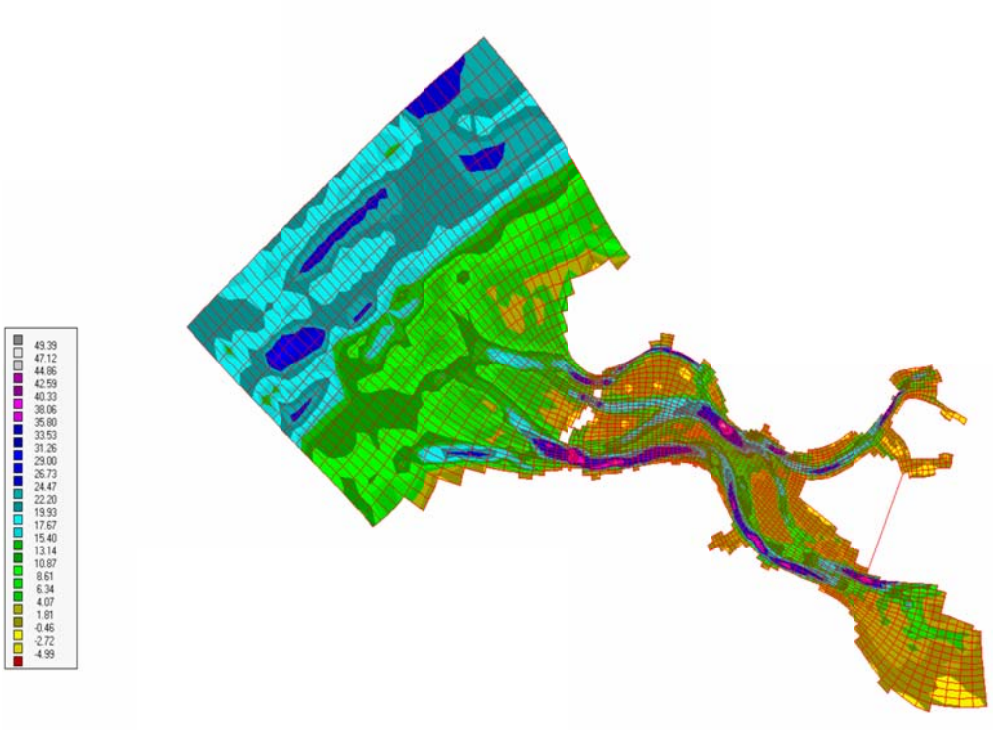

Figure 3.35: Schematised model domain of the D3D Oosterschelde model. Colours indicate the bathymetry and the square black box indicates the location of the Slaak.

3.1.4 The computational fluid dynamics model

A fine-scale CDF model representing the Slaak branch has been nested in the Oosterschelde GEM model. The commercial CFD package StarCCM+ (ver. 9.05), which is used to carry on the model set-up, the simulation work and the post processing. This model currently comprises 55 million cells, and is currently in the validation phase, using sets of simplified conditions.
Simulations were carried out using the following starting points and assumptions:

- Two-phase flow of sea water (ρ=1023 kg/m^3) and air (incompressible gas at 20ºC and 1 Atm) is solved in transient mode.
- The Volume of Fluid (VOF) method has been used to model the two phases.
- Computations were done intransient mode to comply with the unsteady nature of the flow.
- The k-Ω/SST turbulence closure method has been used to take the momentum exchange by turbulent motions into account.
- All solid surfaces are considered to be hydraulically smooth
- The net structures are assumed to be rigid
- Wall boundary conditions are enforced at the sea bottom, and on one domain boundary, as shown in Figure 3.40.
- On all remaining boundaries, pressure is enforced: a hydrostatic pressure profile is applied, consistent with the local water level. The water level is set to change over time, following a sine law with period of 12.5 hours.

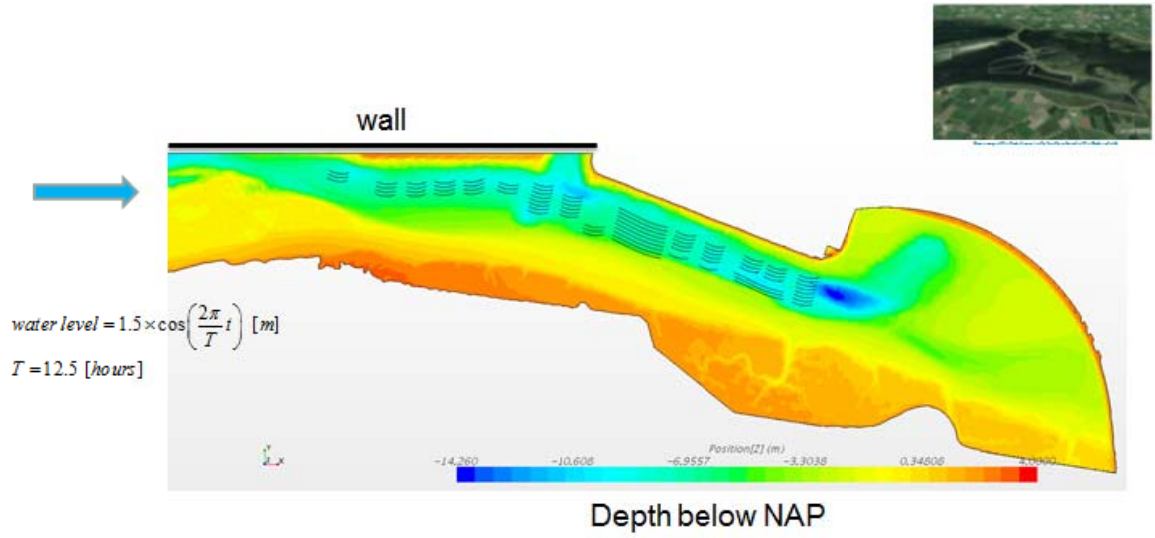

Figure 3.36: Slaak CFD model with the mussel cultures inserted: contour plot displays the depth of the bathymetry with respect to the reference level (NAP); (arbitrary) boundary conditions are shown.

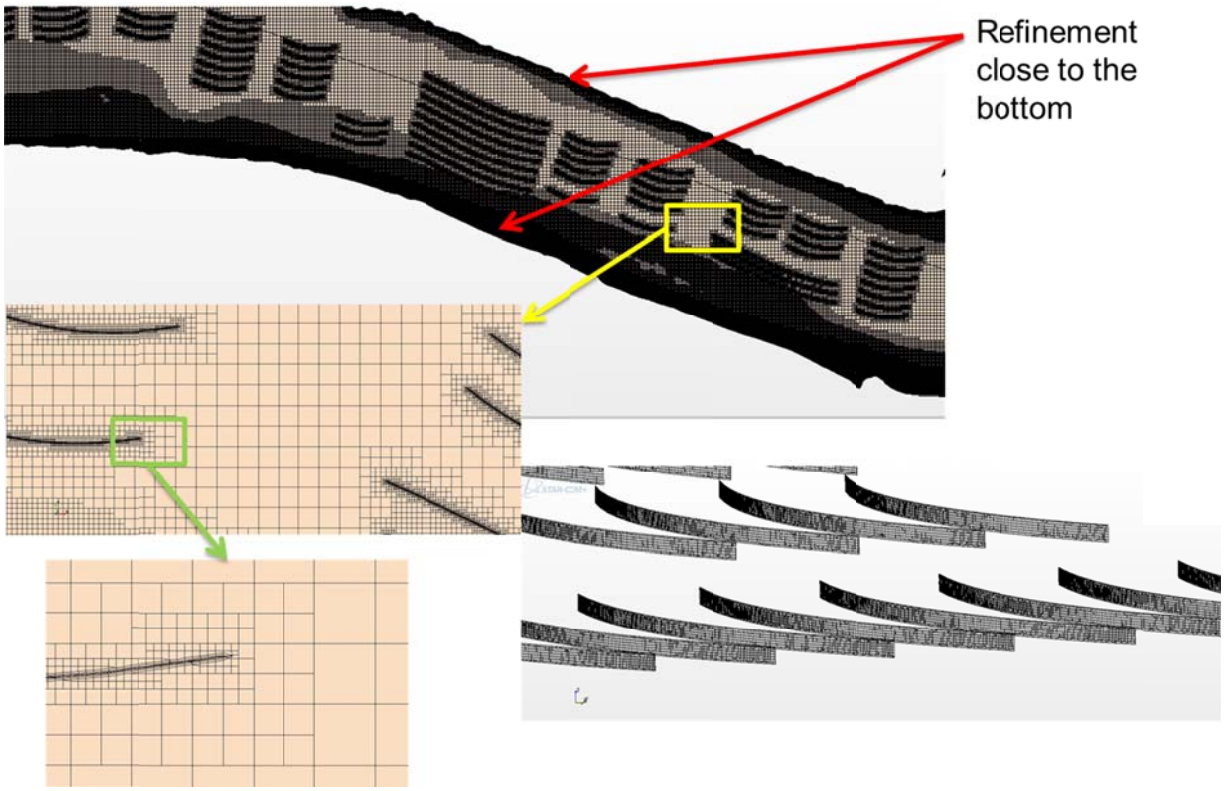

Figure 3.37 Details of the computational grid.

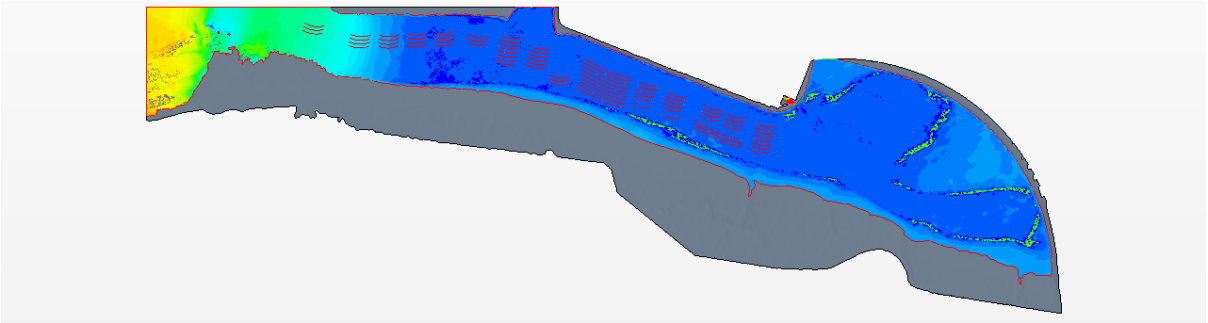

Figure 3.38 Impression of the free surface during the flood tide

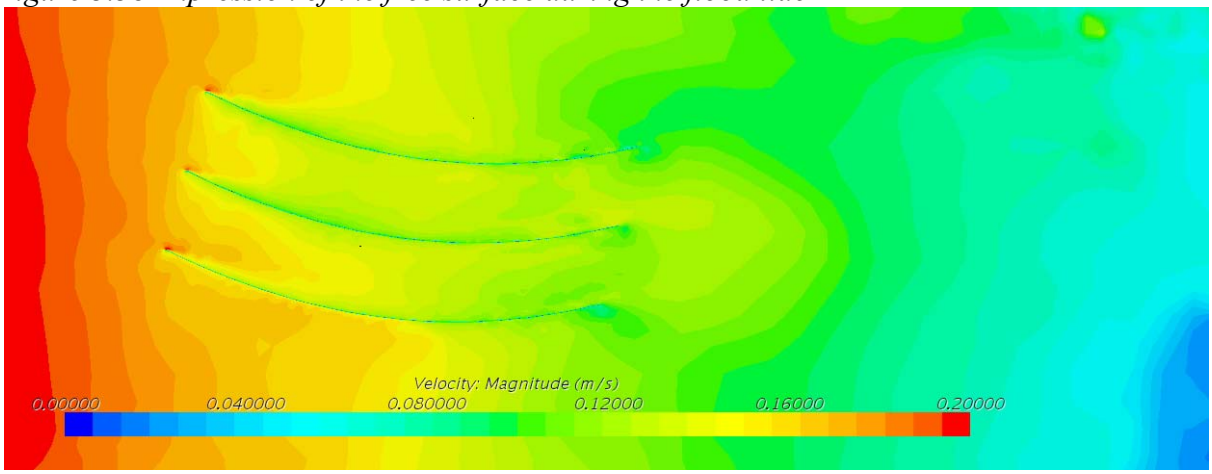

Figure 3.39 Detail of the velocity field around the first array of nets

The CFD results compare fairly well with analogous output of a hydrodynamic model in Delft3D-flow (not shown here). Several techniques are being investigated at the moment, to improve the numerical stability of the model, while keeping the throughput time of the simulation within acceptable levels: the size of the domain is approximately 4000 x 700 x 14 m3 which is a very large (by CFD standards) domain with a very large aspect ratio between horizontal and vertical dimensions. This occurrence, together with the presence of very small features (the farming nets are modeled as thin baffles with a size of about 300x 3 m2, requires that a relative large model is generated, with large gradients in cell size, and large aspect ratios. All these features may have detrimental effects on the stability and accuracy of the solution, and require monitoring.
The coupling procedure between CFD and D-WAQ, has been developed and tested: validation of the output of the coupled model against measured data is at the time of writing in progress. Once validated, this approach will give the user a detailed understanding of how the carrying capacity is obtained, and how it can be improved.
For example, it would be possible

- to study the effect of the type, number, arrangement, location of the farming structure, and determine the resulting carrying capacity.
- To quantify the load on the structures,
- To design artefacts that, coupled with the farming structures, would enhance the carrying capacity by affecting some flow parameters, e.g. turbulence in some areas.

3.5.4 **Borssele Offshore Wind Farm**

This pilot case displays the potential of the CFD tool, when representing a real-life scenario: a monopile, having a diameter d=7 m is built on a realistic representation of the bathymetry in the area of the Borssele offshore wind farm. The monopile is at the center of a square area of 500x500 m2 (such is the spacing between wind turbines): this area is the subject of a detailed hydrodynamic computation, including water up to the sea surface, and an air column of approximately 20 m above the sea level.

Three nets, used for mussel farming, are added to the simulation set-up. They are represented as rigid 2-D baffles, with a size of 100x5 m2, 200x5 m2 and 300x5 m2. The top edge of the baffles is coincident with the reference water level. An impression of the simulation domain is given in Figure 3.32 to Figure 3.34.

The commercial CFD package StarCCM+ (ver. 9.05), which is used to carry on the model set-up, the simulation work and the post processing. Simulations were carried out using the following starting points and assumptions:

- Two-phase flow of sea water (ρ=1023 kg/m^3) and air (incompressible gas at 20ºC and 1 Atm) is solved in transient mode.
- The Volume of Fluid (VOF) method has been used to model the two phases.
- Computations were done intransient mode to comply with the unsteady nature of the flow.
- The k-Ω/SST turbulence closure method has been used to take the momentum exchange by turbulent motions into account.
- All solid surfaces are considered to be hydraulically smooth

The fluid domain is subdivided into a collection of polyhedral cells, using the Star-CCM+ polyhedral trimmer algorithm with prism layers; a grid refinement is performed near the weir, to obtain a sufficiently sharp definition of the interface. A grid sensitivity study is performed, with the aim to find a reasonably fine mesh, which is able to give accurate results.

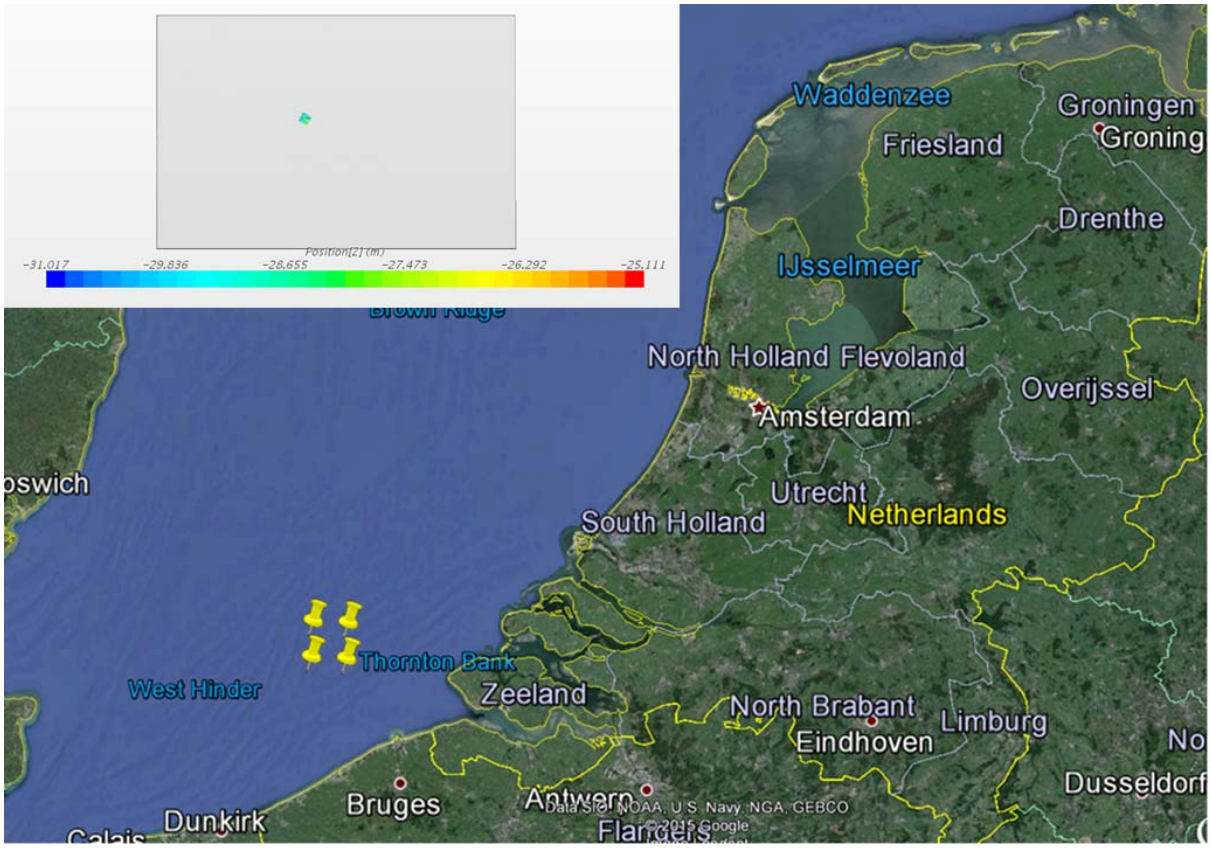

Figure 3.40 Overview of the simulation domain: the rectangular area enclosed by the yellow pins is depicted in grey in the above box: the square colored box represents the domain of the CFD simulation.

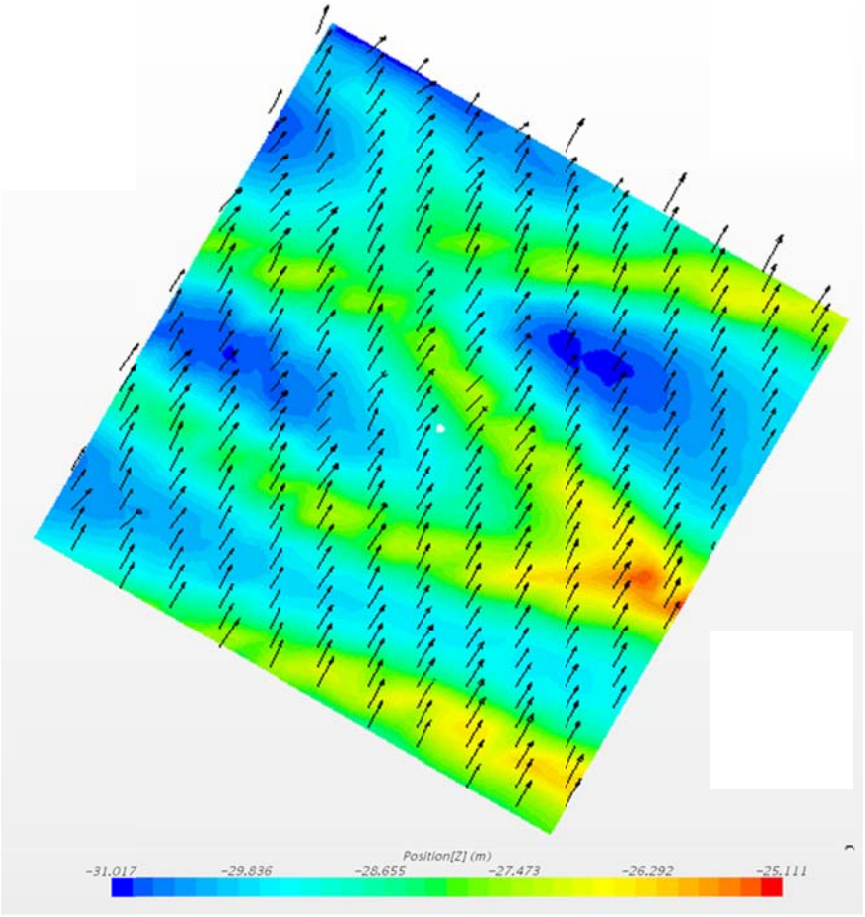

Figure 3.41 Detail of the computational domain: the contour plot displays the bottom depth. Vectors show the velocity profile

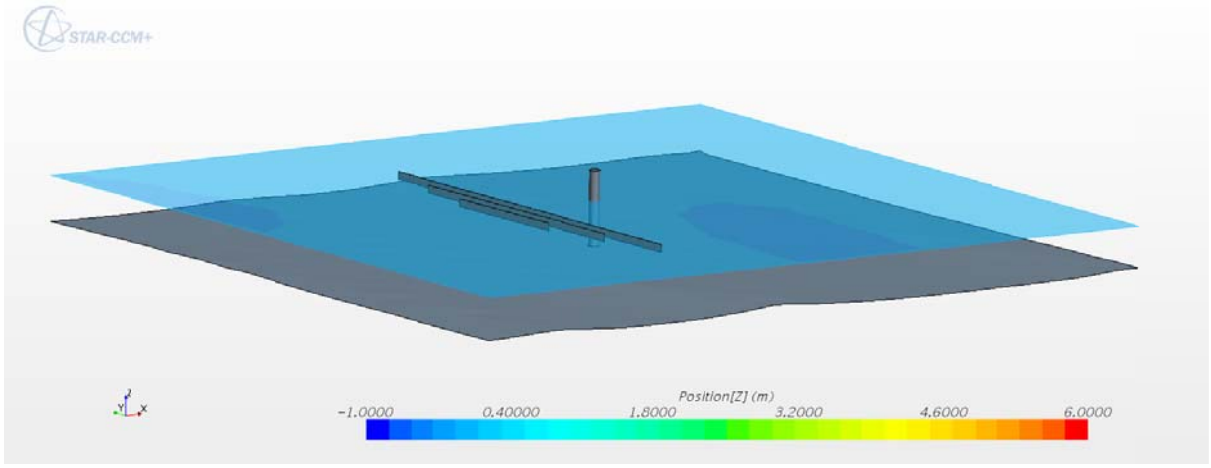

Figure 3.42 Detail of the free surface, the monopile, the bathymetry and the mussel nets.

Once the simulation results are validated, this model may evolve into a design tool for the development of wind farm: for example, coupling to D-WAQ would allow the optimization of the farming nets for carrying capacity.

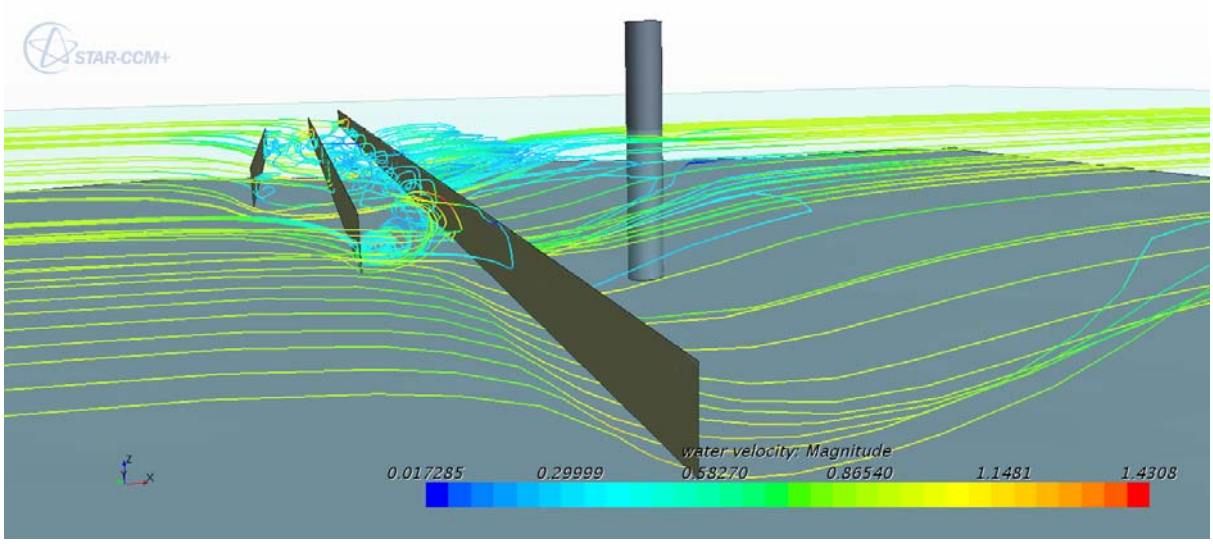

Figure 3.43 Impression of streamlines of the water flow in proximity of highly loaded farming nets

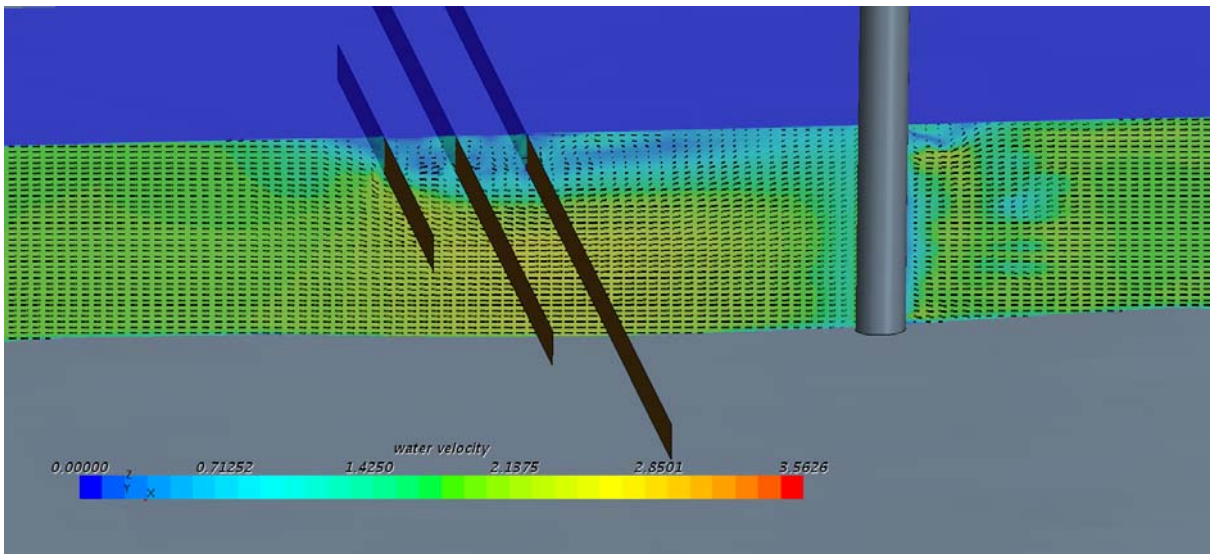

Figure 3.44 Impression of velocity vectors and magnitude (band plot) on a vertical cross section through the farming nets and the monopile: the farming nets are assumed to be highly loaded (low porosity).

Moreover, the effect of the presence of the nets on the loading on the monopile (due to current and waves) might be estimated. Coupling of other effects, such as scouring and (rigid body) motion of e.g. the farming nets, into the model is also under investigation. The vision is to develop an integrated tool, capable to simulate a large number of physical effects, and their interaction.

3.5.5 **Discussion and further work**

Aquaculture has to maximize profits to be economically sustainable while minimizing negative environmental impacts to be ecologically sustainable. As extractive aquaculture removes nutrients

and / or algae from aquatic systems it is theoretically plausible to use such aquaculture set-ups to mitigate the effects of eutrophication. However, the optimal set-up to maximize yield may be quite different from the set-up required for minimizing eutrophication. Set-ups will also differ per system, depending on local hydrodynamics, nutrient dynamics and other human usage of the system.
Tools to optimize aquaculture (in terms of yield, in terms of combining ecosystem services) have to be able to assess the underlying processes at different scales. If a particular configuration appears to have limited negative impacts on the ecosystem scale, but is not particularly profitable because of resource depletion at the smaller scale, it is not going to be economically sustainable. We think that the combination of modeling techniques offers a good basis to build the type of tools as required in this project. The pilot in the Oosterschelde shows that the principle is valid and can lead to a meaningful optimization tool for aquaculture. However, the research is still in its preliminary phase of development.

The Oosterschelde case is a typical case in which detailed hydrodynamics is critical in the modeling of the ecology: the size and distribution of the farming nets in a closed water stretch are such that the resulting flow field is strongly three-dimensional. Although some measurement data are available on flow and chlorophyll near the culture sites, measurements are required at different scales in order to fully validate the model. In order to make the tool more widely applicable it needs to be applied to different systems with different physical boundary conditions. It also needs to be validated with targeted measurements on the hydrodynamics, water quality, primary and secondary production at the appropriate scales.

The basics of the current tool development are still in terms of carbon and nutrient flows. This will ultimately yield a tool to assess the impact of extractive aquaculture on ecological and production carrying capacity. It should also be an extremely useful tool in designing optimal Integrated Multi-Trophic Aquaculture (IMTAs) set-ups. Multi-scale models such as these should be able to provide information on the most appropriate spacing and positioning of different trophic components of the IMTA taking local hydrodynamic conditions into account. Whether or not to take up IMTAs as a case study in this proposal is open for discussion.

In theory it is possible to set up extractive aquaculture in such a way that it serves multiple purposes. E.g. seaweed farms can directly reduce the amount of nutrients in the environment (reducing eutrophication) and shellfish farms can reduce the algal biomass in a system (reducing the effects of eutrophication). However, optimising yield and optimising water quality may have different requirements. Sustainable aquaculture also needs to be profitable. To what extent the economic side of aquaculture needs to be incorporated in this project is also open to debate.

3.5.6 References

Blauw, A. N., H. F. J. Los, M. Bokhorst, and P. L. A. Erftemeijer. 2009. GEM: A generic ecological model for estuaries and coastal waters. Hydrobiologia 618:175-198.

Byron, C., J. Link, B. Costa-Pierce, and D. Bengtson. 2011. Calculating ecological carrying capacity of shellfish aquaculture using mass-balance modeling: Narragansett Bay, Rhode Island. Ecological Modelling 222:1743-1755.

Cranford, P. J., P. M. Strain, M. Dowd, B. T. Hargrave, J. Grant, and M. C. Archambault. 2007. Influence of mussel aquaculture on nitrogen dynamics in a nutrient enriched coastal embayment. Marine Ecology Progress Series 347:61-78.

Cubillo, A. M., L. G. Peteiro, M. J. Fernández-Reiriz, and U. Labarta. 2012. Influence of stocking density on growth of mussels (Mytilus galloprovincialis) in suspended culture. Aquaculture 342-343:103-111.

Dolmer, P. 2000. Algal concentration profiles above mussel beds. Journal of Sea Research 43:113-119.

Ferreira, J. G., A. J. S. Hawkins, P. Monteiro, H. Moore, M. Service, P. L. Pascoe, L. Ramos, and A. Sequeira. 2008. Integrated assessment of ecosystem-scale carrying capacity in shellfish growing areas. Aquaculture 275:138-151.

Grant, J., K. J. Curran, T. L. Guyondet, G. Tita, C. Bacher, V. Koutitonsky, and M. Dowd. 2007. A box model of carrying capacity for suspended mussel aquaculture in Lagune de la Grande-Entrée, Iles-de-la-Madeleine, Québec. Ecological Modelling 200:193-206.

Guyondet, T., S. Roy, V. G. Koutitonsky, J. Grant, and G. Tita. 2010. Integrating multiple spatial scales in the carrying capacity assessment of a coastal ecosystem for bivalve aquaculture. Journal of Sea Research 64:341-359.

McKindsey, C. W., T. Landry, F. X. O'Beirn, and I. M. Davies. 2007. Bivalve aquaculture and exotic species: A review of ecological considerations and management issues. Journal of Shellfish Research 26:281-294.

McKindsey, C. W., H. Thetmeyer, T. Landry, and W. Silvert. 2006. Review of recent carrying capacity models for bivalve culture and recommendations for research and management. Aquaculture 261:451-462.

Petersen, J. K., M. Maar, T. Ysebaert, and P. M. J. Herman. 2013. Near-bed gradients in particles and nutrients above a mussel bed in the limfjorden: Influence of physical mixing and mussel filtration. Marine Ecology Progress Series 490:137-146.

Petersen, J. K., T. G. Nielsen, L. A. van Duren, and M. Maar. 2008. Effects of raft cultivation of Mytilus galloprovincialis on plankton community structure in Ría de Vigo, NW Spain. I: Phytoplankton. Aquatic Biology 4:113-125.

Troost, T. A., J. W. M. Wijsman, S. Saraiva, and V. Freitas. 2010. Modelling shellfish growth with dynamic energy budget models: An application for cockles and mussels in the Oosterschelde (southwest Netherlands). Philosophical Transactions of the Royal Society B: Biological Sciences 365:3567-3577.

4 Wave-structure interaction with structural components in a Multi-Use platform

This chapter deals with different aspects of wave-structure-interaction of Multi-Use-Platforms. In section 4.1 OWC modules have been tested as fixed modules for floating platforms. The interaction of these modules with the incoming waves is described and results of a parametric study are reported. In section 0 the interaction of breaking waves and structures are described. The focus is on the secondary structures, such as boat-landings on wind turbine foundation, and railings on transformer stations. This is followed with a section on the wave current interaction of fish cages in section 0.

4.1 Hydraulic model tests on OWC modules of platforms

Andreas Kortenhaus, LWI (present University of Ghent)

Due to its simplicity and reliability, the Oscillating Water Column (OWC) Wave Energy Converter (WEC) is probably one of the most attractive ways of converting the energy from waves into electricity. The OWC device comprises a partly submerged concrete or steel structure, open below the water surface, inside which the air is trapped above the water free surface. The oscillating motion of the internal free surface produced by the incident waves makes the air flowing through a turbine that drives an electrical generator. The turbine used in these devices usually has the ability to rotate regardless of the direction of the airflow (self-rectifying), so it is specifically designed so that the blades turn the same direction of the airflow (ingoing or outgoing flux).

The design and construction of the structure (apart from the air turbine) are the most critical issues in OWC technology, and the most influential in the economics of energy produced from the waves. One of the main issues regarding this technology is the achievement of resonance conditions, which makes it possible to enhance the oscillation of the water column, hence the power sent to the turbine.

Theoretical and numerical models based on linear water wave theory are an essential step in the development of WEC in general and OWC in particular. They are used to assess the performance, at an early stage of development, to test different configurations and to optimize the shape of the converter so as to maximize the power extraction. Thus they provide details and important information at moderate costs, and in a relatively fast way.

However, numerical models cannot represent non-linear effects which are, amongst others, those a) associated with large amplitude waves, b) the OWC large amplitude motions, and c) the real fluid effects due for instance to viscosity, turbulence and vortex shedding. To take into account such effects, physical model tests in a wave flume or a wave basin is required, with scales ranging between about 1:100 in small flumes to about 1:10 in the largest wave basins.

4.1.1 Literature review of OWC devices

Principally two types of OWC devices can be distinguished: a) fixed structure OWC (bottom standing or built on rocky sloping wall); and b) floating structure OWC. Fixed structure OWC prototypes were built and tested e.g. in:

- Norway, in Toftestallen, 1985, (Bønke and Ambli 1986);
- Japan, Sakata, 1990, (Ohneda et al 1991);

- India, Trivandrum, 1990, (Ravindran and Koola 1991);
- UK, Islay island, Scotland (Whittaker et al. 1993);
- UK, Dounreay, Scottland, 1995, named Osprey, (Thorpe 1999);
- Portugal, in Pico, Azores, 1999, (Falcao 2000),
- UK, Islay island, Scotland, 2000, named Limpet, (Heath et al 2000).
- Australia , Port Kembla, 2005 (Alcorn et al. 2005);
- Spain, Mutriku, 2010, (Torre et al 2009);
- Italy, Messina, named REWEC (Boccotti et al. 2007)

Floating structure OWC prototypes were built and tested in:

- Japan, 1965 (Masuda and McCormick 1987);
- Japan, 1976, named Kaimei, (Masuda and McCormick 1987);
- Ireland, Galway Bay, named BBDB, 2006 (Masuda et all 1993.
- Japan, Gokasho Bay, 1998, named Mighty Whale (Washio et al. 2000)

Other OWC devices under development are e.g. the spar buoy and the Orecon (Lye et al. 2009). The few prototype models operating to date have demonstrated to have poor efficiency, compared with the estimations. Further research efforts are necessary in order to get a better knowledge in the various power conversion processes behind the performance of an OWC-WEC device. Experimental studies are certainly fundamental to better understand and utilise the OWC concept.

Experimental studies were conducted to test the efficiency of new devices on one side and to examine non-linearity effects of already developed devices on the other side. This has helped to improve the knowledge of the working principle by identifying the processes causing major energy losses and trying to reduce them by modifying the device geometry. Most of these experimental studies were aimed at evaluating the overall energy performance of a device, assuming the validity of the energy conservation principle. There are studies, however, which proposed an insight on the hydraulic performance, or on the way the wave induced force exhibits in the water column movements. In fact it is important to understand the real behaviour of the water column (i.e. to study its free oscillation modes), in order to identify the processes where losses occur.
Only few studies regarded the structural behaviour of the overall structure, which is very relevant when OWC WECs are integrated in other structures, e.g. coastal breakwaters or offshore multipurpose platforms.
Here below an overview on the findings resulting from previous researches are reported, as well as on the shortcomings present. Besides a look on the instruments used for measuring the investigated physical quantities are reported. A brief overview is also given on the techniques used for modelling the air turbine, or the PTO mechanism, since it is believed that what emerged from previous experience is useful as a guideline for further and new research in the OWC WECs topic. A summary list of hydraulic model tests is reported hereinafter

- 1986, Whittaker and McPeake (Whittaker et al., 1986). Their work was initially based on the geometry of a navigation buoy which was optimised through the variation of several parameters.
- 1992, Sarmento carried out experiments on a two-dimensional bottom standing OWC. A scaled model was subjected to a parametric study, in order to find the optimal geometry and dimensions for the maximum efficiency of the device (Sarmento, 1992, Sarmento et al., 1993);

- 1994, Muller and Whittaker conducted tests on a scaled model of the limpet OWC and proposed a visual observation of the chamber by means of a camera and tracer particles (polystyrene); the scaled model was specifically made in perspex to allow observation of the inside chamber.
- 1995, Koola et al. 1995, conducted similar tests of Sarmento for another shoreline OWC, designed for the integration in a multifunctional breakwater in India.
- 1997, Melby and Appleton 1997, conducted model scale experiments on the OSPREY wave power plant for Noyo Bay California; The experiments included measurements of the oscillating water column free surface displacements within the OSPREY along with air pressure from inside the chamber. Forces on the unit were measured using pressure transducers mounted on the face and a load table mounted under the model OSPREY.
- 2000, Tseng, R.-S., & Al. (2000) conducted tests on a scaled model of a shoreline multi-chamber OWC, designed for integration in a breakwater on the coasts of Taiwan. In this case the main aim was to assess the efficiency of the wave-to-pneumatic power conversion (hydraulic performance) and of the overall conversion process (wave-to-mechanical).
- 2002, Folley and Whittaker, conducted another scaled model experimental campaign on the Limpet OWC. In this case the main aim was to investigate the possible relation between the hydrodynamics of shallow water and flow characteristics inside the OWC chamber. The Limpet OWC model was modified with respect to the previous tests. In fact an inclined back wall was introduced, in order to eliminate the destructive wave observed in (Muller & Whittaker, 1994).
- 2005, Soruso tested the performance of a shoreline cylindrical OWC, designed for Indonesian coasts. A parametric study was conducted to test the device efficiency, in presence or absence of a reflector, applied at the rear bottom of the cylinder. Reflectors with different slopes were also tested in order to find the optimum geometry for the OWC-Caisson.
- 2007, Morris-Thomas performed a two-dimensional fixed OWCs in order to study the effect of the front wall configuration upon the hydrodynamic efficiency (Morris-Thomas et al., 2007) and the air flow in the chamber through the use of the particle image velocimetry technique (Ram et al., 2010).
- 2007, the J-OWC patented by Boccotti, a shoreline OWC caisson breakwater, was the subject of an experimental campaign aimed at the estimation of the power conversion efficiency for the modified geometry of the OWC caisson type device. The scaled model (length scale 1/10) was tested under real sea waves, in the Natural Laboratory in the Straits of Messina.
- 2011, Sykes et al. carried out experiments on a fixed cylindrical OWC that has been object of some experimental studies due to its simplicity and to the availability of analytical solutions in regular waves. This geometry was used to validate hydrodynamic models and to study discrete control strategies (Lopes et al., 2009).
- 2011, Sykes et al. (2011 and 2012) studied the floating version of the cylindrical OWC, moored to the tank floor, that was the object of studies with and without a turbine simulator under regular and irregular wave conditions.

- 2012, Fleming et al. studied the energy transfer processes occurring in a near-shore OWC device, namely a Forward Facing Bent Duct (FFBD) OWC WEC, and to investigate in the various energy sources, stores and sinks associated with the system performance.
- 2013, within similar tests as conducted by Fleming, Martinelli et al. (2013) conducted experimental model tests to size the geometry of a new OWC device with reference to the Mediterranean Sea wave environment.

The main findings from the experimental campaigns conducted to date are:

- there is still much space for investigations on off-shore devices since research has mainly focused on near-shore and shoreline devices;
- medium scales are recommended for these studies but small scales can give good results as well, especially if the whole energy conversion is regarded;
- the turbine damping effect can be achieved in many different ways, also by using variable orifices;
- to combine instrumental measurements with visual observation has proved be a good way for a more efficient analysis of experimental data;
- the splitting of the wave-to-mechanic power conversion into 2 sub-processes (wave-to-pneumatic and pneumatic-to-mechanic) by means of different specific measurements (pressures in the air chamber, outgoing fluxes and water surface oscillations) is better in order to locate where the major losses occur;
- an efficient device needs an efficient geometry and dimensioning, depending on the wave attack;
- tests with irregular waves are necessary in order to get more realistic results;
- air compressibility should be considered in model tests but needs other scaling factors;
- the structural response of OWC caissons requires further investigations both for near-shore and for off-shore breakwaters.

Starting from these observations, the steps for a new experimental campaign on OWC-WECs will be outlined in the following section.

4.1.2 Set-up of model tests and test programme

The physical model has been performed in the wave-current flume of the Maritime Engineering Laboratory (COAST-Lab) of the Civil and Environmental Department of Florence University (DICeA). The wave-flume is a structure completely made of steel and glass, with a total length of 37 m and 0.8 m wide and high.

The wave maker is installed at one end of the flume and it has a stroke equal to 1600 mm driven by an electromechanical system with an extremely high accuracy (0.1 mm in position). By means of a software based on the Deterministic Spectral Amplitude Method (DSAM), the wave maker can generate random sea waves equal to real waves, with maximum significant wave height H_s of 0.20 m for peak periods of T_p = 1.5 s in a water depth of up to 0.50 m.

The wave-flume is also equipped with a bidirectional recirculation system having a maximum flow rate of 20 l/s (a new recirculation system rated to 100 l/s is under construction). Spherical valves are

used to control the recirculation discharge that is measured using a magneto-electric flow meter with declared accuracy of 0.15%.

Figure 4.1 COAST-Lab wave-current flume of Florence University.

As for the set-up of the flume, a 0.50 m water depth (25 m in prototype scale) was kept constant all along the channel, being the offshore conditions represented here. The setup considered is equal to 1 cm. This setting remained unchanged throughout the tests. During each wave attack, the time-history of water surface elevation both in front and at the back of the model was measured by ultrasonic wave gauges (WG), which are set with a sampling frequency of 20 Hz and are characterized by a nominal accuracy of 1 mm.

In order to detect the pressure variations inside the air chamber a pressure transducer is connected to the device by means of a preformed hole, specially designed for its placing at the OWC top cover (see Figure 4.1 COAST-Lab wave-current flume of Florence University.. The pressure sensor is a submersible capacitive transmitter (Series 46X, by KELLER) with a full scale (FS) of 100mbar and an accuracy of ± 0.1% FS. The OWC chambers were equipped with an hot-wire anemometer to measure the air velocity in the duct placed on the top cover.

The air flow rate, through the duct representing the air turbine, was measured by a constant temperature anemometer (CTA). The air flow sensor is characterized by a platinum plated tungsten wire with a diameter of 5μm and a length of 1.25mm (Probe type 55 P11 by DANTEC).

For each of the 36 OWC configurations measures of the flow rates, the pressure drops and water level variations inside the air chamber of the OWC were obtained. Since Froude similarity cannot reproduce properly the compressibility effect of the air in the chamber above the oscillating column, a reservoir 49 times greater of the smallest OWC air chamber was added to the OWC tested.

The OWC model was installed at a distance of 21.9 m from the wave maker. To avoid the generation of reflected waves, an absorbing beach was built on the rear end of the wave flume, approximately at a distance of 10.8 m from the model.

During each wave attack, the time-history of water surface elevation both in front and at the back of the model was measured by seven ultrasonic wave gauges (WG) which are set with a sampling

frequency of 20 Hz and are characterized by a nominal accuracy of 1 mm. The seven wave gauges were grouped into four arrays displaced along the wave-flume as follows:

- the FIRST array is constituted by one wave gauge (WG1) located at a distance of 4m from the wave maker, in order to measure the characteristic parameters of the waves generated;
- the SECOND array comprises three wave gauges (WG2, WG3 and WG4) which are placed at a distance of 3.6 m from the OWC model (approximately equal to 2 wavelengths) and 18.4 m from the wave maker, in order to separate the incident waves from the reflected waves;
- the THIRD array is organized in order to collect the data on the fixed OWC model, which will be instrumented with a pressure transducer (PT) and an ultrasonic wave gauge (WG5) located on the OWC air chamber at a distance of 50mm from the top cover centre, in which the vent is located. Moreover, a hot wire anemometer (HW) was located in a proper duct located in correspondence with the vent, in order to measure the airflow rate (Figure 4.2);
- the FOURTH array is constituted of two wave gauges (WG6 and WG7) placed on the back of the model, at a distance of 3m, for the transmitted waves separation from the reflected waves.

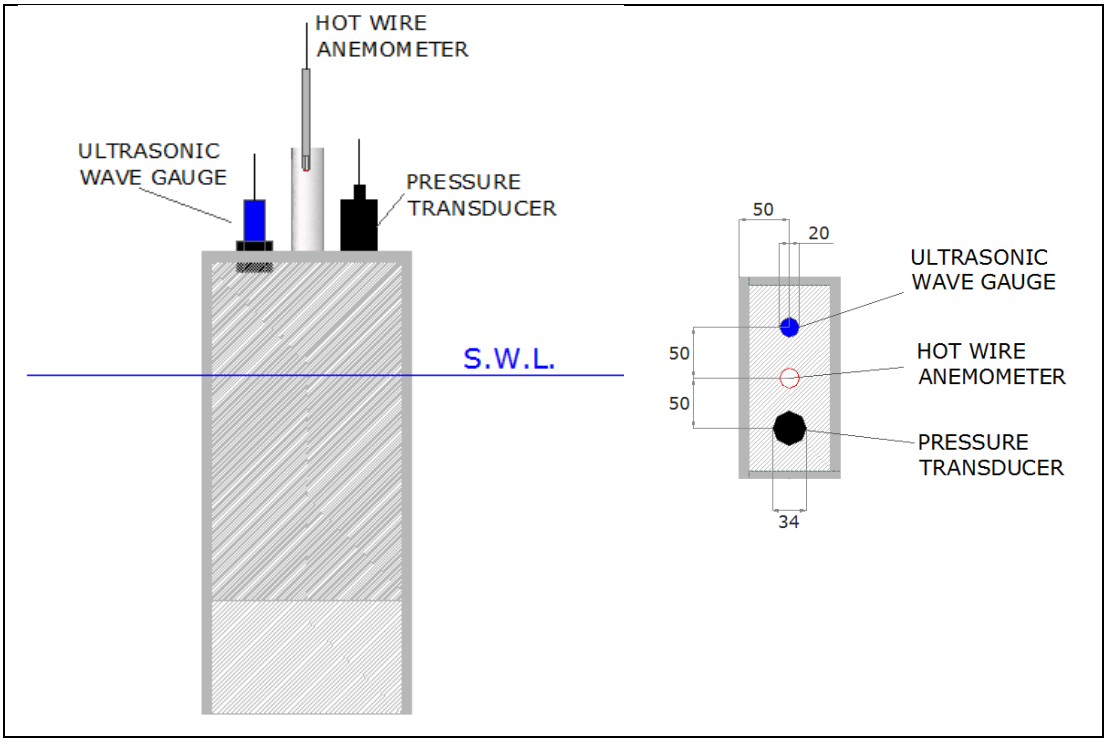

Figure 4.2 A Sketch of the PT, WG and HW locations for the measuring section (all measures are in mm)

4.2 Breaking wave interaction with secondary structures- physical and numerical analyses

Danilo Tomaselli and Erik Damgaard Christensen, DTU-MEK

4.2.1 Introduction

The design of Multi-Use offshore Platforms (MUP's) has to take into account the interaction of the structure with waves. MUP's are thought to be built in intermediate depth (20-60 m): in this region the waves often break as spilling breakers under storm conditions. Even though the phenomenon is less violent than in a shallow water region, it cannot be neglected because the impact of the waves on secondary structures such as boat-landings and railings can change compared to non-breaking waves. In fact, the air entrapped in the wave front has an influence over the kinematics of the wave. Hydrodynamic of breaking waves and their interaction waves with offshore structures are subject of intensive numerical and experimental studies. All topics involved in the problem are described in the following sections and a solution through a numerical methodology is presented.

4.2.2 Breaking Waves

Wave breaking plays an important role in the evaluation of wave-induced forces on offshore structures as well as in sediment transport processes in coastal zone.
Waves undergo deformation and shoaling when approaching the coastline; moreover, the wave height increases and the celerity decreases. This process cannot continue because the wave front becomes unstable and the wave breaks (Figure 4.3).

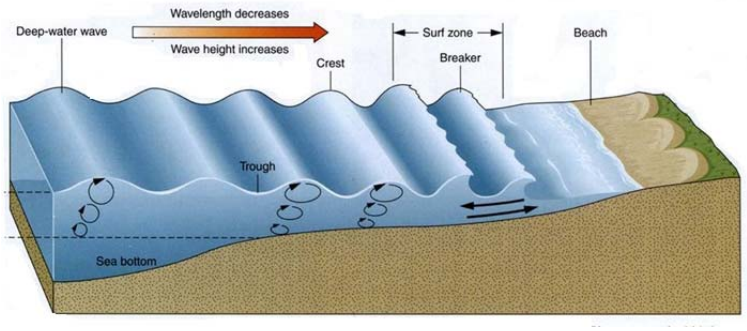

Figure 4.3: Deformation and shoaling of wave – from (Plummer et al., 2001)

Breakers are commonly classified as: spilling, plunging and surging (Figure 4.4). A plunging breaker starts by the wave front turning over and projecting forward as a tongue of water or a jet, which then falls down at the trough in front of the crest. A spilling breaker may be seen to start as a very weak plunging breaker at the crest of the wave; the rotational flow generated by the plunger then spreads down along the front of the wave developing into a surface roller. The surging breaker builds up as if to form a plunging breaker but the base of the wave surges up the beach before the crest can plunge forward.

A large range of turbulent scales forms when a wave breaks in a surf zone. The turbulent kinetic energy originates from the roller (Figure 4.5) and structure as vortices comparable to the water depth to eddies down to a size of fractions of a millimetre are generated.

When breaking a wave loses energy: the large almost two-dimensional vortices break up into three-dimensional flow structures generating the large scales turbulent motion and the energy moves through the cascade process from these larger scales to the smaller ones and finally it is dissipated to heat by the viscous forces.

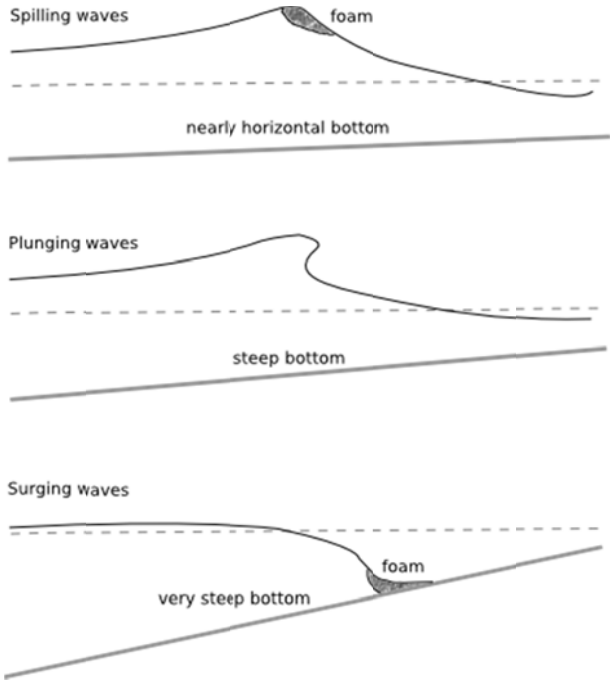

Figure 4.4: Classification of breakers: spilling, plunging and surging

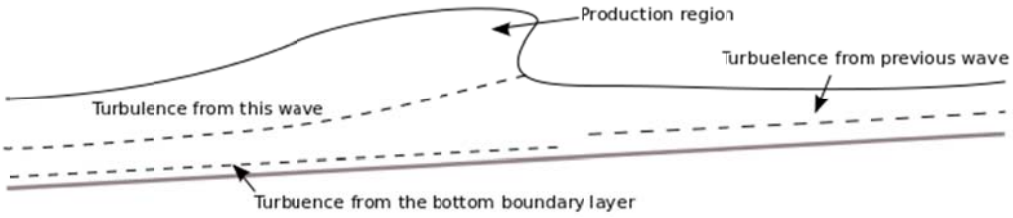

Figure 4.5: Sketch of the production and dissipation of turbulent kinetic energy - from (Svendsen, 1987)

The mechanism of breaking waves in the surf zone is well described by (Peregrine, 1983), (Battjes, 1988) and (Christensen, Walstra, & Emerat, 2002). (Peregrine, 1983) emphasizes the approach to wave breaking and the wave overturning, whereas (Battjes, 1988) is more focused on the post-breaking mechanics. (Christensen et al., 2002) describes the vertical variation of the flow structures in the surf zone.

The turbulent flow field and correspondent coherent structures in breaking waves have been treated extensively by many experimental studies. The followings are among the most important ones.
(Nadaoka, Ueno, & Igarashi, 1988) and (Nadaoka, Hino, & Koyano, 1989) observed that the wave breaking process generates spanwise vortices with axis of rotation parallel to the wave crest. Behind the wave crest, vortices with counter-rotating vorticity were seen to descend obliquely downward.

(Nadaoka et al., 1989) suggested that the formation and evolution of the obliquely descending vortices are related to the stretched velocity field around the saddle point of streamlines between adjacent spanwise vortices.
(Ting & Kirby, 1994), (Ting & Kirby, 1995) and (Ting & Kirby, 1996) demonstrated many of the differences between the turbulence in spilling and plunging breakers. In a spilling breaker much of the turbulence is dissipated in the upper part of the water column, close to the location of production of turbulence under the surface roller. In a plunging breaker the turbulence is initially associated with large vortices that rapidly spread the turbulence over the vertical saturating the whole water column. The intensity of the turbulence under the plunger is much higher under the wave front, and it decays very much from the passage of one wave to the next. This is in contrast to spilling breakers, where the intensity of the turbulence at a given level may not decay considerably between each passage of a wave front.

(Ting, 2006) and (Ting, 2008) extended the investigation of the flow structures under solitary breaking waves. The advantage of studying a single broken wave is that the evolution of the associated turbulent velocity field can be studied separately from the effects of return flow and residual turbulence. In these studies the instantaneous turbulent velocity field was measured in the near-bed region and in the middle part of the water column. Those measurements showed that large-scale organized flow structures are the sources of most of the turbulent kinetic energy and shear stresses under broken waves. The type of organized flow structures most frequently observed was a downburst of turbulence descending from above and diverging at the bed.

(Sumer et al., 2011) and (Sumer, Guner, Hansen, Fuhrman, & Freds??e, 2013) provided an improved understanding of the entire sequence of wave breaking (solitary plunging and regular plunging respectively), especially on the resulting bed shear stresses, sediment transport patterns, and related bed morphology.

During the last few decades, progress in applied mathematics and computer architecture has offered the opportunity of developing numerical models for studying the breaking processes by solving the equations governing the motion of a fluid, the so-called Navier-Stokes (N-S) equations:

$$\frac{\partial \rho}{\partial t} + \nabla \cdot (\rho \boldsymbol{U}) = 0 \tag{4.1}$$

$$\frac{\partial (\rho \boldsymbol{U})}{\partial t} + \nabla \cdot (\rho \boldsymbol{U}\boldsymbol{U}) = -\nabla p + \rho \boldsymbol{g} + \nabla \cdot \boldsymbol{\Gamma} \tag{4.2}$$

Where:

- t is the time;
- ρ is the density of the fluid;
- $\boldsymbol{U}$ is the velocity;
- p is the pressure;
- $\boldsymbol{g}$ is the gravity acceleration;
- $\boldsymbol{\Gamma}$ is the viscous stress tensor.

This method is called Computational Fluid Dynamics (CFD). By discretizing the equations and the physical domain, the method is capable of calculating the flow in complex geometries to give very precise information about the most important parameters of the simulated flow.

The first and simplest way of solving the N-S equations is the Direct Numerical Simulation (DNS). It is defined direct because the equations are solved without a turbulence model under the assumption that the mesh grid size used to discretize the domain is sufficiently refined to take into account all the length-scales of the flow. Simulations by DNS are therefore computationally demanding.

Among the most important numerical investigations using DNS are: (A. Iafrati, Di Mascio, & Campana, 2001), (Lubin, Vincent, Caltagirone, & Abadie, 2003) and (a. Iafrati, 2011). These works give very good results for the overall flow description, including the shoaling and the breaking of the waves, but the turbulence is not described or analysed; in particular, in (a. Iafrati, 2011) the attention was focused on the early stage of the breaking when most of the energy is dissipated.

Turbulence can be handled by time-averaging the N-S equations which become Reynolds-averaged Navier-Stokes equations (RANS). The velocity components are assumed as consisting of a fluctuating and time averaged component. Some numerical studies which implement the RANS modeling of the surf zone are (Lin & Liu 1998a), (Lin & Liu 1998b) and (Bradford, 2000). These studies considerably improve in the understanding of the processes taking place in the surf zone but the turbulence levels at breaking is found to be over-estimated.

Another approach to treat the effects of turbulence is Large Eddy Simulation (LES) which has gain popularity recently. The larger eddies are directly simulated as DNS, while the smaller ones, i.e. smaller than the grid scale, are accounted for through a sub-grid-scale model. Therefore the computational cost is reduced compared with DNS and moreover the approach is much simpler than RANS because a smaller part of the turbulence is simulated. In general, DNS and LES require a fine resolution in three spatial dimensions.

Among the most important numerical investigations involving the LES method are: (Christensen & Deigaard, 2001), (Watanabe, Saeki, & Hosking, 2005), (Christensen, 2006), (Lubin, Vincent, Abadie, & Caltagirone, 2006).
In (Christensen & Deigaard, 2001) spilling, weakly and strongly plunging breakers are analysed. Some very interesting visualizations and good results describing the internal velocity field perturbed by three-dimensional vortices were shown.

(Watanabe et al., 2005) computed the three-dimensional vortex structures under spilling and plunging regular waves. They found that perturbation and stretching of vorticity in the saddle region between the rebounding jet and the primary spanwise vortex can lead to the formation of stretched vortex loops with counter-rotating vorticity, which were suggested to be the descending eddies observed by (Nadaoka et al., 1989) and others.

(Lubin et al., 2006) conducted three-dimensional large-eddy simulation of plunging breaking waves by solving the N-S equations in a two-phase flow (air and water). The two fluids are treated as a single "mixture" fluid whose density and viscosity are a weighted average of those ones of air and water. They discussed the physical processes of overturning, splash-up, vortex generation, air entrainment and energy dissipation.

(Christensen, 2006) satisfactorily simulated the set-up, undertow and turbulence levels in periodic spilling and plunging breakers by the means of a three-dimensional N-S solver with a free surface model (based on the Volume of Fluid concept). Simulated wave height and velocity profiles were in good agreement with experimental measurements in (Ting & Kirby, 1994); turbulence levels were found to be over-predicted.

4.2.3 **Air-entrainment in breaking waves**

As seen in the previous section, wave breaking in the surf zone generates intense turbulence and coherent eddy structures in the underlying flow field. These processes entrain large volumes of air bubbles into the water column, enhancing wave energy dissipation and air-sea mass transfer.

In (Lamarre & Melville, 1991) and (Lamarre & Melville, 1994) measurements of air entrainment by controlled deep-water breaking waves were presented; results showed that the bubble plumes generated by breaking waves contain such large volume fraction of air that even the air-sea gas transfer and the sound propagation in the sea are influenced.

(Deane & Stokes, 2002) conducted photographic studies of the air entrainment mechanism under laboratory plunging breaking waves. The elaboration of these photos revealed the space-time evolution of bubble size distribution in the generated plumes. Plume lifetime can be divided into two main phases: the acoustic phase when bubbles are formed, and the quiescent phase which begins when active bubble formation ceases. In particular the initial bubble size distribution is induced by two mechanisms occurring during the acoustic phase:

- the jet and drop entrainment which is active during the entire acoustic phase and determines the size distribution for bubbles smaller than the so-called Hinze scale;

- the bubble fragmentation which operates during the wave cavity collapse, and determines the distribution for bubbles larger than the Hinze scale.

The initial bubble size distribution observed by the authors showed a marked change in slope at a radius of 1 mm that was identified as the Hinze scale.

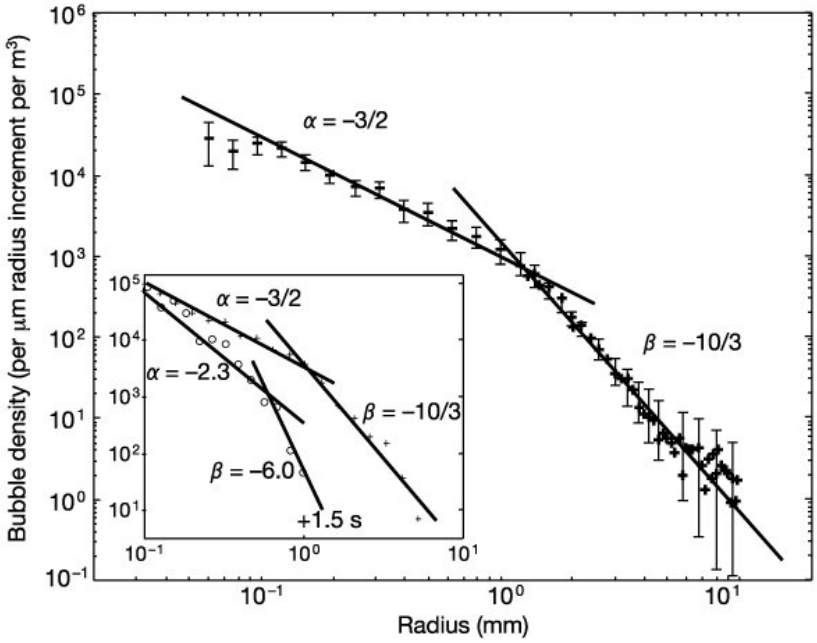

Figure 4.6: Initial bubble size distribution after the acoustic phase. In the inset, the evolution with the time of the distribution during the quiescent phase is shown.

The power-law scaling of bubble density on radius is $-3/2$ for bubbles smaller than the Hinze scale and $-10/3$ otherwise. As it possible to see, the observed bubble size distribution covers a broad range of radius, from circa 0.1 mm up to 10 mm
Buoyant degassing, turbulent diffusion, advection and dissolution influence the evolution of the plume during the quiescent phase.

(Chanson, Aoki, & Maruyama, 2002) studied experimentally the mechanisms of air bubble entrainment due to plunging breakers. The results highlight strong vertical motions induced by the rising air bubbles.
(Kimmoun & Branger, 2007) performed Particle Image Velocimetry (PIV) measurements of water waves propagating and breaking in a wave tank. The complete space-time evolution of velocity field was measured over the whole surf zone and the phase-averaged components of the flow with their associated fluctuating parts were determined. Moreover, the PIV images and velocity measurements were used to estimate the void fraction in each point of the surf zone.

The air entrainment process in breaking waves and the induced bubbly flow have been investigated also numerically. Such simulations are really challenging because of the variety and the complexity of the physical processes involved.

Breaking waves are commonly simulated by the means of algorithms with interface tracking capabilities. Nevertheless, this kind of model has an obvious limitation: it loses its physical meaning when the interface is so dispersed that the discrete grid doesn't allow the reconstruction of the interface. Bubbles due to air entrainment present dispersed interface then they are hardly trackable unless the domain is discretized with a grid size of a fraction of millimeters, making the computational demand not affordable in practice.

As example, Lubin et al. (2006) used a really fine grid for their three-dimensional large-eddy simulations of plunging breaking waves to recognize some complicated flow structures such as spinning air pockets.

For the reasons above, the so-called *two-fluid Eulerian approach* (Drew & Prassman, 1999; Ishii, 1975) seems best suited to simulate dispersed (bubbly) flow where the length scale of the interface is smaller than the grid size. In this model, the two fluids (or phases), air and water, occupy the whole domain and interface is not calculated explicitly; this may result in one phase completely dispersed in the other. In this approach, momentum and mass conservation are solved per both phases; the N-S equations are averaged and the fraction α_i of the phase *i* is introduced, see eq. (4.3) and eq. (4.4). The phase fraction can be seen as the probability of the phase existing at a given time and position in the domain considering all the possible realizations of the two-phase flow.

$$\frac{\partial \alpha_i \rho_i}{\partial t} + \nabla \cdot (\alpha_i \rho_i \boldsymbol{U}_i) = S_i \tag{4.3}$$

$$\frac{\partial (\alpha_i \rho_i \boldsymbol{U})}{\partial t} + \nabla \cdot (\alpha_i \rho_i \boldsymbol{U}\boldsymbol{U}) = -\alpha_i \nabla p + \alpha_i \rho_i \boldsymbol{g} + \nabla \cdot \alpha_i \boldsymbol{\Gamma}_i + \boldsymbol{M}_i \tag{4.4}$$

S_i represents the mass transfer between water and air, e.g. evaporation and condensation of water. $\boldsymbol{M}_i$ is the sum of all interfacial forces acting between continuous and dispersed phase (drag, lift, virtual mass force as example). Both terms can be seen as closure (sub-grid) terms necessary to model the loss of information due to the averaging operation. In particular, $\boldsymbol{M}_i$ is necessary to take into account the smaller scale deformations of the interface which disappear when a filter is applied to the governing equations in an Eulerian framework (Bestion, 2012).Therefore the accuracy of the averaging approach mainly depends on the reliability of the chosen expressions for the closure terms (S_i and $\boldsymbol{M}_i$). The grid density still affects the results, but not as much as for the interface-capturing models.

Nevertheless, it has to be stressed that the governing equations used in an interface-tracking algorithm are still more accurate than those one of the Eulerian approach, but, as said, the latter requires a really fine grid to be meaningful (Cerne, Petelin, & Tiselj, 2001).
Since the interfacial forces commonly included in the momentum equation are function of the bubble diameter, a description of air as poly-dispersed gas is needed. As seen above, the size distribution of entrained bubbles in breaking waves is quite broad then bubbles behaves differently.
The poly-dispersion of air can be handled by extending the Eulerian approach to *n+1* phases (*multi-fluid Eulerian approach*), where *n* is the number of different bubble size classes (diameters) and the remaining phase is the continuous water. Obviously, the larger *n*, the better the description of the multi-scale flow, but this increases the computational cost because a set of N-S equations have to be solved for each phase. Moreover, coalescence and breakage between bubbles should be computed in order to achieve more reliable results; therefore the source term S_i of the continuity equations of the gaseous phases will include also the effect of mass transfer between bubbles. In this case the continuity equation is referred to as Boltzmann equation or population balance equation.

(Carrica, Drew, Bonetto, & Jr, 1999) reported a multiphase model for simulating bubbly two-phase flow around a surface ship. The bubble phase is modeled using the integrated Boltzmann transport equation for the bubble size distribution function and the momentum equations for the gaseous phase. The liquid phase is modeled using mass and momentum equations for liquid along with a turbulence closure. The gas-liquid interactions are represented by drag, pressure, lift and buoyancy

forces. The bubbles entrainment is treated as boundary condition, i.e. a fixed amount of air being introduced in the domain.

The modelling of the acoustic phase, i.e. the first mechanism in air entrainment, requires high space-time resolution in order to capture all details. This makes computations too much expensive and limited to the study of the bubble creation mechanisms. For this reason, the air entrainment process is often expressed through a sub-grid formulation, whereas the evolution of bubbles is simulated. These models, fed with the initially entrained bubbles, simulate bubble plumes and require much less spatial and temporal resolution than needed to capture the air entrainment process. The initial bubble number density and bubble size distribution are formulated based on theoretical and observational studies. Among these works are: (Moraga, Carrica, Drew, & Lahey, 2008), (F. Shi, Kirby, & Ma, 2010) and (Ma, Shi, & Kirby, 2011).

(Moraga et al., 2008) presented a sub-grid model for breaking bow waves and naval surface ships that detects the location of the air bubble entrainment region. The localized region of high void fraction is bounded by the surface at which the downward liquid velocity reaches a certain value. The initial bubble size distribution in the localized region follows the bubble size spectrum measured by Deane and Stokes (2002). The model was able to deal with the variation of the size distribution and the locus of bubble injection.

(F. Shi et al., 2010) used the same approach of (Buscaglia, Bombardelli, & García, 2002) to simulate air bubbles induced by breaking waves. A double-averaged multiphase model without taking into account the momentum balance in the bubble phase was adopted. The authors claimed that the exclusion of momentum equations for the bubble phase makes the model more efficient, especially in a simulation involving a number of bubble groups with different sizes. The initial air bubble entrainment is formulated by connecting the flow shear stress at air-water interface and the bubble number intensity with the bubble size spectra as observed by (Deane & Stokes, 2002). The bubble velocity was assumed to be function of its radius. The model was used to simulate wave transformation, breaking, and bubble generation and evolution processes over a barred beach in a large wave flume.

(Ma et al., 2011) used a polydispersed bubbly flow model based on Carrica et al. (1999) to simulate bubbles in surf zone. Inertia and shear stress tensors for the gas phase are neglected due to the relatively small gas volume and density. Unlike the model of Buscaglia et al. (2002) and Shi et al. (2010), this model solves the momentum conservation equation for bubble phase to obtain the bubble velocity instead of using simplified formulas. The air entrapment is taken into account through a sub-grid formulation which connects the number and the distribution of entrained bubbles with the turbulent dissipation rate at the air-water interface.

4.2.4 **Wave loads on a vertical structure**

Wave loads are associated with the sea state at the location of the structure which is usually described in terms of a wave spectrum. The loads can be divided into fatigue loads and extreme loads. The former are not critical for the stability of the structure at the time scale of a wave episode. The latter may cause severe damage during a single event and are often associated with breaking waves. The simplest prediction of structural wave loads is based on application of linear wave theory to all components of a wave spectrum to obtain the undisturbed wave kinematics at the

location of the structure. This is often combined with Wheeler stretching (Wheeler, 1970) that addresses the over-prediction by the linear velocity field above still water level.

Since many offshore and harbour structures are considered as slender cylindrical piles or composed of slender cylindrical members, wave forces on slender cylinders have very often been analyzed in detail.

The Morison equation (Morison, O'Brien, Johnson, & Schaaf, 1950) is widely used as approximation to calculate the forces acting on a slender cylinder:

$$F = F_M + F_D = \int_{-d}^{\eta} \frac{1}{2} \cdot \rho \cdot C_D \cdot D \cdot u(z)|u(z)|dz + \int_{-d}^{\eta} \rho \cdot C_M \cdot \frac{\pi D^2}{4} \cdot \dot{u}(z)dz \qquad (4.5)$$

where:
- D is the diameter of the cylinder;
- ρ is the water density;
- η is the water surface elevation;
- $u(z)$ and $\dot{u}(z)$ are the velocity and the acceleration of the water respectively;
- C_D and C_M are two experimentally determined force coefficients.

The wave force is provided as the sum of the inertia force F_M and the drag force F_D. The inertia force depends on the acceleration of the water particles and the drag force depends on the square of the water particle velocity. The total force is determined by integrating the forces along the height of the cylinder. The physical foundation of this equation has often been discussed, especially with regard to the validity of neglecting further forces (e.g. wave run-up is ignored), to the dependency on the two empirical coefficients C_D and C_M and to the linear superposition of the two force components. Nevertheless, the Morison equation is still a proper engineering approximation.
For structures that are not slender compared to a wave length, the diffraction correction of (MacCamy & Fuchs, 1954) can be applied.

Fully nonlinear kinematics can be taken into account by the means of a CFD computation of the wave loads. As example (Bredmose et al. 2006) numerically reproduced a laboratory extreme impact on a gravity foundation of offshore wind turbines exposed to current and waves.
Both in physical and numerical modelling, the low probability for occurrence of extreme wave load events causes difficulties. During a 3-hour storm realization, only a few extreme events will occur and most of the computational or laboratory time is thus spent on less significant events. Numerically this problem is often overcome by combining the CFD model with a simpler and thus numerically cheaper model for the wave field away from the structure. (Christensen et al. 2009) described how a Boussinesq wave model can be used to drive a CFD model that is applied locally around a wind turbine foundation.

Another method for concentrating the computational or laboratory time on extreme events is the application of focused wave groups. In this approach the wave components of a sea spectrum are phase aligned to have coinciding crests (or down-crossing point) at one particular location at a predefined time. The technique has received significant attention in the field of Offshore Engineering, as it offers a simple and practical way of constructing extreme events from a given sea spectrum.

4.2.5 **Breaking waves-induced forces**

Wave breaking, especially plunging breakers, may induce very high impact forces on a slender structure. An additional term which takes into account the impact effects has to be included in the Morison equation. Nevertheless, a detailed analysis of the breaking wave force is difficult, since the duration of these impact forces is extremely short. A quite straightforward method in (Shore Protection Manual 1984) prescribes to multiply the drag force component F_D by a factor of 2.5.
However the temporal evolution of the impact force should be considered when a structural or stability analysis is performed. (Goda, Haranaka, & Kitahata, 1966) suggested an expression for the maximum line force at the beginning of the impact of a breaking wave.
Generally the experimental studies focus on impact due to plunging waves since it is much more violent compared to that one due to spilling waves.

In (Wienke & Oumeraci, 2005) the plunging waves impact on vertical and inclined slender cylinders was examined by a series of large-scale model experiments using Gaussian wave packets to generate plunging breakers at given locations in a large wave flume. The impact force was found to be strongly dependent on the distance between breaking location and cylinder. Results showed that the maximum impact force on the cylinder occurred when the wave broke immediately in front of the cylinder and the velocity of the water mass hitting the cylinder reached the value of the wave celerity at the breaking location. Moreover, the breaking wave impact force is shown to be proportional to the so-called "curling factor" (to be determined experimentally), which depends on the inclination angle of the cylinder and on the angle of the breaker front inclination. The authors investigated the development of the breaking wave impact force at the cylinder theoretically too. They developed 2D-3D analytical model to determine the total duration of the impact and the magnitude of the force. This analytical model takes into account the so-called pile-up effect, i.e. the deformation of the free water surface during the immersion process of a slender cylinder, which influences both the duration and the magnitude of the impact force.

The air entrainment in breaking waves largely affects the wave loads. The influence of air during wave impact on structures is a difficult topic and has attracted many researchers. (Bagnold, 1939) and (Hattori, Arami, & Yui, 1994) observed that the most violent impacts for coastal structures with a vertical face such as breakwaters or seawalls, occur when a breaking wave approaches the structure with almost vertical front and entraps a small air pocket at the wall. The shape and size of the entrained air (single pocket or cloud of small bubbles) influence the impact phenomenology. The entrapment of air bubbles prolongs the impact duration and also results in pressure oscillations on the wall due to compressions and expansions of the air bubbles; this will consequently increases the pressure impulse on the wall.

The evaluation of wave loads under breaking waves has been investigated numerically by many researchers. (H. Bredmose, Peregrine, & Bullock, 2009) studied violent wave impacts of breaking waves against vertical walls by a compressible flow model that accommodates both entrained and trapped air. The compressible model is based on conservation equations for mass, momentum, air mass and energy and is solved in a finite-volume framework. Their results confirmed the experimental observations of (Bagnold, 1939) and (Hattori et al., 1994): the association of the highest impact pressures with the entrapment of small pockets of air and the oscillating pressures and forces associated with the alternate compression and expansion of trapped air pockets. For offshore monopiles the work of (Nielsen, Schlütter, Sørensen, & Bredmose, 2012) suggests a similar behavior.

(Henrik Bredmose & Jacobsen, 2010) investigated breaking wave impacts on an offshore wind turbine foundation numerically. The authors applied the focused wave group technique to the amplitudes of a spectrum. Three-dimensional CFD computations for varying choice of focus point were carried out leading to a series of computed wave impacts ranging from waves with well-developed breaking to a wave hitting the cylinder at an early stage of breaking. The results suggested that the impact force peak is reduced the more developed the breaking is.

4.2.6 **A CFD approach to design the secondary structures of MUP's**

Secondary structures such as boat-landings and railings supporting transformation stations are crucial for the use of MUP's, because they allow the access to the platforms. Therefore an accurate design is needed. Moreover, the stability of this kind of structures contributes to the overall stability of the main structure. In intermediate depth, these structures should be designed taking into account the forces due to spilling breaking waves. This kind of breakers is not characterized by entrapment of air pockets, therefore the impact is not as much violent and pulsing as in case of plunging waves. The spilling breaker is characterized by a roller this is a mixture of air and water that travels with the wave front with approximately the wave celerity. This large amount of entrained bubbles may have an influence on the design.

As seen in the previous section the experimental studies focus on plunging waves impact generally, then physical processes in case of spilling waves impact are not known in details. In particular, the role of the air needs to be investigated greater detail.

The presented CFD model could help in this analysis and it could also be a reliable and powerful tool for the design of secondary structures.

The main challenge for this CFD model turns out to be the fact that a breaking wave-induced bubbly flow is a multi-scale problem regarding interfacial structures (*Figure 4.7*). The largest scales are localized at the free surface and can be reconstructed by an interface tracking method, being larger than the grid size; the smallest scales are those one related to the dispersed entrained bubbles and they need to be treated by an Eulerian approach.

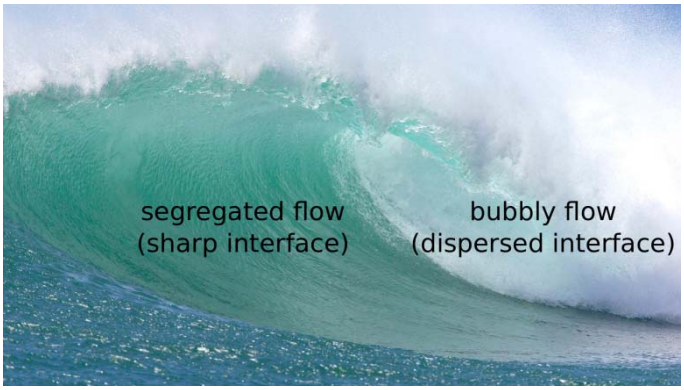

Figure 4.7: the breaking wave-induced bubbly flow

Such multiphase flows involving a broad range of interfacial structures are encountered in various fields of science and industry. The problem has been being faced for the last years by the means of a coupled (or hybrid) approach. The basic idea is to couple an interface tracking algorithm for segregated flows with the multi-fluid Eulerian model for dispersed flow.

(Cerne et al., 2001) was one of the first examples in this field. The authors explicitly coupled the interface capturing VOF-method (Hirt & Nichols, 1981) with the two-fluid Eulerian approach. A special criterion based on the error of the VOF-method was used to switch between the two different sets of governing equations to be solved: whenever the interface became too dispersed to be reconstructed, the Eulerian approach was used.

The presented CFD approach adopts an approach different than the pure coupling described above which is gaining much popularity recently. The idea is to use the Eulerian framework, extended to ($n+1$) phases as described in sec. 4.2.3, in the whole domain and to implement an additional interface sharpening which should be operative when the flow is segregated. In this way, the sharpening of the interface is a result of a numerical artefact rather than the solution of a solver for segregated flow. The advantage is that only one kind of governing equations is solved; nevertheless, it should be pointed out that the interface obtained by an Eulerian algorithm, even if sharpened somehow, cannot be as precise as the one obtained by a tracking method.

An example of this approach can be found in (Wardle & Weller, 2013) who presented a CFD solver where the original two-fluid Eulerian framework was extended to n phases. A mass and momentum conservation equations are solved per each phase. Drag force and virtual mass were taken into account as interfacial momentum transfer between phases; no mass transfer terms were added to the continuity equation. The interface can be sharpened by specifying the interface compression method of (Weller, 2008) between whatever pair of phases. The authors developed such model to solve the multi-scale flow in stage-wise liquid-liquid extraction devices where typically two liquids are mixed (dispersed) and a sharp interface between liquids and air exists.

As said in sec. 4.2.3, the computational demanding increases when n phases are dispersed, because ($n+1$) continuity and (n+1) momentum equations need to be solved. Moreover, the investigations show that an adequate description of the air fraction would require decades of bubble size making the computational cost too high.
In order to reduce the computational cost, the proposed CFD methodology adopts the GEneralized TwO-Phase flow (GENTOP) model of (Hänsch et al. 2012), which is in turn an extension of the inhomogeneous Multi-Size-Group (MUSIG) concept of (J. Shi, Zwart, Frank, Rohde, & Prasser, 2004). In MUSIG the dispersed air is divided into N classes called velocity groups because each of them has its own velocity field Vj. Each velocity group is sub-divided into Mi size fractions under the assumption that all of them share the same velocity, the one of the velocity group they belong to.

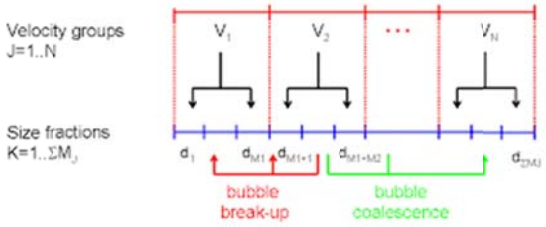

Figure 4.8: structure of MUSIG - from (Krepper et al., 2009)

As Figure 4.8 shows, the polydispersed air is described through $\sum M_j$ bubble classes. The system of governing equations is simplified because only *N+1* momentum equations (instead of $\sum M_j + 1$) need to be solved, although an additional continuity equation is needed per each size fraction in order to consider the mass transfer within the same velocity group. A continuity equation has to be solved per each velocity group as well. In order to further reduce the computational cost, the presented methodology takes into account only one size fraction per each velocity group.
Actually, the evolution introduced by GENTOP is considered appropriate for the object of the problem. It simply consists in an additional gaseous phase, i.e. an additional velocity group, which represents the continuous air. This new velocity group includes only one size fraction which should represents all gas structures exceeding a fixed value of the diameter d_{max} (Figure 4.9).

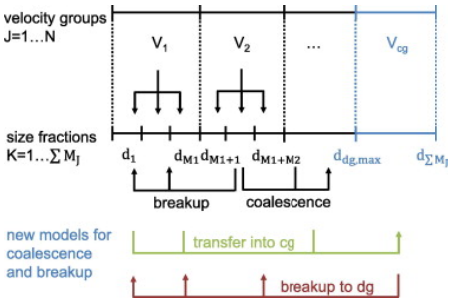

Figure 4.9: structure of GENTOP; the continuous air is the last velocity group - from (Hänsch, Lucas, Krepper, & Höhne, 2012)

GENTOP was shown to be a reliable approach in (Hänsch et al. 2012). The authors developed a model based on the multi-fluid Eulerian framework where GENTOP is combined with a numerical sharpening of the interface occurring between continuous air and continuous water. The authors successfully simulated the impingement of a liquid jet on a free surface and a vertical bubble column. The first case focused on the capability of the model in handling the mass transfer of air which occurs from the continuous air phase to the bubbles of different size (Figure 4.10). The second one on the opposite process, i.e. from bubbles to continuous air.

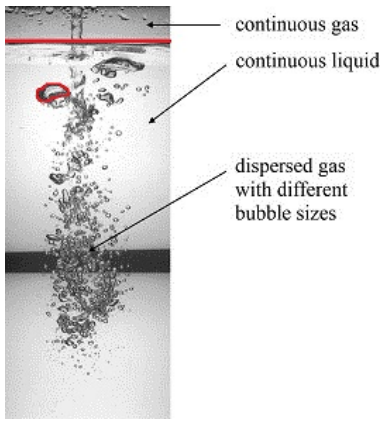

Figure 4.10: the multi-scale flow due to an impinging jet: the same physical processes happen in case of breaking waves-induced air entrainment - from (Hänsch et al. 2012)

The model utilized an algebraic method to localize the interface between continuous air and continuous water. As depicted in Figure 4.10 (red line), such interface occurs not only at the free surface but also at the surface surrounding bubbles which may be larger than the grid size. In this case the interface was sharpened numerically by adding an extra force in the momentum equation of the continuous air (and of the continuous water with opposite sign).

GENTOP is chosen because it provides an accurate modelling of the transition between the different gas morphologies occurring during the breaking wave-induced air entrainment. Actually, the reliability of results depends on the accuracy of the closure terms modelling the mass transfers and the interfacial forces between phases. Details about the relations used in the proposed methodology are presented below.

Mass transfer between continuous air phase and dispersed phases
The mass transfer between the continuous air phase and dispersed phases consists of two contributions. The first one is the breakage of bubbles of the air above the free surface into the water, and then it is essentially the air entrainment process. The second one is the escaping through the free surface of the dispersed bubbles into the continuous .
The sub-grid air entrainment model of (Ma et al., 2011) is adopted. The bubble size distribution *f* of (Deane & Stokes 2002) is used as initial distribution of entrained bubbles (Figure 4.6). In the spirit of the GENTOP-concept, the size distribution is divided into *n* classes with constant radius a_i and width Δa_i. The bubble entrainment rate per unit volume $B(a_i)$ for the i*th* group can be written as:

$$B(a_i) = f_0 f(a_i) \Delta a_i \quad (4.6)$$

Where f_0 is a coefficient and $f(a_i)$ is $a^{-10/3}$ if $a \geq 1\ mm$, $a^{-3/2}$ otherwise.

The energy required to entrain a single bubble with a radius of a_i is function of the surface tension σ as follows:

$$E_b(a_i) = 4\pi a_i^2 \sigma \quad (4.7)$$

It is assumed that the energy required for the entrainment of bubbles of radius a_i is linearly proportional to the turbulent dissipation rate ε:

$$E_b B(a_i) = c_b \rho_w \alpha_w \varepsilon \quad (4.8)$$

where:
- a_i is the radius of created bubbles;

- E_b is the energy required to create a single bubble;
- $B(a_i)$ is the creation rate per cubic meter of bubble with a radius of a_i;
- c_b is a coefficient to be calibrated;
- ρ_w and α_w are density and phase fraction of the water respectively.

The total energy required for the bubbles entrainment can be expressed as:

$$\sum_{1}^{n} 4\pi a_i^2 \sigma\, B(a_i) = c_b \rho_l \alpha_l \varepsilon \tag{4.9}$$

Combining(4.6) and (4.9) the following equations is derive:

$$f_0 = \frac{c_b}{4\pi}\frac{\rho_l}{\sigma}\alpha_l \frac{1}{\sum_1^n a_i^2 f(a_i)\Delta a_i}\varepsilon \tag{4.10}$$

Thus bubble entrainment rate per unit volume is given by

$$B(a_i) = \frac{c_b}{4\pi}\frac{\rho_l}{\sigma}\alpha_l \frac{f(a_i)\Delta a_i}{\sum_1^n a_i^2 f(a_i)\Delta a_i}\varepsilon \tag{4.11}$$

The coefficient c_b needs to be calibrated through comparisons with experimental data.
The air entrainment is localized in those cells of the domain where ε is larger than a fixed threshold.

The escape of bubble from water to continuous air is modelled by the complete merging model of (Hänsch et al., 2012). The mass transfer rate from the dispersed bubbles of class a_i to the continuous air is expressed as

$$C_{g,i}(a_i) = (1-\varphi_s)\cdot\varphi_{morph}\cdot\rho_i\cdot\alpha_i\cdot 1/20\Delta t \tag{4.12}$$

where
- φ_s a blending function used to identify the surface between continuous air and continuous water. It is based on the gradient of the phase fraction of the continuous air and it is given by

$$\varphi_s = 0.5tanh[100\Delta x(|\nabla\alpha_{ca}| - |\nabla\alpha_{ca}|_{crit})] + 0.5, \text{ being } |\nabla\alpha_{ca}|_{crit} = 1/(4\Delta x) \tag{4.13}$$

- φ_{morph} is another blending function expressed as:

$$\varphi_{morph} = 0.5tanh\big[100(\alpha_{ca} - \alpha_{ca,crit})\big] + 0.5, \text{ being } \alpha_{ca,crit} = 0.3; \tag{4.14}$$

- Δt is the time step of the simulation.

Break-up and coalescence between bubbles
Following (Ma et al., 2011) coalescence is not taken into account, whereas the breakage is modelled with (Martìnez-Bazàn, Moñtanès, & Lasheras, 1999). In this approach, the breakage is considered binary, meaning that a bubble may split into two smaller bubbles.
Thus the mass transfer of a dispersed phase of diameter D_i consists of two contributions: a source term due to the bubbles originated by the breakage of bubbles with diameter $D_j > D_i$ and a sink term due to the opposite process. It is expressed as:

$$S_{g,i} = \int_{D_i}^{\infty} 2g(\varepsilon, D_0) f(D_i, D_0) N_{g,0}\, \delta D_0 - g(\varepsilon, D_i) N_{g,i} \tag{4.15}$$

where:
- $g(\epsilon, D_0)$ is the number of bubbles of diameter D_i which are originated from the breakage of a bubble of diameter D_0 per unit volume and per unit time. It is given by:

$$g(\varepsilon, D_0) = \frac{0.25}{D_0}\sqrt{8.2(\varepsilon D_0)^{2/3} - 12\sigma/(\rho_l D_0)} \tag{4.16}$$

- $f(D_i, D_0)$ is the size distribution of daughter bubbles of size D_i formed from the breakage of a mother bubble of size D_0. It is:

$$f(D_i, D_0) = D_0^{-1} \frac{D^{*2}\left[D^{*2/3} - \Lambda^{5/3}\right]\left[(1-D^{*3})^{2/9} - \Lambda^{5/3}\right]}{\int_{D^*_{min}}^{D^*_{max}} D^{*2}\left[D^{*2/3} - \Lambda^{5/3}\right]\left[(1-D^{*3})^{2/9} - \Lambda^{5/3}\right]\delta(D^*)} \quad (4.17)$$

being $D^* = D_i/D_0$, $\Lambda = D_c/D_0$, $D_c = \varepsilon^{-1}(12\sigma/(8.2\rho_l))^{3/2}$, $D^*_{min} = (D_0\varepsilon)^{-1}(12\sigma/(8.2\rho_l D_0))^{3/2}$, $D_{max} = D_0\left[1 - (\frac{D_{min}}{D_0})^3\right]^{1/3}$

- $N_{g,0}$ is the number of bubbles of diameter D_0 per unit volume;
- $g(\epsilon, D_i)$ is the number of bubbles of diameter D_i which undergo breakage per unit volume and per unit time;
- $N_{g,i}$ is the number of bubbles of diameter D_i per unit volume;

Interfacial forces between water and air phases

The momentum transfer between dispersed phases is neglected because of the relatively small bubble density (Ma et al., 2011). Therefore, interfacial forces act between bubbles and continuous water as well as between continuous water and continuous air. Only drag force and virtual mass force are considered. The former accounts for the resistance experienced by bubbles moving in the water; the latter for the acceleration of the water in the wake of the bubbles.

The drag force is modelled using the relation of (Schiller & Naumann, 1935) which reads:

$$\boldsymbol{M}_i^{Drag} = \frac{3}{4}\rho_w\alpha_w\alpha_i C_D \frac{|\boldsymbol{U}_i - \boldsymbol{U}_w|(\boldsymbol{U}_i - \boldsymbol{U}_w)}{D_i} \quad (4.18)$$

C_D is the drag coefficient given by $C_D = \begin{cases} \frac{24(1+0.1Re)^{0.683}}{Re} & , \ Re \le 1000 \\ 0.44 & , \ Re > 1000 \end{cases}$ with $Re = \frac{|\boldsymbol{U}_i - \boldsymbol{U}_w|}{\nu_w} D_i$

The virtual mass force is expressed as:

$$\boldsymbol{M}_i^{VM} = \rho_w\alpha_w\alpha_i C_{VM}\left(\frac{D\boldsymbol{U}_w}{Dt} - \frac{D\boldsymbol{U}_i}{Dt}\right) \quad (4.19)$$

C_{VM} is a constant coefficient usually taken as 0.5.

In conclusion, the presented CFD methodology is summarized as follows (Figure 4.11):
- Multi-fluid Eulerian framework combined with the GENTOP-concept;
- (*n+2*) phases taken into account: *n* dispersed air phases (bubbles) + 1 continuous water + 1 continuous air. Eqs. (4.3) and (4.4) are solved per each phase: (*n+2*) velocity field are calculated, whereas the pressure field is the same for all phases. Pressure-velocity coupling is treated with the PISO algorithm (Issa, 1985);
- Interface between continuous water and continuous air sharpened with the compression method of (Weller, 2008);
- Mass transfer between continuous and dispersed air: entrainment sub-grid model of (Ma et al., 2011) as source term and coalescence model of (Hänsch et al., 2012) as sink term;
- Breakage of bubbles by (Martìnez-Bazàn et al., 1999);
- Momentum exchange between air, either dispersed or continuous, and water: drag force by (Schiller & Naumann, 1935) and virtual mass force by Eq.(4.19).

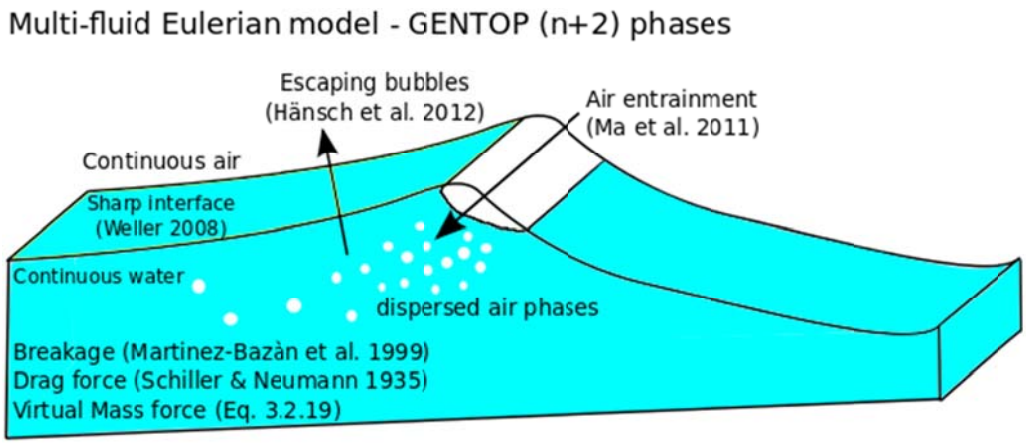

Figure 4.11: Sketch of the proposed CFD methodology.

The CFD methodology presented in this section allows calculating the pressure field under the influence of the air present in the water medium. By taking into account the presence of the MUP's secondary structures in the discretized domain, numerical investigations can be carried out in order to evaluate the magnitude of the acting forces and proceed with the structural design.

4.2.7 References

Bagnold, A. (1939). Interim report on wave-pressure research. *Proc. Inst, Civil Eng.*, *12*, 201–226.

Battjes, J. A. (1988). Surf-zone dynamics. *Annual Review of Fluid Mechanics*, *20*, 257–293.

Bestion, D. (2012). Applicability of two-phase CFD to nuclear reactor thermalhydraulics and elaboration of Best Practice Guidelines. *Nuclear Engineering and Design*, *253*, 311–321. doi:10.1016/j.nucengdes.2011.08.068

Bradford, S. F. (2000). NUMERICAL SIMULATION OF SURF ZONE DYNAMICS. *Journal of Waterway, Port, Coastal, and Ocean Engineering*, *126*(1, January/February), 1–13.

Bredmose, H., & Jacobsen, N. G. (2010). Breaking Wave Impacts on Offshore Wind Turbine Foundations: Focused Wave Groups and CFD. In *Proceedings of the ASME 2010 29th International Conference on Ocean, Offshore and Arctic Engineering OMAE2010*.

Bredmose, H., Peregrine, D. H., & Bullock, G. N. (2009). Violent breaking wave impacts. Part 2: modelling the effect of air. *Journal of Fluid Mechanics*, *641*, 389–430. doi:10.1017/S0022112009991571

Buscaglia, G. C., Bombardelli, F. a., & García, M. H. (2002). Numerical modeling of large-scale bubble plumes accounting for mass transfer effects. *International Journal of Multiphase Flow*, *28*(11), 1763–1785. doi:10.1016/S0301-9322(02)00075-7

Carrica, P. M., Drew, D., Bonetto, F., & Jr, R. T. L. (1999). A polydisperse model for bubbly two-phase flow around a surface ship. *International Journal of Multiphase Flow*, *25*, 257–305.

Cerne, G., Petelin, S., & Tiselj, I. (2001). Coupling of the Interface Tracking and the Two-Fluid Models for the Simulation of Incompressible Two-Phase Flow. *Journal of Computational Physics*, *171*, 776–804. doi:10.1006/jcph.2001.6810

Chanson, H., Aoki, S., & Maruyama, M. (2002). Unsteady air bubble entrainment and detrainment at a plunging breaker : dominant time scales and similarity of water level variations. *Coastal Engineering*, *46*, 139–157.

Christensen, E. D. (2006). Large eddy simulation of spilling and plunging breakers. *Coastal Engineering*, *53*, 463–485. doi:10.1016/j.coastaleng.2005.11.001

Christensen, E. D., & Deigaard, R. (2001). Large eddy simulation of breaking waves. *Coastal Engineering*, *42*(1), 53–86. doi:10.1016/S0378-3839(00)00049-1

Christensen, E. D., Johnson, M., Sørensen, O. R., Hasager, C. B., Badger, M., & Larsen, S. E. (2013). Transmission of wave energy through an offshore wind turbine farm. *Coastal Engineering*, *82*, 25–46. doi:10.1016/j.coastaleng.2013.08.004

Christensen, E. D., Petersen, S. E., & Deigaard, R. (2014). IMPACT OF AN OFFSHORE WIND FARM ON WAVE CONDITIONS AND SHORELINE. In *International Conference on Coastal Engineering (ICCE)* (pp. 1–13). Seoul, South Korea.

Christensen, E. D., Walstra, D., & Emerat, N. (2002). Vertical variation of the flow across the surf zone. *Coastal Engineering*, *45*, 169–198.

Deane, G. B., & Stokes, M. D. (2002). Scale dependence of bubble creation mechanisms in breaking waves. *Nature*, *418*(6900), 839–44. doi:10.1038/nature00967

Drew, D., & Prassman, S. (1999). *Theory of multicomponents fluids*. Springer.

Goda, Y., Haranaka, S., & Kitahata, M. (1966). *Study of impulsive breaking wave forces on piles*.

Hattori, M., Arami, A., & Yui, T. (1994). Wave impact pressure on vertical walls under breaking waves of various types. *Coastal Engineering*, *22*, 79–114.

Hirt, C. ., & Nichols, B. . (1981). Volume of fluid (VOF) method for the dynamics of free boundaries. *Journal of Computational Physics*, *39*, 201–225.

Hänsch, S., Lucas, D., Krepper, E., & Höhne, T. (2012). A multi-field two-fluid concept for transitions between different scales of interfacial structures. *International Journal of Multiphase Flow*, *47*, 171–182. doi:10.1016/j.ijmultiphaseflow.2012.07.007

Iafrati, a. (2011). Energy dissipation mechanisms in wave breaking processes: Spilling and highly aerated plunging breaking events. *Journal of Geophysical Research*, *116*(C7), C07024. doi:10.1029/2011JC007038

Iafrati, A., Di Mascio, A., & Campana, E. F. (2001). A level set technique applied to unsteady free surface flows. *International Journal for Numerical Methods in Fluids*, *35*(3), 281–297. doi:10.1002/1097-0363(20010215)35:3<281::AID-FLD91>3.0.CO;2-V

Ishii, M. (1975). *Thermo-fluid dynamic theory of two-phase flow.* Paris: Eyrolles.

Issa, R. I. (1985). Solution of the Implicitly Discretised Fluid Flow Equations by Operator-Splitting. *Journal of Computational Physics*, *62*, 40–65.

Kimmoun, O., & Branger, H. (2007). A particle image velocimetry investigation on laboratory surf-zone breaking waves over a sloping beach. *Journal of Fluid Mechanics*, *588*, 353–397. doi:10.1017/S0022112007007641

Krepper, E., Ruyer, P., Beyer, M., Lucas, D., Prasser, H.-M., & Seiler, N. (2009). CFD Simulation of Polydispersed Bubbly Two-Phase Flow around an Obstacle. *Science and Technology of Nuclear Installations*, *2009*, 1–12. doi:10.1155/2009/320738

Lamarre, E., & Melville, W. K. (1991). Air entrainment and dissipation in breaking waves. *Nature*, *351*, 469–472.

Lamarre, E., & Melville, W. K. (1994). Void-fraction measurements and sound-speed fields in bubble plumes generated by breaking waves. *Journal of Acoustical Society of America*, *95*(3), 1317–1328.

Lin, P., & Liu, P. L. F. (1998a). A numerical study of breaking waves in the surf zone. *Journal of Fluid Mechanics*, *359*, 239–264.

Lin, P., & Liu, P. L. F. (1998b). Turbulence transport, vorticity dynamics, and solute mixing under plunging breaking waves in surf zone. *Journal of Geophysical Research*, *103*, 677–694.

Lubin, P., Vincent, S., Abadie, S., & Caltagirone, J. (2006). Three-dimensional Large Eddy Simulation of air entrainment under plunging breaking waves. *Coastal Engineering*, *53*, 631–655. doi:10.1016/j.coastaleng.2006.01.001

Lubin, P., Vincent, S., Caltagirone, J., & Abadie, S. (2003). Fully three-dimensional direct numerical simulation of a plunging breaker. *Comptes Rendus de l'Ácademie Des Sciences*, *331*, 495–501. doi:10.1016/S1631-0721(03)00108-6

Ma, G., Shi, F., & Kirby, J. T. (2011). A polydisperse two-fluid model for surf zone bubble simulation. *Journal of Geophysical Research*, *116*(C5), C05010. doi:10.1029/2010JC006667

MacCamy, R. C., & Fuchs, R. A. (1954). *Wave forces on piles: a diffraction theory*.

Martìnez-Bazàn, C., Moñtanès, J. L., & Lasheras, J. C. (1999). On the breakup of an air bubble injected into a fully developed turbulent flow . Part 1 . Breakup frequency. *Journal of Fluid Mechanics*, *401*, 183–207.

Moraga, F. J., Carrica, P. M., Drew, D. a., & Lahey, R. T. (2008). A sub-grid air entrainment model for breaking bow waves and naval surface ships. *Computers & Fluids*, *37*(3), 281–298. doi:10.1016/j.compfluid.2007.06.003

Morison, J. R., O'Brien, M. P., Johnson, J. W., & Schaaf, S. A. (1950). The Force Exerted by Surface Waves on Piles. *Journal of Petroleum Technology*, *AIME 189*, 149–154.

Nadaoka, K., Hino, M., & Koyano, Y. (1989). Structure of the turbulent flow field under breaking waves in the surf zone. *Journal of Fluid Mechanics*, *204*, 359–387.

Nadaoka, K., Ueno, S., & Igarashi, S. (1988). Field observations of three-dimensional large-scale eddies and sediment suspension in the surf zone. *Coastal Engineering in Japan*, *31*(2), 277–287.

Nielsen, A. W., Schlütter, F., Sørensen, J. V. T., & Bredmose, H. (2012). Wave loads on a monopile in 3D waves. In *Proceeding of the ASME 2012 31st International Conference on Ocean, Offshore and Arctic Engineering*.

Peregrine, D. H. (1983). Breaking waves on beaches. *Annual Review of Fluid Mechanics*, *15*, 149–178.

Plummer, L. N., Busenberg, E., Böhlke, J. K., Nelms, D. L., Michel, R. L., & Schlosser, P. (2001). Groundwater residence times in Shenandoah National Park, Blue Ridge Mountains, Virginia, USA: a multi-tracer approach. *Chemical Geology*, *179*(1-4), 93–111. doi:10.1016/S0009-2541(01)00317-5

Schiller, L., & Naumann, Z. (1935). A drag coefficient correlation. *Zeitschrift Des Vereins Deutscher Ingenieure*, *77*, 318.

Shi, F., Kirby, J. T., & Ma, G. (2010). Modeling quiescent phase transport of air bubbles induced by breaking waves. *Ocean Modelling*, *35*(1-2), 105–117. doi:10.1016/j.ocemod.2010.07.002

Shi, J., Zwart, P., Frank, T., Rohde, U., & Prasser, H. (2004). Development of a multiple velocity multiple size group model for poly-dispersed multiphase flows. *Annual Report of Institute of Safety Research.*, *Forschungs*, 21–26.

Sumer, B. M., Guner, H. A. A., Hansen, N. M., Fuhrman, D. R., & Freds??e, J. (2013). Laboratory observations of flow and sediment transport induced by plunging regular waves. *Journal of Geophysical Research C: Oceans*, *118*, 6161–6182. doi:10.1002/2013JC009324

Sumer, B. M., Sen, M. B., Karagali, I., Ceren, B., Fredsøe, J., Sottile, M., … Fuhrman, D. R. (2011). Flow and sediment transport induced by a plunging solitary wave. *Journal of Geophysical Research*, *116*(C1), C01008. doi:10.1029/2010JC006435

Ting, F. C. K. (2006). Large-scale turbulence under a solitary wave. *Coastal Engineering*, *53*, 441–462. doi:10.1016/j.coastaleng.2005.11.004

Ting, F. C. K. (2008). Large-scale turbulence under a solitary wave: Part 2 Form and evolution of coherent structures. *Coastal Engineering*, *55*, 522–536. doi:10.1016/j.coastaleng.2008.02.018

Ting, F. C. K., & Kirby, J. T. (1994). Observation of undertow and turbulence in a laboratory surf zone. *Coastal Engineering*, *24*, 51–80.

Ting, F. C. K., & Kirby, J. T. (1995). Dynamics of surf-zone turbulence in a strong plunging breaker. *Coastal Engineering*, *24*, 177–204.

Ting, F. C. K., & Kirby, J. T. (1996). Dynamics of surf-zone turbulence in a spilling breaker. *Coastal Engineering*, *27*, 131–160.

Wardle, K. E., & Weller, H. G. (2013). Hybrid Multiphase CFD Solver for Coupled Dispersed / Segregated Flows in Liquid-Liquid Extraction. *International Journal of Chemical Engineering*.

Watanabe, Y., Saeki, H., & Hosking, R. J. (2005). Three-dimensional vortex structures under breaking waves. *Journal of Fluid Mechanics*, *545*, 291–328. doi:10.1017/S0022112005006774

Weller, H. G. (2008). A new approach to VOF-based interface capturing methods for incompressible and compressible flow. *Tech. Rep., OpenCFD*.

Wheeler, J. D. (1970). Method for Calculating Forces Produced by irregulat forces. *Journal of Petroleum Technology*, 119–137.

Wienke, J., & Oumeraci, H. (2005). Breaking wave impact force on a vertical and inclined slender pile—theoretical and large-scale model investigations. *Coastal Engineering*, *52*(5), 435–462. doi:10.1016/j.coastaleng.2004.12.008

4.3 Methods for current and wave interaction with fish cages: A review

Hao Chen and Erik Damgaard Christensen, DTU-MEK

4.3.1 Introduction

Globally the aquaculture industry is in a phase of steady expansion and the aquaculture production has continued to grow in the new millennium. As fresh water aquaculture has been increasingly constrained, space and water availability is driving aquaculture growth towards mariculture, from the bays and fjords with sheltered water to more exposed sites with large currents and waves. This leads to a better water quality and the localized water quality problems and ecosystem issues in the sheltered water do not exist anymore.

However the move to open-ocean locations will result in some other issues. Strong currents cause large net deformation and the current forces depend highly on the deformation of the net. Further fish welfare depends on a certain minimum volume within the fish cage. Other issues are of more

technical concern. Design of mooring lines requires reliable assessment of the current and wave forces on the total system. The probability of contact between the net and the chains/ropes sustaining the bottom weights or ring weight with increased wear and tear must be accounted for. Operations with a wellboat moored to fish farm may be challenging in harsh conditions. For instance, the net may be sucked into the propeller and ruptured with fish escape as a possible result. In large waves, overtopping waves on the floater with possible fish escape is of concern (Kristiansen and Faltinsen, 2012).

In order resolve the above issues, an accurate prediction of wave and current interaction with this kind of offshore porous structures are of vital importance. The present review is mainly focused on the numerical simulation of current and wave interaction with fish cages. The biological factors, e.g. fouling, fish density, distribution of the oxygen, are not in the scope of this review.

A complete numerical model appropriate for dynamic analysis of current and wave interaction with fish cages should contain a hydrodynamic force model which is able to calculate forces acting on fish cages, a hydrodynamic flow model which is capable to predict flow field through and around fish cages, and a structural model, which can calculate cage deformations. These are the major topics covered in this review.

The review is structured as follows: Section 4.3.2 discusses the main parameters in the analysis of fish cages since the hydrodynamic forces acting on fish cages have a clear dependence on these parameters. Section 4.3.3 and Section 4.3.4 gives an overview on different types of hydrodynamic flow and force model while Section 4.3.5 focuses on the structural model. In the following part, a brief review is given on the topic of integrated hydroelastic analysis for fish cages in current and waves and finally a short conclusion is provided.

4.3.2 Main parameters in the analysis of fish cages

Fish cages have some properties that are usually not encountered in traditional marine structures, namely permeability and flexibility. The permeability allows the flow to go through and around the fish cage while the flexibility allows the fish cage to change shape under the action of current and wave forces (Løland, 1993).

Based on (Fredheim, 2005) there are four main parameters which are relevant when discussing the flow through and around fish cages. Here we clarify the definition of these parameters on a flat net panel as an example. But these definitions can be easily extended to fish cages.

- The angle of attack for the net panel, is defined as the angle between the plane of net panel and incoming flow direction, see Figure 4.12.

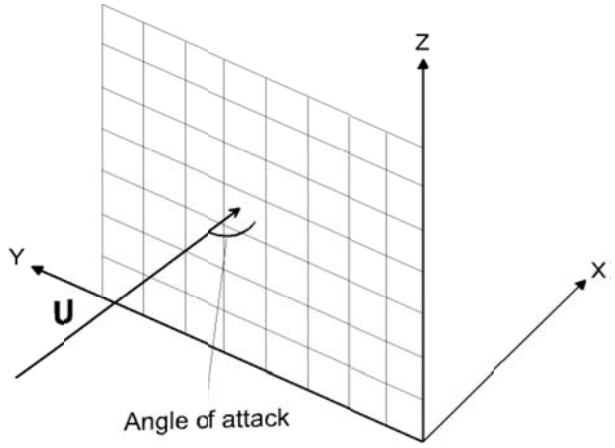

Figure 4.12 Definition of angle of attack. Reproduction of Figure 1.5 from (Fredheim, 2005).

- The Hanging ratios E_1 and E_2 of the mesh describe the diamond shape of the mesh in horizontal and vertical direction respectively, and they are a function of the angle of the mesh opening. For a flat net panel they can be obtained by

$$E_1 = \frac{D_1 \pi}{T_1 l_m} = \sin \alpha \tag{4.20}$$

And in the vertical direction as

$$E_2 = \frac{L}{N T_1 l_m} = \cos \alpha \tag{4.21}$$

where D_1 is the length at the top layer and T_1 is the number of meshes at the top layer of the net panel, L is the length between the top and bottom layer of the net panel, N is the number of meshes in the vertical direction, $\frac{1}{2} l_m$ is the side length of the mesh and 2α is the angle of the mesh opening. Figure 4.13 illustrates these geometrical variables.

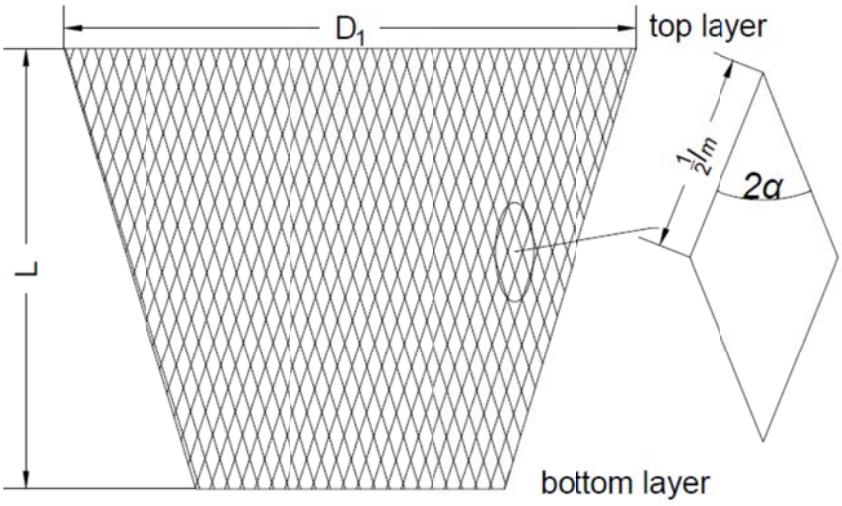

Figure 4.13 Definition of mesh properties.

However for aquaculture farming cages, square mesh is the most commonly used and $E_1 = E_2 = 0.707$.

- The solidity ratio S_n, describes the ratio of the projected area of the net A_p over the total area A, enclosed by the net and it is complementary to the net porosity. In general the solidity ratio will become a function of the hanging ratios E_1 and E_2:

$$S_n = \frac{2d}{l_m E_1 E_2} - \left(\frac{d}{l_m}\right)^2 \left(\frac{1}{E_1^2} + \frac{1}{E_2^2}\right) \tag{4.22}$$

where d is the twine diameter. For a square mesh the angle of the mesh opening 2α will become equal to 90°, the solidity ratio can be expressed as:

$$S_n = \frac{2d}{\lambda} - \left(\frac{d}{\lambda}\right)^2 \tag{4.23}$$

where λ is defined as the half mesh equal to 0.5 l_m and is the same as the length of one side in a square mesh, as show in Figure 4.14.

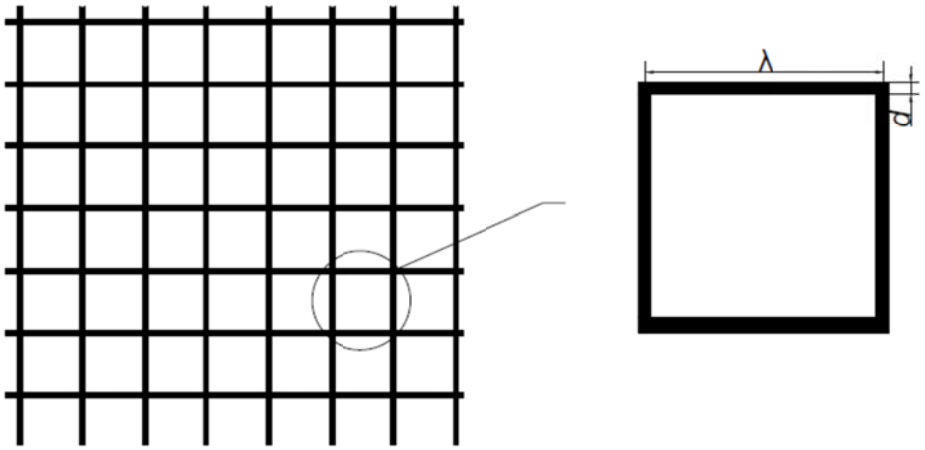

Figure 4.14 Illustration of solidity ratio for square mesh net panels

- The Reynolds number R_n of the individual twines defined as

$$R_n = \frac{Ud}{\upsilon} \tag{4.24}$$

where υ is the kinematic viscosity and U is the incoming flow velocity.

It has been demonstrated by both numerical simulation and experiments that when discussing velocity reduction in the downstream of the flow and the drag and lift forces acting on the cages, there is a clear dependence on these four parameters, see *e.g.* Section 4.3.3.

4.3.3 Hydrodynamic Flow Model

A flow model should be capable for solving the flow field through and around fish cages. The proposed methods so far include empirical formulations and a variety of disturbance source techniques by which the effects of fish cages on the flow are accounted for.

Empirical Formulations

Traditionally the research on flow through and around net cages focuses on velocity reduction in the downstream. (Løland, 1991) proposed an estimation of velocity reduction factor as a function of solidity ratio. (Fredriksson, *et al*. 2007) conducted field measurements for velocity reduction with different cage solidity ratios and for solidity ratio of 19.7%, 40.8% and 58.8%, the velocity reduction factors are 0.8, 0.7 and 0.42, respectively. (Bi, *et al*. 2013) conducted a series of laboratory experiments to investigate flow velocity reduction in downstream of fishing nets with different net solidities, attack angles and with multiple fishing nets.

Wake model

(Løland, 1993) proposed and developed the plane wake model to analyze wakes behind the fish cages. The fish cages are approximated by a number of cylinders and the wake behind each independent cylinder is of a boundary layer nature thus the governing equations are the equations in boundary layer flow from (Schlichting, 1979):

$$\frac{\partial u_1}{\partial t} + U\frac{\partial u_1}{\partial x} = \varepsilon_\tau \frac{\partial^2 u_1}{\partial y^2} \tag{4.25}$$

where U is the free velocity, ε_τ is the eddy viscosity approximated as:

$$\varepsilon_\tau = 0.0222 U C_D D \tag{4.26}$$

where C_D is the drag force coefficient and D is the diameter of the cylinder. u_1 is a perturbed velocity defined as:

$$u_1 = U - u \tag{4.27}$$

where u is the velocity in the wake.

Due to the linearity of the equation, the wake behind fish cages can be approximated by the sum of wakes from all the cylinders. However this will overestimate velocity defect far downstream and in order to satisfy the asymptotic condition in the far field wake, modifications have been done and the asymptotically correct velocity field can be obtained.

This work was generalized by (Fredheim, 2005) in which the flow distribution around a three dimensional net structure is the superposition of the effects due to not only twins (modelled as cylinders) but also knots (modelled as spheres) as shown in Figure 4.15. The disturbance of the flow field due to both twins and knots is described as two parts:

a) The upstream effect, which describes the disturbance on the flow field outside the wake region due to the presence of the cylinders and spheres. The disturbance of cylinders and spheres are modelled as line source distributions and point sources. The source strength can be calculated by Lagally's theorem (Milne-Thomson 1968).
b) The downstream effect where the wake is described using the "far wake mean velocity deficit" model in (Schlichting, 1979) which gives time averaged mean velocity in the wake behind a body with some modifications for near field of the cylinders based on (Blevins, 1990).

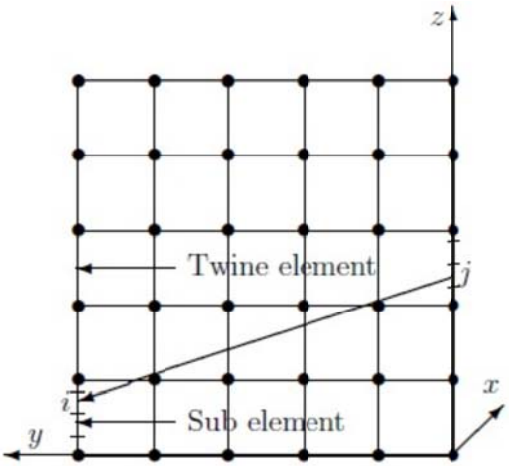

Figure 4.15 Illustration of modelling of the net by twine and knot elements. Reproduction of Figure 1.12 from (Fredheim, 2005).

CFD approach combined with a porous media model

With the fast development of computational fluid dynamics (CFD), attentions have been paid to simulate the flow around fish cages by using CFD techniques. However, if the net structure is approximated by small cylinders connected at knots, the number of cylinders required to model the net is typically at the order of 10 million. Thus it is impractical to model the fish cage directly and a realistic approach is to model the net as a sheet of porous media where the nets are represented by source terms in momentum equations. A thorough investigation of porous media equation in coastal engineering is shown in (Jensen et al., 2014).

A few studies on flow through fish cages base their investigations on a porous media model. (Patursson et al., 2006) conducted a series of 2D simulations of the flow through a net panel situated in the center of a channel at different angles of attack. (Patursson et al., 2010) applied this model with a $k-\varepsilon$ turbulence model to describe the 3D flow through and around a net panel. The model resistance coefficients needed for the porous media equations were found by optimizing the fit between computed lift and drag forces on the net panel and lift and drag measure in tow tank experiments. (Zhao et al., 2013) performed a three dimensional numerical simulation for the flow field inside and around the gravity cages in a current. The unknown coefficients were determined from the hydrodynamic force in the net under different flow velocities and attack angles using least square method.

However, application of these methods requires the resistance coefficients for each individual net that is modeled and normally this should be obtained from experiments. Further research could be done to develop new methods for finding the porous media resistance coefficients.

4.3.4 Hydrodynamic force model

This section gives an introduction on different hydrodynamic force models proposed for fish cages. It starts with a summary on empirical or semi-empirical formulas for calculation of force coefficients. Then follows parts focused on numerical approaches. In principle there are two main numerical approaches. One is to model the net as individual knots and twines, calculate the total

drag on the net as sum of the drag of individual elements, *e.g.* Morison type models. This approach makes it possible to model details in the net structures. Another is to model the net by dividing it into surface elements, where each element has properties that simulate the twine and knot structure of the netting. The hydrodynamic forces on the net element can be divided into drag and lift components, *e.g.* screen type model.

Empirical formulation for the force coefficient

Historically there have been lots of experiments conducted to measure the drag forces coefficients as functions of the parameters listed in Section 4.3.2. This lays the foundation for development of screen type models.

Various formulations have been proposed regarding force coefficients acting on net structures. (Milne, 1970) proposed an analytical formulation that was verified against nets with a relatively low range of solidity ratio. (Milne, 1972) also considered the knot factor (knotted or knotless net). (Aarsnes et al., 1990) proposed an empirical formulation, which was based on experiments by towing plane nets with different solidity ratios through a towing rank at different velocities and angle of attack. (Løland, G. 1991) combined theoretical work with experimental data in (Rudi *et al.*, 1988) to derive drag and lift coefficients. (Zhan et al., 2006) performed experiments in a towing tank with net panels of different solidity. The effects of the Reynolds number, net solidity, and mesh pattern and flow direction on the drag force on submerged nets of fish cages were studied and the author proposed new equations for the drag force coefficient. (Balash et al., 2009) performed experiments with a net panel and measured the hydrodynamic loads in both steady and oscillating flow. Figure 4.16 depicts the above mentioned results with an angle of rotation of 90° and for a velocity of 0.25 m/s.

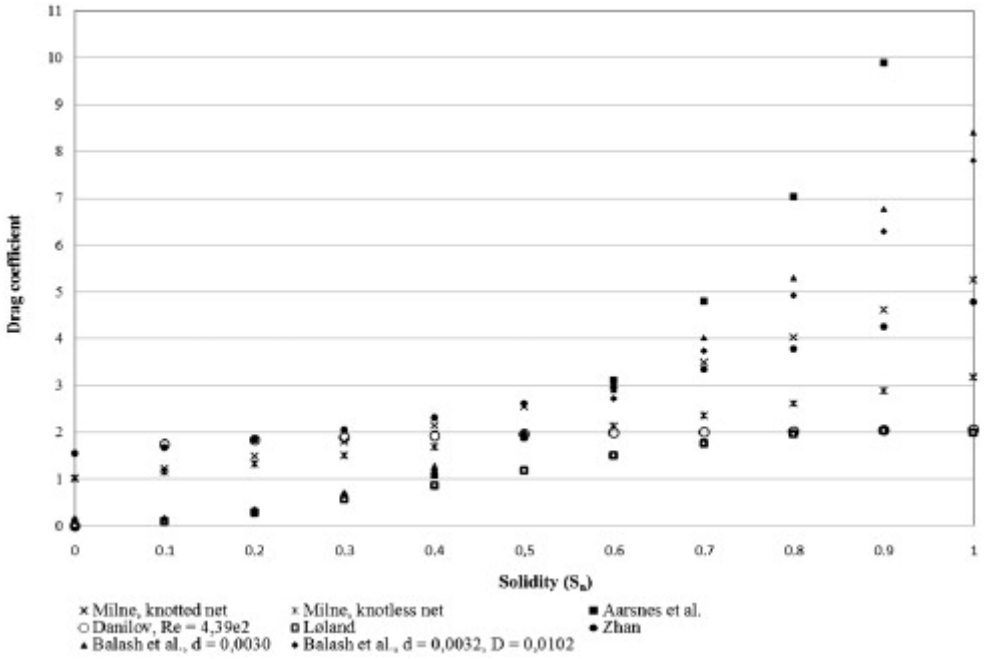

Figure 4.16 Overview of the empirical and semi-empirical drag formulations versus solidity ratios. Reproduction of Figure 1 from (Klebert et al., 2013).

Morison type force model

(Morison et al., 1950) proposed equations for calculating the forces acting on the stationary slender members under the influence of surface waves and (Brebbia and Walker, 1981) generalized the equation for moving bodies as follows:

$$\mathrm{F} = \frac{1}{2}\rho C_d A V_R |V_R| + \rho \vee C'_m \frac{\partial V_R}{\partial t} + \rho \vee \frac{\partial V}{\partial t} \tag{4.28}$$

where ρ is the density of the fluid, C_d is the drag force coefficient and C'_m is the added mass coefficient, A is the member area, ∨ is the displaced volume of structure member and V_R is the relative velocity of the fluid and the slender member:

$$V_R = V - R \tag{4.29}$$

where V is the water particle velocity and R is the velocity of the slender structure.

For the Morison type force model, net cages are represented by equivalent twines or trusses and the hydrodynamic force acting on the net structure is calculated by applying Morison equation on the twines or trusses, this method is adopted in a list of publications, *e.g.* (Li *et al.* 2006), (Huang *et al,* 2008) and (Moe, 2010).

A main deficiency of this approach is that a drag model based on the cross flow principle cannot be justified when the inflow angle is larger than about 45°, the drag force will be highly over predicted, see *e.g.* (Carrothers and Baines, 1975). Meanwhile the interaction between twines is not accounted for. There are mainly two interaction effects, the shading effect of the downstream twines from the upstream twines for large inflow angles and the local speed up of the flow in between the twines, which increases with the high solidity ratio (Kristiansen and Faltinsen, 2012).

Screen type force model

Screen type force model is a typical force model that uses super surface elements. For screen type force model, the net cage is divided into a number of 2D net panels, or in some publications, it is called screens. However, they are equivalent. Each panel consists of a number of physical twins and knots and represent their properties under current and wave conditions. The hydrodynamic force acting on the net panel are decomposed into drag and lift components and they can be calculated as:

$$\mathrm{d}\, F_D = \frac{1}{2}\rho C_d U^2 \ \mathrm{dA} \tag{4.30}$$

$$\mathrm{d}\, F_L = \frac{1}{2}\rho C_L U^2 \ \mathrm{dA} \tag{4.31}$$

where C_d and C_L are the drag and lift forces coefficients, dA is the area of net panel, U is the incoming velocity and ρ is the density of water.

This method is used in *e.g.* (Løland, G. 1991), (Kristiansen and Faltinsen, 2012), (Lader *et al,* 2006). However, the error for this method mainly comes from the determination of drag and lift force coefficient, since it is not possible to find general expression for these coefficients valid for all combination of Reynolds number and solidity ratio.

4.3.5 **Structural model**

A structural model is necessary for the analysis of fish cage deformation. In the previous work, a fish cage has been modeled using truss, beam, spring or membrane elements. A general overview on the structural model is given in this section.

(Li et al., 2006) proposed a lumped mass model to simulate the net structures. They assumed that there is only tension in the axis direction of a mesh bar and the netting twine is completely flexible and easily bent without resistance. The fishing net is approximated as a series of lumped point masses that are interconnected with springs without mass. Lumped point masses are set at each knot and at the center of the mesh bar. Since the mesh bar is cylindrical, the fluid forces acting on the point masses at each mesh bar should differ in different directions. Therefore it is assumed that the fluid force coefficients vary with the relative fluid velocity direction. Figure 4.17 depicts the schematic diagram of this model.

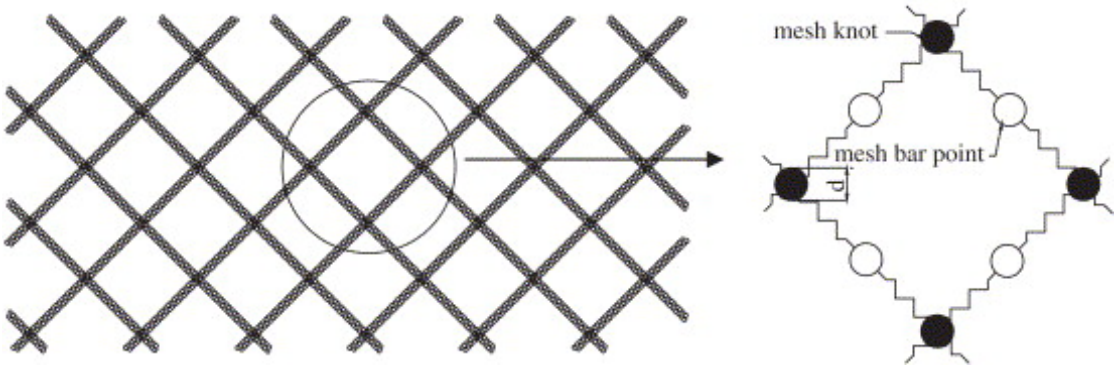

Figure 4.17 The schematic diagram of the mass spring model. Reproduction of Figure 1 from (Li et al., 2006).

Alternatively the net structure can be modelled as individual knots and twines by using truss or beam elements (1D elements) in a standard finite element program. (Tsukrov et al., 2000) analysed open ocean aquaculture fish cages using the equivalent truss approach in which a deformable truss structure was used to represent each net panel. The truss has same drag force, buoyancy, gravity and stiffness as the original net panel, but the condition of the same inertia is not satisfied. (Tsukrov et al., 2003) proposed a special consistent finite element in AQUA-FE program developed at the University of New Hampshire to model net panels which has the same hydrodynamic and elastic parameters. (Moe et al., 2010) and (Fredheim, 2005) performed the structural analysis of a fish cage with finite element commercial software package ABAQUS Explicit. The net cage model is built up of 3-D truss elements and each truss element represents several parallel twines in the netting thus to simplify the model and reduce the computation time to an acceptable level. The netting material does not carry compressive loads so each global truss element is divided into several sub-elements, allowing the twines to buckle when subjected to compression. The comparison of deformed shape from FE model with simplified mesh, detailed mesh and physical model are shown in Figure 4.18

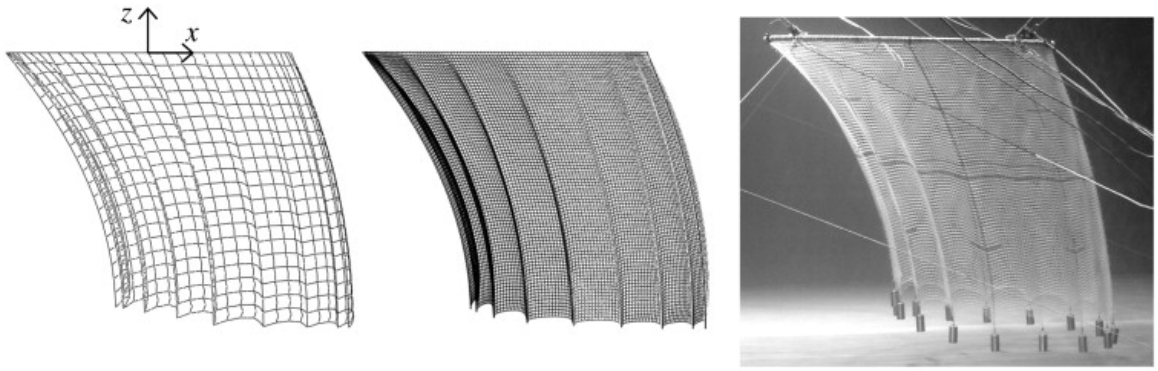

Figure 4.18 Comparison of deformed shape from FE model with simplified mesh (left), detailed mesh (middle) and physical model (right). Reproduction of Figure 2 from (Moe et al., 2010)

(Lader and Fredheim, 2006) and (Lader et al., 2001) proposed a method to simulate a single net sheet exposed to wave and current. In their work the net was modelled by divided into 2D super-elements, where each element has properties that simulates the twine and knot structure of the netting, as seen in Figure 4.19. The structural and hydrodynamic forces are calculated for each element and the deformation of the net is found from time integrating the equation of motion at each node.

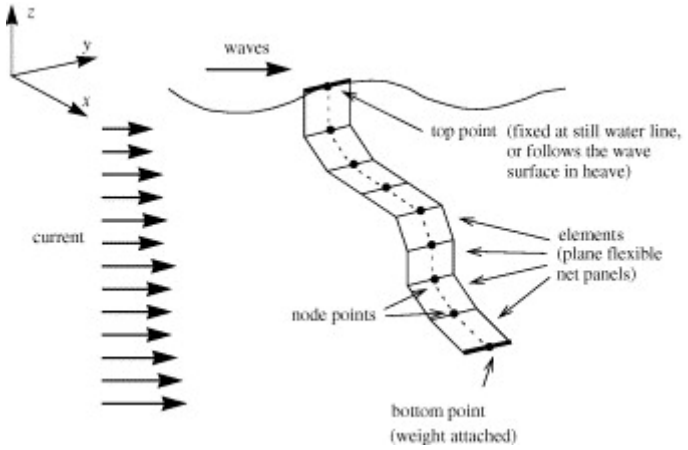

Figure 4.19 Net model with super elements. Reproduction of Figure 1 from (Lader and Fredheim, 2006)

4.3.6 **Hydroelastic analysis of net structure**

It is not straightforward to analyse the dynamics of a fish farm or a single net cage. The load acting on the structure will be a fluid-structure interaction between moving sea-water and the deformed net. Analysis of net cages involves a high degree of non-linearity, both in loads, deformation and sometimes also material properties. In addition, loads from waves and current, damping and inertia loads are complex to model for netting materials in a general structural analysis, while programs with appropriate load modules often have shortcomings in the structural model. The flexibility of the structure will lead to large deformation which will in contrast affect the flow. So the best way to analyze the problem is to involve a complete CFD and FEA. Unfortunately so far attempts to perform such analysis on net cages have not been performed (Moe et al., 2010).

There are a few publications that conduct the hydroelastic analysis of fish cage. (Fredheim, 2005) proposed a wake model as shown in Section 4.3.3 to obtain the flow field, then the forces on each

elements of the cages was calculated based on the velocity in the flow model, and a truss model was adopted to calculate structure response to the forces on each cylinder, finally the structure analysis led to a new geometry of the net due to the incoming flow. Based on this new geometry a new correction of the inflow could be obtained and it was possible to continue until a specified convergence criterion was met.

(Bi et al., 2014) presented a hydroelastic analysis based on the joint use of the porous-media model and the lumped-mass model. The configuration of flexible nets and the flow field around fishing nets were simulated using the lumped-mass model and the porous-media model respectively. By an iterative scheme the fluid structure interaction was considered in the model.

4.3.7 **Conclusion**

This review aims to give a thorough survey on the wave and current interaction with fish cages. Numerous research has been conducted on this topic and the review attempts to capture the significant research that has been carried out.

The so far proposed hydrodynamic flow model is mainly based on some source techniques to account for the effect of the nets on the flow. Comparing with the simplified wake models, CFD approach is more advances since it can solve three dimensional Navier-Stokes equations. However the porous resistance coefficients should be always prior known values before the simulation is conducted.

On the hydrodynamic force model of the net structure, early research is mainly concentrated on the empirical and semi-empirical formulations. These formulations are easy to use but they do have some limitations. However they are the foundations for the numerical methods. The later developed Morison and screen types force model have their advantages and drawbacks respectively.

When it comes to the structural model, various structural models have also been proposed based on finite element method or lumped mass method. Cage deformation could be modelled with appropriate environmental forces. It is demonstrated that the main error source is the hydrodynamic load rather than the structural model.

In order to account for the fluid structure interaction, hydroelastic analysis is essential. It requires a combination of a hydrodynamic force model, a flow model and a structural model with some iteration schemes. Hydroelastic analysis is supposed to be the trend and it is expected that direct CFD/FEA simulation could be conducted in the close future.

4.3.8 **References**

Aarsnes, J., Rudi, H., and Loland, G. (1990). Current forces on cage, net deflection. ENGINEERING FOR OFFSHORE FISH FARMING, pages 137–152.

Balash, C., Colbourne, B., Bose, N., and Raman-Nair, W. (2009). Aquaculture net drag force and added mass. AQUACULTURAL ENGINEERING, 41(1):14–21.

Bi, C. W., Zhao, Y.P., Dong, G.H., Xu, T.J. and Gui, F.K. (2013). Experimental investigation of the reduction in flow velocity downstream from a fishing net. AQUACULTURAL ENGINEERING. **57,** 71–81.

Bi, C.W., Zhao, Y.P., Dong, G.H., Xu, T.J, Gui, F.K. (2014). Numerical simulation of the interaction between flow and flexible nets. Journal of Fluids and Structures, 45:180–201.

Blevins, R. D. (1990). *Flow Induced Vibration*, Van Nostrand Reinhold.

Brebbia, C. and Walker, S. (1981). Dynamic analysis of offshore structures. Applied Ocean Research, 3(4):205.

Carrothers, P. and Baines, W. (1975). Forces on screens inclined to a fluid-flow. JOURNAL OF FLUIDS ENGINEERING-TRANSACTIONS OF THE ASME, 97(1):116–117.

Fredriksson, D.W., Decew, J.C., Tsukrov, I., Swift, M.R. and Irish, J.D. (2007). Development of large fish farm numerical modeling techniques with in situ mooring tension comparisons. AQUACULTURAL ENGINEERING, 36(2), pp.137–148.

Fredheim, A. (2005). Current Forces on Net Structure. PhD thesis, Norwegian University of Science and Technology, Faculty of Engineering Science and Technology.

Fredheim, A. and Faltinsen, O. M. (2003). Hydroelastic analysis of a fishing net in steady inflow conditions. *HYDROELASTICITY IN MARINE TECHNOLOGY*, (3):1–10.

Huang, C.C., Tang, H.J. and Liu, J.Y. (2008). Effects of waves and currents on gravity-type cages in the open sea. AQUACULTURAL ENGINEERING, 38, pp.105–116.

Jensen, B., Jacobsen, N. G. and Christensen, E. D. (2014). Investigations on the porous media equations and resistance coefficients for coastal structures. *Coastal Engineering*, 84:56–72.

Klebert, P., Lader, P., Gansel, L., and Oppedal, F. (2013). Hydrodynamic interactions on net panel and aquaculture fish cages: A review. *Ocean Engineering*, 58:260.

Kristiansen, T. and Faltinsen, O. M. (2012). Modelling of current loads on aquaculture net cages. *JOURNAL OF FLUIDS AND STRUCTURES*, 34:218–235.

Lader, P. F. and Fredheim, A. (2006). Dynamic properties of a flexible net sheet in waves and current – a numerical approach. *AQUACULTURAL ENGINEERING*, 35(3):228–238.

Lader, P. F., Fredheim, A., and Lien, E. (2001). Dynamic behaviour of 3d nets exposed to waves and current. *PROCEEDINGS OF THE INTERNATIONAL CONFERENCE ON OFFSHORE MECHANICS AND ARCTIC ENGINEERING*, 1(20TH):411–418.

Li, Y. C., Zhao, Y. P., Gui, F. K., and Teng, B. (2006). Numerical simulation of the hydrodynamic behaviour of submerged plane nets in current. *OCEAN ENGINEERING*, 33(17-18):2352–2368.

Løland, G. (1991). *Current forces on and flow through fish farms*.

Løland, G. (1993). Current forces on, and water flow through and around, floating fish farms. *Aquaculture International*, 1(1):72–89.

Milne, P. H. (1970). Fish farming: A guide to the design and construction of net enclosures. *Marine research 1*.

Milne, P. H. (1972). *Fish and Shellfish Farming in Coastal Waters*.

Milne-Thomson, L. M. (1968), Theoretical Hydrodynamics, MacMillian & Co. Ltd.

Moe, H., Fredheim, A., and Hopperstad, O. S. (2010). Structural analysis of aquaculture net cages in current. *JOURNAL OF FLUIDS AND STRUCTURES*, 26(3):503–516.

Morison, J., Obrien, M., Johnson, J., and Schaaf, S. (1950). The force exerted by surface waves on piles. *TRANSACTIONS OF THE AMERICAN INSTITUTE OF MINING AND METALLURGICAL ENGINEERS*, 189:149–154.

Patursson, O., Swift, A. R., Baldwin, K., Tsukrov, I., and Simonsen, K. (2006). Modeling flow through and around a net panel using computational fluid dynamics. *OCEANS 2006, VOLS 1-4*, pages 1308–1312.

Patursson, O., Swift, M. R., Tsukrov, I., Simonsen, K., Baldwin, K., Fredriksson, D. W., and Celikkol, B. (2010). Development of a porous media model with application to flow through and around a net panel. *OCEAN ENGINEERING*, 37(2-3):314–324.

Rudi, H., Løland, G. and Furunes, I. (1988). Experiments with nets; forces on and flow through net panels and cage systems. Technical Report MT 51 F88-0215, MARINTEK, Trondheim, Norway.

Schlichting, H. (1979). *BOUNDARY LAYER THEORY*.

Tsukrov, I., Eroshkin, O., Fredriksson, D., Swift, M., and Celikkol, B. (2003). Finite element modeling of net panels using a consistent net element. *OCEAN ENGINEERING*, 30(2):251–270.

Tsukrov, I. I., Ozbay, M., Fredriksson, D. W., Swift, M. R., Baldwin, K., and Celikkol, B. (2000). Open ocean aquaculture engineering: Numerical modeling. *MARINE TECHNOLOGY SOCIETY JOURNAL*, 34(PART 1):29–40.

Zhan, J. M., Jia, X. P., Li, Y. S., Sun, M. G., Guo, G. X., and Hu, Y. Z. (2006). Analytical and experimental investigation of drag on nets of fish cages. *AQUACULTURAL ENGINEERING*, 35(1):91–101.

Zhao, Y.-P., Bi, C.-W., Dong, G.-H., Gui, F.-K., Cui, Y., and Xu, T.-J. (2013). Numerical simulation of the flow field inside and around gravity cages. *Aquacultural Engineering*, 52:1.

5 Scour around typical Multi-use offshore platforms structures

5.1 Scour and backfilling around foundations

Cüneyt Baykal and B. Mutlu Sumer, DTU-MEK

Scour and backfilling processes could possibly be best described with reference to wind turbine foundations. Foundation structures may be of four types (Figure 5.1): monopiles, tripods, jackets, and gravity base, with the monopiles used for very shallow (or mildly shallow) waters up to O(20-30) m.

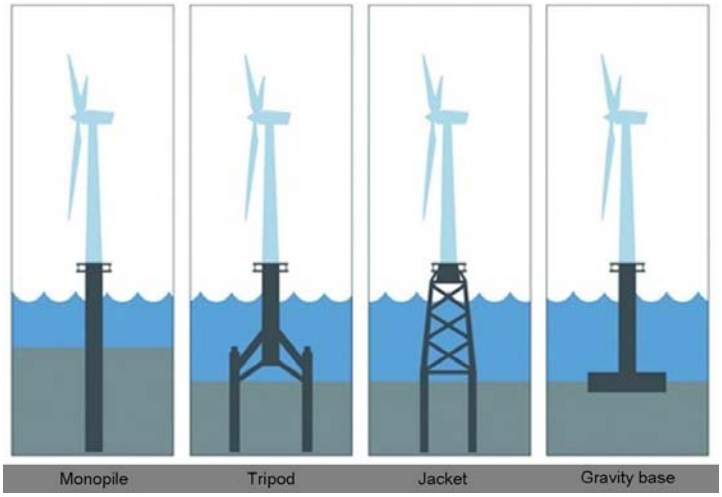

Figure 5.1 Wind turbine foundation types.

When foundation-supported wind turbines are installed offshore, heavy scour will take place around each individual foundation. Figure 5.2 (taken from Roulund *et al*. 2005) illustrates the scour around a model monopile foundation in a current, obtained in a computer simulation.

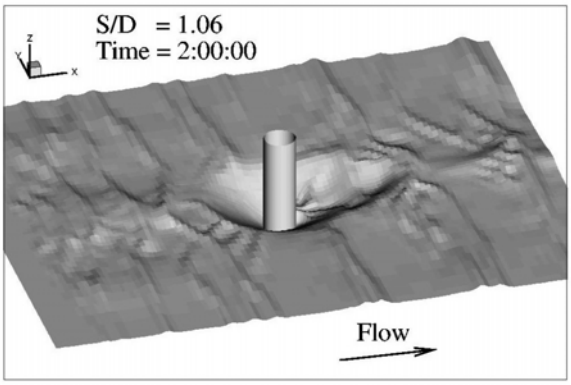

Figure 5.2 Scour hole in the equilibrium stage around a model monopile obtained in Roulund et al.'s (2005) numerical simulation.

Clearly, scour is a threat for the stability of the turbine structure. Therefore these structures are almost invariably protected against scour with rock protection installed around the foundation, although an installation with no protection is also a viable option (Wittrup 2012).

In the case of no protection (or for situations where the protection is not yet installed), the following three factors are important for the design of the wind turbine and its foundation: (1) maximum loading, to determine the size and the depth (below the seabed surface) of the foundation; (2) the fatigue load, to determine the wall thickness of the foundation or foundation elements; and (3) Eigen frequencies (or natural frequencies), to determine the operation of the turbine itself. These three factors are heavily influenced by the depth of the scour hole around the foundation. The depth of the scour hole changes continuously; The seabed around the foundation experiences scour and backfilling in an alternating fashion, under an ever changing wave and current climate (Sumer *et al*. 2013).

Numerical modelling of scour and backfilling has been a growing area in the field of scour and erosion. Early examples of numerical modelling of scour date back to nineties, e.g., Olsen et al. (1993, 1998). There are several reviews on the subject, Sumer and Fredsøe (2002), Sumer (2004, 2007). The review by Sumer (2007) covers the work on scour around piers/piles and pipelines, two important benchmark cases, as well as scour around other structures such as groins in streams, breakwaters, and seawalls. Sumer (2007) also gives future research suggestions and challenges.

5.1.1 Highlights of numerical modelling of scour. A general review

Mathematical models of local scour may be divided in two categories: simple models and advanced models (Sumer and Fredsøe, 2002). The present review concerns with the advanced models. The advanced models have essentially two components: a hydrodynamic model and a morphologic model. Next, each component will be considered individually.

Hydrodynamic model

This subsection will give a brief account of hydrodynamic models. Detailed discussions of the subject can be found in, e.g., Sumer and Fredsøe (2002), Sumer (2004, 2007 and 2008) among others.

Hydrodynamic models essentially solve the classic Reynolds-averaged Navier-Stokes (RANS) equations. The RANS equations are closed with a turbulence model, the so-called turbulence closure, e.g., k-ε or k-ω models, (Wilcox, 2006, 2008).

The RANS equations (incorporated with a turbulence model) are solved in a computational domain characterized with an inlet on the left hand side, an outlet at the right hand side, a top boundary, and a bottom boundary.

The top boundary is usually treated as a frictionless slip wall with, e.g., vertical velocities set to zero, and horizontal velocities and scalar hydrodynamic quantities having zero normal gradients,

with no free-surface representation, although there are studies (yet, a few) where the free surface was handled properly (e.g., Gothel and Zielke, 2006, and Gothel, 2007).

At the bottom boundary (i.e., the seabed, or the river bed), the no-slip condition is used.
At the inlet boundary, there may be a number of options available; for instance, in the case of currents, current flow conditions are obtained from a preliminary hydrodynamic simulation where the flow is driven by a body force for the domain in the absence of the structure. In the case of waves, in order to drive desired oscillatory wave flow conditions, the familiar oscillatory flow conditions are usually used.

At the right hand boundary, several options are available, such as zero-gradient boundary conditions to name but one example.

Finally, like the boundary condition on the bottom, at the surface of the structure, the no-slip condition is used.

Baykal et al. (2014 a, 2014 b), two end products of the present project, MERMAID, describes the results of a typical hydrodynamic-modelling exercise on scour/backfilling around a monopile, and can be consulted for further details, as far as the hydrodynamic modelling is concerned.

Morphologic model

A morphologic model normally consists of three elements: a sediment transport model; a sand-slide model; and the so-called sediment continuity equation (the Exner equation).

The sediment transport model may be a bedload sediment transport formula such as, for example, the Engelund and Fredsøe (1976) bedload equation. The model may, additionally, include the suspended load. The latter is handled through a turbulent diffusion equation. The latter equation is solved for the sediment concentration with a boundary condition for the sediment concentration at the bottom boundary. This boundary condition appears to be a challenging issue. Fuhrman et al. (2014), for scour/backfilling simulations below a pipeline, tackled this problem, and, for this boundary condition, adopted a reference level for sediment concentration at $3.5d$, rather than using the standard $2d$ level, the quantity d being the grain size. (See also Liang and Cheng, 2005 a, who also adopted a similar reference level in their work.) This reference level ($3.5d$) turns out to be very close to the top mean vertical position reached by single “bedload” particles, obtained by Sumer and Deigaard (1981) in their single-particle experiments, and therefore gives a sound, physical interpretation for the adopted boundary condition. See Fuhrman et al. (2014) for a detailed discussion of the topic.

Regarding the sediment continuity (the Exner) equation, this equation involves four terms, namely the rate at which the bed elevation changes, the spatial variation of the bedload, and two further terms, the deposition and the erosion. The sediment concentration enters into the sediment continuity equation through the latter two terms. The sediment continuity equation is solved to obtain the morphologic change of the bed elevation. Although, in order to avoid excessive computational times, the hydrodynamic calculations are normally carried out at time steps large compared with those of the morphologic calculations (Figure 5.3), there are examples where the

hydrodynamic time steps are taken exactly the same as the morphologic ones (Fuhrman et al., 2014 and Baykal et al., 2014 a and b).

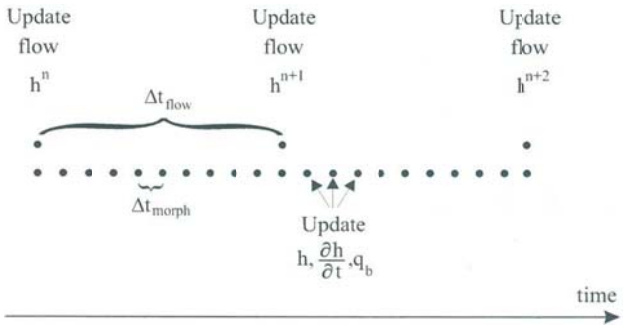

Figure 5.3. Hydrodynamic time step, Δt_{flow}, and morphologic time step, Δt_{morph}, in a typical numerical modelling exercise. The quantity h is the bed elevation, t time, and q_b the bedload.

The solution of the Exner equation can lead to local bed slopes in excess of the angle of repose, when left un-checked. To avoid this, a sand slide model, the third element of the morphologic model, may be employed (see, e.g., Roulund et al., 2005). In this exercise, the sand-slide model is activated at positions where the local bed angle exceeds the angle of repose of the sediment.

For the numerical calculations, the computational domain is discretized into finite volumes of blocks in varying shapes and dimensions, and during the live-bed calculations, the mesh is continuously updated to adjust the changes of bed topography. To get a sense of the number of cells as well as the dimensions of the computational domain required in a typical modelling work, refer to e.g., Fuhrman et al. (2014), and Baykal et al. (2014 a and b), all three studies undertaken under MERMAID. These references can also be consulted for typical computational times for the simulations.

The preceding paragraphs have summarized the underlying principles involving in and standard practices associated with a regular numerical modelling exercise of scour and backfill around structures.

Next, we shall turn our attention to the work conducted in the MERMAID project.

5.1.2 Numerical modelling of scour and backfilling in the MERMAID project

Numerical modelling of scour around a monopile

In the present project, flow and scour around a monopile exposed to current are investigated, using a three-dimensional numerical model based on incompressible Reynolds-averaged Navier-Stokes equations, described in greater details in the previous section.

The model incorporates (1) *k-omega* turbulence closure, (2) vortex shedding processes, (3) sediment transport (both bed and suspended load), as well as (4) the bed morphology.

Of particular interest has been the influence of vortex shedding and suspended load on scour. This could be investigated fairly easily as the numerical modelling enables one to switch on and off various features of the hydrodynamic processes, and therefore enables one to investigate the influence of these features in a systematic manner. Two major effects investigated in the present work are (1) the influence of the suspended sediment transport, and (2) that of the vortex shedding on scour. For the selected geometry and flow conditions, it is found that the equilibrium scour depth is decreased by 50% when the suspended sediment transport is not accounted for (Baykal et al., 2014 a). Similarly, the effect of the vortex shedding is also investigated, and found to be limited to the very early stage of the scour process.

In the study, flow features such as the horseshoe vortex, as well as lee-wake vortices, including their vertical frequency variation, are also discussed, on the basis of the obtained results from extensive simulation tests (Baykal et al., 2014 a).

One major finding of the study is that the numerical simulations revealed the presence of two large scale counter-rotating streamwise vortices in the lee wake of the pile (Baykal et al., 2014). These vortices were first noticed in the Ph.D. study of Petersen (2014), also partially supported by MERMAID. These vortices are the major mechanism of edge scour in tidal flows, as revealed by Petersen's (2014) study. The latter will be described in details under Section 4.3.

Numerical modelling of backfilling around a monopile

As mentioned previously, an offshore wind turbine foundation continuously experiences scour and backfilling in an alternating manner under an ever changing wave and current climate. The scour hole created, for example, under current or under a severe wave climate is backfilled in a milder wave climate.

Engineering models for predicting the time history of scour and backfilling for large times (weeks, months, or years) have essentially two components: scour and backfilling. The existing information on scour has been successfully incorporated in these models. This was not so, however, until quite recently because there was a significant lack of knowledge on backfilling (Sumer et al., 2013, 2014).

Sumer et al. (2013) have reported the results of an experimental study on backfilling around piles exposed to waves and currents. The latter has shed light onto the understanding of the backfilling process. It has also presented a comprehensive set of data on various properties of the backfilling process, particularly for the time scale, a crucially important quantity used in the previously mentioned engineering models.

Under MERMAID project, we have initiated a numerical modelling effort to simulate backfilling of scour holes. This has been achieved for two benchmark cases: pipelines (Fuhrman et al., 2014), and

piles (Baykal et al., 2014 b). The present section will highlight the key results of the latter two studies. A detailed discussion can also be found in Sumer et al. (2014).

In Fuhrman et al. (2014), a fully-coupled hydrodynamic/morphodynamic numerical model is adopted and utilized for the simulation of wave-induced scour and backfilling processes beneath submarine pipelines. The model is based on solutions to RANS equations, coupled with k-ω turbulence closure, with additional bed and suspended load descriptions forming the basis for seabed morphology. As mentioned previously, the morphology is updated continuously, rather than being based on period- or other time-averaging techniques. Simulations involving wave-induced scour over the range of Keulegan-Carpenter number $5.6 < KC < 30$ demonstrate reasonable agreement with previous experiments.

Fuhrman et al. (2014) implemented the same model to investigate the backfilling process numerically beneath pipelines. In the backfilling simulations, the initial conditions were taken from the scour simulations with larger KC numbers to new wave climates characterized by lower KC values. The simulations demonstrated the ability of the model to predict backfilling towards expected equilibrium scour depths based on the new wave climate, in line with experimental expectations (Fredsøe et al., 1992). The results showed that the simulated backfilling process is characterized by two stages: (1) An initial, fast re-distribution phase involving re-organization of sediments in the immediate vicinity of the pipeline, potentially followed by (2) a more lengthy backfilling evolution towards equilibrium scour depth. From the simulation results, the initial, fast backfilling is evidently associated with the two humps at the two sides of the scour hole; sediment being brought into the scour hole from these humps. Fuhrman et al.'s (2014) work is discussed at a great length also in Sumer et al. (2014).

In a separate study, the same numerical model has been implemented and utilized for the simulation of scour and backfilling processes around, a model monopile of an offshore wind turbine (Baykal et al., 2014 b). The initial scour hole is generated numerically by the same numerical model.

The simulation results show that, regardless of the initial scour hole geometry (flat or scoured), the equilibrium scour depth of the backfilling process is the same as that of the ordinary scour process for the same Keulegan-Carpenter number, KC, a result first obtained experimentally by Sumer et al. (2013).

As in the case of the pipeline, the simulation results also show that the backfilling process occurs in two stages: A rapid, first stage, followed by a rather slow backfilling process. The first stage is associated with the backfilling with the sediment originating from the bed feature(s) in the immediate neighbourhood of the initial scour hole. It may be expected, however, that the backfilling takes place only with the second, slow stage in the absence of the bed features, for example, in the case of a pile with a long-duration current scour where the bed features (the downstream dunes) are washed away; see the discussion in Sumer et al. (2014).

Figure 5.4 displays a sequence of scour pictures illustrating backfilling in a simulation where the flow is changed from steady current to waves with KC=10, reproduced from Baykal et al. (2014 b). The median grain size diameter is 0.17 mm and the model pile diameter D=0.04 m. The equilibrium scour profile used as the initial bed profile (Time=0) for backfilling simulations is achieved with a

steady current scour simulation, in which the current velocity is V=41 cm/s, the friction velocity is U_f =1.9 cm/s, and the corresponding Shields parameter is θ=0.13, larger than the critical value for the initiation of motion, θ_c =0.05, implying that the scour is in the live-bed regime. The equilibrium scour depth obtained in the steady current simulation is S/D=0.91, where S is the scour depth in front of the pile. This value agrees well with the existing data, for the present water-depth-to-pile-diameter ratio δ/D=2 in the simulation (Sumer and Fredsøe, 2002).

In the backfilling with KC=10, the maximum value of the free-stream velocity of the oscillatory flow in the test is U_m=22.5 cm/s and the wave period is T_w=1.79 s, giving a Keulegan-Carpenter number of KC=10. The Shields parameter is θ=0.15, implying that the live bed conditions prevail, revealed by the presence of ripples in the far field.

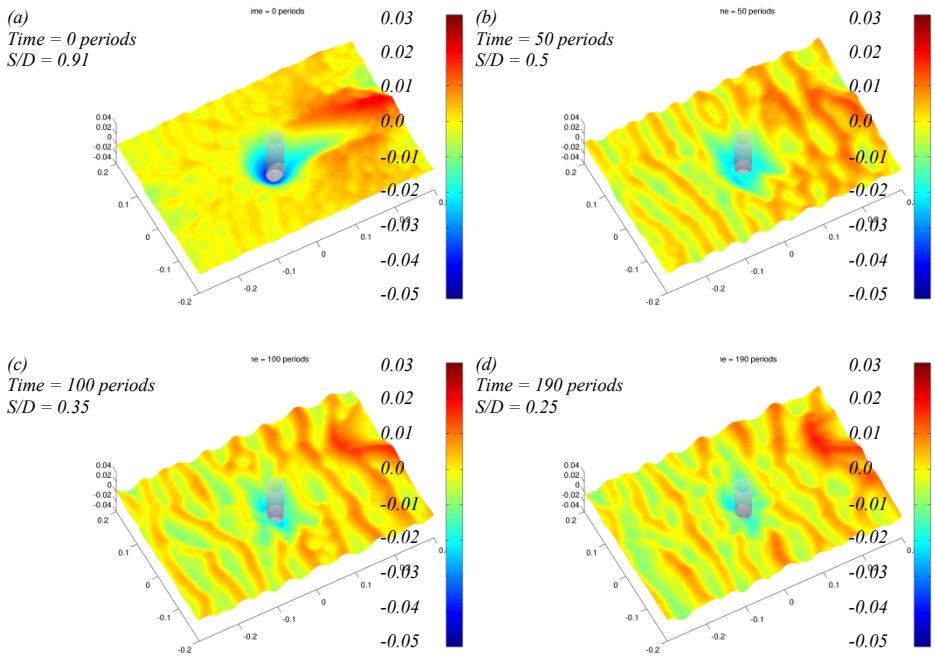

Figure 5.4 Development of backfilling. Initial scour morphology (Panel Time=0) generated by a current is obtained by the present code. Backfilling occurs with the flow switching from current to waves with KC=10. Scales are in m.

At this juncture, we note the following. The current state-of-art in numerical simulations of scour/backfilling below pipelines allow one to predict the alternating scour and backfilling below pipelines for large times (days, weeks) in real life situations, an important point for assessments of fatigue life of marine pipelines (Fuhrman et al., 2014). (Sumer et al., 2014, comment, however, that this is for 2D calculations, noting that ocean waves and currents are often not perpendicular nor co-linear to the pipe. In addition, the scour hole also introduces 3D effects near the span shoulders.)

By contrast, Baykal et al.'s (2014 a and b) pile simulations indicate that large time (weeks, months) predictions of alternating scour and backfilling of scour holes around piles seem not to be feasible at

the present time due to “prohibitively” large computational times for large-time predictions, as noted by Sumer et al. (2014).

5.1.3 List of publications produced during the project cycle on the topic

- Baykal, C., Sumer, B. M., Fuhrman, D. R., Jacobsen, N. G. and Fredsøe, J., (2014 a). Numerical investigation of flow and scour around a vertical circular cylinder. To appear in Philosophical Transactions of the Royal Society of London A. Special Issue on Advances in Fluid mechanics for Offshore Engineering. Accepted.

- Baykal, C., Sumer, B. M., Fuhrman, D. R., Jacobsen, N. G. and Fredsøe, J., (2014 b). Numerical modelling of backfilling process around monopiles. To appear in Proceedings of Coastal Engineering Conference, ICCE 2014.

- Fuhrman, D. R., Baykal, C., Sumer, B. M., Jacobsen, N. G. and Fredsøe, J., (2014). Numerical simulation of wave-induced scour and backfilling processes beneath submarine pipelines. Coastal Engineering, vol. 94, 10-22.

- Sumer, B.M., Baykal, C., Fuhrman, N.G., Jacobsen, N.G. and Fredsøe, J. (2014). Numerical calculation of backfilling of scour holes. Proc. 7th Int. Conf. Scour Erosion, ICSE, Perth, Australia.

- Sumer, B.M. (2014). A review of recent advances in numerical modelling of local scour problems. Keynote paper. Proc. 7th Int. Conf. Scour Erosion, ICSE, Perth, Australia.

- Sumer, B.M. (2014). Flow-structure-seabed interactions in coastal and marine environments. Vision Paper. Journal of Hydraulic Research, vol.52, No. 1, 1-13.

5.1.4 References

Baykal, C., Sumer, B. M., Fuhrman, D. R., Jacobsen, N. G. and Fredsøe, J., (2014 a). Numerical investigation of flow and scour around a vertical circular cylinder. To appear in Philosophical Transactions of the Royal Society of London A. Special Issue on Advances in Fluid mechanics for Offshore Engineering. Accepted.

Baykal, C., Sumer, B. M., Fuhrman, D. R., Jacobsen, N. G. and Fredsøe, J., (2014 b). Numerical modelling of backfilling process around monopiles. To appear in Proceedings of Coastal Engineering Conference, ICCE 2014

Engelund F, Fredsøe J. 1976 A sediment transport model for straight alluvial channels. *Nordic Hydrol.* **7**, 293–306.

Fuhrman DR, Baykal C, Sumer BM, Jacobsen NG, Fredsøe J. 2014 Numerical simulation of wave-induced scour and backfilling processes beneath submarine pipelines. *Coast. Eng*. **94**, 10–22

Gothel O, Zilke V. 2006 Numerical modeling of scour at offshore wind turbines. In *Proc. 30th Int. Conf. on Coastal Engineering, San Diego, CA, 3–8 September 2006*, vol. 3, pp. 2343–2353. Singapore:World Scientific.

Gothel O. 2008 Numerical modeling of flow and wave-induced scour around vertical structures. PhD thesis, Leibniz University of Hanover, Faculty of Civil Engineering and Geodesy, Hanover, Germany.

Liang, D., Cheng, L., 2005. Numerical model for wave-induced scour below a submarine pipeline. J. Waterw. Port Coast. ASCE 131, 193–202.

Olsen NRB, Melaaen M. 1993 Three-dimensional calculation of scour around cylinders. *J. Hydraul. Eng. ASCE* **119**, 1048–1054.

Olsen NRB, Kjellesvig HM. 1998 Three-dimensional numerical flow modeling for estimation of maximum local scour depth. *J. Hydraul. Eng. ASCE* **36**, 579–590.

Petersen TU. 2014 Scour around offshore wind turbine foundations. PhD thesis, Technical University of Denmark, Kongens Lyngby, Denmark.

Roulund A, Sumer BM, Fredsøe J, Michelsen J. 2005 Numerical and experimental investigation of flow and scour around a circular pile. *J. FluidMech.* **534**, 351–401.

Sumer, B.M., Deigaard, R., 1981. Particle motions near the bottom in turbulent flow in an open channel. Part 2. J. Fluid Mech. 109, 311–337.

Sumer BM, Fredsøe J. 2002 *The mechanics of scour in the marine environment*. Singapore: World Scientific.

Sumer, BM 2004, 'Physical and mathematical modelling of scour'. in Y-M Chiew, S-Y Lim & N-S Cheng (eds), Procedings of Second International Conference on Scour and Erosion. Stallion Press, Singapore, 14-17 November, pp. 29-46.

Sumer, B. M. (2007). “Mathematical modelling of scour: A review.” J. Hydraul. Res., 45(6), 723e735.

Sumer, BM, Petersen, TU, Locatelli, L, Fredsøe, J, Musumeci, RE & Foti, E 2013, 'Backfilling of a Scour Hole around a Pile in Waves and Current' *Journal of Waterway, Port, Coastal, and Ocean Engineering*, vol 139, no. 1, pp. 9-23.

Sumer, BM 2014, 'Flow-structure-seabed interactions in coastal and marine environments' *Journal of Hydraulic Research*, vol 52, no. 1, pp. 1-13

Wilcox DC. 2006 *Turbulence modeling in CFD*, 3rd edn. La Canada, CA: DCW Industries, Inc.

Wilcox DC. 2008 Formulation of the *k*- ω turbulence model revisited. *AIAA J.* **46**, 2823–2838.

Wittrup, S. (2012). Horseshoe vortex washes out the sediment around offshore wind turbines. An article published in Ingeniøren/energi&miljø, 16 January, 2012. Danish. http://ing.dk/artikel/125792-hestesko-hvirvler-vasker-bunden-omkring-havvindmoeller-vaek.

5.2 Edge Scour

Thor Ugelvig Petersen, B. Mutlu Sumer, Jørgen Fredsøe, Tim C. Raaijmakers, Jan-Joost Schouten,

This research has been submitted to Coastal Engineering for its possible publication. The full manuscript is obtainable from B. Mutlu Sumer (bms@mek.dtu.dk). The following is an extended abstract, highlighting the key findings of the study.

When building offshore wind turbines with monopile foundations, scour protection typically is placed to avoid scouring of the soil close to the monopile. An important aspect is that the scour protection itself causes erosion, inflicted by the local increase in current and/or wave velocities and in turn increased bed shear stresses, the so-called edge scour Figure 5.5.

The edge scour alongside the scour protection may cause deformations and failure of the scour protection of offshore wind turbine foundations. This can reduce the stability of the stone layer and cause exposure of cables running between the monopiles where they go from buried to the transition piece on the foundation.

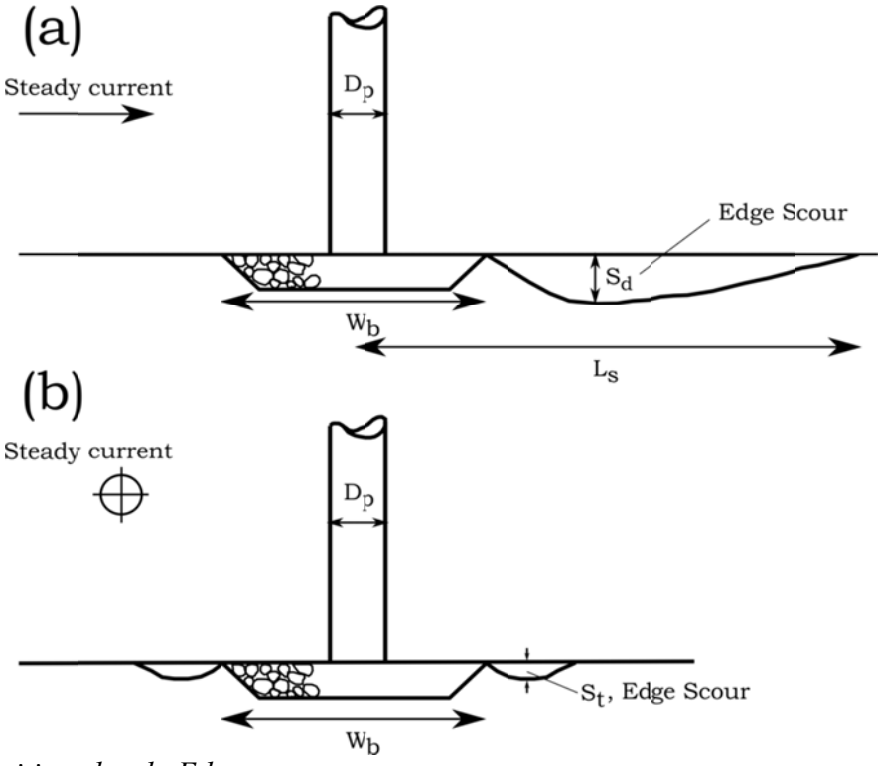

Figure 5.5 Definition sketch. Edge scour.

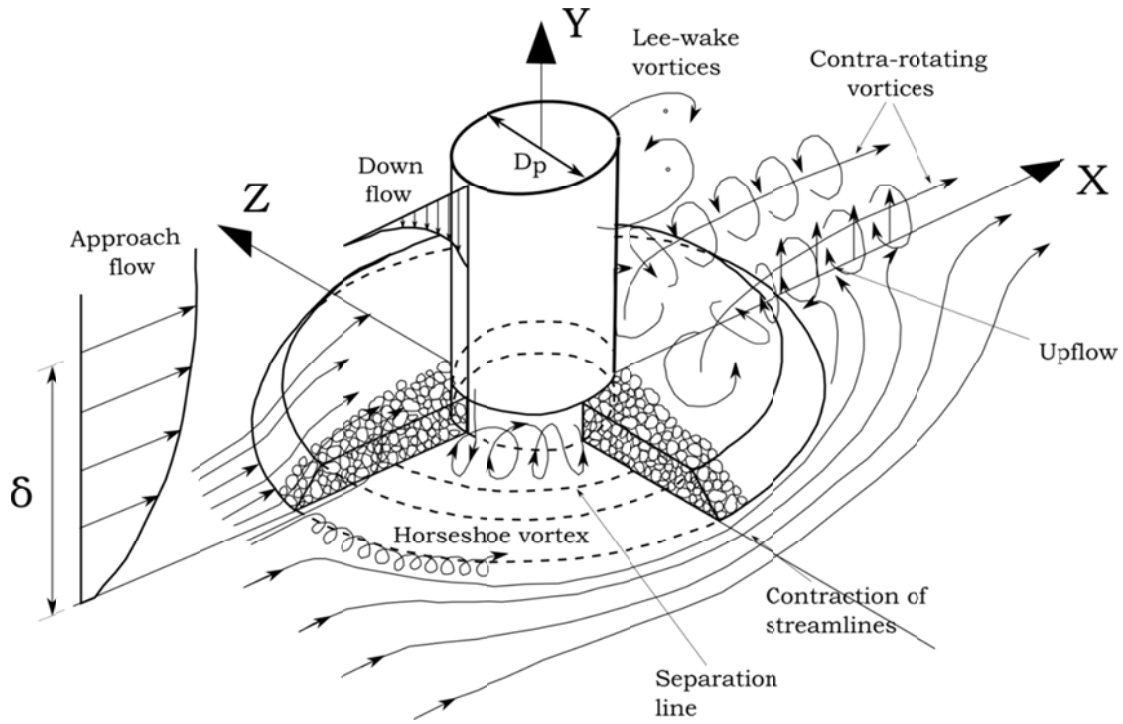

Figure 5.6. Flow around a monopile and its scour protection. Edge scour is, for the most part, governed by the counter-rotating vortices at the lee-wake side of the pile and scour-protection system.

Although much information is available on the design of scour protection systems around monopiles, little is known on the mechanisms causing edge scour and the equilibrium stages of the edge scour process in steady current, waves and combined waves and current.

The paper presents the results of an extensive experimental campaign to explain the edge sour process in current and combined waves and current. The three-dimensional flow field around the pile and scour protection is resolved by particle image velocimetry and bed shear stress measurements, showing a local increase in the hydrodynamic field leading to increased sediment transport and scour.

The governing process in steady current is a pair of symmetric counter-rotating vortices (Figure 5.6 and Figure 5.7, emerging in the near bed region in the wake of the pile and scour protection, causing a significant downstream scour hole. The “signature” or “foot-print” of these counter-rotating vortices on the sediment bed can be seen in Figure 5.7 in which the arrows depict the sense of rotation of the vortices.

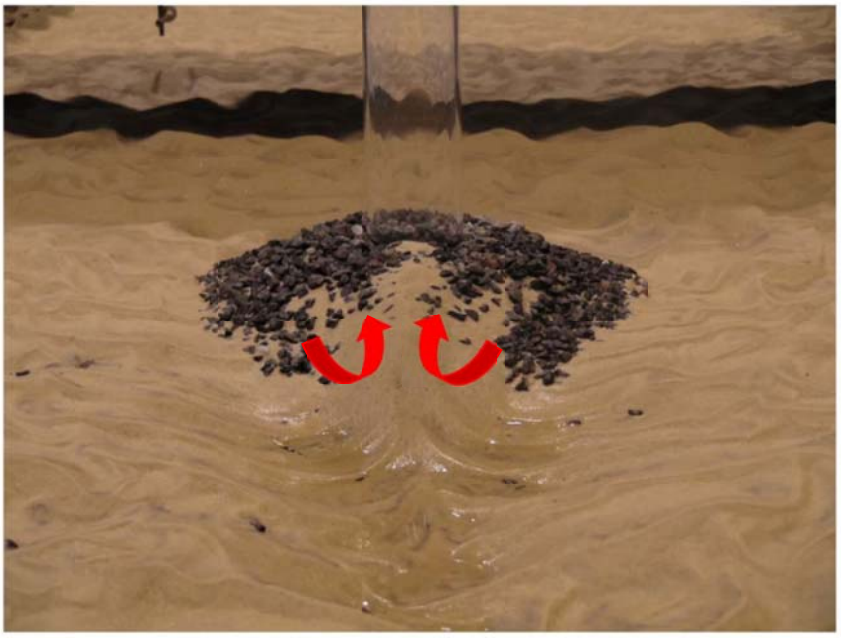

Figure 5.7 Image taken downstream of a pile with scour protection, facing upstream. Notice the foot-print of the counter-rotating vortices on the sediment bed.

The present experiments show that the depth and length of the equilibrium scour hole scale with the pile diameter and the ratio between the thickness- and the width of the scour protection Figure 5.8.

In the second part of the paper, the results from the laboratory experiments are compared with the edge scour experienced in the field, outlined by a survey programme of the offshore wind park Egmond Aan Zee Figure 5.9, and a published field investigation of Scroby Sands OWF by Whitehouse et al. (2011) Figure 5.10.

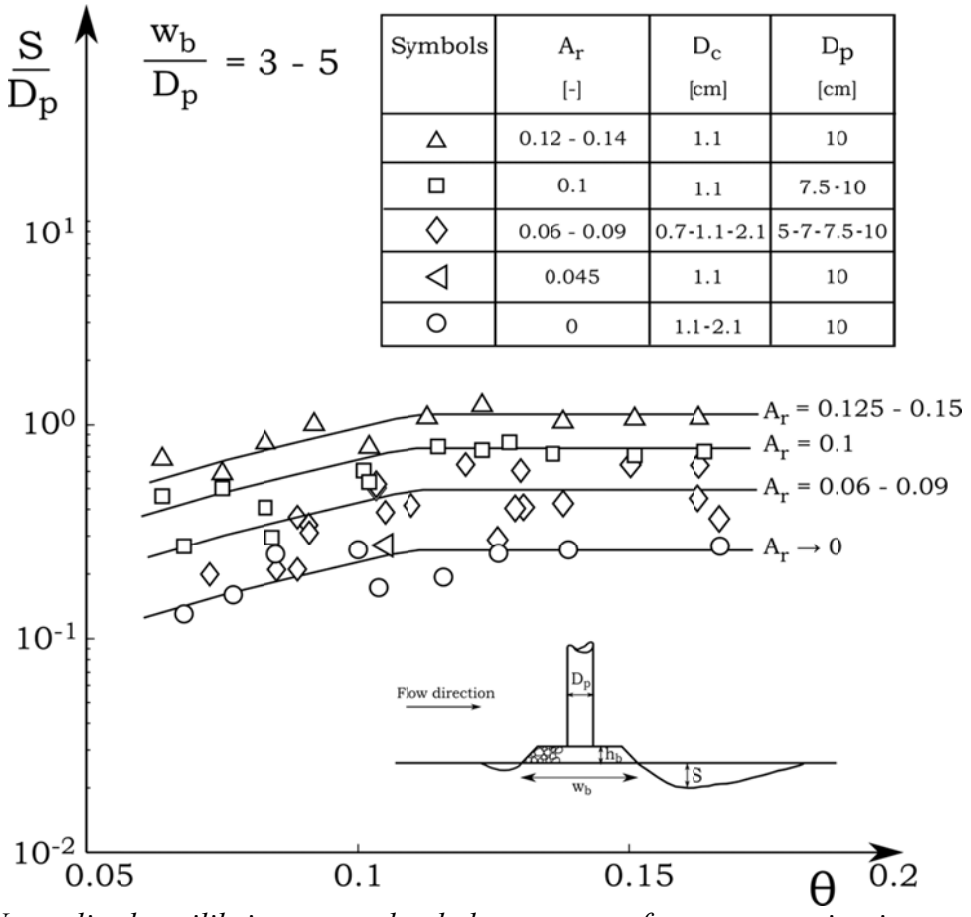

Figure 5.8 Normalized equilibrium scour depth downstream of scour protection in steady current. Live bed $(\theta > \theta_c)$*. Here the aspect ratio* $A_r = \frac{h_b}{w_b}$.

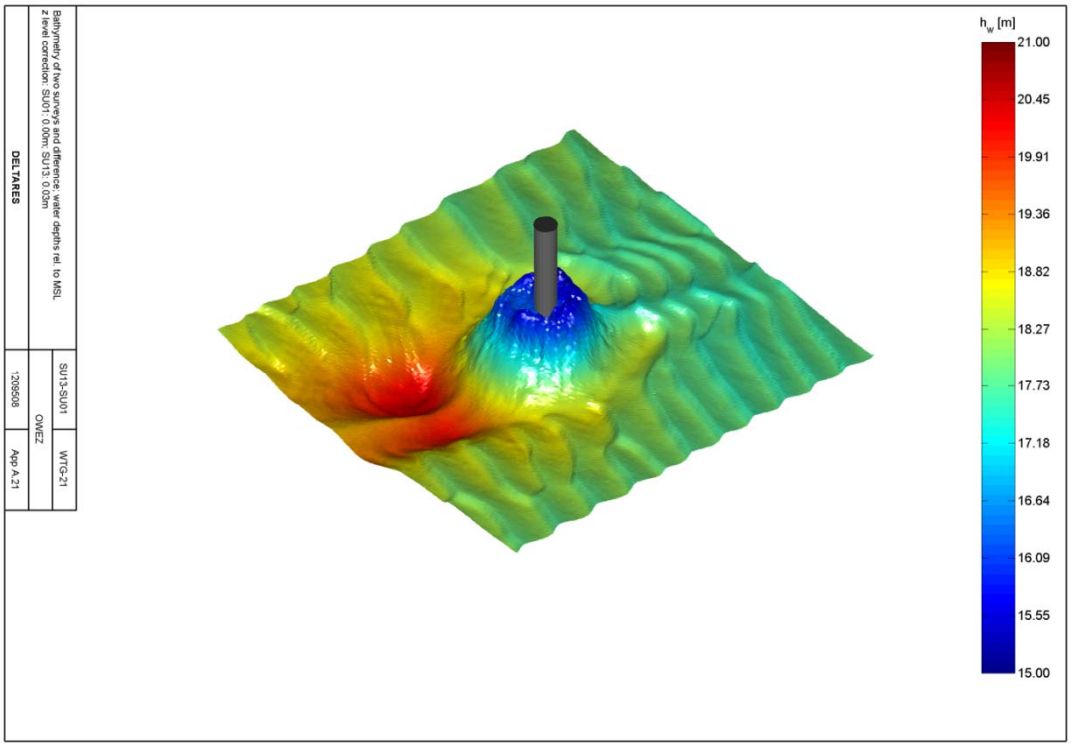

Figure 5.9 D-bathymetry around an individual monopile. Offshore wind park Egmond Aan Zee. In order to show more clearly the bed level elevations, the vertical axis is five times stretched, relative to the horizontal axis.

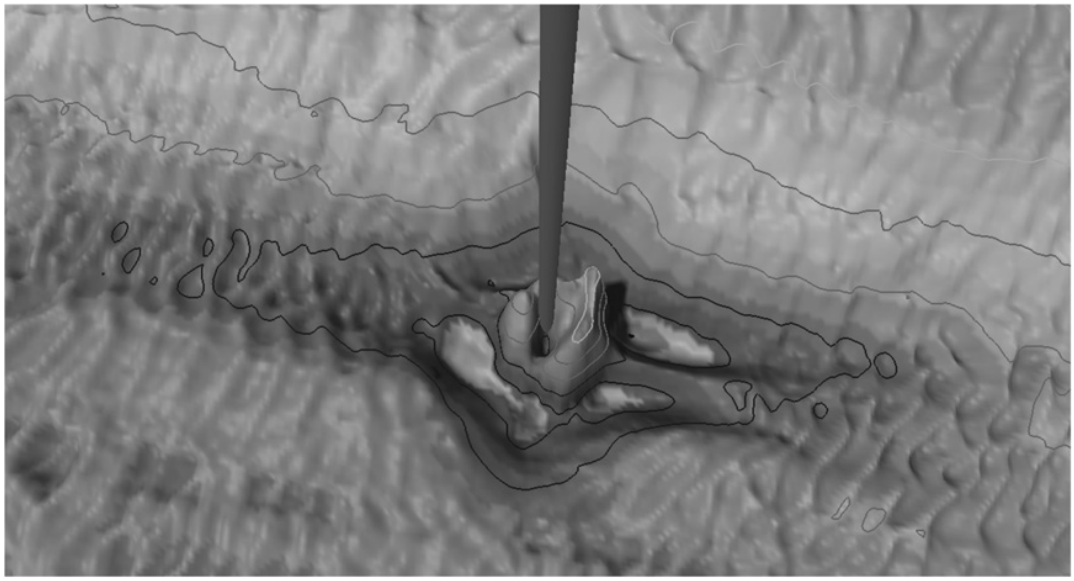

Figure 5.10. Typical scour hole with scour protection installed. Scroby Sands OWF, view looking east with depth contours at 1 m intervals (vertical exaggeration x 10). Reproduced with permission from Figure 5.8Fig. 4 in Whitehouse et al. (2011).

5.2.1 **References:**

Whitehouse, R. J. S., Harris, J. M., Rees, J. (2011) “The nature of scour development and scour protection at offshore windfarm foundations.” Marine Pollution Bulletin 62 (2011) 73-88.

6 Discussion

The processes described and the suggested methodologies are valid for single use as well as for multi-use of an offshore area. The way MERMAID sees the multi –use concept it will primarily be a combination of different functionalities within the same area.

The environmental impact of MUOP in general will be treated in details in other deliverables. However, certain aspects should be mentioned here where we address the interaction between different functionalities in a MUOP. The implementation phases of the different structures has to be addressed as spreading of sediment from dredging operations related to foundations etc. might have a negative impact on aquaculture production. Here the near field spreading mechanisms as detailed in this report becomes very important. An efficient planning of installation processes could potentially reduce the negative impact substantial.

The numerical tools have been used to analyse carbon and nutrient flows. These tools estimate the impact of extractive aquaculture on ecological and production carrying capacity. This is extremely important in designing optimal Integrated Multi-Trophic Aquaculture (IMTAs) set-ups. Multi-scale models such as these should be able to provide information on the most appropriate spacing and positioning of different trophic components of the IMTA taking local hydrodynamic conditions into account.

In theory it is possible to set up extractive aquaculture in such a way that it serves multiple purposes. E.g. seaweed farms can directly reduce the amount of nutrients in the environment (reducing eutrophication) and shellfish farms can reduce the algal biomass in a system (reducing the effects of eutrophication). However, optimising yield and optimising water quality may have different requirements. Sustainable aquaculture also needs to be profitable.

One of the effects that arise from the multi-use concept is the shadow effect. This can lead to less harsh conditions and therefore safer design in the lee area. For instance (Christensen et al., 2013) and (Christensen, Petersen, & Deigaard, 2014) analysed the impact of offshore wind turbines on the wave field and the resulting sediment transport on a typical high energy coast. The most important conclusion from that study was that the effect on the wave field was up to a few percent. The largest impact was observed on the lee side of the offshore wind farm. Similar studies have been made of wave energy converters (WEC), where the WEC's reduce the wave energy on the lee side of the structures. These lee side effects should be taken into account when designing the MUOP as they can reduce the risk and increase the safety of the structures situated in the lee area.

In deeper waters it might be an advantage to build functionalities into one structure. This could for instance be a combination of a fish cage around a floating foundation for an offshore wind turbine. The combination increases typically the force on the structure, which might be undesirable. However the fish cage structure acts as a porous medium. The porous medium dampens the movements of the entire structure that will make the wind turbine less vulnerable to wave induced

motions of the entire structure. As fatigue of the structure is often the most critical part of the structure this might lead to less expensive designs as fish cage reduces the motion of the structure. These phenomena can be analysed with the methodologies that has been developed or are under development in the MERMAID project, such as physical model experiments and advanced numerical methods based on for instance computational fluid dynamics (CFD).

In shallow to intermediate depth (10-40 m) support structures for offshore wind turbines are often bottom mounted. The foundations typically interact with a loose sandy seabed. The interaction results in erosion round the structure called scour. Scour holes can be several meters deep, typically up to a diameter of a monopile or even larger. This means that for a pile diameter of 5 m the hole can be 5-7 m deep. Therefore scour protection layers are used to avoid the development of the scour hole. These phenomena have been described in more detail in the previous chapters of this report. The installation of the scour protection layers does not fully stop morphological changes of the seabed, as scour will take place on the edge of the scour protection layer. The overall impact of many scour protection layers on the morphology inside an offshore wind farm or even more complex, a wind farm with aquaculture is not known and calls for more research and development.

6.1 References

Christensen, E.D., Johnson, M., Sørensen, O.R., Hasager, C.B., Badger, M., Larsen, S.E., 2013. Transmission of wave energy through an offshore wind turbine farm. Coast. Eng. 82, 25–46.

Christensen, E.D., Petersen, S.E., Deigaard, R., 2014. IMPACT OF AN OFFSHORE WIND FARM ON WAVE CONDITIONS AND SHORELINE, in: International Conference on Coastal Engineering (ICCE). Seoul, South Korea, pp. 1–13.